

# Engineering Nanostructures of Inorganic Materials for Optical and Chemical Applications

Guest Editors: Yong Yang, Masayuki Nogami, Zhengren Huang,  
and Yongsheng Li





---

# **Engineering Nanostructures of Inorganic Materials for Optical and Chemical Applications**

Journal of Nanomaterials

---

**Engineering Nanostructures of  
Inorganic Materials for Optical  
and Chemical Applications**

Guest Editors: Yong Yang, Masayuki Nogami,  
Zhengren Huang, and Yongsheng Li



---

Copyright © 2013 Hindawi Publishing Corporation. All rights reserved.

This is a special issue published in "Journal of Nanomaterials." All articles are open access articles distributed under the Creative Commons Attribution License, which permits unrestricted use, distribution, and reproduction in any medium, provided the original work is properly cited.

## Editorial Board

Katerina E. Aifantis, Greece  
Nageh K. Allam, USA  
Margarida Amaral, Portugal  
Xuedong Bai, China  
Lavinia Balan, France  
Enrico Bergamaschi, Italy  
Theodorian Borca-Tasciuc, USA  
C. Jeffrey Brinker, USA  
Christian Brosseau, France  
Xuebo Cao, China  
Shafiq Chowdhury, USA  
Kwang-Leong Choy, UK  
Cui ChunXiang, China  
M. A. Correa-Duarte, Spain  
Shadi A. Dayeh, USA  
Claude Estourns, France  
Alan Fuchs, USA  
Lian Gao, China  
Russell E. Gorga, USA  
Hongchen Chen Gu, China  
Mustafa O. Guler, Turkey  
John Zhanhu Guo, USA  
Smrati Gupta, Germany  
Michael Harris, USA  
Zhongkui Hong, China  
Michael Hu, USA  
David Hui, USA  
Y.-K. Jeong, Republic of Korea  
Sheng-Rui Jian, Taiwan  
Wanqin Jin, China  
Rakesh K. Joshi, UK  
Zhenhui Kang, China  
Fathallah Karimzadeh, Iran  
Alireza Khataee, Iran  
Do Kyung Kim, Republic of Korea

Alan K. T. Lau, Hong Kong  
Burtrand Lee, USA  
Benxia Li, China  
Jun Li, Singapore  
Xing-Jie Liang, China  
Shijun Liao, China  
Gong Ru Lin, Taiwan  
J. -Y. Liu, USA  
Tianxi Liu, China  
Songwei Lu, USA  
Daniel Lu, China  
Jue Lu, USA  
Ed Ma, USA  
Gaurav Mago, USA  
Santanu K. Maiti, India  
Sanjay R. Mathur, Germany  
Vikas Mittal, United Arab Emirates  
Weihai Ni, Germany  
Sherine Obare, USA  
Atsuto Okamoto, Japan  
Abdelwahab Omri, Canada  
Edward Andrew Payzant, USA  
Kui-Qing Peng, China  
Anukorn Phuruangrat, Thailand  
Mahendra Rai, India  
Suprakas Sinha Ray, South Africa  
Ugur Serincan, Turkey  
Huaiyu Shao, Japan  
Donglu Shi, USA  
Vladimir Sivakov, Germany  
Marinella Striccoli, Italy  
Bohua Sun, South Africa  
Saikat Talapatra, USA  
Nairong Tao, China  
Titipun Thongtem, Thailand

Somchai Thongtem, Thailand  
Alexander Tolmachev, Ukraine  
Valeri P. Tolstoy, Russia  
Tsungh-Yen Tsai, Taiwan  
Takuya Tsuzuki, Australia  
Raquel Verdejo, Spain  
Mat U. Wahit, Malaysia  
Shiren Wang, USA  
Yong Wang, USA  
Ruiping Wang, Canada  
Cheng Wang, China  
Zhenbo Wang, China  
Jinquan Wei, China  
Ching-Ping Wong, Hong Kong  
Xingcai Wu, China  
Guodong Xia, Hong Kong  
Zhi Li Xiao, USA  
Ping Xiao, UK  
Shuangxi Xing, China  
Yangchuan Xing, USA  
N. Xu, China  
Doron Yadlovker, Israel  
Yingkui Yang, China  
Khaled Youssef, USA  
Kui Yu, Canada  
William W. Yu, USA  
Haibo Zeng, China  
Tianyou Zhai, Japan  
Renyun Zhang, Sweden  
Bin Zhang, China  
Yanbao Zhao, China  
Lianxi Zheng, Singapore  
Chunyi Zhi, Hong Kong

## Contents

**Engineering Nanostructures of Inorganic Materials for Optical and Chemical Applications**, Yong Yang, Masayuki Nogami, Zhengren Huang, and Yongsheng Li  
Volume 2013, Article ID 157869, 1 page

**Engineering Metal Nanostructure for SERS Application**, Yanqin Cao, Dan Li, Fang Jiang, Yong Yang, and Zhengren Huang  
Volume 2013, Article ID 123812, 12 pages

**Nucleation and Growth Mechanism of Si Amorphous Film Deposited by PIAD**, D. Li, G. L. Liu, Y. Yang, J. H. Wu, and Z. R. Huang  
Volume 2013, Article ID 383867, 7 pages

**Shape-Controlled Metal Nanoparticles and Their Assemblies with Optical Functionalities**, Go Kawamura, Masayuki Nogami, and Atsunori Matsuda  
Volume 2013, Article ID 631350, 17 pages

**Ferromagnetic Behaviors in Fe-Doped NiO Nanofibers Synthesized by Electrospinning Method**, Yi-Dong Luo, Yuan-Hua Lin, Xuehui Zhang, Deping Liu, Yang Shen, and Ce-Wen Nan  
Volume 2013, Article ID 252593, 4 pages

**Research Progress of Optical Fabrication and Surface-Microstructure Modification of SiC**, Fang Jiang, Yan Liu, Yong Yang, Zheng-Ren Huang, Dan Li, Gui-ling Liu, and Xue-Jian Liu  
Volume 2012, Article ID 984048, 9 pages

**Microstructure and Glass Phase of Inorganic Binder Coated on Mold for Thin Casting**, Eun-Hee Kim, Geun-Ho Cho, Yeon-Gil Jung, Je-Hyun Lee, Baig-Gyu Choi, and Chang Young Jo  
Volume 2012, Article ID 126567, 6 pages

**GaN Schottky Diode with TiW Electrodes on Silicon Substrate Based on AlN/AlGaN Buffer Layer**, Sheng-Po Chang  
Volume 2012, Article ID 452310, 5 pages

**Polyol-Free Synthesis of Uniformly Dispersed Pt/Graphene Oxide Electrocatalyst by Sulfuric Acid Treatment**, Tae Kyu Lee, Hyang Jin Park, Min Ki Kwon, Ju Hae Jung, Junbom Kim, and Seung Hyun Hur  
Volume 2012, Article ID 418737, 6 pages

**Aluminum Silicate Nanotube Coating of Siloxane-Poly(lactic acid)-Vaterite Composite Fibermats for Bone Regeneration**, Shuji Yamazaki, Hiroataka Maeda, Akiko Obata, Keiichi Inukai, Katsuya Kato, and Toshihiro Kasuga  
Volume 2012, Article ID 463768, 7 pages

**Effect Factors of Benzene Adsorption and Degradation by Nano-TiO<sub>2</sub> Immobilized on Diatomite**, Lijun Cheng, Yong Kang, and Guishui Li  
Volume 2012, Article ID 593924, 6 pages



---

**Participation of the Third Order Optical Nonlinearities in Nanostructured Silver Doped Zinc Oxide  
Thin Solid Films**, C. Torres-Torres, L. Castañeda, M. Trejo-Valdez, A. Maldonado, and R. Torres-Martínez  
Volume 2012, Article ID 353061, 5 pages

## Editorial

# Engineering Nanostructures of Inorganic Materials for Optical and Chemical Applications

Yong Yang,<sup>1</sup> Masayuki Nogami,<sup>1</sup> Zhengren Huang,<sup>1</sup> and Yongsheng Li<sup>2</sup>

<sup>1</sup> State Key Laboratory of High Performance Ceramics and Superfine Microstructure, Shanghai Institute of Ceramics, Chinese Academy of Sciences, Shanghai 200050, China

<sup>2</sup> East China University of Science and Technology, Shanghai 200237, China

Correspondence should be addressed to Yong Yang; yangyong@mail.sic.ac.cn

Received 26 November 2013; Accepted 26 November 2013

Copyright © 2013 Yong Yang et al. This is an open access article distributed under the Creative Commons Attribution License, which permits unrestricted use, distribution, and reproduction in any medium, provided the original work is properly cited.

Considerable interest is being exhibited in the novel and enhanced properties of nanostructured materials. These materials, with their constituent phase or grain structures modulated on a length scale of less than 100 nm, are now artificially synthesized by a wide variety of physical, chemical, and mechanical methods. Today, scientists and engineers have access to a wealth of technologies such as self-assembly, chemical template, electron-beam lithography, focused-ion-beam (FIB) lithography, nanoimprint, nanomolding, and scanning-probe lithography to build nanostructures at unprecedented scales, resolution, and throughput. The art of developing functionalized nanostructured materials exploiting unusual interfacial properties seems to have produced hitherto unknown man-made materials. Exploitations of nanostructured metal and oxide materials with many excited optical, chemical, and mechanical properties will lead to the broad range of potential applications including catalyst, drug discovery, sensing, nanoimaging, spectroscopy, optoelectronics, data storage, and structured-materials with enhanced mechanical properties.

In this special issue, a series of contributed papers is focused on the function-motivated nanostructure design, fabrication, characterization, and application including metal, oxide, and ceramics. A wide range of recent progress on the chemical and physical fabrication methods of metal nanostructures, their optical properties, and application has been reviewed by G. Kawamura's and Y. Yang's groups. C. T. Torres et al. reported the transmittance modulation of optical signals in a nanocomposite integrated by two

different silver doped zinc oxide thin solid films. T. K. Lee et al. reported polyol-free synthesis of highly loaded Pt catalysts on sulfuric-acid-treated graphene oxide (SGO) and their catalytic properties. Y. H. Lin's group reported Fe-doped NiO nanofibers synthesized by electrospinning method and studied their ferromagnetic behaviors. The surface modification of SiC ceramics and the optical application have been reviewed by F. Jiang. The nanostructures of Si, GaN, and TiO<sub>2</sub> and their optical-electric properties were studied by D. Li et al., S. P. Chang et al., and L. Cheng et al., respectively. Kasuga's group demonstrated aluminum silicate nanotube coating of siloxane-poly (lactic acid)-vaterite composite fibermats by electrospinning. This approach may provide a new method of improving the surface of polymer-based biomaterials.

## Acknowledgments

We would like to express our sincere appreciation to all the authors and coauthors and to all the reviewers for their contribution to this special issue. We also thank the reviewers for their time and valuable comments.

Yong Yang  
Masayuki Nogami  
Zhengren Huang  
Yongsheng Li

## Review Article

# Engineering Metal Nanostructure for SERS Application

Yanqin Cao,<sup>1,2</sup> Dan Li,<sup>1,2</sup> Fang Jiang,<sup>1,2</sup> Yong Yang,<sup>1</sup> and Zhengren Huang<sup>1</sup>

<sup>1</sup> State Key Laboratory of High Performance Ceramics and Superfine Microstructure, Shanghai Institute of Ceramics, Chinese Academy of Sciences, 1295 Dingxi Road, Shanghai 200050, China

<sup>2</sup> Graduate University of Chinese Academy of Sciences, Beijing 100049, China

Correspondence should be addressed to Yong Yang; yangyong@mail.sic.ac.cn

Received 4 October 2012; Accepted 10 December 2012

Academic Editor: Yongsheng Li

Copyright © 2013 Yanqin Cao et al. This is an open access article distributed under the Creative Commons Attribution License, which permits unrestricted use, distribution, and reproduction in any medium, provided the original work is properly cited.

Surface-enhanced Raman scattering (SERS) has attracted great attention due to its remarkable enhancement and excellent selectivity in the detection of various molecules. Noble metal nanomaterials have usually been employed for producing substrates that can be used in SERS because of their unique local plasma resonance. As the SERS enhancement of signals depends on parameters such as size, shape, morphology, arrangement, and dielectric environment of the nanostructure, there have been a number of studies on tunable nanofabrication and synthesis of noble metals. In this work, we will illustrate progress in engineering metallic nanostructures with various morphologies using versatile methods. We also discuss their SERS applications in different fields and the challenges.

## 1. Introduction

The physical phenomenon behind Raman spectroscopy is an inelastic scattering of a photon from a molecule in which the frequency changes precisely matching the difference in vibrational energy levels [1]. Raman spectroscopy offers rich information of molecules, such as molecular structures, surface information, interface reactions, and so forth [2]. The Raman signal is several orders of magnitude weaker than the fluorescence emission in most cases because of its very small scattering cross-section [3], thus preventing its applications in many fields. However, the discovery of the surface-enhanced Raman scattering (SERS) phenomenon renews interests in Raman scattering due to the improved signal intensity.

The first measurement of SERS was reported by Fleischmann et al. in 1974, who observed intense Raman signal from pyridine adsorbed onto a roughened silver electrode surface [4]. In 1977, Van Duyne and Jeanmaire reported that the enhanced Raman signal intensity was due to an increase of  $10^5$ - $10^6$  times from the scattering cross-section compared to the signal intensity of the bulk pyridine [5]. The effect was later called surface-enhanced Raman scattering (SERS).

Generally, noble metals and some oxides [6] are used as SERS substrates, but the SERS enhancement originated from metal oxides is not strong [7]. In this paper, we mainly discuss noble metal nanoparticles and their SERS applications.

Following the discovery of SERS, there have been an extensive amount of fundamental researches and theoretical studies on the SERS effect. After much debate, the general consensus is achieved that there are two important mechanisms underlying SERS: the electromagnetic enhancement and chemical enhancement, and the former is responsible for the major portion of SERS enhancement [8]. We will discuss the theories in detail in the following part.

There have emerged a number of reports focusing on metal substrates with various morphologies for SERS applications, such as nanospheres, nanocubes, aggregate [9], as well as well-designed one-dimensional (1D), two-dimensional (2D), three-dimensional (3D) arrays and patterns [8, 10]. With those special structures, SERS has been used in various fields, such as trace detection of chemical and biological molecules and fast and effective detection of food additives, illicitly sold narcotics, and explosives. Although there are so many methods and different designs, it is still a challenge

to produce highly sensitive, greatly selective, stable, reproducible substrates using a facile, robust, low-cost, and high-yield method.

In this paper, we will briefly review the theoretical background of SERS firstly. Then some typical methods for metallic SERS substrates will be demonstrated. At last, we will report popular applications of SERS in different practical fields.

## 2. Theoretical Background

Since the discovery of SERS, researchers have devoted much effort to understand the mechanism for the enhancement. At present, the electromagnetic enhancement and chemical enhancement are regarded as the two predominant mechanisms. While electromagnetic enhancement arises from increasing the applied electric field, chemical enhancement derives from amplifying the molecular polarizability. For electromagnetic enhancement, the intensity of Raman spectrum is proportional to the square of the induced dipole moment, which is a product of the molecular polarizability and the applied electric field [1].

Electromagnetic (EM) enhancement is due to that the optical field is facilitated by localized surface plasmon resonance (LSPR) of metallic nanostructure, which results in the enhanced Raman signal intensity [1]. At a certain excitation frequency, collective oscillation of electrons in the conduction band of the metal will resonate with the incident light, resulting in a strong oscillation of the surface electrons, which commonly known as LSPR [11]. LSPR may appear only when dimensions of the structure are much smaller than the wavelength of the light. Besides, the shape, architecture, composition, and surrounding environment of metal nanomaterials also affect the LSPR; thus, it is of great importance to design these parameters of nanomaterials for high SERS enhancement [1, 8, 12].

Chemical enhancement is considered to be relative to the direct interaction between the adsorbed molecule and the metal surface, which lead to an increased Raman cross-section for the adsorbed molecule [13]. The most attractive way is charge transfer between the adsorbed molecule and the metal surface [14]. Because of the chemisorptions of the molecules on the surface, new electronic states become accessible, which serves as resonant intermediate states resulting in the increase of the intensity. Ultimately, the chemical enhancement mechanism is a short-range effect due to the required direct adsorbate-surface interaction, which generally limits to only the first layer of adsorbed molecules [3, 14].

One of the important parameters to characterize SERS substrates is the enhancement factor (EF), which is especially true for the practical application of SERS and the comparison with the theoretical calculation [10, 15]. In fact, the most widely used definition of the enhancement factor is according to the following equation [1, 15, 16], which describes the overall enhancement in Raman scattering

$$EF = \frac{I_{\text{SERS}}/N_{\text{Surf}}}{I_{\text{RS}}/N_{\text{Vol}}} \quad (1)$$

In the above equation, while  $I_{\text{SERS}}$  denotes the intensity of the special band for the spectra of probe molecules which absorb

on the SERS substrate,  $I_{\text{RS}}$  denotes the intensity of the same band for the spectra of probe molecules in the Raman (non-SERS) measurement.  $N_{\text{Surf}}$  and  $N_{\text{Vol}}$  are the corresponding number of analyte molecules in the focal volume. Generally the magnitude of EF is in the range of  $10^4$ – $10^8$ ; however, in the single molecule SERS detection, the EF can reach up to  $10^{14}$ . A comprehensive study of enhancement factor was reported according to [15].

In general, the EM and chemical enhancement exist simultaneously, but the proportion of contributions is different, in which the former can give  $10^4$ – $10^6$  enhancement and the latter usually provides 10–100 enhancement. At present, researchers focus on the EM enhancement because the EM enhancement is stronger than the chemical enhancement and more helpful for the practical applications of SERS substrates.

## 3. Noble Metallic Nanostructures Used as SERS Substrates

According to the theoretical background mentioned before for SERS, the EM enhancement provides the most contribution to the total enhancement of Raman signal. However, the EM enhancement is mainly due to LSPR, which is dependent on the shape, size, and structure of the material [17]. Hence, it is of great importance to design rational materials for achieving the strongest enhancement.

Noble metallic nanostructures have been widely used in SERS because of their LSPR properties [11]. As a result, there have appeared many researches focusing on preparing ideal noble metallic nanostructures as SERS substrates [5]. Taking Ag and Au nanostructures as examples, various shapes have emerged [10], such as nanocubes [18, 19], nanorods [20, 21], nanocaps [16], nanochains [22, 23], nanoplates [24], honeycomb and hexagonally structured patterns [25], and nanoclusters [26]. Monodisperse nanoparticles show high SERS enhancement because of their special shapes and sizes. For example, a systematic study on Ag nanocubes with a size ranging from 60 to 200 nm, in which the intensity of SERS increased with the size and the particles with sharper curvature showed a high sensitivity in contrast to normal particles with the similar size [27]. The size of nanoparticles must be smaller than the wavelength of the light to produce LSPR, but it should not be too small, otherwise it may result in poor polarization of nanoparticles and hence poor plasmon resonance [8]. For the nanoclusters and nanopatterns, the shape of patterns and the size of gaps between particles may influence the interparticle coupling, which plays an important role in generating enhanced signals [28].

As a result, to achieve high sensitive SERS signals, fabrication of effective noble metallic nanostructures is crucial.

## 4. Fabrication of Metallic Nanostructures for SERS

With the development of nanotechnology, nanofabrication has improved for meeting simple, low-cost, large-scale, and green requirements. In this section, we will introduce several common methods, which have been used to generate noble metal nanostructures for SERS applications.

#### 4.1. Solution-Phase Synthesis

**4.1.1. Polyol Process.** The polyol process is a simple and versatile method for preparing metal nanostructures with various shapes and sizes [11, 29–31], which show potential optical applications. The enhancement effect of SERS is dependent on the shape and size of materials; thus, the polyol process is a good choice for preparing SERS substrates.

In a typical polyol synthesis [32, 33], the salt precursor and polymeric capping agent are injected into a preheated polyol, especially ethylene glycol, which serves as both a solvent and a reducing agent. The nucleation and growth could be controlled through varying the reaction conditions, such as temperature, reagent concentration, and types of additive ions, thus controlling the final products.

The nucleation and growth mechanisms in the polyol process have been discussed in detail [11, 29]. In this section, we take the synthesis of Ag nanostructures as an example. Typically, to obtain Ag nanostructures, silver nitrate ( $\text{AgNO}_3$ ) is used as metal salt precursor, ethylene glycol (EG) as the reductant and solvent, poly(vinyl pyrrolidone) (PVP) as the stabilizer and crystal-habit modifier [11, 30]. During the reaction process, initially formed small Ag clusters grow larger and become more stable which usually called seeds. The seeds may show three different structures: single crystalline, single twinned, and multiply twinned. By introducing additive chemical agents or ions, the growth speed of different crystalline faces can be changed, resulting in the formation of nanoparticles with different shapes by the selective growth of dominate crystalline faces. There are many works using different additive ions leading to different shapes with SERS applications. For example, Wiley et al. reported shape-controlled synthesis of various Ag nanostructures with this method [32] as shown in Figure 1. According to their study multiply twinned seeds grew into Ag pentagonal nanowires with addition of chloride and  $\text{Fe}^{3+}$ , in which chloride prevents seeds from aggregating and  $\text{Fe}^{3+}$  protects twinned seeds from etching by chloride and oxygen. Without adding  $\text{Fe}^{3+}$ ,  $\text{Cl}^-/\text{O}_2$  pair will dissolve both multiply twinned and singly twinned seeds, resulting in the products dominated by Ag cuboctahedrons or cubes. By adding  $\text{Br}^-$  into the solution, only single twinned seeds retained, ultimately resulting in the formation of Ag nanobars or right bipyramids. More recently, they produced large-scale Ag nanocubes by introducing argon into the NaHS-mediated synthesis [18]. However, in contrast to Ag synthesis, there is a notable difference in the mechanism for growing Au nanostructures: PVP preferentially promote the growth of  $\{111\}$  facets but not the  $\{100\}$  facets for Ag nanostructures, thus resulting in different shapes [29, 34, 35]. When using tetrachloroaurate trihydrate ( $\text{HAuCl}_4 \cdot 3\text{H}_2\text{O}$ ) as precursor, diethylene glycol (DEG) or tetraethylene glycol (TEG) as reductant, PVP as capping agent, various polyhedral nanostructures have been prepared [34]. Moreover, adding  $\text{Ag}^+$  into the solution, Au nanocubes with the size in the range of ~100 nm have been fabricated [35].

**4.1.2. Seed-Mediated Growth.** Another popular chemical synthesis method for preparing well-defined shapes and sizes is using preformed nanocrystals as seeds for further growth,

which is generally called seed-mediated growth [11, 36]. As a major advantage over conventional methods, the introduction of preformed seeds into a synthesis process allows nucleation and growth separately, thus making it easier to obtain a desired morphology by only manipulating the growth process. In general, metal atoms could deposit on seeds with the same composition or different composition, which are respectively called homogeneous or heterogeneous growth. The difference in lattice constant between the seed and the deposited metal will influence the final products. Besides, there are other influence factors [29, 36]: (1) the internal structure of the seed, for example, twin defects, stacking faults, and grain boundaries, which show a higher reactivity; (2) the presence and types of capping agents, such as surfactants, polymer stabilizers, ionic species, as well as unknown contaminants, which could bond selectively to different crystalline facets; and (3) the reduction or growth kinetics, which may influence the forming and dissolve of the seeds. Therefore, we can receive products with different shapes and morphologies through using different seeds and under different experimental conditions.

By using preformed spherical or cubic seeds, Ag nanocubes with uniform edge lengths controllable in the range of 30–200 nm have been prepared, in which the size was adjusted by varying the amount of  $\text{AgNO}_3$  precursor added in the reaction solution [19]. In their study, the calculated EFs of Ag nanocubes did not vary much with the increase of size because  $I_{\text{SERS}}$  and  $N_{\text{SERS}}$  both became larger with increasing size of the cube. However, the enhancement factors have a relationship with the laser polarization. Recently by adding ionic or covalent bromides into the typical seed-mediated system, Ag nanobars with different aspect ratios were achieved [37], in which EFs showed anisotropy and were found to be dependent on the aspect ratios of nanobars, its orientation is relative to laser polarization, as well as the wavelength of excitation, as shown in Figure 2. A characteristic feature of anisotropic structures such as nanorods, nanowires is that its plasmonic band splits into two components, which corresponds to the longitudinal and transverse components of the localized surface plasmon resonance [20]. Faceted pentagonal Ag nanorods with tunable dimensions have also been reported by using photochemically synthesized decahedra seeds, in which the SERS enhancement dropped with the increase of the aspect ratio [21]. The report also suggests that interparticle cavities play a dominant role in SERS enhancement.

In addition, special Au nanostructures could be readily achieved by using different preformed seeds. For example, recently Au nanohexapods were prepared with single-crystal Au octahedral seeds, in which the seeds were also produced by seeded growth [38]. Core-shell nanostructure has also been prepared through an improved seed-mediated growth [39].

**4.1.3. Self-Assembly.** According to the two methods described above, they are usually used to prepare various monodisperse metal nanoparticles. While self-assembly is a typical process, in which metal nanoparticles spontaneously organize into special arrays or patterns with controllable size, structure,

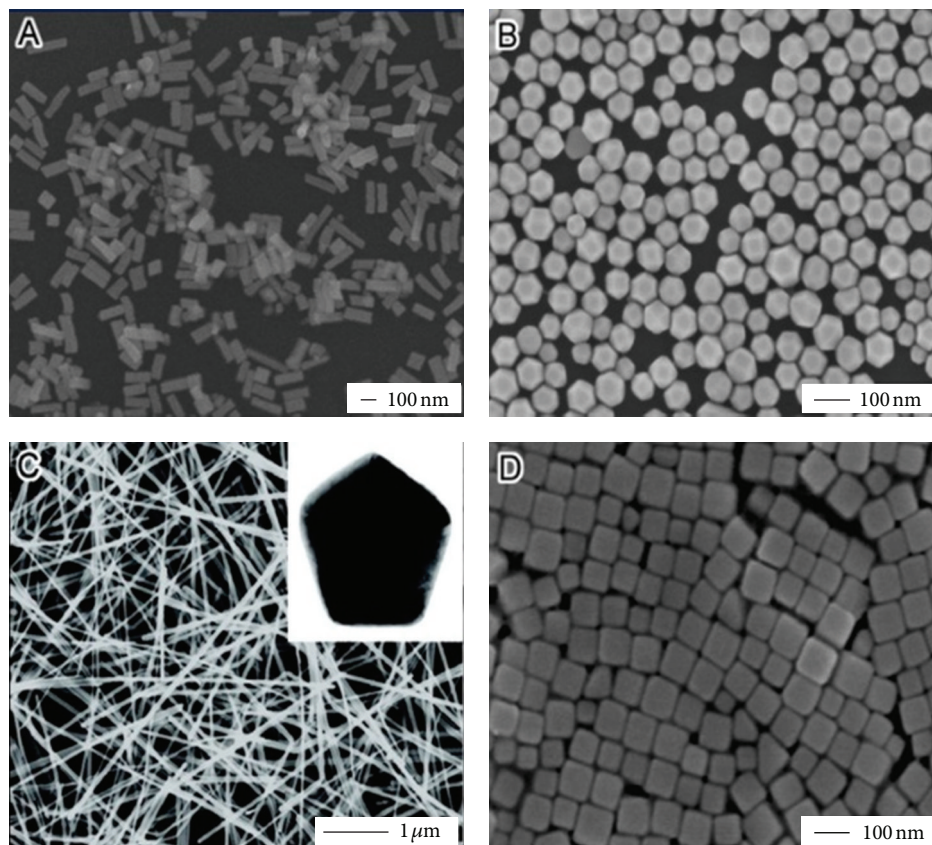


FIGURE 1: Scanning electron microscopy (SEM) images of representative silver nanostructures: (A) nanobars, (B) truncated cubes, (C) cubes, and (D) wires, all at the same scale. Insets show TEM images of the nanowires. Reprinted with permission from [32]. Copyright 2007 American Chemical Society.

and composition. To date, different assembly approaches have been employed to assemble different dimensional metal nanoarchitectures based on corresponding metal nanoparticles [40, 41]. These typical assembly approaches include layer-by-layer (LBL) assembly [42, 43], solvent-induced evaporation [44], Langmuir-Blodgett assembly [45], external field-driven assembly [46], ion or small molecule or polymer induced assembly [22, 23, 47], liquid-liquid interface assembly [48], and so forth.

Chainlike 1D nanostructure has been widely fabricated through assembling nanoparticles [49–51]. For example, Yang et al. reported the assembly of Ag nanoparticles into nanochains under the inducing of cetyltrimethylammonium bromide (CTAB) and the assistance of 11-mercaptoundecanoic acid (MUA) [22] as shown in Figure 3. In their process, CTAB linked together the {100} facets of neighboring Ag nanoparticles and MUA prevented excess aggregations of nanoparticles. Their results show that the chain length could be easily controlled by adjusting the amount of CTAB and MUA. The maximum SERS enhancement factor around  $2.6 \times 10^8$  was observed on the Ag monolayer mainly composing of four-particle nanochains, which was due to the enhancement of localized electromagnetic field. The localized surface plasmon coupling at the interstitial

sites of Ag nanochains resulted in the enhanced localized electromagnetic field. More Recently gold nanoparticle linear aggregates were generated by using a siloxane surfactant, in which the enhancement factor reached to  $2.4 \times 10^6$ , that was about 5 times stronger than the isolated Au nanosphere [23]. In 2011, acid-directed self-assembly of Ag nanoparticles into special nanostructures has been achieved without using any polymer surfactant or capping agent [47]. In the process, ascorbic acid reduced the precursor solution, and with the assistance of citric acid perfect microspheres composing of nanosheets were produced. Helical nanochains were also prepared by self-assembly of spherical colloids in V-shaped grooves [52].

In addition, metal nanoparticles can be immobilized on solid substrates resulting in 2D structures through chemical attachment [53, 54], electrostatic interaction [55], capillary force driving [56], and direct transfer of pre-assembled nanoparticle film [45], focusing on which numerous works have been published [57]. Recently under the guiding of polystyrene-*b*-poly(4-vinylpyridine) (P4VP-*b*-PS) block copolymer, citrate-stabilized gold nanospheres assembled into arrays on the Si substrate driving by electrostatic interaction between the positively charged pyridinium groups on the substrate and the negatively charged surface ligands of

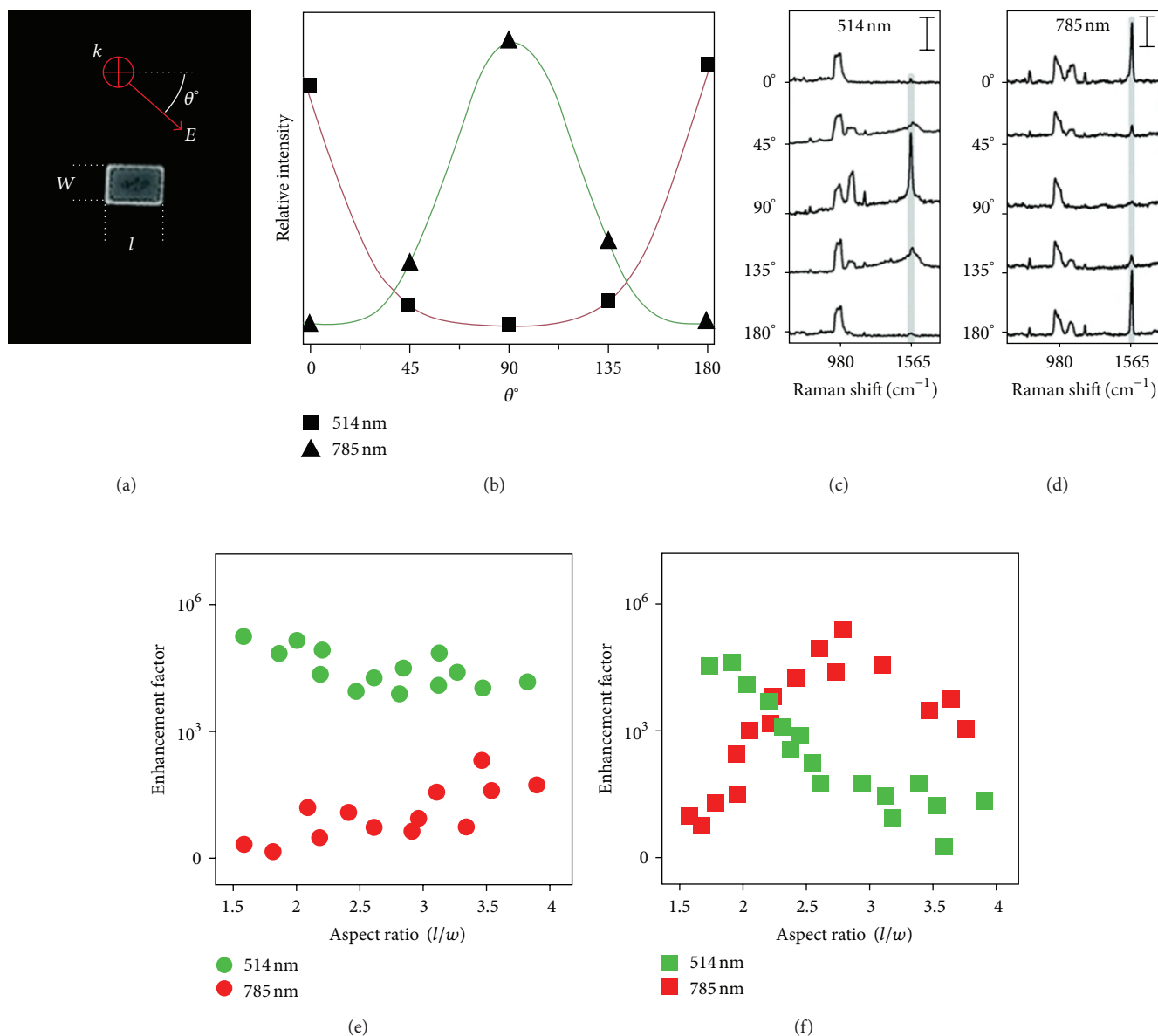


FIGURE 2: SERS spectra taken from a single Ag nanobar at two wavelengths and different orientations relative to the laser polarization. (a) SEM image of a typical Ag nanobar of 150 nm in length ( $l$ ) and 75 nm in width ( $w$ ) supported on a Si wafer. The 514 or 785 nm laser was propagating perpendicular to the Si substrate and the polarization angle ( $\theta$ ) with respect to the nanobar was varied from  $0^\circ$  to  $180^\circ$ . (b) SERS intensity as a function of  $\theta$ , with the fit to  $\cos^4(\theta)$ . ((c), (d)) SERS spectra for 1, 4-BDT are plotted for 514 and 785 nm lasers at different polarization angles. The peak at  $\sim 980 \text{ cm}^{-1}$  was from the Si substrate. The 1, 4-BDT peaks at  $1562 \text{ cm}^{-1}$  are highlighted in gray. ((e), (f)) Enhancement factors of individual nanobars calculated from the peaks of 1, 4-BDT for transverse (circles) and longitudinal (squares) polarizations, and with 514 nm (green) and 785 nm (red) excitations. Reprinted with permission from [37]. Copyright 2007 American Chemical Society.

the nanoparticles [55]. Their products showed a uniform response regardless of orientation and excellent reproducibility, which are very important for practical applications of SERS. Besides, nanoparticle cluster arrays were reported by using nanopatterns of poly(styrene-block-2-vinylpyridine) (PS-*b*-P2VP) [58].

Finally, the metal nanoparticle clusters have been obtained through controllable assembly. Different morphologies can be generated under usage of molecular linkers

[59], asymmetrically functionalized nanoparticles [60], and controlling the aggregation kinetics [61].

**4.2. Template Technique.** Template technique offers another way to prepare nanostructures with well-defined size and shape under the assistance of templates. By using different templates, different morphologies could be obtained. There are many approaches for preparing metal nanomaterial through hard templates, such as anodic alumina oxide

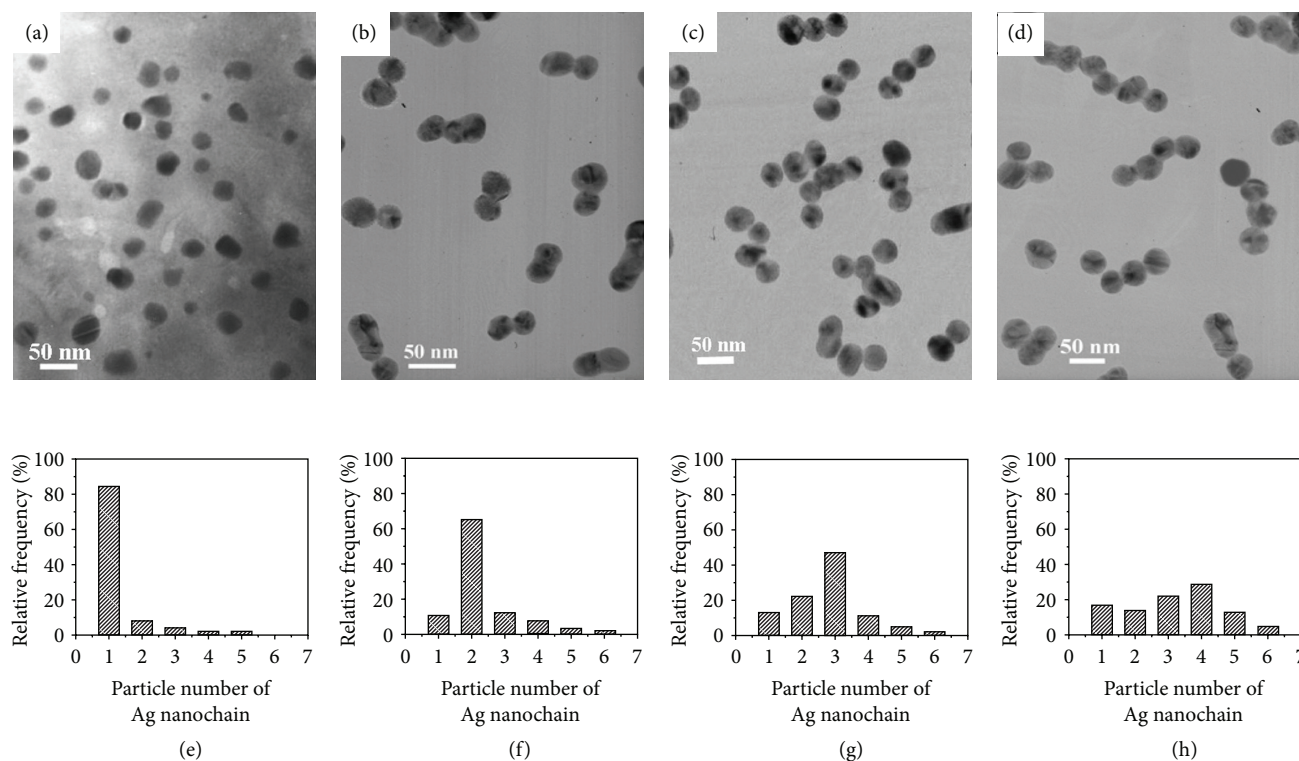


FIGURE 3: TEM images of Ag colloids: (a) sol-1, (b) sol-2, (c) sol-3, and (d) sol-4. All scale bars represent 50 nm. ((e)–(h)) Particle number distribution in Ag nanochains for related TEM images. The criterion to judge whether a group of Ag particles form a chain or not is that the distance between neighboring particles is less than the chain length of CTAB molecules. Reprinted with permission from [22]. Copyright 2007 American Chemical Society.

(AAO) [62, 63], polycarbonate membranes (PCM) [64], polymethylmethacrylate (PMMA) [65], monolayer colloidal crystal [66], and so forth, as well as soft templates, including micelles [67], reverse micelles, DNA, and so forth [11, 68]. In this section, we will describe some popular templates used to generate special noble metal nanostructures.

Anodic alumina oxide (AAO), also known as porous anodic alumina (PAA), is a very popular substrate for producing various metal nanostructures, such as nanowire, nanorod, nanopore, and nanodot arrays. Silver nanopores with abundant sub-5 nm gaps as SERS substrates were reported by electron beam deposition Ag on the porous side through controlling the temperature and the deposited Ag thickness, of which the EF reached to  $10^7$  using rhodamine 6G (R6G) as the probe molecule [62]. High ordered gold nanodots were also fabricated by using AAO template with the thickness of 750 nm [63], in which Raman signal of thin silicon membranes on polyethylene terephthalate (PET) substrates was enhanced and exhibited structure information.

Monolayer colloidal crystal (MCC) is another interested template for producing various metal nanopatterns, which is also widely used in fabricating SERS substrates. In general, there are two cases: metal materials depositing on the top of colloidal crystals and metal materials depositing on the interspaces of the colloidal crystal monolayer, which result in nanocaps, honeycomb, and hexagonal arrays. MCC could

be prepared by self-assembly process [68]. The target metal material can be deposited on the prepared MCC templates through plasma sputtering [69], magnetron sputtering [16], and so forth. In most cases, the templates finally need to be removed to produce ideal metal nanopatterns. For example, tunable Au nanoshell arrays were prepared by using pretreated uniform polystyrene (PS) monolayer colloidal crystals as template [69]. By varying the plasma sputtering deposition time, different nanopatterns with different spacing were generated, which showed different SPR intensity, thus tuning the SERS intensity. An order Ag nanocaps were also fabricated through magnetron sputtering Ag on the two-dimensional PS monolayer colloidal crystal template, which showed a high SERS intensity with an enhance factor  $\sim 10^{12}$  using 4-mercaptopyridine (4-Mpy) as the probe molecule [16].

In addition, recently by sputtering deposition Ag and Au nanoneedles arrays were obtained, in which the firstly deposited carbon nanoneedles arrays serve as an template inducing the formation of final products [70, 71]. Rodríguez-Fernández fabricated Au semishells using Janus silica particles as templates [72].

**4.3. Other Methods.** Besides the methods mentioned before for fabricating SERS substrates, there have been other methods, such as combination of nanoparticles with special

structure or material [73, 74], screen printing [75], and sonochemical synthesis [76], and winkle-confined drying of collides [77].

For example, Ag nanoparticles deposited on the porous silicon in the  $\text{AgNO}_3$  solution, in which Ag aggregates formed and the sizes could be controlled by varying the concentration of  $\text{AgNO}_3$  solution [73]. The SERS performance was measured by detecting R6G and crystal violet (CV), which showed remarkable Raman signal enhancement. Besides, a facile and fast method was reported by chemically depositing Ag on polyaniline films treated by hydrazine in  $\text{AgNO}_3$  solution, as well as adding lactic acid, which ultimately forming flower-like Ag nanostructure in less than one minute [74]. The prepared Ag nanostructure showed highly response to 4-mercaptobenzoic acid (4-MBA) up to ppb level. Large-scale fabrication was achieved through screen printing [75]. The printing ink consisted of Ag nanoparticles and sodium carboxymethylcellulose (CMC), in which the nanoparticles were reduced by sodium citrate and CMC was used to adjust the viscosity of the ink. The ink was placed on the woven mesh and forced into the image areas of the woven mesh as hard squeegee moving across the mesh. 3D Ag microflowers have been prepared by a simple and sonochemical method, which showed high sensitivity of SERS for R6G and 4-mercaptobenzoic acid (MBA) molecule [76]. In the procedure,  $\text{AgNO}_3$  and L-ascorbic acid (AA) were mixed and sonicated using an ultrasonic generator at room temperature. The Ag nanoparticles of different sizes were achieved through controlling the ultrasonic time and power, as well as the reactant molar ratio. Gold nanoparticle arrays were produced through confining gold nanoparticle collides by wrinkled polydimethylsiloxane (PDMS) during drying [77].

## 5. Practical Applications of SERS

Raman spectrum can inherently imply rich information of analyte molecules, and SERS with higher signal intensity make it possible to detect analyte in very low concentration, which improves its practical applications. There have been a large number of works focusing on applications of SERS in various fields, including trace chemical detection, such as dye molecules [70, 78, 79], illicitly sold narcotics [70], food additives [47], and residual pesticide trace detection [20, 80, 81], as well as bioanalysis [82, 83] and explosives detection [84, 85].

**5.1. Applications of SERS in Trace Chemical Detection.** Dye molecules such as R6G and MG are reported to be used as SERS probe molecules. For example, Ag nanoneedles array substrates prepared by a simple  $\text{Ar}^+$  ion sputtering technology were used to detect R6G at a very low concentration  $\sim 10^{-11}$  M [70]. Besides, many bands are distinctly observed in the spectra even when the R6G concentration was down to  $10^{-15}$  M, by using Ag nanosheets-assembled micro-hemispheres as SERS substrates [78]. There was another report showing that the detection concentration for R6G on the Ag microflower substrates was as low as  $10^{-17}$  M [79]. Because of the low detection limit of R6G, it is useful for studies on single

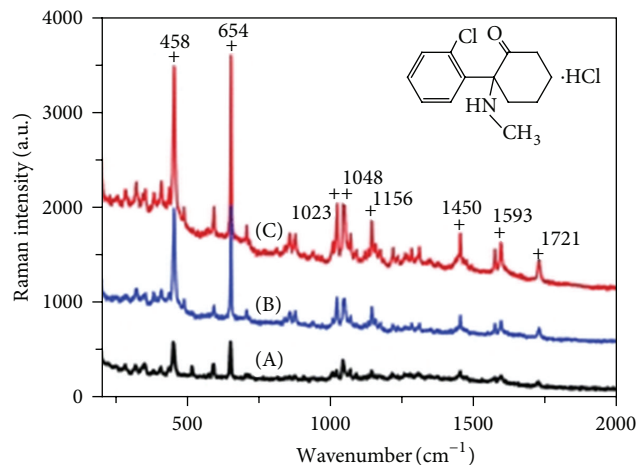
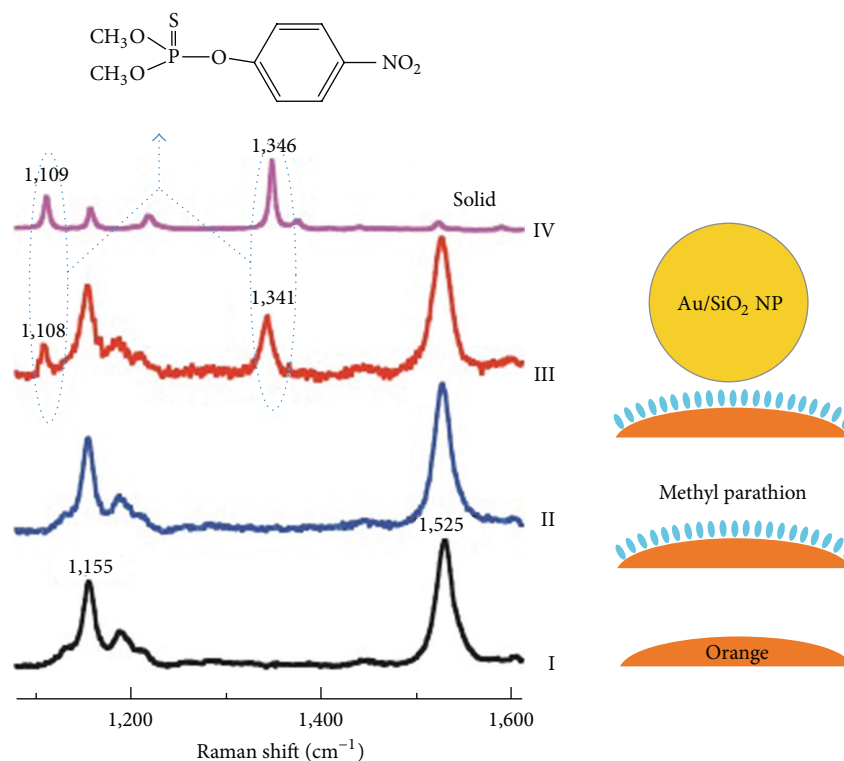


FIGURE 4: Raman spectra of ketamine hydrochloride with different concentration of (A) 27 ppb, (B) 275 ppb, and (C) 2.7 ppm adsorbed on Ag nanoneedles (633 nm, 3s) [70]. Reproduced by the permission of the Royal Society of Chemistry.

molecule SERS. In addition, dyes can produce vibrant colors, thus make it treasured since antiquity [86]. The easy and facile detection of dye molecules may promote the historical and cultural research.

The detection of trace-level hazardous chemicals is also in high demand because of the increasing threat from harmful environments and unreliable food safety. For example, Yang et al. detected ketamine hydrochloride down to 27 ppb within 3 s, which offers significant applications in both biomedical diagnostics and forensics field [70] as shown in Figure 4.

Melamine, a chemical compound, has been widely used in milk, infant formula, and pet food as an additive to increase protein content because of its high nitrogen content (66% by mass). However, since 2007, melamine, with its contaminant cyanuric acid, has become prominent because of the milk scandal. As a facile and simple spectroscopy technique, SERS has been used to detect melamine content. For instance, Zhang et al. reported that melamine with a concentration of  $\sim 5$  ppm could be readily detected by using the core-shell Ag nanostructure assembled by nanosheets [47]. In addition, pesticide residues have also been detected through SERS and using metal nanostructure substrates. For example, gold nanorods and silver nanocubes were used to detect three different herbicides: the organochlorine compound 2,4-D, the organophosphorus compound trichlorfon, and the triazinic compound ametryn, which were fabricated in solution phase [20]. Silver nanoparticles decorated silicon nanowires have been used to in situ detect pesticide residues on a cucumber surface with a high SERS intensity, which were prepared using CTAB as the soft template to induce nanoparticles absorbing on the nanowires [80]. Moreover, Li et al. in situ detected parathion residues on fresh orange using Au-SiO<sub>2</sub> core-shell nanostructure [81] as shown in Figure 5. And this provides an important potential to rapidly detect pesticide residue on the fruits and vegetables, which is crucial to diet safety.



(a)



(b)

FIGURE 5: In situ inspection of pesticide residues on food/fruit. (a) Normal Raman spectra on fresh citrus fruits. Curve I, with clean pericarps. Curve II, contaminated by parathion. Curve III, Shiners spectrum of contaminated orange modified by Au/SiO<sub>2</sub> nanoparticles. Curve IV, Raman spectrum of solid methyl parathion. Laser power on the sample was 0.5 mW, and the collected times were 30s. (b) Schematic of the Shiners experiment. Reprinted with permission from reference 81. Copyright 2010 Nature Publishing Group.

**5.2. Applications of SERS in Biosensing.** SERS has been widely used for bioanalysis [82], including detecting biomolecules [87, 88], pathogens sensing [89, 90], cancer diagnosis [91, 92], urine components detection [93], and in vivo molecular probing in live cells [94], which play an important role in the life science for health care or therapeutic treatment.

Biomolecules, such as DNA, can be detected using SERS. There have been reports focusing on detecting the sequence of DNA molecule by SERS technique, which based on the mixed DNA-functionalized silver nanoparticles probe [87] or using gold nanoparticle aggregates [88]. Bacteria, one

of the pathogens, have been identified using SERS through internally or externally depositing Ag and Au colloids on bacteria [89]. The applications of SERS on cells for detecting pathogens have also been studied, as well as the SERS-based immunoassay. Binding the antibody and the metal nanoparticles can be used to detect the special antigen, which serves as biomarker of corresponding cancer [91]. Moreover, recently there has been a study focusing on the detection of  $\beta$ -agonist in urine, in which the chemometric method was introduced for high sensitivity [93]. Their work provided a potential use of SERS in drug test and clinic detection.

Much effort to meet reliable, fast, and high specific detection requirements remains to be proceeded.

**5.3. Applications of SERS in Explosives Detection.** The detection and analysis of explosives are important to homeland security, environment cleaning, military issues, and land mine detection. For instance, Ni–Au nanocarpets (NCs) were prepared through a galvanic replacement reaction, starting from prefabricated Ni NCs, which showed high activity and reproducibility as SERS substrates for detecting explosives with a low concentration about  $10^{-7}$  M [84]. Silver-gold bimetallic nanostructures were achieved by sunlight inducing and DNA template assisting [85]. By varying the molar ratio of silver to gold, the morphologies of products could be controlled. The prepared Ag-Au nanostructure showed a very low detection concentration of TNT down to  $10^{-15}$  M through SERS technology. Stable and reproducible substrates for detecting explosives are still challenging.

## 6. Conclusion

In this paper, we mainly discuss the theoretical background of SERS, some synthesis methods of SERS substrates, and their applications in different fields. Although there have been many studies focusing on the theories, some issues remain unclear and unsure, such as the attribution of chemical mechanism. With the development of designing various nanostructures, it is possible to further understand the enhancement theories and the factors influencing the enhancement. Different dimensional nanostructures have been prepared through various methods, such as polyol process, seed-mediated synthesis, self-assembly and template technique. Using these noble metal nanostructures, SERS has been used in detecting various molecules and thus has been applied into different real fields. However, it is still a challenge to produce highly sensible, reproducible, and stable substrates using a simple, low-cost, large-scale, and rapid method. Further works should be continued to generate high-performance SERS substrates for wider applications.

## Acknowledgments

Y. Yang thanks the Century Program (One-Hundred-Talent Program) of the Chinese Academy of Sciences for special funding support. This study was also supported in part by Funds from the National Natural Science Foundation of China (no. 51071167, 51102266), the Instrument Developing Project of the Chinese Academy of Sciences (no. YZ200939), the Shanghai Yangtze River Delta Science Project (no. 11495810100), and the Shanghai Pujiang Program (10PJ1410700). Y. Yang is also thankful for the support by Fund from Key Laboratory of Nanodevices and Applications, Suzhou Institute of Nano-Tech and Nano-Bionics, Chinese Academy of Sciences (no. 12CS01).

## References

- [1] P. L. Stiles, J. A. Dieringer, N. C. Shah, and R. P. Van Duyne, "Surface-enhanced Raman spectroscopy," *Annual Review of Analytical Chemistry*, vol. 1, no. 1, pp. 601–626, 2008.
- [2] T. Vo-Dinh, "Surface-enhanced Raman spectroscopy using metallic nanostructures," *Trends in Analytical Chemistry*, vol. 17, no. 8–9, pp. 557–582, 1998.
- [3] C. L. Haynes, A. D. McFarland, and R. P. Van Duyne, "Surface-enhanced: Raman spectroscopy," *Analytical Chemistry*, vol. 77, no. 17, pp. 338A–346A, 2005.
- [4] M. Moskovits, "Surface-enhanced spectroscopy," *Reviews of Modern Physics*, vol. 57, no. 3, pp. 783–826, 1985.
- [5] Z. Q. Tian, B. Ren, and D. Y. Wu, "Surface-enhanced Raman scattering: from noble to transition metals and from rough surfaces to ordered nanostructures," *Journal of Physical Chemistry B*, vol. 106, no. 37, pp. 9463–9483, 2002.
- [6] X. Wang, W. Shi, G. She, and L. Mu, "Surface-Enhanced Raman Scattering (SERS) on transition metal and semiconductor nanostructures," *Physical Chemistry Chemical Physics*, vol. 14, no. 17, pp. 5891–5901, 2012.
- [7] Y. Wang, W. Ruan, J. Zhang et al., "Direct observation of surface-enhanced Raman scattering in ZnO nanocrystals," *Journal of Raman Spectroscopy*, vol. 40, no. 8, pp. 1072–1077, 2009.
- [8] H. Ko, S. Singamaneni, and V. V. Tsukruk, "Nanostructured surfaces and assemblies as SERS media," *Small*, vol. 4, no. 10, pp. 1576–1599, 2008.
- [9] Y. Yang, S. Matsubara, L. Xiong, T. Hayakawa, and M. Nogami, "Solvothermal synthesis of multiple shapes of silver nanoparticles and their SERS properties," *Journal of Physical Chemistry C*, vol. 111, no. 26, pp. 9095–9104, 2007.
- [10] G. V. P. Kumar, "Plasmonic nano-architectures for surface enhanced Raman scattering: a review," *Journal of Nanophotonics*, vol. 6, no. 1, Article ID 064503, 2012.
- [11] M. Rycenga, C. M. Cobley, J. Zeng et al., "Controlling the synthesis and assembly of silver nanostructures for plasmonic applications," *Chemical Reviews*, vol. 111, no. 6, pp. 3669–3712, 2011.
- [12] R. J. C. Brown, J. Wang, and M. J. T. Milton, "Electromagnetic modelling of Raman enhancement from nanoscale structures as a means to predict the efficacy of SERS substrates," *Journal of Nanomaterials*, vol. 2007, Article ID 12086, 10 pages, 2007.
- [13] A. Campion, J. E. Ivanecky III, C. M. Child, and M. Foster, "On the mechanism of chemical enhancement in surface-enhanced Raman scattering," *Journal of the American Chemical Society*, vol. 117, no. 47, pp. 11807–11808, 1995.
- [14] A. Campion and P. Kambhampati, "Surface-enhanced Raman scattering," *Chemical Society Reviews*, vol. 27, no. 4, pp. 241–250, 1998.
- [15] E. C. Le Ru, E. Blackie, M. Meyer, and P. G. Etchegoin, "Surface enhanced Raman scattering enhancement factors: a comprehensive study," *Journal of Physical Chemistry C*, vol. 111, no. 37, pp. 13794–13803, 2007.
- [16] Y. X. Wang, S. S. Liu, W. T. Gao, W. Li, Y. J. Zhang, and J. H. Yang, "Surface-enhanced Raman spectroscopy based on ordered nanocap arrays," *Superlattices and Microstructures*, vol. 52, no. 4, pp. 750–758, 2012.
- [17] K. A. Willets and R. P. Van Duyne, "Localized surface plasmon resonance spectroscopy and sensing," *Annual Review of Physical Chemistry*, vol. 58, pp. 267–297, 2007.
- [18] Q. Zhang, C. Cobley, L. Au et al., "Production of Ag nanocubes on a scale of 0.1 g per batch by protecting the NaHS-mediated polyol synthesis with argon," *ACS Applied Materials & Interfaces*, vol. 1, no. 9, pp. 2044–2048, 2009.
- [19] Q. Zhang, W. Li, C. Moran et al., "Seed-mediated synthesis of Ag nanocubes with controllable edge lengths in the range of 30–200 nm and comparison of their optical properties," *Journal of*

- the American Chemical Society*, vol. 132, no. 32, pp. 11372–11378, 2010.
- [20] J. C. Santos Costa, R. A. Ando, A. C. Sant'ana et al., "High performance gold nanorods and silver nanocubes in surface-enhanced Raman spectroscopy of pesticides," *Physical Chemistry Chemical Physics*, vol. 11, no. 34, pp. 7491–7498, 2009.
- [21] B. Pietrobon, M. McEachran, and V. Kitaev, "Synthesis of size-controlled faceted pentagonal silver nanorods with tunable plasmonic properties and self-assembly of these nanorods," *ACS Nano*, vol. 3, no. 1, pp. 21–26, 2009.
- [22] Y. Yang, J. Shi, T. Tanaka, and M. Nogami, "Self-assembled silver nanochains for surface-enhanced Raman scattering," *Langmuir*, vol. 23, no. 24, pp. 12042–12047, 2007.
- [23] H. Jia, X. Bai, N. Li, L. Yu, and L. Zheng, "Siloxane surfactant induced self-assembly of gold nanoparticles and their application to SERS," *CrystEngComm*, vol. 13, no. 20, pp. 6179–6184, 2011.
- [24] I. Pastoriza-Santos and L. M. Liz-Marzán, "Colloidal silver nanoplates. State of the art and future challenges," *Journal of Materials Chemistry*, vol. 18, no. 15, pp. 1724–1737, 2008.
- [25] C. L. Haynes and R. P. Van Duyne, "Nanosphere lithography: a versatile nanofabrication tool for studies of size-dependent nanoparticle optics," *Journal of Physical Chemistry B*, vol. 105, no. 24, pp. 5599–5611, 2001.
- [26] P. H. C. Camargo, L. Au, M. Rycenga, W. Li, and Y. Xia, "Measuring the SERS enhancement factors of dimers with different structures constructed from silver nanocubes," *Chemical Physics Letters*, vol. 484, no. 4–6, pp. 304–308, 2010.
- [27] J. M. McLellan, A. Siekkinen, J. Chen, and Y. Xia, "Comparison of the surface-enhanced Raman scattering on sharp and truncated silver nanocubes," *Chemical Physics Letters*, vol. 427, no. 1–3, pp. 122–126, 2006.
- [28] S. K. Ghosh and T. Pal, "Interparticle coupling effect on the surface plasmon resonance of gold nanoparticles: from theory to applications," *Chemical Reviews*, vol. 107, no. 11, pp. 4797–4862, 2007.
- [29] Y. Xia, Y. Xiong, B. Lim, and S. E. Skrabalak, "Shape-controlled synthesis of metal nanocrystals: simple chemistry meets complex physics?" *Angewandte Chemie*, vol. 48, no. 1, pp. 60–103, 2009.
- [30] A. R. Tao, S. Habas, and P. Yang, "Shape control of colloidal metal nanocrystals," *Small*, vol. 4, no. 3, pp. 310–325, 2008.
- [31] C. M. Cobby, S. E. Skrabalak, D. J. Campbell, and Y. Xia, "Shape-controlled synthesis of silver nanoparticles for plasmonic and sensing applications," *Plasmonics*, vol. 4, no. 2, pp. 171–179, 2009.
- [32] B. Wiley, Y. Sun, and Y. Xia, "Synthesis of silver nanostructures with controlled shapes and properties," *Accounts of Chemical Research*, vol. 40, no. 10, pp. 1067–1076, 2007.
- [33] A. Tao, P. Sinsersuksakul, and P. Yang, "Polyhedral silver nanocrystals with distinct scattering signatures," *Angewandte Chemie*, vol. 45, no. 28, pp. 4597–4601, 2006.
- [34] D. Seo, C. I. Yoo, I. S. Chung, S. M. Park, S. Ryu, and H. Song, "Shape adjustment between multiply twinned and single-crystalline polyhedral gold nanocrystals: decahedra, icosahedra, and truncated tetrahedra," *Journal of Physical Chemistry C*, vol. 112, no. 7, pp. 2469–2475, 2008.
- [35] D. Seo, C. P. Ji, and H. Song, "Polyhedral gold nanocrystals with Oh symmetry: from octahedra to cubes," *Journal of the American Chemical Society*, vol. 128, no. 46, pp. 14863–14870, 2006.
- [36] J. Zeng, X. Xia, M. Rycenga, P. Henneghan, Q. Li, and Y. Xia, "Successive deposition of silver on silver nanoplates: lateral versus vertical growth," *Angewandte Chemie*, vol. 50, no. 1, pp. 244–249, 2011.
- [37] Q. Zhang, C. H. Moran, X. Xia, M. Rycenga, N. Li, and Y. Xia, "Synthesis of Ag nanobars in the presence of single-crystal seeds and a bromide compound, and their surface-enhanced Raman scattering (SERS) properties," *Langmuir*, vol. 28, no. 24, pp. 9047–9054, 2012.
- [38] D. Y. Kim, T. Yu, E. C. Cho, Y. Ma, O. O. Park, and Y. Xia, "Synthesis of gold nano-hexapods with controllable arm lengths and their tunable optical properties," *Angewandte Chemie*, vol. 50, no. 28, pp. 6328–6331, 2011.
- [39] T. Liu, D. Li, D. Yang, and M. Jiang, "An improved seed-mediated growth method to coat complete silver shells onto silica spheres for surface-enhanced Raman scattering," *Colloids and Surfaces A*, vol. 387, no. 1–3, pp. 17–22, 2011.
- [40] S. Guo and S. Dong, "Metal nanomaterial-based self-assembly: development, electrochemical sensing and SERS applications," *Journal of Materials Chemistry*, vol. 21, no. 42, pp. 16704–16716, 2011.
- [41] J. M. Romo-Herrera, R. A. Alvarez-Puebla, and L. M. Liz-Marzán, "Controlled assembly of plasmonic colloidal nanoparticle clusters," *Nanoscale*, vol. 3, no. 4, pp. 1304–1315, 2011.
- [42] X. Zhang, H. Chen, and H. Zhang, "Layer-by-layer assembly: from conventional to unconventional methods," *Chemical Communications*, no. 14, pp. 1395–1405, 2007.
- [43] Y. Huang, Y. Yang, Z. Chen, X. Li, and M. Nogami, "Fabricating Au-Ag core-shell composite films for surface-enhanced Raman scattering," *Journal of Materials Science*, vol. 43, no. 15, pp. 5390–5393, 2008.
- [44] S. Peng, Y. Lee, C. Wang, H. Yin, S. Dai, and S. Sun, "A facile synthesis of monodisperse Au nanoparticles and their catalysis of CO oxidation," *Nano Research*, vol. 1, no. 3, pp. 229–234, 2008.
- [45] A. R. Tao, J. Huang, and A. P. Yang, "Langmuir–blodgett of nanocrystals and nanowires," *Accounts of Chemical Research*, vol. 41, pp. 1662–1673, 2008.
- [46] H. Wu, F. Bai, Z. Sun et al., "Nanostructured gold architectures formed through high pressure-driven sintering of spherical nanoparticle arrays," *Journal of the American Chemical Society*, vol. 132, no. 37, pp. 12826–12828, 2010.
- [47] B. Zhang, P. Xu, X. Xie et al., "Acid-directed synthesis of SERS-active hierarchical assemblies of silver nanostructures," *Journal of Materials Chemistry*, vol. 21, no. 8, pp. 2495–2501, 2011.
- [48] H. Duan, D. Wang, D. G. Kurth, and H. Möhwald, "Directing self-assembly of nanoparticles at water/oil interfaces," *Angewandte Chemie*, vol. 43, no. 42, pp. 5639–5642, 2004.
- [49] Y. Yang, M. Nogami, J. Shi, H. Chen, G. Ma, and S. Tang, "Controlled surface-plasmon coupling in SiO<sub>2</sub>-coated gold nanochains for tunable nonlinear optical properties," *Applied Physics Letters*, vol. 88, no. 8, Article ID 081110, 2006.
- [50] Y. Yang, S. Matsubara, M. Nogami, J. Shi, and W. Huang, "One-dimensional self-assembly of gold nanoparticles for tunable surface plasmon resonance properties," *Nanotechnology*, vol. 17, no. 11, pp. 2821–2827, 2006.
- [51] G. Kawamura, Y. Yang, and M. Nogami, "End-to-end assembly of CTAB-stabilized gold nanorods by citrate anions," *Journal of Physical Chemistry C*, vol. 112, no. 29, pp. 10632–10636, 2008.
- [52] Y. Yin and Y. Xia, "Self-assembly of spherical colloids into helical chains with well-controlled handedness," *Journal of the American Chemical Society*, vol. 125, no. 8, pp. 2048–2049, 2003.

- [53] T. Makiabadi, A. Bouvrée, V. Le Nader, H. Terrisse, and G. Louarn, "Preparation, optimization, and characterization of SERS sensor substrates based on two-dimensional structures of gold colloid," *Plasmonics*, vol. 5, no. 1, pp. 21–29, 2010.
- [54] J. L. Seung, M. B. Jeong, and M. Moskovits, "Polarization-dependent surface-enhanced raman scattering from a silver-nanoparticle-decorated single silver nanowire," *Nano Letters*, vol. 8, no. 10, pp. 3244–3247, 2008.
- [55] W. Lee, S. Y. Lee, R. M. Briber, and O. Rabin, "Self-assembled SERS substrates with tunable surface plasmon resonances," *Advanced Functional Materials*, vol. 21, no. 18, pp. 3424–3429, 2011.
- [56] A. Cerf, G. Molnár, and C. Vieu, "Novel approach for the assembly of highly efficient SERS substrates," *ACS Applied Materials and Interfaces*, vol. 1, no. 11, pp. 2544–2550, 2009.
- [57] M. Fan, G. F. S. Andrade, and A. G. Brolo, "A review on the fabrication of substrates for surface enhanced Raman spectroscopy and their applications in analytical chemistry," *Analytica Chimica Acta*, vol. 693, no. 1-2, pp. 7–25, 2011.
- [58] F. L. Yap, P. Thoniyot, S. Krishnan, and S. Krishnamoorthy, "Nanoparticle Cluster Arrays for SERS through direct self-assembly," *Acs Nano*, vol. 6, pp. 2056–2070, 2012.
- [59] M. A. Olson, A. Coskun, R. Klajn et al., "Assembly of polygonal nanoparticle clusters directed by reversible noncovalent bonding interactions," *Nano Letters*, vol. 9, no. 9, pp. 3185–3190, 2009.
- [60] R. Sardar and J. S. Shumaker-Parry, "Asymmetrically functionalized gold nanoparticles organized in one-dimensional chains," *Nano Letters*, vol. 8, no. 2, pp. 731–736, 2008.
- [61] G. Chen, Y. Wang, L. H. Tan et al., "High-purity separation of gold nanoparticle dimers and trimers," *Journal of the American Chemical Society*, vol. 131, no. 12, pp. 4218–4219, 2009.
- [62] J. Wang, L. Huang, L. Yuan et al., "Silver nanostructure arrays abundant in sub-5nm gaps as highly Raman-enhancing substrates," *Applied Surface Science*, vol. 258, no. 8, pp. 3519–3523, 2012.
- [63] L. Nataraj and S. G. Cloutier, "Highly ordered periodic array of metallic nanodots fabricated through template-assisted nanopatterning and its use for surface-enhanced Raman scattering spectroscopy of flexible crystalline-silicon nanomembranes," *Journal of Raman Spectroscopy*, vol. 42, no. 6, pp. 1294–1297, 2011.
- [64] E. A. Batista, D. R. D. Santos, G. F. S. Andrade, A. C. Sant'Ana, A. G. Brolo, and M. L. A. Temperin, "Using polycarbonate membranes as templates for the preparation of au nanostructures for surface-enhanced raman scattering," *Journal of Nanoscience and Nanotechnology*, vol. 9, no. 5, pp. 3233–3238, 2009.
- [65] C. Tian, Z. Liu, J. Jin et al., "Gold mesoflower arrays with sub-10 nm intraparticle gaps for highly sensitive and repeatable surface enhanced Raman spectroscopy," *Nanotechnology*, vol. 23, no. 16, Article ID 165604, 2012.
- [66] S. Yang and Y. Lei, "Recent progress on surface pattern fabrications based on monolayer colloidal crystal templates and related applications," *Nanoscale*, vol. 3, no. 7, pp. 2768–2782, 2011.
- [67] W. Zhang, X. Qiao, and J. Chen, "Synthesis of silver nanoparticles—effects of concerned parameters in water/oil micro-emulsion," *Materials Science and Engineering B*, vol. 142, no. 1, pp. 1–15, 2007.
- [68] J. Zhang, Y. Li, X. Zhang, and B. Yang, "Colloidal self-assembly meets nanofabrication: from two-dimensional colloidal crystals to nanostructure arrays," *Advanced Materials*, vol. 22, no. 38, pp. 4249–4269, 2010.
- [69] G. Liu, Y. Li, G. Duan et al., "Tunable surface plasmon resonance and strong SERS performances of Au opening-nanoshell ordered arrays," *ACS Applied Materials & Interfaces*, vol. 4, no. 1, pp. 1–5, 2011.
- [70] Y. Yang, Z. Y. Li, K. Yamaguchi et al., "Controlled fabrication of silver nanoneedles array for SERS and their application in rapid detection of narcotics," *Nanoscale*, vol. 4, no. 8, pp. 2663–2669, 2012.
- [71] Y. Yang, M. Tanemura, Z. Huang et al., "Aligned gold nanoneedle arrays for surface-enhanced Raman scattering," *Nanotechnology*, vol. 21, no. 32, Article ID 325701, 2010.
- [72] D. Rodríguez-Fernández, J. Pérez-Juste, I. Pastoriza-Santos, and L. M. Liz-Marzán, "Colloidal synthesis of gold semishells," *ChemistryOpen*, vol. 1, no. 2, pp. 90–95, 2012.
- [73] J. C. Yang, C. H. Chen, and R. J. Wu, "Facile growth of silver crystals with greatly varied morphologies by PEO-PPO-PEO tri-block copolymers," *CrystEngComm*, vol. 14, pp. 2871–2878, 2012.
- [74] J. He, X. Han, J. Yan et al., "Fast fabrication of homogeneous silver nanostructures on hydrazine treated polyaniline films for SERS applications," *CrystEngComm*, vol. 14, no. 15, pp. 4952–4954, 2012.
- [75] L. L. Qu, D. W. Li, J. Q. Xue, W. L. Zhai, J. S. Fossey, and Y. T. Long, "Batch fabrication of disposable screen printed SERS arrays," *Lab on a Chip*, vol. 12, no. 5, pp. 876–881, 2012.
- [76] X. Hong, D. Wang, and Y. Li, "Kinked gold nanowires and their SPR/SERS properties," *Chemical Communications*, vol. 47, no. 35, pp. 9909–9911, 2011.
- [77] N. Pazos-Pérez, W. Ni, A. Schweikart, R. A. Alvarez-Puebla, A. Fery, and L. M. Liz-Marzán, "Highly uniform SERS substrates formed by wrinkle-confined drying of gold colloids," *Chemical Science*, vol. 1, no. 2, pp. 174–178, 2010.
- [78] C. Zhu, G. Meng, Q. Huang et al., "Ag nanosheet-assembled micro-hemispheres as effective SERS substrates," *Chemical Communications*, vol. 47, no. 9, pp. 2709–2711, 2011.
- [79] M. F. Zhang, A. W. Zhao, H. H. Sun et al., "Rapid, large-scale, sonochemical synthesis of 3D nanotextured silver microflowers as highly efficient SERS substrates," *Journal of Materials Chemistry*, vol. 21, no. 46, pp. 18817–18824, 2011.
- [80] X. Han, H. Wang, X. Ou, and X. Zhang, "Highly sensitive, reproducible, and stable SERS sensors based on well-controlled silver nanoparticle-decorated silicon nanowire building blocks," *Journal of Materials Chemistry*, vol. 22, no. 28, pp. 14127–14132, 2012.
- [81] J. F. Li, Y. F. Huang, Y. Ding et al., "Shell-isolated nanoparticle-enhanced Raman spectroscopy," *Nature*, vol. 464, no. 7287, pp. 392–395, 2010.
- [82] S. Pahlow, A. März, B. Seise et al., "Bioanalytical application of surface- and tip-enhanced Raman spectroscopy," *Engineering in Life Sciences*, vol. 12, no. 2, pp. 131–143, 2012.
- [83] J. Kneipp, H. Kneipp, and K. Kneipp, "SERS—a single-molecule and nanoscale tool for bioanalytics," *Chemical Society Reviews*, vol. 37, no. 5, pp. 1052–1060, 2008.
- [84] P. R. Sajjalal and T. Pradeep, "Functional hybrid nickel nanostructures as recyclable SERS substrates: detection of explosives and biowarfare agents," *Nanoscale*, vol. 4, no. 11, pp. 3427–3437, 2012.
- [85] L.-B. Yang, G.-Y. Chen, J. Wang, T.-T. Wang, M.-Q. Li, and J.-H. Liu, "Sunlight-induced formation of silver-gold bimetallic nanostructures on DNA template for highly active surface enhanced Raman scattering substrates and application in

- TNT/tumor marker detection,” *Journal of Materials Chemistry*, vol. 19, no. 37, pp. 6849–6856, 2009.
- [86] K. L. Wustholz, C. L. Brosseau, F. Casadio, and R. P. Van Duyne, “Surface-enhanced Raman spectroscopy of dyes: from single molecules to the artists’ canvas,” *Physical Chemistry Chemical Physics*, vol. 11, no. 34, pp. 7350–7359, 2009.
- [87] Z. Zhang, Y. Wen, Y. Ma, J. Luo, L. Jiang, and Y. Song, “Mixed DNA-functionalized nanoparticle probes for surface-enhanced Raman scattering-based multiplex DNA detection,” *Chemical Communications*, vol. 47, no. 26, pp. 7407–7409, 2011.
- [88] N. T. B. Thuy, R. Yokogawa, Y. Yoshimura, K. Fujimoto, M. Koyano, and S. Maenosono, “Surface-enhanced Raman spectroscopy for facile DNA detection using gold nanoparticle aggregates formed via photoligation,” *Analyst*, vol. 135, no. 3, pp. 595–602, 2010.
- [89] S. Efrima and L. Zeiri, “Understanding SERS of bacteria,” *Journal of Raman Spectroscopy*, vol. 40, no. 3, pp. 277–288, 2009.
- [90] L. Yang, B. Yan, W. R. Premasiri, L. D. Ziegler, L. D. Negro, and B. M. Reinhard, “Engineering nanoparticle cluster arrays for bacterial biosensing: the role of the building block in multiscale SERS substrates,” *Advanced Functional Materials*, vol. 20, no. 16, pp. 2619–2628, 2010.
- [91] A. Samanta, K. K. Maiti, K. S. Soh et al., “Ultrasensitive near-infrared Raman reporters for SERS-based in vivo cancer detection,” *Angewandte Chemie*, vol. 50, no. 27, pp. 6089–6092, 2011.
- [92] A. Kumar, B. M. Boruah, and X. Liang, “Gold nanoparticles: promising nanomaterials for the diagnosis of cancer and HIV/AIDS,” *Journal of Nanomaterials*, vol. 2011, pp. 1–17, 2011.
- [93] F. Zhai, Y. Huang, X. Wang, and K. Lai, “Surface-enhanced Raman spectroscopy for rapid determination of  $\beta$ -agonists in swine urine,” *Chinese Journal of Analytical Chemistry*, vol. 40, no. 5, pp. 718–723, 2012.
- [94] J. Kneipp, H. Kneipp, M. McLaughlin, D. Brown, and K. Kneipp, “In vivo molecular probing of cellular compartments with gold nanoparticles and nanoaggregates,” *Nano Letters*, vol. 6, no. 10, pp. 2225–2231, 2006.

## Research Article

# Nucleation and Growth Mechanism of Si Amorphous Film Deposited by PIAD

D. Li,<sup>1,2</sup> G. L. Liu,<sup>1</sup> Y. Yang,<sup>1</sup> J. H. Wu,<sup>3</sup> and Z. R. Huang<sup>1</sup>

<sup>1</sup> State Key Laboratory of High Performance Ceramics and Superfine Microstructure, Shanghai Institute of Ceramics, Chinese Academy of Sciences, 1295 Dingxi Road, Shanghai 200050, China

<sup>2</sup> Graduate University of Chinese Academy of Sciences, Beijing 100049, China

<sup>3</sup> Energy Materials Research Center, Shanghai Institute of Ceramics, Chinese Academy of Sciences, 1295 Dingxi Road, Shanghai 200050, China

Correspondence should be addressed to Y. Yang; yangyong@mail.sic.ac.cn

Received 3 October 2012; Revised 28 December 2012; Accepted 4 January 2013

Academic Editor: Masayuki Nogami

Copyright © 2013 D. Li et al. This is an open access article distributed under the Creative Commons Attribution License, which permits unrestricted use, distribution, and reproduction in any medium, provided the original work is properly cited.

The nanoscale Si films with the thickness of 2 nm, 5 nm, 10 nm, and 20 nm were deposited by plasma ion assisted deposition (PIAD) on glass substrate, in order to investigate the initial stage and the nucleation and growth mechanism of the Si film. The atomic force microscopy (AFM) was used to investigate the surface topography of the as-deposited Si film. The initial nucleation and growth process of the film was described. The continuous film had been already formed when the film thickness was 10 nm. The growth of the deposited Si film accorded with the Volmer-Weber growth mode.

## 1. Introduction

The use of surface coating for surface modification of ceramics is an important alternative as a means of extending the performance of ceramic materials in a wide range of applications [1]. The amorphous silicon (a-Si) film was deposited as surface-modification film on the SiC ceramic matrix which was applied in advanced optical systems, in order to modify the microstructure defects or pores on the substrate surface and provide an alternative surface which would make the polishing process more easily [2, 3]. Besides, the a-Si film was the precursor of the crystalline Si film which was widely used in photovoltaic industry and extensive investigations on the technique and mechanism of the crystallization were carried out [4, 5].

The a-Si has been reported to be deposited by typical physical vapor deposition (PVD), hot-wire chemical vapor deposition (HWCVD) [6], plasma-enhanced chemical vapor deposition (PECVD) [4], magnetron sputtering deposition [7], ultrahigh vacuum ion beam sputtering (UHV IBS) [8], and so on.

The PVD process which is an environmental friendly technology could prepare a compact and uniform a-Si film [9]. The PVD techniques including thermal evaporation techniques, sputtering technique, and ion assisted deposition have been used to fabricate Si modification films. In the typical process of the vacuum evaporation, the migration rate of atom on the surface of substrate is confined by the low incident energy (only the kinetic energy of thermal motion, ~1 eV), and the preferred orientation growth and shadow effect could also result in the loose structure with columnar growth and holes in the final as-deposited film [10]. To solve this problem, the thermal evaporation techniques are combined with ion sources which provide additional energy and momentum to influence the properties of the as-deposited films, known as ion assisted deposition (IAD) [11–13]. To reinforce the chemical reaction between the substrate and the as-deposited materials atoms which would finally improve the compactness and the adhesive strength of the deposited film, the plasma ion assisted deposition (PIAD), as one of the ion plating method, was introduced into the deposition process. The plasma produced by the advance

plasma sources (APS) was distributed in the whole cavity, which would interact with the as-deposited material atoms to transfer high energy and to ionize the as-deposited atoms. The technological merits of this plasma source are recognized by the production of high performance coatings [14].

The microstructures of the a-Si film prepared by PIAD have been investigated and the excellent properties were proved for various applications [1, 9]. But little attention was paid to the initial stage and the growth mechanism of the a-Si film deposited by PIAD, which would be important to the microstructure and the final surface morphology of the amorphous film.

One of the reasons to this neglect is that most of the surface-sensitive analytical techniques applied in coating study could not be available for nanoscale observation. The nuclei with the size larger than 50 nm could be successfully observed by high-resolution SEM [15, 16]. The topography of the nuclei with the size of several nanometers could be clearly observed by the atomic force microscopy (AFM) [17]. So, only the atomic force microscopy (AFM) has been widely used to study the growth mechanisms and dynamics and the nanometer scale morphology of crystal surfaces, since its invention in 1986 [18].

In this work, a detailed study of the nucleation and growth mechanism of the PIAD a-Si film on silicate glass substrate has been performed. The Si films with different thickness of 2 nm, 5 nm, 10 nm, and 20 nm were prepared. The nucleation and growth process of the film was observed by AFM technique. The mean size and height of the nucleus (island) was estimated by line scan in the AFM images. The nucleation and growth phenomenon had been described and analyzed. The continuous film had been already formed when the film thickness was 10 nm, and the growth process of Si film deposited on glass substrate by PIAD was found to accord with Volmer-Weber growth mode. The deposited Si clusters with the size of 1-2 nm, as the deposition unit, were always present on the surface of as-deposited continuous Si film in the PAID process.

## 2. Experimental Details

The nanosilicon film was deposited on silicate glass in a box-type vacuum coating machine (Leybold APS 1104 coater, Germany) with plasma ion source assisted. The target was a high-purity polycrystalline Si source (99.999%, Special Alloy Powder Metallurgy Materials, General Research Institute for Nonferrous Metals (GRINM)). Before the deposition, the substrates were cleaned successively with water in an ultrasonic cleaner and then rinsed by acetone. All samples were performed at 200°C. The vacuum in the chamber before deposition was  $2.0 \times 10^{-3}$  Pa. The deposition rate remained 0.1 nm/s and the power of ion source was 6 kW during the deposition process. The mean thickness of Si film was designed to be 2 nm, 5 nm, 10 nm, and 20 nm, which was real-time monitored by a quartz crystal oscillator.

The surface topographic signatures of the substrate and the Si films were observed in detail by the atomic force microscope (AFM) (SPI3800N and 144 SPA300HV, SEIKO II, NSK Ltd., Japan) in ambient atmosphere at room temperature

in contact mode. The average height (thickness) and the size of the crystalline grain in full width at half maximum (FWHM) were estimated by the line scan in the AFM images and the surface roughness reported as peak value (PV) and root mean square roughness (RMS) was also calculated.

## 3. Results

**3.1. The Surface Morphology of the Substrate.** It is known that the properties of the substrate surface would significantly affect not only the microstructure but also the growth mechanism especially at the initial stage of the film deposition. The defect or impurity sites on the substrate surface would be the priority areas of nucleation. To investigate the growth process of the nanoscale film, the required properties of the substrate surface was even crucial.

The typical AFM images of glass substrate surface in two-dimensional (2D) and three-dimensional (3D) and the line scan profile on the image were shown in Figure 1. The surface was flat without defects or scratch. The RMS of substrate surface was 0.9 nm measured by AFM at a scan size of  $400 \mu\text{m}^2$ . The line scan in the image showed that the surface fluctuation was gentle and the PV was about 1 nm, which means the deposition films which were designed with more than 2 nm thick in this work would be obviously observed on this substrate.

**3.2. The Surface Morphology of the Si Film.** Si films with the thickness of 2 nm, 5 nm, and 10 nm were deposited on glass substrate and the AFM topographic images of the surfaces were shown in Figure 2. Figures 2(a), 2(c), and 2(e) were the 2D surface topography of the 2 nm, 5 nm, and 10 nm Si film, respectively, and Figures 2(b), 2(d), and 2(f) were the 3D images of the selected area in the corresponding 2D images.

The light spheroids randomly dispersed on the surface of the 2 nm Si film in Figure 2(a) which could associate with the spheroids observed in Figure 2(b). This surface topography signature which was quite different from the surface of substrate could be induced by the deposition process. And the spheroids/protuberances could be the nucleus of Si crystallization at the initial stage of the film forming. In Figures 2(c) and 2(d) which showed the topography of the 5 nm Si film, the density and the size of the dispersed nanocrystallites, which have been confirmed in the 2 nm film, were obviously increased. As the thickness of the Si film increased to 10 nm, the surface topography became smooth without nanocrystallites structure which has been seen in the 2 nm or 5 nm film; besides more and smaller spheroids were dispersed in Figure 2(f).

**3.3. The Line Scan Profile of the Nuclei.** The line scan profiles of the Si film with different thickness were shown in Figure 3, and the mean height and full width at half maximum (FWHM) of the spheroids on the surface of the Si film with different thickness were summarized in Table 1.

The height and the FWHM of the protuberances on the 2 nm Si surface were 1.4 nm and 100 nm, respectively. When the thickness of the deposited film increased to 5 nm, the height and FWHM of the nuclei increased to 3.7 nm and

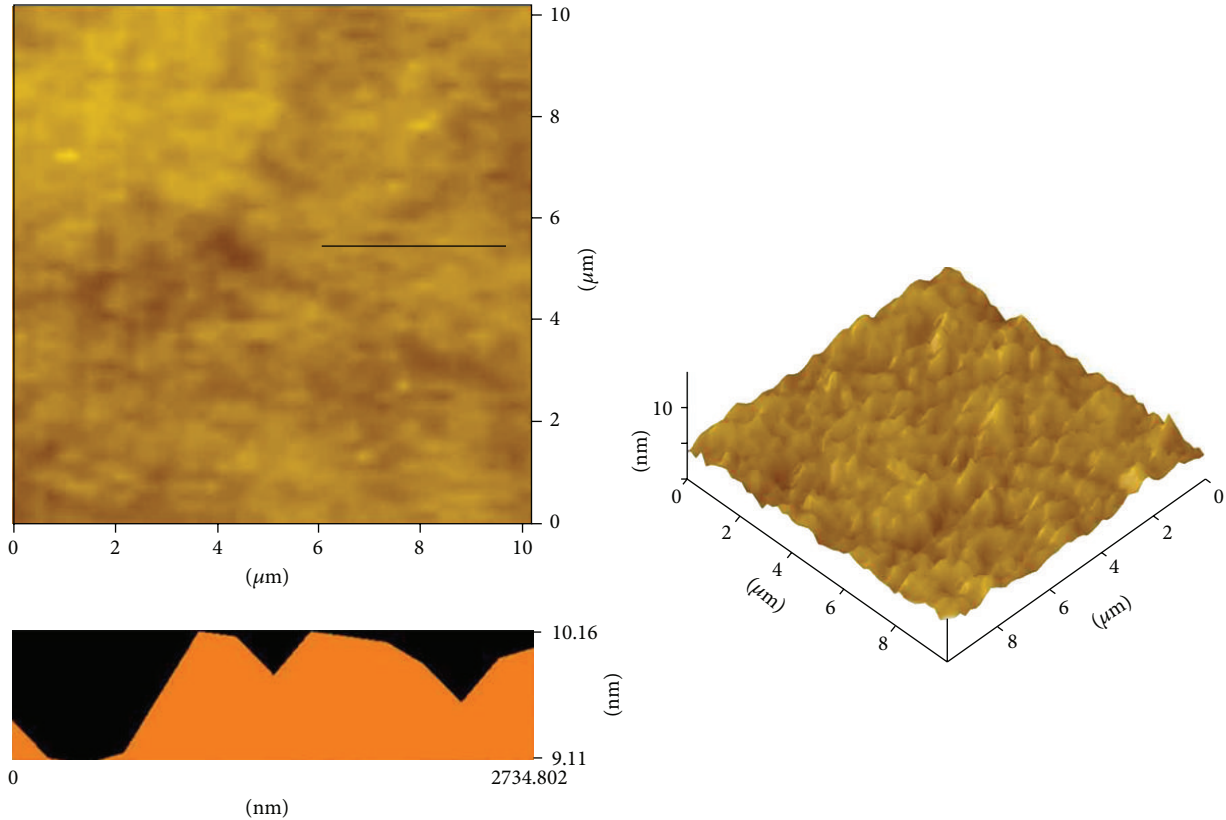


FIGURE 1: The AFM topographic image and line scan profile of glass substrate surface.

TABLE 1: The height and the FWHM of the nuclei on the surface of the Si film with different thickness.

Thickness	2 nm	5 nm	10 nm
Height	1.4	3.7 nm	0.9
FWHM	106.05 nm	164.05 nm	75.77 nm

164 nm, respectively. The Si nuclei with the intermediate state of merging were pointed out by arrows in Figure 3(c), which means that the coalescence process of the nuclei was progressively undergoing with the growth of the nuclei. The line scan profile of the film surface exhibited that the height and FWHM of the nuclei decreased to 0.9 nm and 75.8 nm instead of increasing with the film thickness, which indicated the growth stage/module of the deposited film was totally changed. The statistic results which have great dispersion indicated the grains in each early growth stage were presented on the film surface.

**3.4. The Surface Roughness of Si Film.** The surface roughness (PV and RMS) of the Si film with different thickness was measured at a scan size of  $10 \mu\text{m} \times 10 \mu\text{m}$  which was shown in Table 2. The surface roughness increased when the Si film deposited on the substrate and with the thickness increase of the Si film from 2 nm to 5 nm, which was consistent with the results of the line scan profiles on the Si film surface. The surface roughness of the Si film with 10 nm thick was

10.2 nm (PV) and 0.8 nm (RMS) which would be comparable to the surface roughness of the substrate. The fundamental changes of the film surface roughness indicated there is no deep canyon across the whole film thickness between the independently grown-up islands. So the continues deposited film was expected.

#### 4. Discussion

The emphases of this work were focused on the topographic signature of the Si nucleate on the substrate, the growth process, and mechanism of the nanoscale film. The whole process of the Si film growth on substrate would be described as the schematic diagram shown in Figure 4, by studying the AFM images of all the growth stages of the deposited film. The surface topography and the line scan profile of the 2 nm Si film indicated that the spheroid nuclei have been formed (Figures 2(a) and 3(a)). The nucleus shape was determined by the noninfiltration phenomenon between the substrate and the film component, which means the deposited Si atoms were more strongly bound to each other than they were bound to the substrate. This nucleation process was described as the first stage in Figure 4. The height and FWHM of the nuclei increased when the deposition thickness increased to 5 nm, which indicated the nuclei were at the growth stage. The nuclei grew up independently or by nuclei coalescence which was proved by the line scan profile in Figure 3(b) and depicted as second stage in Figure 4. The nuclei continued to grow and

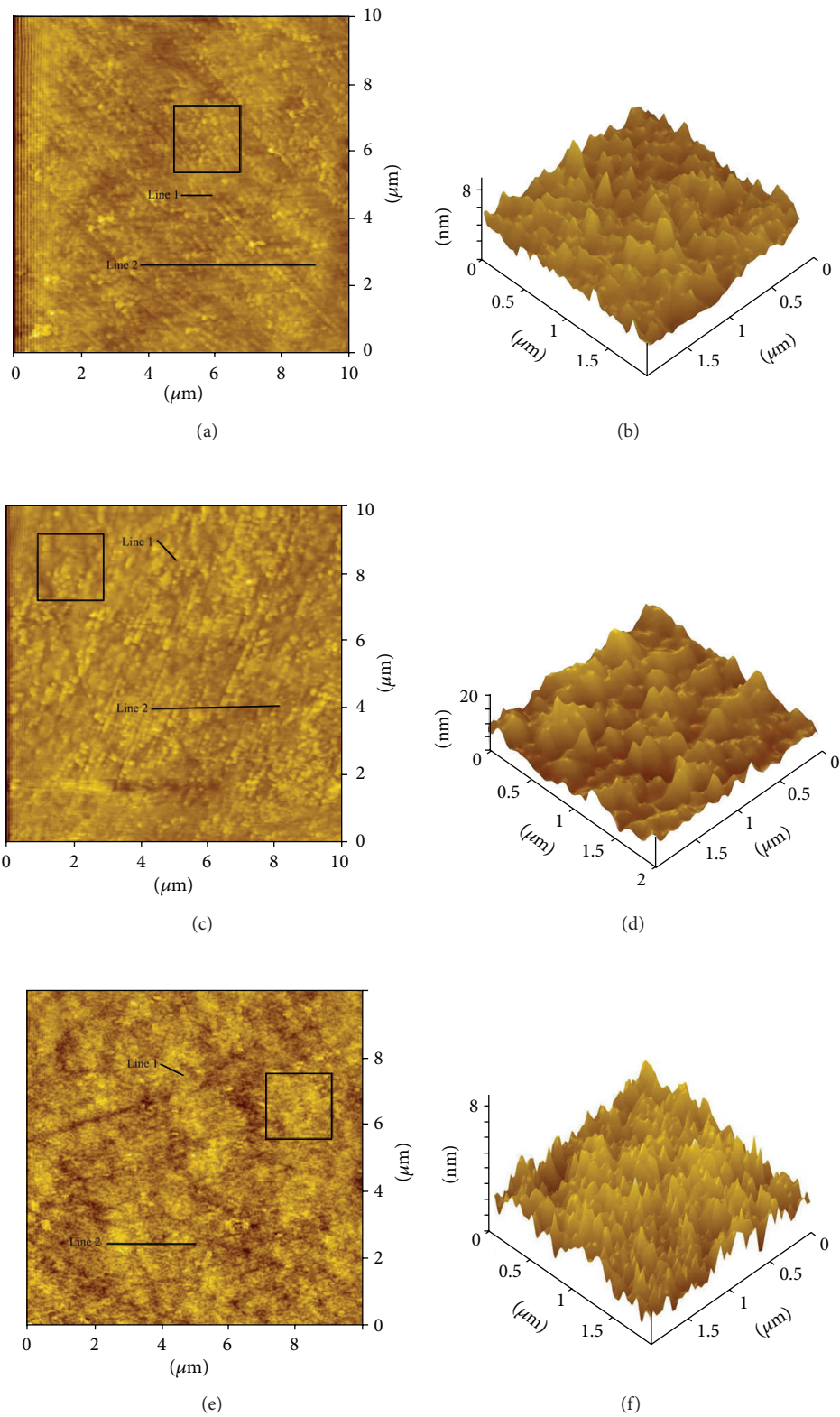


FIGURE 2: The surface topography images of the Si film with different thickness. The (a), (c), and (e) were the  $10\ \mu\text{m} \times 10\ \mu\text{m}$  2D images of 2 nm, 5 nm, and 10 nm Si film respectively, and the (b), (d), and (f) were the 3D images of the selected area in the 2D images of the corresponding Si films.

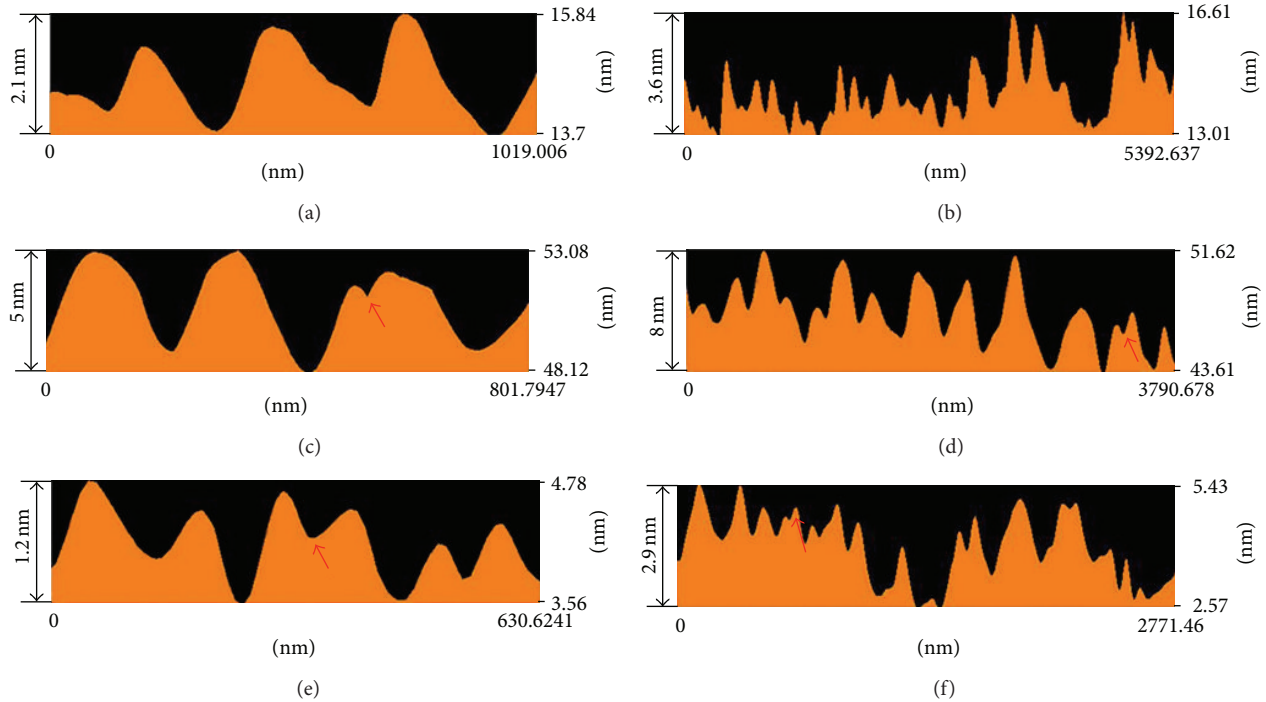


FIGURE 3: The line scan profiles of the Si film with different thickness. The (a) and (b) were the profiles of the line scan marked in Figure 2(a), the (c) and (d) were the profiles of the line scan marked in Figure 2(c), and the (e) and (f) were the profiles of the line scan marked in Figure 2(e).



FIGURE 4: The schematic diagram of the deposition process of Si film on glass substrate.

coalesce until a continuous film formed which was depicted as the third stage in Figure 4. Those growth processes were accorded with the typical processes of Volmer-Weber growth mode [19, 20].

When the film thickness reached 10 nm, the surface topography was totally changed without obviously crystallize nuclei but smooth surface was observed, and the surface roughness was also reduced to be comparable with the initial substrate surface. To figure out whether the 10 nm Si film was completely continuous or not, the surface of the 20 nm Si film was also observed by AFM. The surface topography image and line scan profile were shown in Figure 5. The surface of the 20 nm film showed the same feature with the 10 nm film,

TABLE 2: The surface roughness of the substrate and deposited Si films with different thickness.

	PV (nm)	RMS (nm)
Substrate	10.1	0.8
2 nm Si film	17.3	1.0
5 nm Si film	58.1	3.0
10 nm Si film	10.2	0.8

and the profile of the grains on the surface was of 1~2 nm height which was also similar with that of the 10 nm film. There was no obvious change in the surface topography of the film with more thickness and we could conclude that the deposited 10 nm Si film was already continuous.

Besides, the nuclei with the size of 1~2 nm distributed on the continuous Si film, which were even smaller than the initial crystallize nuclei, were considered as the deposition unit in deposition process. The nanoscale cluster was refined by the impact of the plasma ions and the ionized to-be-deposited Si atoms with high energy. The nanoscale deposition units would effectively increase the interaction between the deposited Si units and realize the densification of the film which could finally improve the macroscopic properties of the deposited film.

## 5. Conclusion

In this work, the nanoscale Si films were deposited by plasma ion assisted deposition (PIAD) on glass substrate. Our emphases were focused on the topographic signature of the Si

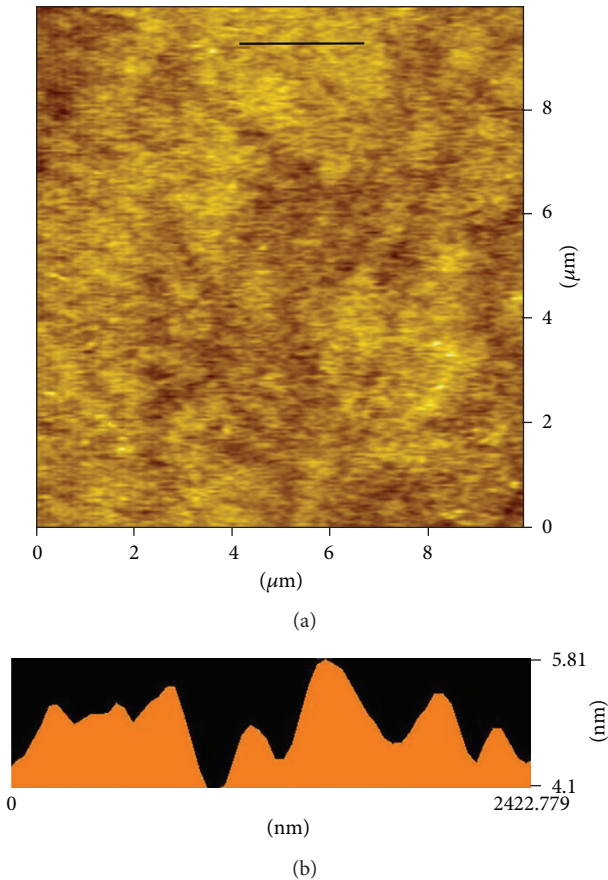


FIGURE 5: The AFM topographic image and the line scan profile of the surface of the 20 nm Si deposited film.

nucleate and the growth mechanism of the film. The AFM was used to investigate the surface topography of the deposited Si film. The nucleation of the deposited Si on the substrate was observed and the spheroid nuclei were explored on the surface of the substrate at the initial stage of the film forming. As the deposition continued, the nucleus grew larger in size and the evidence of the nucleus coalescence was also shown in the line scan profile. The continuous film had been already formed when the film thickness reached 10 nm. The growth process of Si film was found to accord with the Volmer-Weber growth mode, and the deposited Si clusters with the size of 1-2 nm, as the deposition units, were always present on the surface of the as-deposited continuous Si film in the PAID process.

## Acknowledgments

Y. Yang thanks the Century Program (One-Hundred-Talent Program) of the Chinese Academy of Sciences for special funding support, and thanks for the support by fund from Key Laboratory of Nanodevices and Applications, Suzhou Institute of Nano-Tech and Nano-Bionics, Chinese Academy of Sciences (no. 12CS01). This study was also supported in part by a fund from the National Natural Science Foundation

of China (NSFC, Contract no. 51071167, 51102266), Shanghai Pujiang Program (no. 10PJ1410700), and Yangtze River Delta Science Project (11495810100).

## References

- [1] G. L. Liu, Z. R. Huang, J. H. Wu et al., "Surface morphology evolution and properties of silicon coating on silicon carbide ceramics by advanced plasma source ion plating," *Surface and Coatings Technology*, vol. 207, pp. 204–210, 2012.
- [2] M. A. Ealey and J. A. Wellman, "Polishability of CERAFORM: silicon carbide," in *Advanced Materials for Optical and Precision Structures*, vol. 2857 of *Proceedings of SPIE*, pp. 78–85, 1996.
- [3] L. Rich and D. A. Crowe, "Polishing process for concave light-weight silicon-coated silicon carbide optics," in *Silicon Carbide Materials for Optics and Precision Structures*, vol. 2543 of *Proceedings of SPIE*, pp. 236–247, July 1995.
- [4] A. Wohllebe, R. Carius, L. Houben et al., "Crystallization of amorphous Si films for thin film solar cells," *Journal of Non-Crystalline Solids*, vol. 227–230, no. 2, pp. 925–929, 1998.
- [5] M. Li, Y. Liu, Y. Lin et al., "Study on amorphous silicon thin film by aluminum-induced crystallization," *Physics Procedia*, vol. 18, pp. 77–80, 2011.
- [6] Y. Zhou, B. Zhou, J. Gu, M. Zhu, and F. Liu, "Comparison of growth mechanisms of silicon thin films prepared by HWCVD with PECVD," *Thin Solid Films*, vol. 516, no. 5, pp. 564–567, 2008.
- [7] M. Grischke, K. Bewilogua, K. Trojan, and H. Dimigen, "Application-oriented modifications of deposition processes for diamond-like-carbon-based coatings," *Surface and Coatings Technology*, vol. 74–75, no. 2, pp. 739–745, 1995.
- [8] C. K. Chung and B. H. Wu, "Effect of amorphous Si layer on the reaction of carbon and silicon in the C/Si multilayer by high vacuum annealing," *Thin Solid Films*, vol. 515, no. 4, pp. 1985–1991, 2006.
- [9] G. L. Liu, *Surface finish, coating and optical properties of SiC materials [Ph.D. thesis]*, Shanghai Institute of Ceramics, CAS, 2009.
- [10] W. Y. Si Lei and L. Guojun, "Deposition techniques for optical thin films," *Journal of ChangChun University of Science and Technology*, vol. 27, p. 4, 2005.
- [11] P. J. Martin, H. A. Macleod, R. P. Netterfield, C. G. Pacey, and W. G. Sainty, "Ion-beam-assisted deposition of thin films," *Applied Optics*, vol. 22, no. 1, pp. 178–184, 1983.
- [12] J. D. Targove and H. A. Macleod, "Verification of momentum-transfer as the dominant densifying mechanism in ion-assisted deposition," *Applied Optics*, vol. 27, pp. 3779–3781, 1988.
- [13] J. Harhausen, I. Meyenburg, A. Ohl, and R. Foest, "Characterization of the plasma plume of a PIAD plasma source by means of optical emission spectroscopy," *Surface and Coatings Technology*, vol. 205, no. 2, pp. S407–S410, 2011.
- [14] A. Zöller, R. Götzelmann, K. Matl, and D. Gushing, "Temperature-stable bandpass filters deposited with plasma ion-assisted deposition," *Applied Optics*, vol. 35, no. 28, pp. 5609–5612, 1996.
- [15] R. Polini, P. D'Antonio, and E. Traversa, "Diamond nucleation from the gas phase onto cold-worked Co-cemented tungsten carbide," *Diamond and Related Materials*, vol. 12, no. 3–7, pp. 340–345, 2003.

- [16] M. D. Whitfield, J. A. Savage, and R. B. Jackman, "Nucleation and growth of diamond films on single crystal and polycrystalline tungsten substrates," *Diamond and Related Materials*, vol. 9, no. 3-6, pp. 262–268, 2000.
- [17] M. Balaji, A. Claudel, V. Fellmann et al., "Effects of AlN nucleation layers on the growth of AlN films using high temperature hydride vapor phase epitaxy," *Journal of Alloys and Compounds*, vol. 526, pp. 103–109, 2012.
- [18] Y. L. Geng, D. Xu, X. Q. Wang, D. Y. Pan, G. H. Zhang, and G. W. Yu, "Investigation of nucleation growth mechanism of MMTC crystal by AFM," *Journal of Crystal Growth*, vol. 280, no. 1-2, pp. 266–270, 2005.
- [19] K. L. Chopra, *Thin Film Phenomena*, Chapter 4, McGraw-Hill, New York, NY, USA, 1969.
- [20] S. K. Mishra, P. K. P. Rupa, and L. C. Pathak, "Nucleation and growth of DC magnetron sputtered titanium diboride thin films," *Surface and Coatings Technology*, vol. 200, no. 12-13, pp. 4078–4081, 2006.

## Review Article

# Shape-Controlled Metal Nanoparticles and Their Assemblies with Optical Functionalities

Go Kawamura,<sup>1</sup> Masayuki Nogami,<sup>2</sup> and Atsunori Matsuda<sup>1</sup>

<sup>1</sup>Department of Electrical and Electronic Information Engineering, Toyohashi University of Technology, 1-1 Hibarigaoka, Tempaku-cho, Toyohashi 441-8580, Japan

<sup>2</sup>Department of Frontier Materials, Nagoya Institute of Technology, Gokiso, Showa-ku, Nagoya 466-8555, Japan

Correspondence should be addressed to Go Kawamura; [gokawamura@ee.tut.ac.jp](mailto:gokawamura@ee.tut.ac.jp)

Received 26 September 2012; Revised 4 December 2012; Accepted 4 December 2012

Academic Editor: Yong Yang

Copyright © 2013 Go Kawamura et al. This is an open access article distributed under the Creative Commons Attribution License, which permits unrestricted use, distribution, and reproduction in any medium, provided the original work is properly cited.

Metal nanoparticles (NPs) possess excellent optical, optoelectronic, and optochemical properties based on their surface plasmon resonance. However, for practical use, the morphology and assembly of metal NPs need to be controlled. Here, we review facile control methods including seed-mediated growth accompanied with a comproportionation reaction of seeds to control their morphology and assembly. Several synthetic conditions have been modified to precisely control the morphology of metal NPs. Functionalized mesoporous oxides have also been used as hard templates to align metal nanorods and control their dimensions. The high performance of such metal nanorods in surface-enhanced Raman scattering, polarization of light, and photocatalysis has been measured, and the reasons for their high performance are discussed.

## 1. Introduction

Collective oscillations of free electrons on the surface of metal nanoparticles (NPs) caused by exposure to light, called surface plasmon resonance (SPR), have been used to color stained glass for the use in churches [1, 2]. Lowered melting point and changed band structure (quantum size effect) are also interesting phenomena observed for metal NPs, so they are being studied actively [3, 4]. Such characteristics can be optimized through the precise control of the morphology of metal NPs. Hence, the NPs have diverse application fields such as photocatalysis, (bio)sensing, and surface-enhanced Raman scattering (SERS) [5–7]. Finding simple, inexpensive ways to fabricate morphology-controlled metal NPs has thus been one of the main themes of recent research in this field [8].

“Top-down” and “bottom-up” approaches are both used to fabricate metal NPs, involving, for example, laser abrasion of bulk metal and accumulation of metal atoms, respectively.

“Bottom-up” approaches normally allow more precise control of morphology than “top-down” ones [9]. In the case where metal ions are the building blocks in a “bottom-up” approach, reduction of the ions leads to the formation of metal atoms, which aggregate through Van der Waals forces to form metal NPs. During the formation of metal NPs, their size, shape, and aggregation can be controlled by choosing appropriate rates of nuclear formation and growth, and/or promoting anisotropic growth by stabilizing specific crystal facets on the surface of metal NPs [10]. Templates with nanosized pores (so-called hard templates) can also be used to fabricate morphology-controlled metal NPs [11]. When hard templates are used, treatments to control dispersion state and immobilization of metal NPs on/in matrices are unnecessary, making such templates a simple fabrication procedure suitable for practical applications.

In this paper, the fabrication of metal NPs using modified seed-mediated growth, which does not use hard templates, and the properties of the resulting metal NPs including SERS

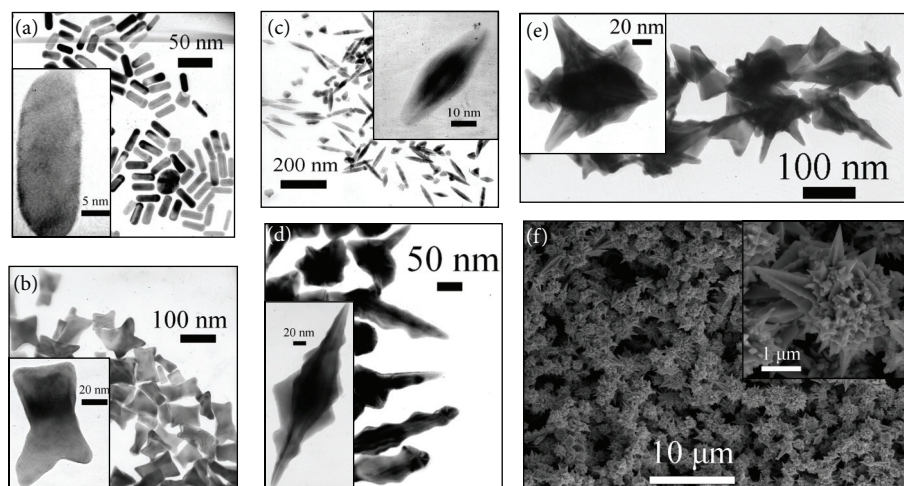


FIGURE 1: Electron microscope images of AuNPs prepared via seed-mediated growth with (a) rod, (b) dog-bone, (c) bipyramidal, (d) roughened bipyramidal, (e) multibranching, and (f) large multibranching morphologies. Magnified images are shown in insets. Reproduced with permission from [18]. Copyright 2009 Elsevier.

[12, 13] are first examined. A different method to fabricate metal NPs using mesoporous oxides [14, 15] as hard templates and the properties including polarization of light and photocatalysis of the resulting metal NPs are then discussed.

## 2. Fabrication of Metal NPs without Hard Templates

When metal NPs are fabricated via a “bottom-up” approach, metal ions in solution are often used as the source of metal. Metal NPs can be obtained by adding a surface-stabilizing agent, such as a surfactant, and a reductant to the solution. Because gold, platinum, and silver possess low ionization tendencies for metals, they scarcely react to surrounding substances, so controlling the morphology of their NPs is easy compared with those of other metals [16, 17]. In particular, gold nanoparticles (AuNPs) can form various morphologies because of their low ionization tendency, so many researchers have explored simple, inexpensive fabrication methods to prepare morphology-controlled AuNPs [18, 19]. From the perspective of SPR characteristics, rod-shaped NPs (nanorods (NRs)) exhibit two-SPR modes because of their shape anisotropy, while multibranching NPs with many sharp apices show an abnormally strengthened electromagnetic field around themselves [20]. To fabricate metal NPs with such unique SPR-related characteristics, appropriate selection of starting materials is of course required besides the precise control of reaction conditions including temperature, pH, and ionic strength. Some typical examples are described in the following sections.

*2.1. AuNPs with Controlled Shape Prepared by Changing the Morphology of Seeds [21].* Seed-mediated growth produces NPs by completely separating nuclear formation and growth stages [22, 23]. AuNPs with various shapes can be obtained

using this method, as shown in Figure 1, simply by changing the morphology of seed particles formed in the nuclear formation stage. For example, we prepared single crystalline ( $\sim 1.5$  nm) and multiple twin ( $\sim 4$  nm) particles as seeds and reduced their sizes in a comproportionation reaction using a growth solution containing  $\text{Au}^{3+}$  ions. To confirm the occurrence of the comproportionation reaction, optical extinction spectra were measured, as shown in Figure 2. The extinction coefficient at 400 nm corresponded to an  $\text{Au}^{3+}$  ion-related compound. The degree of the decrease in the extinction coefficient at 400 nm of a mixture of growth solution and water was smaller than that of a mixture of growth and seed solutions. This indicated that Au atoms in the seeds reacted with  $\text{Au}^{3+}$  ions in the growth solution and both were converted to  $\text{Au}^+$  ions in the comproportionation reaction. The relationship between the morphologies of seeds and AuNPs is illustrated in Figure 3. In the case where single crystalline seeds with a diameter of  $\sim 1.5$  nm were used, the shape of the resulting AuNPs gradually changed from NRs (Figure 1(a)) to multibranching NPs (Figure 1(e)) via a dog-bone shape (Figure 1(b)) by lengthening the comproportionation reaction time. In contrast, when multiple twin seeds with a size of  $\sim 4$  nm were used, the shape of the resulting AuNPs gradually changed from bipyramidal (Figure 1(c)) to multibranching (Figure 1(e)) as the comproportionation reaction time was extended. The size of the multibranching AuNPs increased as the reaction time was increased; the maximum particle size was larger than  $1 \mu\text{m}$  (Figure 1(f)). Large multibranching AuNPs were also obtained without addition of a seed solution, suggesting that the seed particles completely dissociated when the comproportionation reaction was allowed to proceed for 10 min. These results revealed that the morphology of AuNPs can be controlled simply by modifying the size and/or morphology of seeds via the comproportionation reaction.

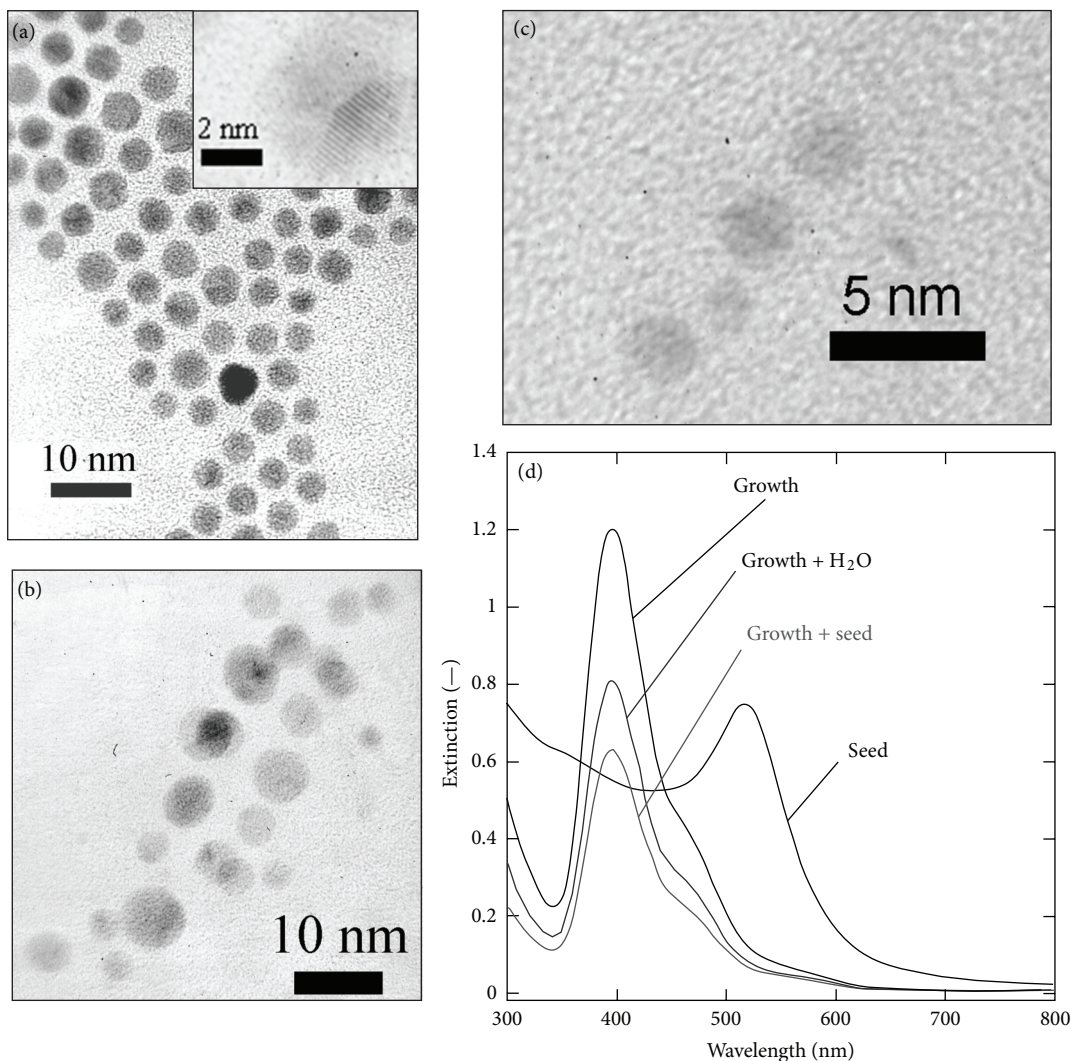


FIGURE 2: Citrate-stabilized seed particles. (a) TEM and HRTEM images of as-prepared particles. TEM images of the particles (b) 10 s and (c) 20 s after being added to the growth solution. (d) Optical extinction spectra of the seed and growth solutions, a mixture of the seed (1 mL) and growth (2 mL) solutions, and a mixture of the growth solution (2 mL) and H<sub>2</sub>O (1 mL). Reproduced with permission from [18]. Copyright 2009 Elsevier.

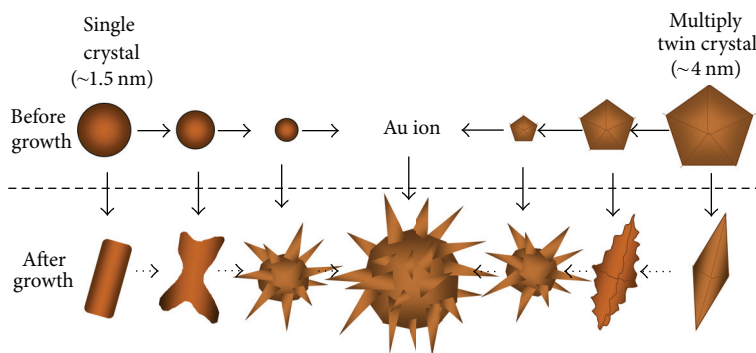


FIGURE 3: Relationship between the morphologies of seeds and grown AuNPs. Reproduced with permission from [18]. Copyright 2009 Elsevier.

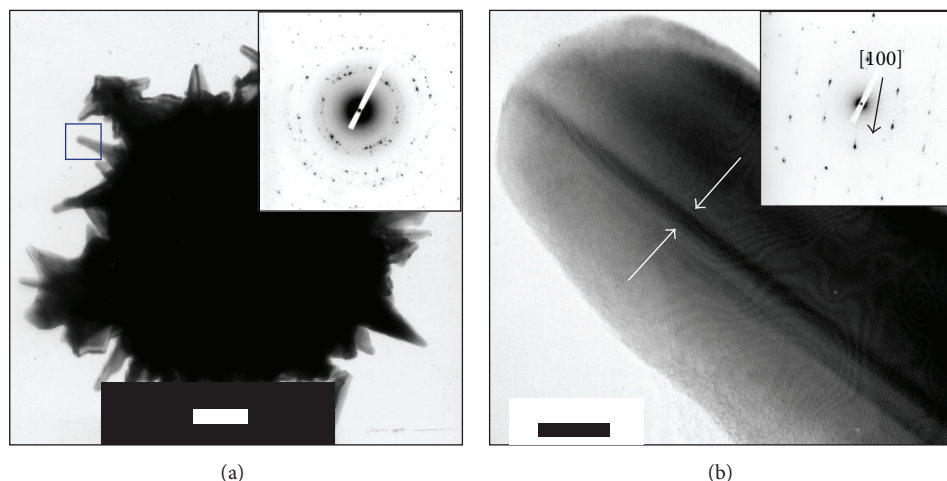


FIGURE 4: (a) TEM image of an isolated multibranched AuNP. (b) HRTEM image of the branch enclosed by the blue square in (a). The white arrows indicate the position of twin defects. SAED patterns are shown as insets. The white and black scale bars are 100 and 5 nm, respectively. Reproduced with permission from [21]. Copyright 2009 Elsevier.

### 2.2. Precise Control of the Shape of Multibranched AuNPs [24].

When AuNPs are prepared by conventional liquid phase synthesis, they normally form particles to minimize their surface energy, resulting in the formation of isotropic Au nanopolygons/spheres, because gold forms face-centered cubic crystals [25, 26]. However, the multibranched AuNPs obtained (Figures 1(e) and 1(f)) are partly anisotropic and possess many sharp apices, which strongly enhances the electromagnetic field near the surface of the particles compared with isotropic/spherical AuNPs. Several methods to fabricate AuNPs with multibranched morphology have been reported [27–31]; however, the precise control of their morphology is still very difficult to achieve. We thus investigated the growth mechanism of multibranched AuNPs using a high-resolution transmission electron microscopy (HRTEM) and selected-area electron diffraction (SAED), as presented in Figure 4. It was concluded that the probable growth mechanism involved a combination of the effects of defect formation in AuNPs and deposition of a small amount of silver atoms on AuNPs. Specifically, in the SAED pattern of an isolated multibranched AuNP (inset of Figure 4(a)), Debye-Scherrer rings are observed, indicating that the particle is polycrystalline. Such particles do not form NRs or cubes but instead assemble into complex structures like multibranched AuNPs. The HRTEM image of a branch enclosed by a blue square in Figure 4(b) shows the existence of stacking faults along the longer axis of the branch (indicated by arrows). The presence of stacking faults is also confirmed by the observation of line reflections along the  $[1\ 0\ 0]$  direction in the SAED pattern. These results suggest that the branches grew in the  $[1\ 0\ 0]$  direction from defect sites in the polycrystalline core particles. It was also found that underpotential deposition [32, 33] of silver on growing AuNPs played an important role in their morphology [24]. Based on the revealed growth mechanism of the particles, the size and morphology of multibranched AuNPs were precisely controlled through the careful selection of the concentrations of seeds, silver ions, and

organic additives in the growth solution (Figure 5). Organic additives such as cyclohexane and acetone were added to tighten and loosen, respectively, the micelle structure of cetyltrimethylammonium bromide (CTAB) in the solution [34–37], allowing the length of branches to be modified.

### 2.3. Control of AuNR Assemblies and Their SPR and SERS [38, 39].

The gold nanorods (AuNRs) shown in Figure 1(a) exhibit two SPR modes because of their anisotropy. The modes ascribed to the oscillations in the directions of the short and long axes resonate with light of shorter and longer wavelength, respectively. The mode that resonates with light of longer wavelength red shifts significantly as the aspect ratio of the AuNRs is increased [40–42]. This characteristic is advantageous to their practical application in wavelength-selective SPR devices. However, AuNRs tend to align parallel to each other as the solvent evaporates, which leads to a capillary force between AuNRs [43–47]. The smectic-like structure (side-to-side assembly) of AuNRs diminishes their SPR characteristics. Conversely, SPR appears more strongly in AuNRs assembled in an end-to-end fashion [48]. Therefore, the control of the assembly and length of AuNRs is important in terms of their SPR properties. In this regard, we prepared AuNRs of controlled length by altering the conditions used for seed-mediated growth (Figure 6). The AuNRs could be induced to assemble in an end-to-end fashion by controlling the concentration of surface stabilizer (CTAB) in solution (Figure 7). In practice, the solution was centrifuged and  $\text{H}_2\text{O}$  substituted for the supernatant to decrease the concentration of CTAB. To increase the concentration of CTAB, it was just added to the solution. The end-to-end assembly of AuNRs presumably occurred because of the stronger affinity of CTAB for the  $\{1\ 0\ 0\}$  and/or  $\{1\ 1\ 0\}$  facets on the sides of the AuNRs, which have larger surface energy than the  $\{1\ 1\ 1\}$  facet on the ends of AuNRs [49]. In other words, the detachment of surface-stabilizing CTAB in the solution with a low concentration of

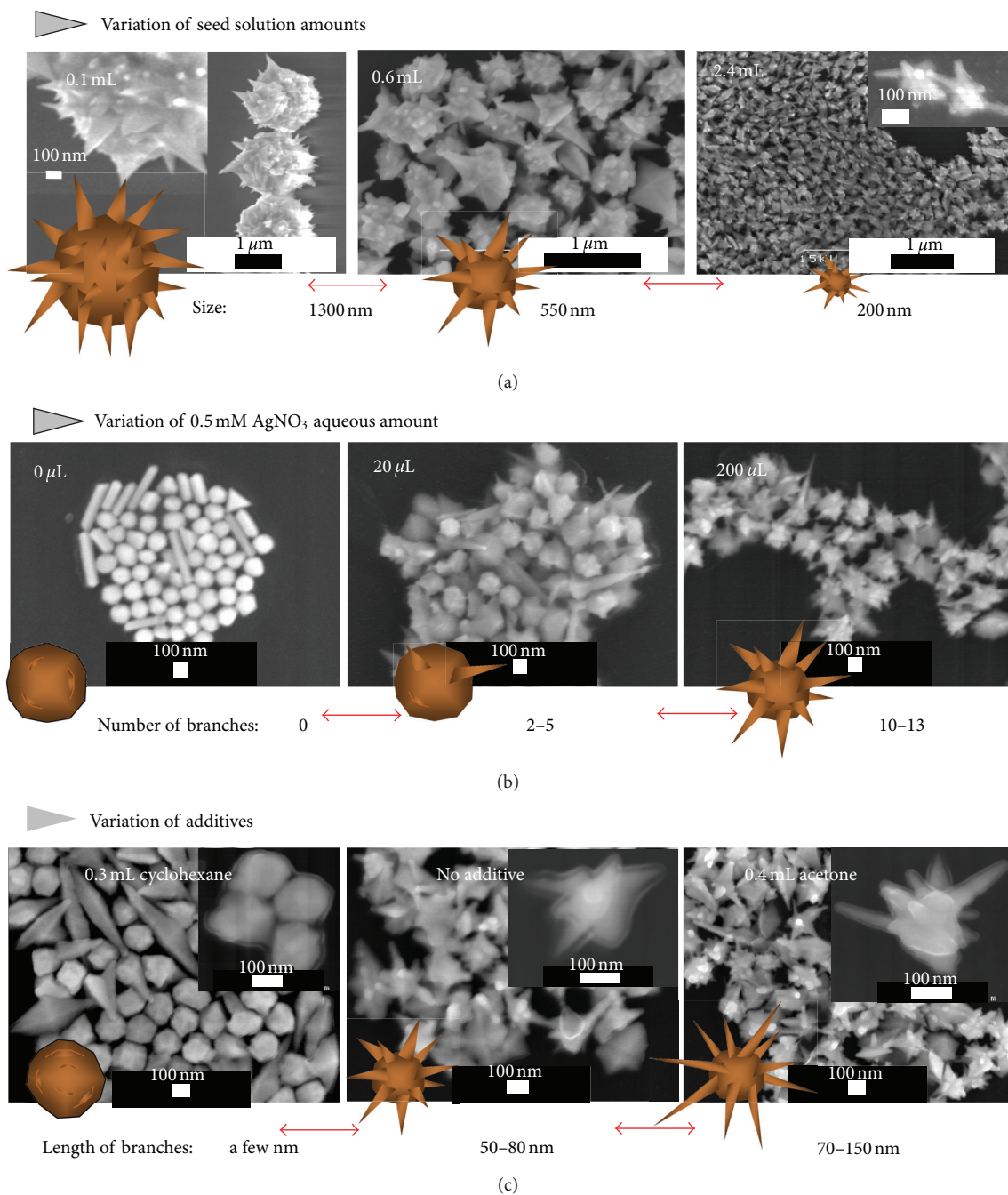


FIGURE 5: SEM images and illustrations of morphology-controlled multibranched AuNPs. Reproduced with permission from [21]. Copyright 2009 Elsevier.

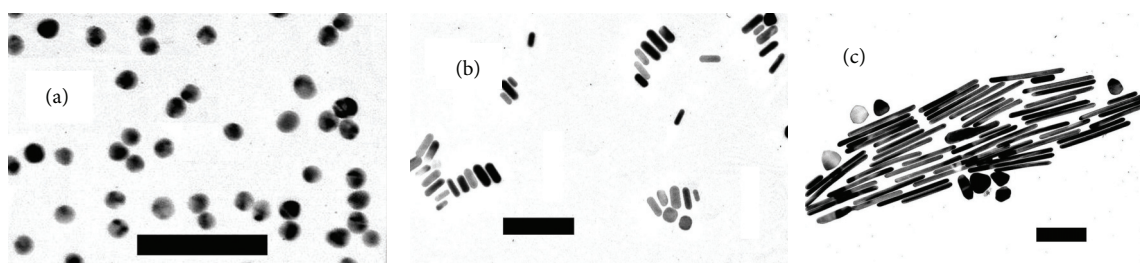


FIGURE 6: TEM images of AuNRs of different lengths. Reproduced with permission from [32]. Copyright 2008 American Chemical Society.

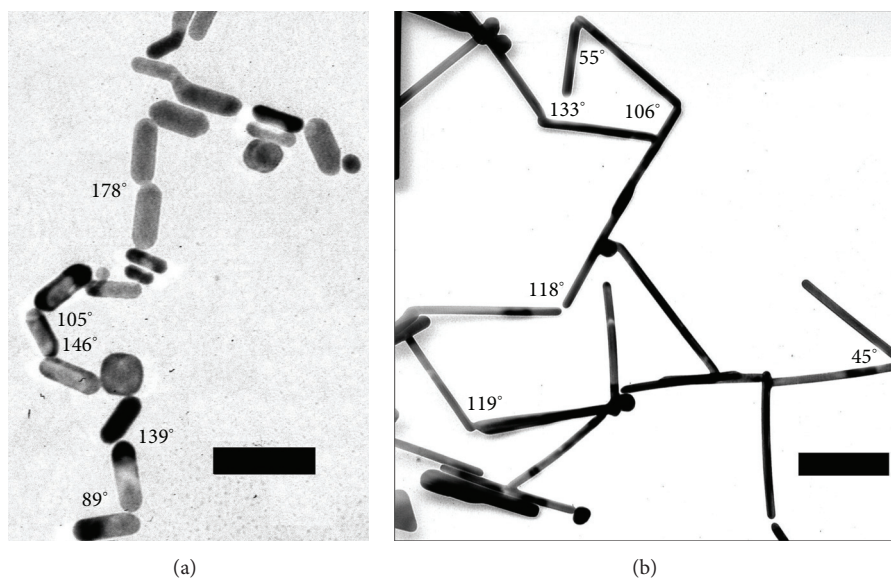


FIGURE 7: TEM images of end-to-end-connected AuNRs shown in Figures 6(b) and 6(c). Reproduced with permission from [32]. Copyright 2008 American Chemical Society.

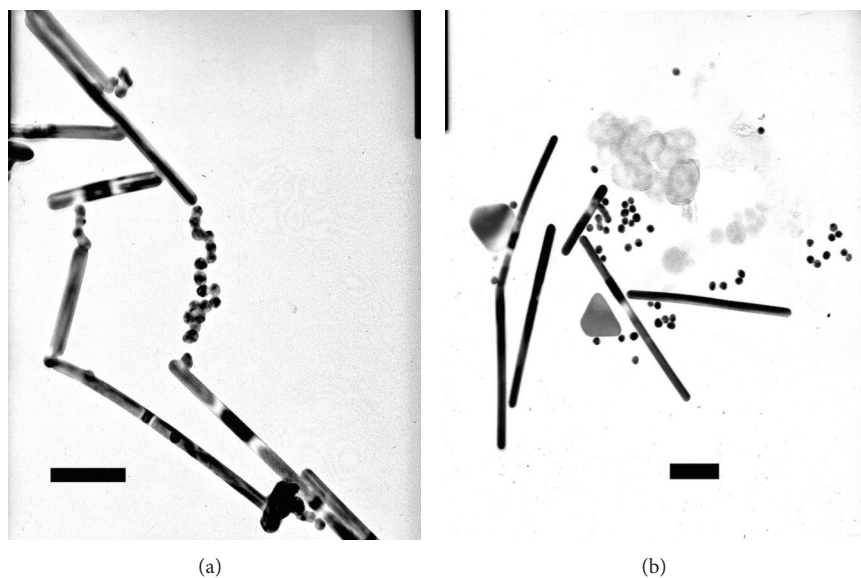


FIGURE 8: TEM images of CTAB-covered AuNRs after reaction with (a) citrate-stabilized AuNSs and (b) CTAB-stabilized AuNSs. The bare ends of AuNRs adsorb the citrate-stabilized AuNSs, whereas CTAB-stabilized AuNSs only accumulate near the sides of AuNRs. CTAB tends to be adsorbed by the sides of AuNRs in solutions containing a low concentration of CTAB. Scale bars are 100 nm. Reproduced with permission from [32]. Copyright 2008 American Chemical Society.

CTAB started from the ends of AuNRs because of their low affinity, which led to an end-to-end assembly of the AuNRs (Figure 8). Although assembly in an end-to-end fashion continued as time progressed, the degree of connection could be controlled by increasing the concentration of CTAB in the solution (Figure 9). The new peaks appeared at the wavelengths longer than 800 nm in Figure 9(a) could be attributed to the coupled SPR modes, of end-to-end AuNR assemblies. Moreover, end-to-end AuNR assemblies with/without connecting molecules (CTAB) could be prepared individually

(Figure 10). End-to-end assemblies of AuNRs with CTAB in the gaps between them could be converted back into dispersions of single AuNRs by increasing the concentration of CTAB.

A suspension of end-to-end-connected AuNRs was drop-cast onto a glass slide and air-dried to obtain a film sample. The morphology of this film was unlike that of a side-to-side-assembled AuNR suspension, as shown in Figure 11. Their extinction spectra were also different; only the film prepared from end-to-end-connected AuNRs exhibited two

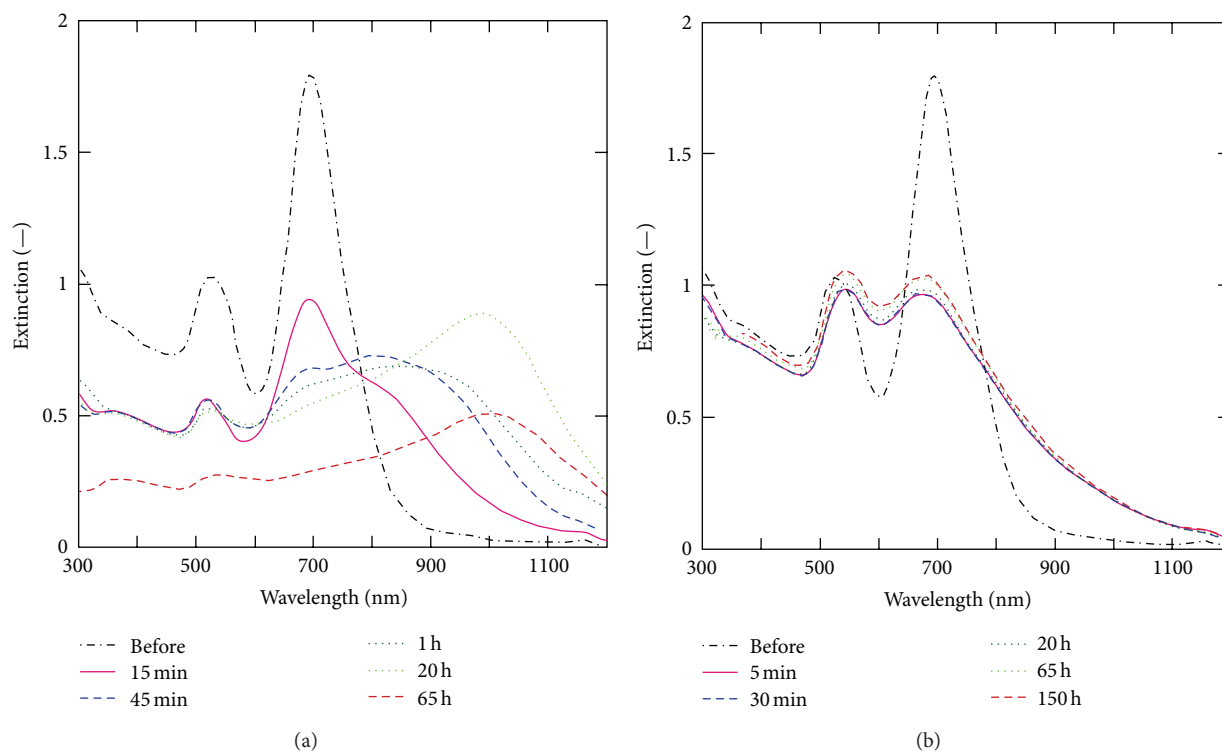


FIGURE 9: Optical extinction spectra of solutions of AuNRs with an aspect ratio of 3 prepared by adding (a) 40  $\mu\text{L}$  of 1 mM sodium citrate and (b) 0.5 mL of 40 mM CTAB 5 min after the addition of 60  $\mu\text{L}$  of 1 mM sodium citrate. The times in (a) and (b) are the time intervals after the addition of sodium citrate and CTAB, respectively. The unchanged spectra in (b) with time indicate the end of growth of end-to-end-connected AuNRs. Reproduced with permission from [32]. Copyright 2008 American Chemical Society.

distinct extinctions (Figure 12). Because AuNRs assembled in a side-to-side (parallel alignment) fashion show reduced SPR, the two observed extinctions from the end-to-end-assembled (linear-aligned) AuNR film were considered to be the intrinsic SPR of AuNRs. In fact, results simulated using Gans' theory indicated that the extinction at 2200 nm could be assigned to the weakly coupled longitudinal mode of AuNRs with an aspect ratio of 16 [50, 51], whereas that at 800 nm was attributed to gold nanodiscs, which are a byproduct of AuNRs and can be seen in Figures 6(c), 7(b), and 8(b). The film prepared from end-to-end-assembled AuNRs exhibited strong extinction peaks and high SERS activity (Figure 13). In contrast, the film prepared from side-to-side-assembled AuNRs showed low SERS activity. These results indicate that there are two reasons for the high SERS activity of the film prepared from end-to-end-assembled AuNRs: the large enhancement of electromagnetic field because of the strong SPR effect, and the proximity of rhodamine 6G (R6G) to the surface of AuNRs because of the low quantity of CTAB on the surface (and especially the ends) of AuNRs. In other words, end-to-end AuNR assemblies escaped the reduction of their SPR [48], and the strong near-field light was utilized to excite R6G which could reach very close to AuNR surface due to the absence of CTAB.

### 3. Fabrication of Metal NPs with Hard Templates

As well as soft templates like the surfactants discussed above, hard templates such as mesoporous oxides, anodized oxide

layers, and zeolites can also be used to fabricate metal NPs [52–55]. When hard templates are used, the porous structures in the template directly determine the morphology of the resulting metal NPs [56]. Furthermore, if the hard templates are used as a matrix for the final product, the processes required to assemble and immobilize metal NPs prepared by soft templates can be bypassed. For example, when a template with a two-dimensional (2D) structure is used, the shape and/or assembly of metal NPs should be anisotropic and thus exhibit unique anisotropic characteristics. In the next section, the syntheses of metal NPs and NRs using mesoporous oxide templates with tubular pores are reviewed. Because the caliber of tubular mesopores is constant in each template (the porous structure is ascribed to 2D hexagonal), the diameter of metal NPs/NRs is fixed. Therefore, the SPR of the NPs/NRs is readily controlled because the wavelength of SPR depends only on their aspect ratio.

**3.1. Anisotropic Assembly of AuNRs and Polarization Effects [57].** Mesoporous silica with 2D hexagonal structure like MCM-41 and SBA-15 contains curving tubular mesopores, so structural anisotropy is not apparent over a wide range (>several tens of  $\mu\text{m}^2$ ). A coating of mesoporous silica on muscovite mica is one of the methods used to realize anisotropy by aligning the tubular mesopores over a wide-range [58, 59]. Figure 14 shows electron microscope images, a schematic illustration, and X-ray diffraction (XRD) patterns of a mesoporous silica film grown on mica. Uniaxially aligned, evenly spaced pores were observed in a region of

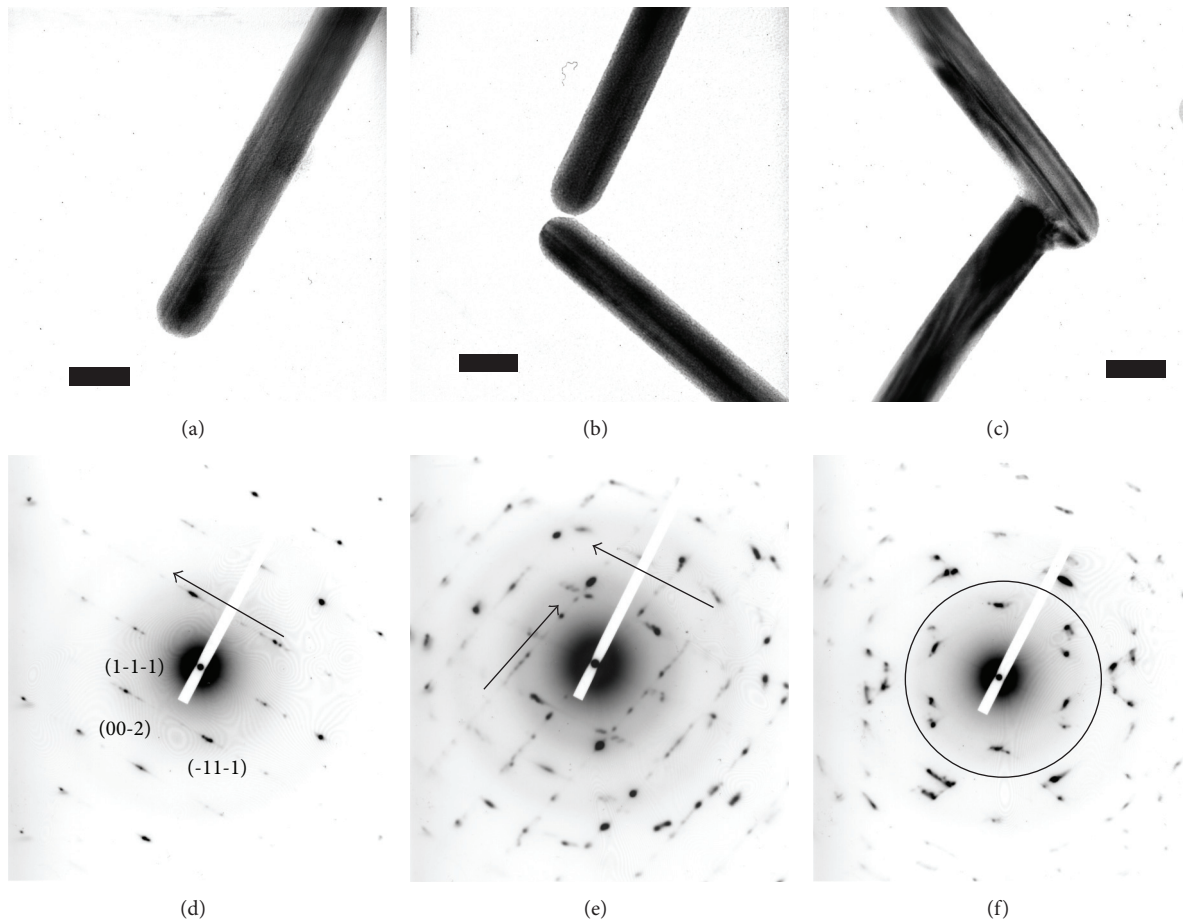


FIGURE 10: TEM images of (a) isolated and end-to-end-connected AuNRs (b) with and (c) without connecting molecules (CTAB) between them. (d–f) Corresponding SAED patterns for AuNRs shown in (a–c), respectively. Scale bars are 20 nm. Reproduced with permission from [32]. Copyright 2008 American Chemical Society.

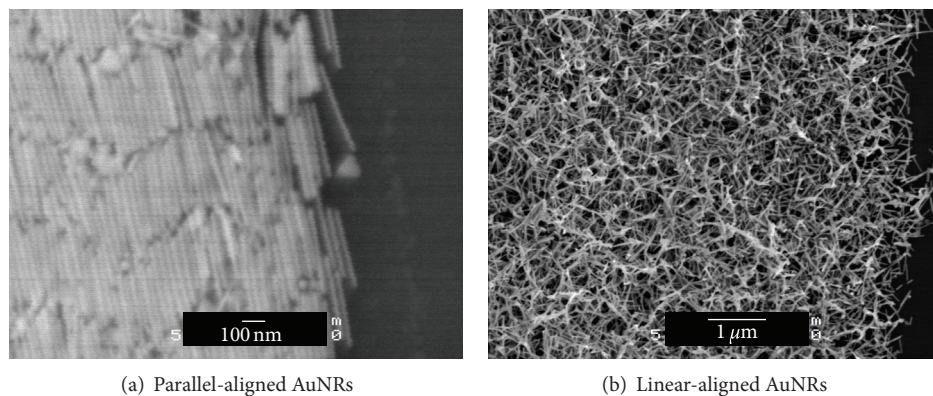


FIGURE 11: SEM images of self-assembled AuNRs on glass substrates prepared using the concentrated solutions shown in Figures 6(c) and 7(b). Reproduced with permission from [31]. Copyright 2007 American Institute of Physics.

$\sim 1 \text{ cm}^2$  at the surface of the film (Figure 14(a)). Similar pores were also observed throughout the depth of the film (Figure 14(b)). These observations confirmed that the prepared film possessed uniaxially aligned tubular mesopores in a wide region, like those illustrated in Figure 14(c). The direction of the longitudinal axis of the tubular mesopores was parallel to

the cleavage direction of the mica substrate. The XRD pattern indicated that the planar distance ( $d$ -value) of the  $\{1\ 0\ 0\}$  planes of the 2D hexagonal structure of the film was 3.6 nm (Figure 14(d)). After the deposition of gold into the pores of the film, interesting results were obtained, as presented in Figure 15. The film showed different appearances when it

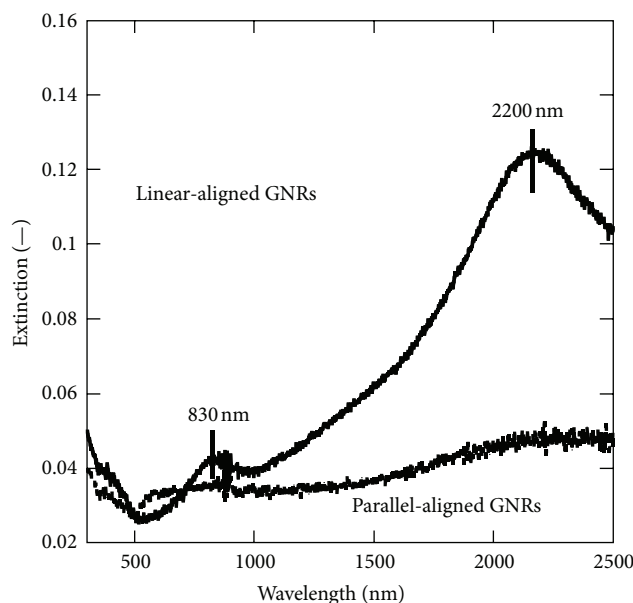
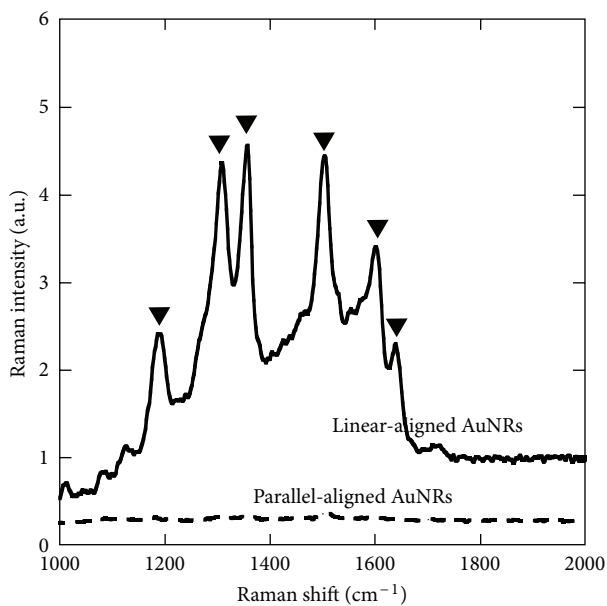


FIGURE 12: Optical absorption spectra of samples shown in Figures 11(a) and 11(b) named parallel-linearaligned (side-to-side-connected) and linear-aligned (end-to-end-connected) AuNRs, respectively. The concentrations of AuNRs in both samples are almost same (about  $10^9 \text{ cm}^{-2}$ ). The spectra include both absorption and scattering by AuNRs. Reproduced with permission from [31]. Copyright 2007 American Institute of Physics.



▼ R6G

FIGURE 13: SERS spectra of R6G adsorbed on samples shown in Figures 11(a) and 11(b). Both samples contained accurate concentrations of AuNRs of  $10^6 \text{ cm}^{-2}$  and R6G of  $10^{-13} \text{ mol}$  in the detection areas: laser wavelength of 1064 nm; laser power of 0.5 W; excitation spot size of  $100 \mu\text{m}$ ; integration number of 254; and spectral resolution of  $2 \text{ cm}^{-1}$ . The samples were positioned perpendicular to the excitation source. Reproduced with permission from [31]. Copyright 2007 American Institute of Physics.

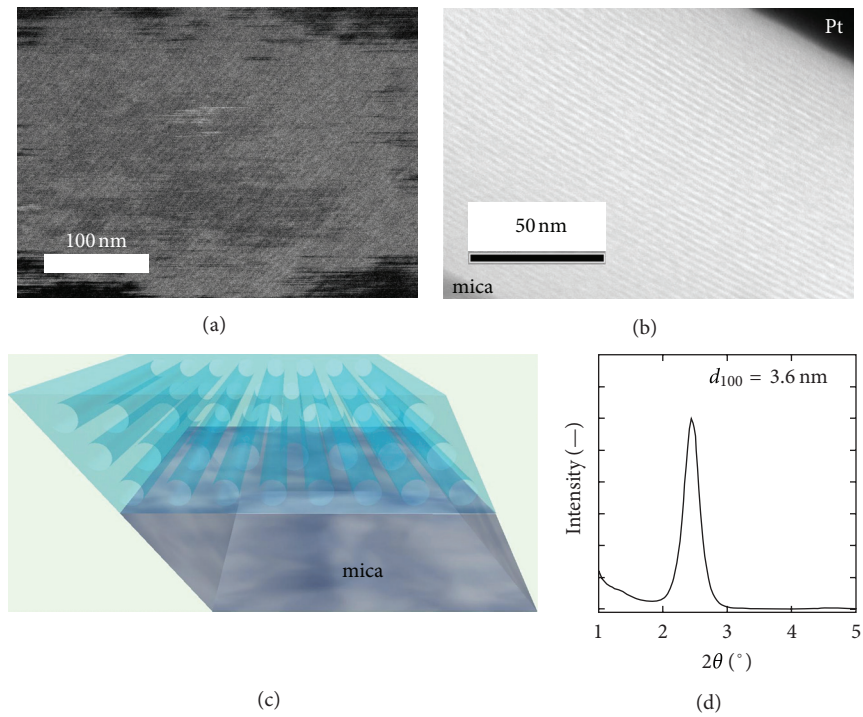


FIGURE 14: (a) SEM and (b) cross-sectional TEM images, (c) schematic illustration, and (d) XRD pattern of the prepared mesoporous silica on mica. Reproduced with permission from [50]. Copyright 2012 Elsevier.

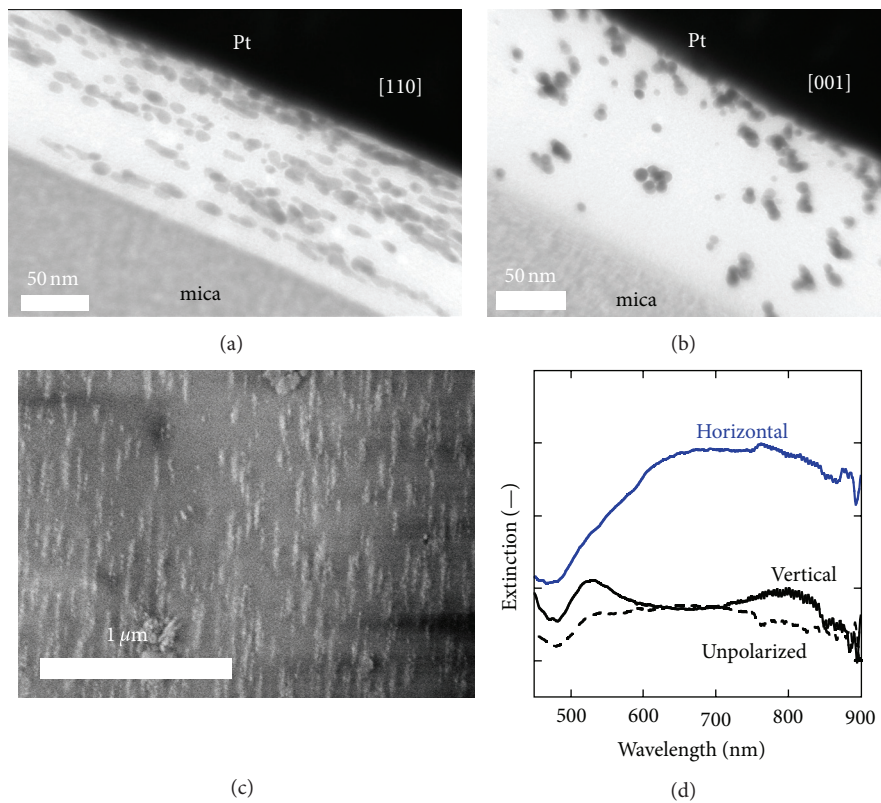


FIGURE 15: (a, b) Cross-sectional TEM and (c) surface SEM images and (d) polarized transmission spectra of the prepared chain-like ellipsoidal AuNP-doped mesoporous silica on mica. Reproduced with permission from [50]. Copyright 2012 Elsevier.

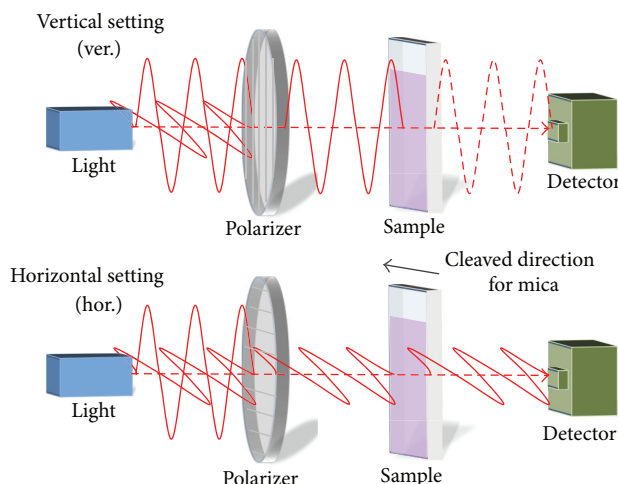


FIGURE 16: Setup for the measurement of polarized transmission spectra. Reproduced with permission from [50]. Copyright 2012 Elsevier.

was observed from two different directions by cross-sectional TEM (Figures 15(a) and 15(b)). The zone axes shown in the images indicate the direction of the 2D hexagonal structure of the film, which were parallel to the electron beam axis of the TEM. The longitudinal axes of the tubular mesopores were horizontal (from upper left to lower right) and vertical to the images in Figures 15(a) and 15(b), respectively. HRTEM and SAED confirmed that the black particles observed in the film were gold. In Figure 15(a), each AuNP was elliptical with a conjugate diameter of  $\sim 3$  nm, and the particles were connected to each other in an end-to-end fashion. The connected particles were aligned in one direction to form a straight chain-like structure. In contrast, the AuNPs in Figure 15(b) were spherical with a diameter of  $\sim 3$  nm and were not aligned in any direction. These results show that the deposition of gold occurred in the tubular mesopores with a caliber of  $\sim 3.5$  nm. The chain-like ellipsoidal AuNP assemblies were also clearly observed over a wide region ( $\sim 1$  cm<sup>2</sup>) with surface scanning electron microscopy (SEM) (Figure 15(c)).

When polarized light, the electric field of which was parallel to the longitudinal axis of the tubular mesopores (the polarizer was set horizontally (hor.), as shown in Figure 16), was used to measure the optical transmission of the film, a broad extinction at  $\sim 700$  nm was observed (hor. in Figure 15(d)). In contrast, light with orthogonal polarization to hor. (the polarizer was set vertically (ver.), as shown in Figure 16) showed an extinction at 520 nm (ver. in Figure 15(d)). These results indicate that the film exhibited macroscopic anisotropic SPR. This is because the transverse SPR mode of the chain-like AuNP assemblies shows a sharp extinction peak at around 520 nm, while the longitudinal SPR mode is induced by light of longer wavelength [1]. Namely, the light of hor. and ver. polarization excited the longitudinal and transverse SPR modes of the chain-like AuNP assemblies, respectively. The spectrum obtained using ver. polarization also contained a small peak of unknown origin at 800 nm. The results reveal that, although similar materials have been reported elsewhere [52–55, 60, 61], such films are an

alternative to conventional organic polarizers because of the advantages including the large extinction coefficient of AuNPs and tunable SPR wavelength.

**3.2. Precise Control of the Length of Silver NRs [62].** The diameter of metal NRs deposited in mesoporous silica with 2D hexagonal structure is readily controlled. However, it is difficult to control the length of metal NRs deposited in tubular mesopores. Controlling the length of metal NRs in mesoporous templates has been attempted by changing the ionic strength and/or temperature of the growth solution of metal NRs. However, the precise control of length was not achieved [63, 64]. With the aim of producing metal NRs of controlled length, we focused on the light-induced oxidation of silver based on the interaction between silver and titania (TiO<sub>2</sub>) crystals. Silver is oxidized when the SPR of silver nanoparticles (AgNPs) in contact with TiO<sub>2</sub> is excited and the excited electrons of silver transfer to TiO<sub>2</sub>, resulting in a lack of electrons in the AgNPs [65]. We oxidized silver nanorods (AgNRs) by irradiating tubular mesopores of silica templates containing TiO<sub>2</sub> nanocrystals with light. After/during the deposition of AgNRs *via* chemical reduction, the samples were exposed to light with a wavelength that induced the SPR of AgNRs, which allowed the precise control of the length of AgNRs in the tubular mesopores. Figure 17 shows an XRD pattern and TEM images of the TiO<sub>2</sub>-doped mesoporous silica template. Anatase TiO<sub>2</sub> nanocrystals were deposited and dispersed in the mesoporous silica framework. The extinction spectra of samples prepared with/without irradiation with light of 570–690 nm after deposition of AgNRs are presented in Figure 18. Irradiation of the sample with light of 570–690 nm after silver deposition resulted in decreased absorbance in the same wavelength region as that of the incident light and increased absorbance at longer wavelength. This was presumably caused by the formation of AgNRs that were too long to exhibit SPR. Namely, some of the Ag<sup>+</sup> ions generated by the dissociation of SPR-active AgNRs were deposited on the long AgNRs that were unaffected by light irradiation (see the illustration in the inset of Figure 18).

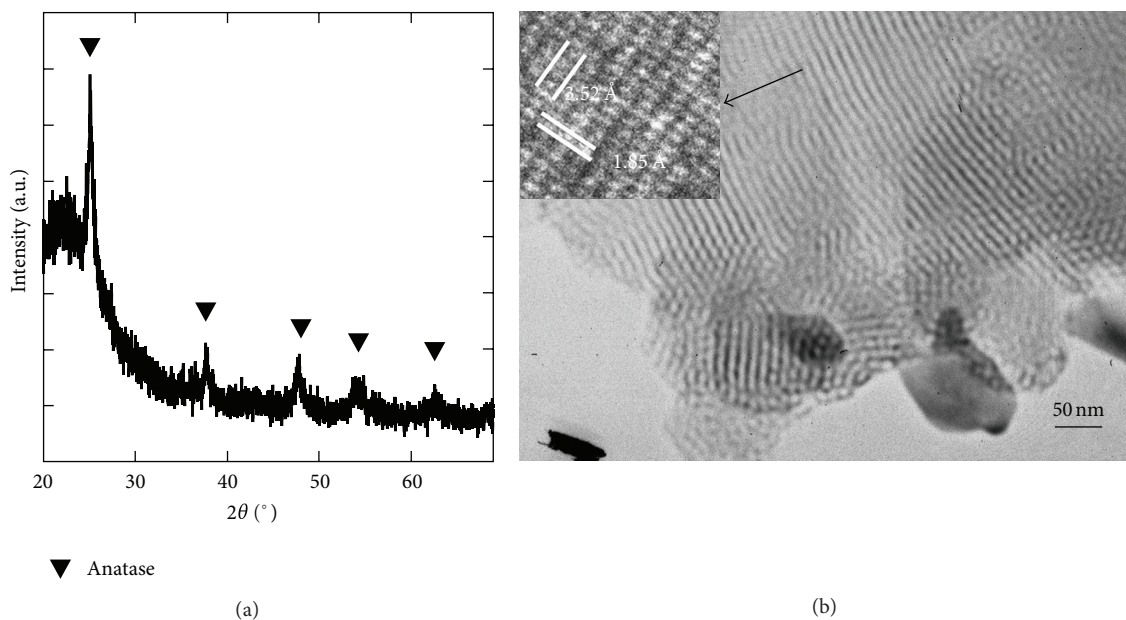


FIGURE 17: XRD pattern and TEM images of the  $80\text{SiO}_2\cdot 20\text{TiO}_2$  template. Reproduced with permission from [53]. Copyright 2011 The Royal Society of Chemistry.

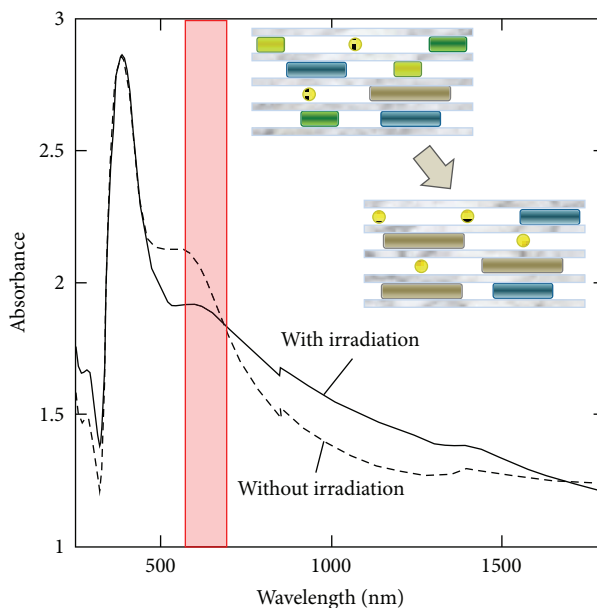


FIGURE 18: DR spectra of samples prepared with/without irradiation with light of 570–690 nm after deposition of AgNRs. The inset shows a schematic illustration of the samples. Reproduced with permission from [53]. Copyright 2011 The Royal Society of Chemistry.

Therefore, the amount of silver atoms in the long AgNRs increased, so the absorbance at longer wavelength was enhanced compared with that of the incident light.

Figure 19 depicts TEM images, histograms showing the aspect ratios of AgNRs, and diffuse reflectance (DR) spectra of samples prepared with/without irradiation of light of specific wavelength during silver deposition. Without irradiation of light, silver was deposited along the inner wall of the tubular mesopores to form AgNRs with various aspect

ratios (Figures 19(a) and 19(d)). In contrast, irradiation with light of 490–550 nm caused the predominant formation of spherical AgNPs (Figures 19(b) and 19(e)). Light of 650–810 nm produced AgNRs with an aspect ratio of 1–4 (Figures 19(c) and 19(f)). The DR spectrum of the sample prepared without light irradiation contained a peak at 395 nm that was attributed to both the SPR of spherical AgNPs and transverse SPR mode of AgNRs, and a peak at 600 nm that was consistent with the longitudinal SPR

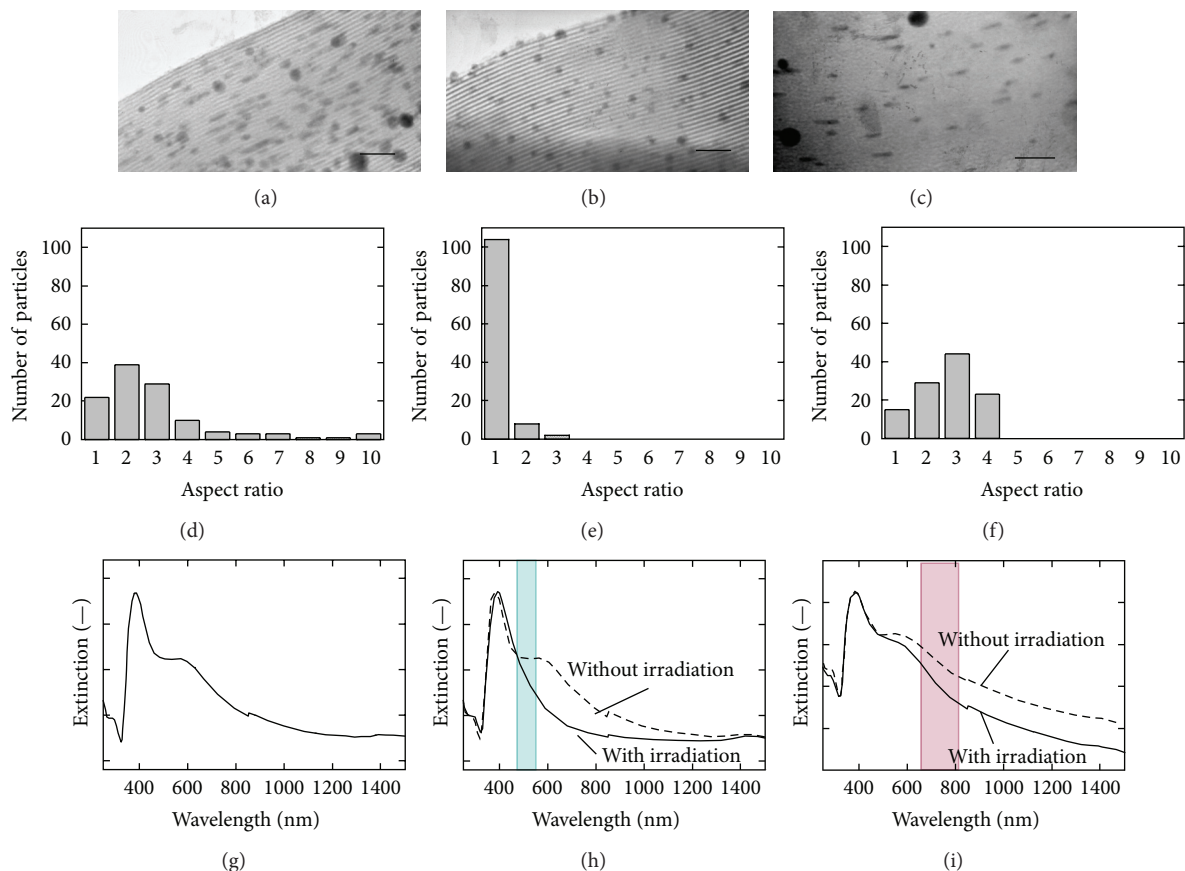


FIGURE 19: TEM images of samples prepared (a) without and with irradiation of light of (b) 490–550 and (c) 650–810 nm (scale bars: 100 nm). (d, e, and f) Histograms showing the distribution of aspect ratios of the AgNRs observed in the samples shown in (a, b, and c), respectively. (g, h, and i) The corresponding DR spectra of the samples shown in (a, b, and c), respectively (the wavelengths of the incident light are indicated by squares). Reproduced with permission from [53]. Copyright 2011 The Royal Society of Chemistry.

mode of AgNRs (Figure 19(g)). The spectrum of the sample prepared under irradiation with light of 490–550 nm showed only one peak at 398 nm (Figure 19(h)). Irradiation with light of 650–810 nm caused a blue shift of the peak at 600 nm to 580 nm (Figure 19(i)), which indirectly suggested that the length of the AgNRs was shortened by irradiation with light of this wavelength range. In other words, the exposure to light of a certain wavelength caused a decrease in absorbance at longer wavelength than that of the incident light. This suggested that when the growing AgNRs reached a critical length, the incident light caused SPR excitation, which induced dissociation of AgNRs. As a result, the formation of AgNRs longer than this critical length was prevented. A schematic illustration of the results presented in Figure 19 is provided in Figure 20. These results implied that irradiation with light of a specific wavelength was a promising tool to control the length of AgNRs in tubular mesoporous templates containing anatase nanocrystals.

### 3.3. Fabrication of AuNP-Doped Mesoporous Oxides with Unique Photocatalytic Activity [66]. Several studies on the

deposition of morphology-controlled metal NPs in mesoporous oxide templates have been reviewed above [53, 54, 59–61]. One of the most probable applications of such materials is as highly efficient photocatalysts, taking advantage of their strong optical absorption induced by SPR and the large specific surface area of the mesoporous templates. Figure 21 shows TEM images and DR spectra of Au-deposited mesoporous silica templates containing anatase nanocrystals prepared with/without ultraviolet (UV) irradiation. AuNRs and gold nanospheres (AuNSs) were observed in the samples prepared without and with UV irradiation, respectively. The extinction peaks except that at 520 nm almost disappeared when the sample was exposed to UV light. The peak at 520 nm was attributed to the SPR of AuNSs and the transverse SPR of AuNRs. The other peaks in the spectrum of the sample prepared without UV irradiation were consistent with the longitudinal SPR of AuNRs. The change of the shape of the AuNPs upon exposure to UV radiation was a result of the photocatalytic activity of the anatase  $\text{TiO}_2$  contained in the template [66].

The samples also exhibited a strong absorption at  $<400$  nm that was related to the band gap of the anatase

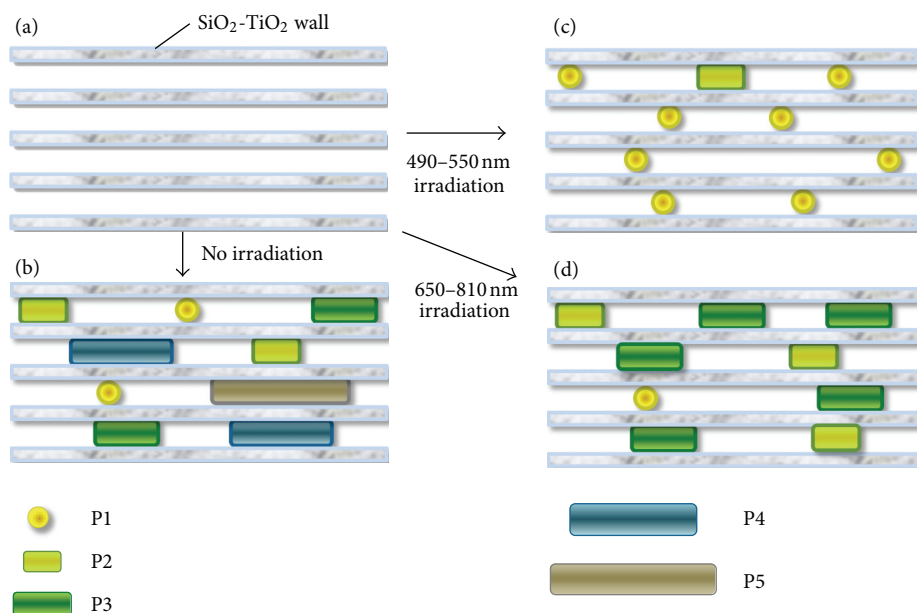


FIGURE 20: Illustration of the results of deposition of AgNRs in tubular mesoporous  $\text{SiO}_2\text{-TiO}_2$  templates with/without light irradiation. Reproduced with permission from [53]. Copyright 2011 The Royal Society of Chemistry.

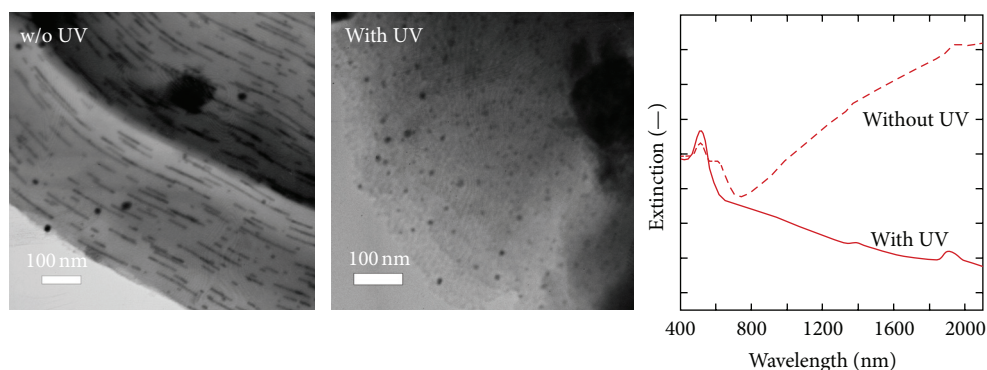


FIGURE 21: TEM images and DR spectra of Au-deposited  $80\text{SiO}_2\text{-}20\text{TiO}_2$  samples prepared with/without UV irradiation. Reproduced from [57]. Copyright 2012 Kawamura et al., licensee Springer.

nanocrystals in the templates. Figure 22 shows the photobleaching dynamics of methylene blue (MB) solution by various samples upon UV irradiation. The mesoporous template was required to bleach MB upon UV irradiation. The deposited AuNPs increased the bleaching rate of MB. This suggested that the photocatalytic activity of the template was improved by the formation of a Schottky barrier between anatase nanocrystals and gold, extending the lifetimes of charge carriers generated by UV irradiation [67]. The deposition of AuNRs increased the bleaching rate of MB more than AuNSs. The quantities of deposited gold in both samples were the same. Thus, it was found that the shape and/or size of AuNPs affected the photocatalytic activity of anatase  $\text{TiO}_2$ .

Furthermore, the mesoporous sample containing AuNPs was capable of visible light-induced photobleaching of MB. The catalytic reaction only occurred upon irradiation with light of wavelengths that matched the SPR absorption peaks of AuNPs and MB (data not shown). Controlling the size and morphology of metal NPs contacting anatase  $\text{TiO}_2$  produced novel photocatalysts with wavelength selectivity because of their variable SPR properties.

#### 4. Summary

Many techniques to prepare metal NPs of controlled shape, dimensions, and orientation using soft/hard templates have

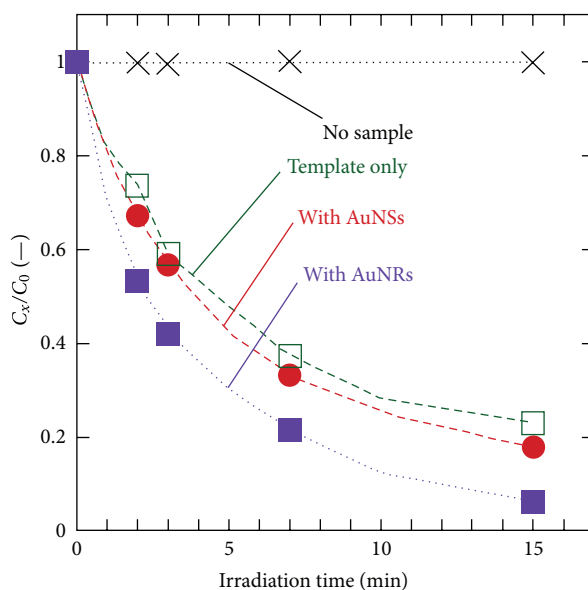


FIGURE 22: Photobleaching dynamics of MB solution with various samples upon UV irradiation.  $C_x$  is the concentration of MB in the solution irradiated with UV light for a certain period, and  $C_0$  is the initial concentration of MB in the solution.

been reported, allowing various nanostructures to be readily obtained. Extensive research has been performed on noble metal NPs, some of which have found application in recent years. However, it is difficult to control the morphology of many base metal nanostructures because they are easily oxidized. Once environmentally-friendly, inexpensive methods to prepare metal nanostructures, including those of base metals, are established, it is expected that the application of metal nanostructures will expand significantly.

## Acknowledgment

This work was supported by JSPS KAKENHI Grant no. 22760539.

## References

- [1] G. Mie, "Contributions to the optics of turbid media, particularly of colloidal metal solutions," *Annals of Physics*, vol. 25, no. 3, pp. 377–445, 1908.
- [2] J. M. Pitarke, V. M. Silkin, E. V. Chulkov, and P. M. Echenique, "Theory of surface plasmons and surface-plasmon polaritons," *Reports on Progress in Physics*, vol. 70, no. 1, pp. 1–87, 2007.
- [3] P. M. Paulus, A. Goossens, R. C. Thiel, A. M. van der Kraan, G. Schmid, and L. J. de Jongh, "Surface and quantum-size effects in Pt and Au nanoparticles probed by  $^{197}\text{Au}$  Mossbauer spectroscopy," *Physical Review B*, vol. 64, no. 20, Article ID 205418, 18 pages, 2001.
- [4] M.-C. Daniel and D. Astruc, "Gold nanoparticles: assembly, supramolecular chemistry, quantum-size-related properties, and applications toward biology, catalysis, and nanotechnology," *Chemical Reviews*, vol. 104, no. 1, pp. 293–346, 2004.
- [5] A. A. Ismail and D. W. Bahnemann, "Mesoporous Pt/TiO<sub>2</sub> nanocomposites as highly active photocatalysts for the photooxidation of dichloroacetic acid," *Journal of Physical Chemistry C*, vol. 115, no. 13, pp. 5784–5791, 2011.
- [6] L. Vigderma, B. P. Khanal, and E. R. Zubarev, "Functional gold nanorods: synthesis, self-assembly, and sensing applications," *Advanced Materials*, vol. 24, pp. 4811–4841, 2012.
- [7] S. Y. Li and M. Wang, "Branched metal nanoparticles: a review on wet-chemical synthesis and biomedical applications," *Nano LIFE*, vol. 2, no. 1, Article ID 123000, 22 pages, 2012.
- [8] I. Lisiecki, "Size, shape, and structural control of metallic nanocrystals," *Journal of Physical Chemistry B*, vol. 109, no. 25, pp. 12231–12244, 2005.
- [9] C. Raab, M. Simko, U. Fiedeler, M. Nentwich, and A. Gazso, "Production of nanoparticles and nanomaterials," *NanoTrust Dossiers*, no. 6, pp. 1–4, 2011.
- [10] J. Eastoe, M. J. Hollamby, and L. Hudson, "Recent advances in nanoparticle synthesis with reversed micelles," *Advances in Colloid and Interface Science*, vol. 128–130, pp. 5–15, 2006.
- [11] E. K. Heidari, E. Marzbanrad, C. Zamani, and B. Raissi, "Nanocasting synthesis of ultrafine WO<sub>3</sub> nanoparticles for gas sensing applications," *Nanoscale Research Letters*, vol. 5, no. 2, pp. 370–373, 2009.
- [12] A. Otto, I. Mrozek, H. Grabhorn, and W. Akemann, "Surface-enhanced Raman scattering," *Journal of Physics*, vol. 4, no. 5, pp. 1143–1212, 1992.
- [13] B. Sharma, R. R. Frontiera, A.-I. Henry, E. Ringe, and R. P. Van Duyne, "SERS: materials, applications, and the future," *Materials Today*, vol. 15, no. 1–2, pp. 16–25, 2012.
- [14] T. Yanagisawa, T. Shimizu, K. Kuroda, and C. Kato, "The preparation of alkyltrimethylammonium-kanemite complexes and their conversion to microporous materials," *Bulletin of the Chemical Society of Japan*, vol. 63, no. 4, pp. 988–992, 1990.
- [15] C. T. Kresge, M. E. Leonowicz, W. J. Roth, J. C. Vartuli, and J. S. Beck, "Ordered mesoporous molecular sieves synthesized by a liquid-crystal template mechanism," *Nature*, vol. 359, no. 6397, pp. 710–712, 1992.
- [16] A. M. James and M. P. Lord, *Macmillan's Chemical and Physical Data*, Macmillan, London, UK, 1992.

- [17] J. E. Huheey, E. A. Keiter, and R. L. Keiter, *Inorganic Chemistry: Principles of Structure and Reactivity*, HarperCollins, New York, NY, USA, 4th edition, 1993.
- [18] S. Mandal, S. K. Arumugam, S. D. Adyanthaya, R. Pasricha, and M. Sastry, "Use of aqueous foams for the synthesis of gold nanoparticles of variable morphology," *Journal of Materials Chemistry*, vol. 14, no. 1, pp. 43–47, 2004.
- [19] C. J. Murphy, T. K. Sau, A. M. Gole et al., "Anisotropic metal nanoparticles: synthesis, assembly, and optical applications," *Journal of Physical Chemistry B*, vol. 109, no. 29, pp. 13857–13870, 2005.
- [20] G. C. Schatz, M. A. Young, and R. P. Van Duyne, "Electromagnetic mechanism of SERS," in *Surface Enhanced Raman Scattering Physics and Applications*, K. Kneipp, M. Moskovits, and H. Kneipp, Eds., vol. 103 of *Topics in Applied Physics*, pp. 19–46, New York, NY, USA, 2006.
- [21] G. Kawamura and M. Nogami, "Application of a disproportionation reaction to a synthesis of shape-controlled gold nanoparticles," *Journal of Crystal Growth*, vol. 311, no. 19, pp. 4462–4466, 2009.
- [22] P. Mulvaney, M. Giersig, and A. Henglein, "Electrochemistry of multilayer colloids: preparation and absorption spectrum of gold-coated silver particles," *Journal of Physical Chemistry*, vol. 97, no. 27, pp. 7061–7064, 1993.
- [23] A. Henglein and M. Giersig, "Radiolytic formation of colloidal tin and tin-gold particles in aqueous solution," *Journal of Physical Chemistry*, vol. 98, no. 28, pp. 6931–6935, 1994.
- [24] G. Kawamura, Y. Yang, K. Fukuda, and M. Nogami, "Shape control synthesis of multi-branched gold nanoparticles," *Materials Chemistry and Physics*, vol. 115, no. 1, pp. 229–234, 2009.
- [25] C. J. Johnson, E. Dujardin, S. A. Davis, C. J. Murphy, and S. Mann, "Growth and form of gold nanorods prepared by seed-mediated, surfactant-directed synthesis," *Journal of Materials Chemistry*, vol. 12, no. 6, pp. 1765–1770, 2002.
- [26] P. L. Gai and M. A. Harmer, "Surface atomic defect structures and growth of gold nanorods," *Nano Letters*, vol. 2, no. 7, pp. 771–774, 2002.
- [27] S. Chen, Z. L. Wang, J. Ballato, S. H. Foulger, and D. L. Carroll, "Monopod, bipod, tripod, and tetrapod gold nanocrystals," *Journal of the American Chemical Society*, vol. 125, no. 52, pp. 16186–16187, 2003.
- [28] J. L. Burt, J. L. Elechiguerra, J. Reyes-Gasga, J. M. Montejano-Carrizales, and M. Jose-Yacamán, "Beyond Archimedean solids: star polyhedral gold nanocrystals," *Journal of Crystal Growth*, vol. 285, no. 4, pp. 681–691, 2005.
- [29] O. M. Bakr, B. H. Wunsch, and F. Stellacci, "High-yield synthesis of multi-branched urchin-like gold nanoparticles," *Chemistry of Materials*, vol. 18, no. 14, pp. 3297–3301, 2006.
- [30] C. L. Nehl, H. Liao, and J. H. Hafner, "Optical properties of star-shaped gold nanoparticles," *Nano Letters*, vol. 6, no. 4, pp. 683–688, 2006.
- [31] D. Wang, Y. Liu, X. Zhou, J. Sun, and T. You, "EDTA-controlled one-pot preparation of novel shaped gold microcrystals and their application in surface-enhanced raman scattering," *Chemistry Letters*, vol. 36, no. 7, pp. 924–925, 2007.
- [32] E. Herrero, L. J. Buller, and H. D. Abruña, "Underpotential deposition at single crystal surfaces of Au, Pt, Ag and other materials," *Chemical Reviews*, vol. 101, no. 7, pp. 1897–1930, 2001.
- [33] M. Liu and P. Guyot-Sionnest, "Mechanism of silver(I)-assisted growth of gold nanorods and bipyramids," *Journal of Physical Chemistry B*, vol. 109, no. 47, pp. 22192–22200, 2005.
- [34] M. Törnblom and U. Henriksson, "Effect of solubilization of aliphatic hydrocarbons on size and shape of rodlike  $C_{16}$ TABr micelles studied by  $^2H$  NMR relaxation," *Journal of Physical Chemistry B*, vol. 101, no. 31, pp. 6028–6035, 1997.
- [35] Y. Y. Yu, S. S. Chang, C. L. Lee, and C. R. C. Wang, "Gold nanorods: electrochemical synthesis and optical properties," *Journal of Physical Chemistry B*, vol. 101, no. 34, pp. 6661–6664, 1997.
- [36] S. S. Chang, C. W. Shih, C. D. Chen, W. C. Lai, and C. R. C. Wang, "The shape transition of gold nanorods," *Langmuir*, vol. 15, no. 3, pp. 701–709, 1999.
- [37] N. R. Jana, L. Gearheart, and C. J. Murphy, "Seed-mediated growth approach for shape-controlled synthesis of spheroidal and rod-like gold nanoparticles using a surfactant template," *Advanced Materials*, vol. 13, no. 18, pp. 1389–1393, 2001.
- [38] G. Kawamura, Y. Yang, and M. Nogami, "Facile assembling of gold nanorods with large aspect ratio and their surface-enhanced Raman scattering properties," *Applied Physics Letters*, vol. 90, no. 26, Article ID 261908, 3 pages, 2007.
- [39] G. Kawamura, Y. Yang, and M. Nogami, "End-to-end assembly of CTAB-stabilized gold nanorods by citrate anions," *Journal of Physical Chemistry C*, vol. 112, no. 29, pp. 10632–10636, 2008.
- [40] J. Aizpurua, G. W. Bryant, L. J. Richter, and F. J. Garcia de Abajo, "Optical properties of coupled metallic nanorods for field-enhanced spectroscopy," *Physical Review B*, vol. 71, no. 23, Article ID 235420, 13 pages, 2005.
- [41] J. Pérez-Juste, I. Pastoriza-Santos, L. M. Liz-Marzán, and P. Mulvaney, "Gold nanorods: synthesis, characterization and applications," *Coordination Chemistry Reviews*, vol. 249, no. 17–18, pp. 1870–1901, 2005.
- [42] N. R. Jana, L. Gearheart, and C. J. Murphy, "Wet chemical synthesis of high aspect ratio cylindrical gold nanorods," *Journal of Physical Chemistry B*, vol. 105, no. 19, pp. 4065–4067, 2001.
- [43] D. Frenkel, H. N. W. Lekkerkerker, and A. Stroobants, "Thermodynamic stability of a smectic phase in a system of hard rods," *Nature*, vol. 332, no. 6167, pp. 822–823, 1988.
- [44] J.-C. P. Gabriel and P. Davidson, "New trends in colloidal liquid crystals based on mineral moieties," *Advanced Materials*, vol. 12, no. 1, pp. 9–20, 2000.
- [45] B. Nikoobakht, Z. L. Wang, and M. A. El-Sayed, "Self-assembly of gold nanorods," *Journal of Physical Chemistry B*, vol. 104, no. 36, pp. 8635–8640, 2000.
- [46] S. Kwan, F. Kim, J. Akana, and P. Yang, "Synthesis and assembly of  $BaWO_4$  nanorods," *Chemical Communications*, no. 5, pp. 447–448, 2001.
- [47] C. J. Orendorff and C. J. Murphy, "Quantitation of metal content in the silver-assisted growth of gold nanorods," *Journal of Physical Chemistry B*, vol. 110, no. 9, pp. 3990–3994, 2006.
- [48] M. Gluodenis and C. A. Foss Jr., "The effect of mutual orientation on the spectra of metal nanoparticle rod-rod and rod-sphere pairs," *Journal of Physical Chemistry B*, vol. 106, no. 37, pp. 9484–9489, 2002.
- [49] Q. Jiang, H. M. Lu, and M. Zhao, "Modelling of surface energies of elemental crystals," *Journal of Physics*, vol. 16, no. 4, pp. 521–530, 2004.
- [50] N. R. Jana, L. Gearheart, and C. J. Murphy, "Wet chemical synthesis of high aspect ratio cylindrical gold nanorods," *Journal of Physical Chemistry B*, vol. 105, no. 19, pp. 4065–4067, 2001.
- [51] J. Aizpurua, G. W. Bryant, L. I. Richter, and F. J. Garcia de Abajo, "Optical properties of coupled metallic nanorods for field-enhanced spectroscopy," *Physical Review B*, vol. 71, no. 23, Article ID 235420, 13 pages, 2005.

- [52] Y. Dirix, C. Bastiaansen, W. Cased, and P. Smith, "Oriented pearl-necklace arrays of metallic nanoparticles in polymers: a new route toward polarization-dependent color filters," *Advanced Materials*, vol. 11, no. 3, pp. 223–227, 1999.
- [53] J. Perez-Juste, B. Rodriguez-Gonzalez, P. Mulvaney, and L. M. Liz-Marzan, "Optical control and patterning of gold-nanorod-poly(vinyl alcohol) nanocomposite films," *Advanced Functional Materials*, vol. 15, no. 7, pp. 1065–1071, 2005.
- [54] C. J. Murphy and C. J. Orendorff, "Alignment of gold nanorods in polymer composites and on polymer surfaces," *Advanced Materials*, vol. 17, no. 18, pp. 2173–2177, 2005.
- [55] T. Sawitowski, Y. Miquel, A. Heilmann, and G. Schmid, "Optical properties of quasi one-dimensional chains of gold nanoparticles," *Advanced Functional Materials*, vol. 11, no. 6, pp. 435–440, 2001.
- [56] I. Bannat, K. Wessels, T. Oekermann, J. Rathousky, D. Bahnemann, and M. Wark, "Improving the photocatalytic performance of mesoporous titania films by modification with gold nanostructures," *Chemistry of Materials*, vol. 21, no. 8, pp. 1645–1653, 2009.
- [57] G. Kawamura, I. Hayashi, H. Muto, and A. Matsuda, "Anisotropically assembled gold nanoparticles prepared using unidirectionally aligned mesochannels of silica film," *Scripta Materialia*, vol. 66, no. 7, pp. 479–482, 2012.
- [58] H. Miyata and K. Kuroda, "Formation of a continuous mesoporous silica film with fully aligned mesochannels on a glass substrate," *Chemistry of Materials*, vol. 12, no. 1, pp. 49–54, 2000.
- [59] T. Suzuki, Y. Kanno, Y. Morioka, and K. Kuroda, "Facile unidirectional alignment of mesochannels in a mesoporous silica film on a freshly cleaved mica surface," *Chemical Communications*, no. 28, pp. 3284–3286, 2008.
- [60] W. Caseri, "Nanocomposites of polymers and metals or semiconductors: historical background and optical properties," *Macromolecular Rapid Communications*, vol. 21, no. 11, pp. 705–722, 2000.
- [61] H. Nakashima, K. Furukawa, Y. Kashimura, and K. Torimitsu, "Self-assembly of gold nanorods induced by intermolecular interactions of surface-anchored lipids," *Langmuir*, vol. 24, no. 11, pp. 5654–5658, 2008.
- [62] G. Kawamura, M. Murakami, T. Okuno, H. Muto, and A. Matsuda, "Length control of Ag nanorods in mesoporous SiO<sub>2</sub>-TiO<sub>2</sub> by light irradiation," *RSC Advances*, vol. 1, no. 4, pp. 584–587, 2011.
- [63] Y. Xie, S. Quinlivan, and T. Asefa, "Tuning metal nanostructures in mesoporous silica by a simple change of metal complexes and by reduction with grafted imines and hemiaminals," *Journal of Physical Chemistry C*, vol. 112, no. 27, pp. 9996–10003, 2008.
- [64] Z. Li, C. Kübel, V. I. Pârvulescu, and R. Richards, "Size tunable gold nanorods evenly distributed in the channels of mesoporous silica," *ACS Nano*, vol. 2, no. 6, pp. 1205–1212, 2008.
- [65] Y. Ohko, T. Tatsuma, T. Fujii et al., "Multicolour photochromism of TiO<sub>2</sub> films loaded with silver nanoparticles," *Nature Materials*, vol. 2, no. 1, pp. 29–31, 2003.
- [66] G. Kawamura, T. Okuno, H. Muto, and A. Matsuda, "Selective preparation of zero- and one-dimensional gold nanostructures in a TiO<sub>2</sub> nanocrystal-containing photoactive mesoporous template," *Nanoscale Research Letters*, vol. 7, no. 1, p. 27, 2012.
- [67] E. Kowalska, O. O. P. Mahaney, R. Abe, and B. Ohtani, "Visible-light-induced photocatalysis through surface plasmon excitation of gold on titania surfaces," *Physical Chemistry Chemical Physics*, vol. 12, no. 10, pp. 2344–2355, 2010.

## Research Article

# Ferromagnetic Behaviors in Fe-Doped NiO Nanofibers Synthesized by Electrospinning Method

Yi-Dong Luo,<sup>1</sup> Yuan-Hua Lin,<sup>1</sup> Xuehui Zhang,<sup>1</sup> Deping Liu,<sup>2</sup> Yang Shen,<sup>1</sup> and Ce-Wen Nan<sup>1</sup>

<sup>1</sup> State Key Laboratory of New Ceramics and Fine Processing, Department of Materials Science and Engineering, Tsinghua University, Beijing 100084, China

<sup>2</sup> Department of Cardiology, Beijing Hospital, The Ministry of Health, Beijing 100730, China

Correspondence should be addressed to Yuan-Hua Lin; [linyh@mail.tsinghua.edu.cn](mailto:linyh@mail.tsinghua.edu.cn)

Received 5 October 2012; Revised 4 December 2012; Accepted 18 December 2012

Academic Editor: Zhengren Huang

Copyright © 2013 Yi-Dong Luo et al. This is an open access article distributed under the Creative Commons Attribution License, which permits unrestricted use, distribution, and reproduction in any medium, provided the original work is properly cited.

Ni<sub>1-x</sub>Fe<sub>x</sub>O nanofibers with different Fe doping concentration have been synthesized by electrospinning method. An analysis of the phase composition and microstructure shows that Fe doping has no influence on the crystal structure and morphology of NiO nanofibers, which reveals that the doped Fe ions have been incorporated into the NiO host lattice. Pure NiO without Fe doping is antiferromagnetic, yet all the Fe-doped NiO nanofiber samples show obvious room-temperature ferromagnetic properties. The saturation magnetization of the nanofibers can be enhanced with increasing Fe doping concentration, which can be ascribed to the double exchange mechanism through the doped Fe ions and free charge carriers. In addition, it was found that the diameter of nanofibers has significant impact on the ferromagnetic properties, which was discussed in detail.

## 1. Introduction

Diluted magnetic semiconductors (DMS) have been intensively studied due to their high potential for applications in spin-dependent semiconductor electronics [1]. Practical spintronic materials should have high Curie temperatures, high spin polarization of charge carriers, and compatibility with semiconductors [2, 3]. Lots of experiments were carried out to study the fascinating properties of the oxide-based DMSs (e.g., ZnO, TiO<sub>2</sub>, SnO<sub>2</sub>, In<sub>2</sub>O<sub>3</sub>, etc.) with various transition metal (TM) ions doped [4–7]. But, compared to the TM-doped oxide-based materials mentioned above, it is more feasible to realize the p-type doping in NiO system.

Recently, one-dimensional nanofibers have received intensive attention due to their excellent magnetic, optical, electric, and chemical properties [8]. The low-symmetry structure will affect their peculiar magnetic properties [9]. In the recent study of DMS materials, nanoparticles, films structure of NiO have already been prepared by sol-gel techniques, hydrothermal route, and Pulsed laser deposition [10–12]. Unfortunately, the investigation of the Fe-doping effect on ferromagnetism of one-dimensional DMS fibers is very limited. Thus, it is necessary to study the influence

of low dimensional structure on NiO-based system. Among all the methods of making one-dimensional nanostructure magnetic materials, electrospinning is a simple, versatile, and convenient approach with the characteristic of easy control and low cost [13].

Our previous works have already reported the room-temperature FM behavior of the Fe-doped NiO nanoparticles [12, 14]. Although pure NiO exhibits insulating character and antiferromagnetic order at room temperature, introduction of Fe ions will break the symmetry of the system in NiO, showing the room-temperature ferromagnetism [15, 16]. Therefore, it is anticipated that Fe-doped NiO nanofiber would exhibit ferromagnetism.

In this work, we prepared Fe-doped NiO nanofibers (NFO) and observed remarkable FM properties at room temperature. The result may be attributed to the double exchange mechanism through the doped Fe ions and free charge carriers.

## 2. Experimental Procedure

**2.1. Preparation of Fe-doped Nanofibers.** Ni(AC)<sub>2</sub>·4H<sub>2</sub>O and the appropriate amount of Fe(NO<sub>3</sub>)<sub>3</sub>·9H<sub>2</sub>O with different

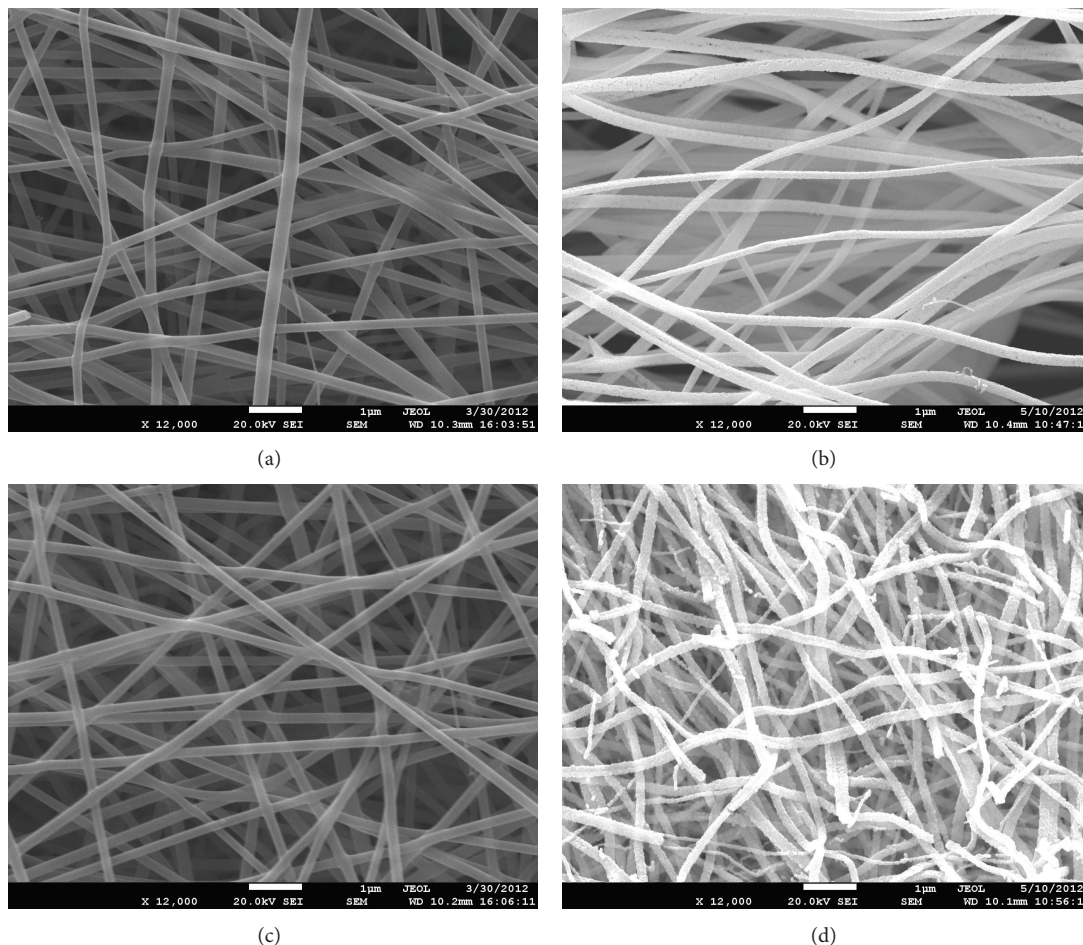


FIGURE 1: (a) SEM images of the undoped NiO/PVP nanofibers before calcination. (b) SEM images of the undoped NiO/PVP nanofibers after calcination. (c) SEM images of the Fe-doped NiO/PVP composite nanofibers before calcination. (d) SEM images of the Fe-doped NiO/PVP composite nanofibers after calcination.

atomic ratios were dropped slowly into the mixed solution (made by 45 mL alcohol and 5 mL water) with stirring. Then 2 g PVP powder were added slowly into the solution under stirring, and the sol solution was obtained for electrospinning. The precursor sol solution was loaded into a 10 mL plastic syringe with a syringe needle of which the internal diameter is 0.5 mm. The needle was connected to a DC high-voltage power supply. In our experiment, a voltage of 12 kV was applied between the copper plate collector and the syringe needle with a distance of 12 cm. The PVP/Ni(CH<sub>3</sub>COO)<sub>2</sub> composite nanofibers were collected on the copper plate during electrospinning processes. Pure NiO and Fe-doped NiO nanofibers were finally obtained by calcination at 660 °C for 3 h in air to remove PVP completely.

**2.2. Characterization.** X-ray diffraction (XRD) was employed to investigate the crystal structure of nanofibers. And the morphologies of nanofibers were characterized by scanning electron microscope (SEM). The valence state of the Fe ions was analyzed by X-ray photoelectron spectroscopy (XPS) and magnetic properties of the samples were measured by Physical Property Measurement System (PPMS).

### 3. Results and Discussion

Figure 1 shows the SEM images of the nanofibers before and after calcination. Figures 1(a) and 1(c) show the SEM images of undoped NiO/PVP and Fe-doped NiO/PVP composite nanofibers with smooth surface before calcination. They are several millimeters long with a diameter of approximate 270 nm. Furthermore, in contrast to pure NiO/PVA composite nanofibers, the doping Fe ions in NiO do not influence the morphologies of doped samples. As shown in Figures 1(b) and 1(d), after calcined at 660 °C, the diameters of all NiO-based nanofibers shrank drastically to 60–100 nm due to the decomposition of PVP and the transformation from metal salts to metal oxides. Figure 2 shows the XRD patterns of various NiO-based nanofiber samples after calcination. Obviously, all of these samples are pure cubic crystalline NiO phase, and no impurity phase appears.

The existence of the Fe ions in the present NFO nanofibers was verified by the XPS measurements as shown in Figure 3. It can be seen that the spectra consist of Fe 2p<sub>3/2</sub> (713.2 eV) and 2p<sub>1/2</sub> (724.5 eV) peaks. The chemical state of the Fe ions may be a mixture of Fe<sup>2+</sup> and Fe<sup>3+</sup> as seen from the broad peaks of

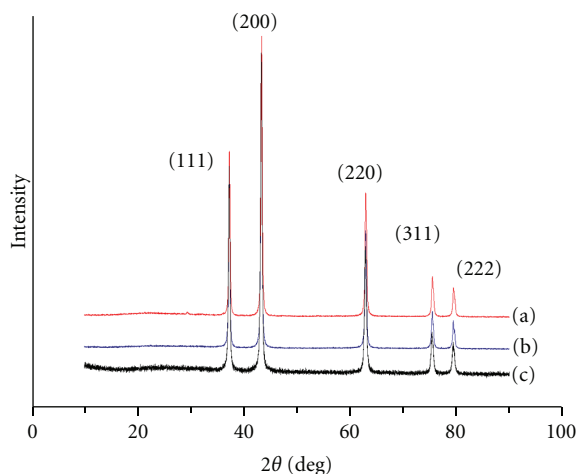


FIGURE 2: XRD patterns of various nanofibers made by electrospinning after calcination. (a) 3% Fe, (b) 5% Fe, (c) 0% Fe.

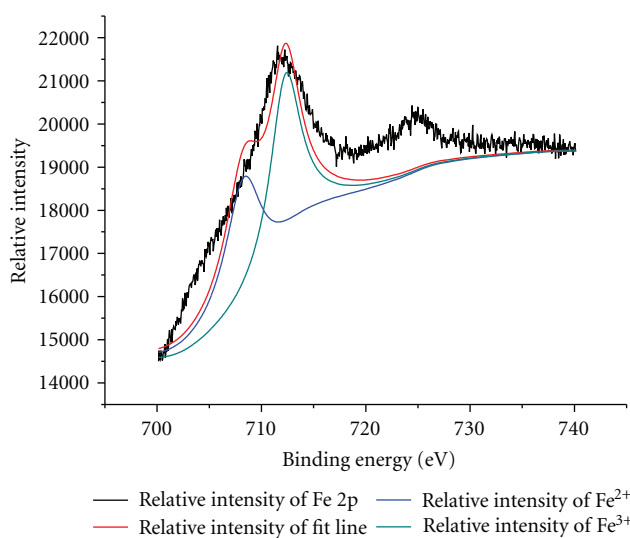


FIGURE 3: Core-level XPS spectra of Fe 2p for  $\text{Ni}_{0.97}\text{Fe}_{0.03}\text{O}$  nanofibers and XPS simulation for Fe 2p spectra.

Fe 2p. As previously reported [17], in the Fe-doped oxides-based DMS systems, the possible presence of a secondary phase (e.g., metallic magnetic Fe particles) can also be the origin of ferromagnetism. However, no metallic  $\text{Fe}^0$  ( $2p_{3/2}$  binding energy  $\sim 706$  eV and  $2p_{1/2}$  binding energy  $\sim 719$  eV) was observed in the present spectra. Therefore, according to the Fe 2p XPS spectra and XRD results, as for our Fe-doped  $\text{Ni}_{1-x}\text{Fe}_x\text{O}$  nanofibers, suggestion of the secondary Fe metal cluster phase as the origin of ferromagnetism can be ruled out.

As shown in Figure 4, with the increasing of the concentration of the Fe-doping, the samples exhibit obvious FM properties at room temperature. In these type Fe-doped NiO samples, the Ni ions are partially substituted by the Fe ions, which are randomly localized over the host lattice. Thus, this kind of disorder certainly breaks the translation symmetry of the system and the original magnetic order in NiO grains is

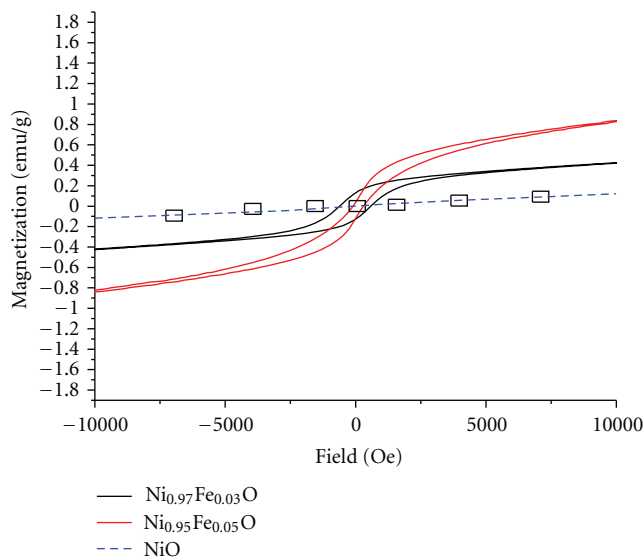


FIGURE 4: Magnetization-field (M-H) loop curves of various NFO nanofibers.

interrupted. The results are similar with the study of the Li-Fe codoped films [14]. The ferromagnetism in the Fe-doped NiO could be caused by the double exchange through the introduced magnetic Fe ions and the related defects (e.g.,  $\text{Fe}_{\text{Ni}}$ ). That is to say, electrons may weakly trapped in the  $\text{Fe}_{\text{Ni}}$  defect site, where the electron occupies an orbital which overlaps the d shells of both Fe neighbors, enhancing the interaction between Fe ions, resulting the ferromagnetism of the nanofibers. In addition, with the increase of doped Fe ions, the amount of the magnetic Fe ions and the  $\text{Fe}_{\text{Ni}}$  defects will also increase, which will enhance the FM double-exchange interaction.

Moreover, compared with the results of Liu's group [9], we find the diameter of nanofibers has significant impact on the ferromagnetic properties. We suppose that there are two possible mechanisms of the remarkable FM properties. The first mechanism is associated with the transition of double sublattice to multisublattice states [18]. Yet, this explanation only suits the particles whose diameter is less than 30 nm. The other mechanism is related to the change of the impurity states. With the decreasing size, the impurity states may become much deeper in energy [19], which may enhance the coupling interaction between the 3d spins of Fe ions and the carriers, giving an obvious enhancement of FM properties of the nanofibers. More experiments are carrying on to confirm this assumption.

#### 4. Conclusions

In conclusion, nanofibers were prepared by electrospinning method. XPS spectra reveal that the Fe 2p core-level photoemission spectra consisted of the  $\text{Fe}^{2+}$  and  $\text{Fe}^{3+}$  components, and no metallic Fe appeared. All the nanofibers exhibited obvious ferromagnetic ordering at room temperature which

should be ascribed to the double exchange through the introduced magnetic Fe ions and related defects.

## Acknowledgments

This work was supported by the Ministry of Science and Technology of China through a 973 Project under Grant no. 2009CB623303, NSF of China (51025205, 51272181, and 51272121).

## References

- [1] H. Ohno, "Making nonmagnetic semiconductors ferromagnetic," *Science*, vol. 281, no. 5379, pp. 951–956, 1998.
- [2] S. A. Wolf, D. D. Awschalom, R. A. Buhrman et al., "Spintronics: a spin-based electronics vision for the future," *Science*, vol. 294, no. 5546, pp. 1488–1495, 2001.
- [3] T. Dietl and H. Ohno, "Engineering magnetism in semiconductors," *Materials Today*, vol. 9, no. 11, pp. 18–26, 2006.
- [4] M. Kobayashi, Y. Ishida, J. L. Hwang et al., "Characterization of magnetic components in the diluted magnetic semiconductor  $Zn_{1-x}Co_xO$  by x-ray magnetic circular dichroism," *Physical Review B*, vol. 72, no. 20, 4 pages, 2005.
- [5] Y. Matsumoto, M. Murakami, T. Shono et al., "Room-temperature ferromagnetism in transparent transition metal-doped titanium dioxide," *Science*, vol. 291, no. 5505, pp. 854–856, 2001.
- [6] S. B. Ogale, R. J. Choudhary, J. P. Buban et al., "High temperature ferromagnetism with a giant magnetic moment in transparent co-doped  $SnO_{2-\delta}$ ," *Physical Review Letters*, vol. 91, no. 7, Article ID 077205, 4 pages, 2003.
- [7] J. Philip, A. Punnoose, B. I. Kim et al., "Carrier-controlled ferromagnetism in transparent oxide semiconductors," *Nature Materials*, vol. 5, no. 4, pp. 298–304, 2006.
- [8] F. Qian, S. Gradečak, Y. Li, C. Y. Wen, and C. M. Lieber, "Core/multishell nanowire heterostructures as multicolor, high-efficiency light-emitting diodes," *Nano Letters*, vol. 5, no. 11, pp. 2287–2291, 2005.
- [9] S. H. Liu, J. F. Jia, J. Wang et al., "Synthesis of Fe-doped NiO nanofibers using electrospinning method and their ferromagnetic properties," *Journal of Magnetism and Magnetic Materials*, vol. 324, no. 13, pp. 2070–2074, 2012.
- [10] S. Manna, A. K. Deb, J. Jagannath, and S. K. De, "Synthesis and room temperature ferromagnetism in Fe doped NiO nanorods," *Journal of Physical Chemistry C*, vol. 112, no. 29, pp. 10659–10662, 2008.
- [11] W. Yan, W. Weng, G. Zhang et al., "Structures and magnetic properties of (Fe, Li)-codoped NiO thin films," *Applied Physics Letters*, vol. 92, no. 5, Article ID 052508, 3 pages, 2008.
- [12] J. Wang, J. Cai, Y. H. Lin, and C. W. Nan, "Room-temperature ferromagnetism observed in Fe-doped NiO," *Applied Physics Letters*, vol. 87, no. 20, 3 pages, 2005.
- [13] M. Zhao, X. Wang, L. Ning et al., "Synthesis and optical properties of Mg-doped ZnO nanofibers prepared by electrospinning," *Journal of Alloys and Compounds*, vol. 507, no. 1, pp. 97–100, 2010.
- [14] Y. H. Lin, J. Wang, J. Cai et al., "Ferromagnetism and electrical transport in Fe-doped NiO," *Physical Review B*, vol. 73, no. 19, 4 pages, 2006.
- [15] J. Van Elp, H. Eskes, P. Kuiper, and G. A. Sawatzky, "Electronic structure of Li-doped NiO," *Physical Review B*, vol. 45, no. 4, pp. 1612–1622, 1992.
- [16] Y. H. Lin, R. J. Zhao, C. W. Nan, and M. H. Ying, "Enhancement of ferromagnetic properties of NiO:Fe thin film by Li doping," *Applied Physics Letters*, vol. 89, no. 20, 3 pages, 2006.
- [17] Y. J. Kim, S. Thevuthasan, T. Droubay et al., "Growth and properties of molecular beam epitaxially grown ferromagnetic Fe-doped TiO<sub>2</sub> rutile films on TiO<sub>2</sub>(110)," *Applied Physics Letters*, vol. 84, no. 18, pp. 3531–3533, 2004.
- [18] L. P. Li, L. J. Chen, R. Qi, and G. S. Li, "Magnetic crossover of NiO nanocrystals at room temperature," *Applied Physics Letters*, vol. 89, no. 13, Article ID 134102, 3 pages, 2006.
- [19] X. Huang, A. Makmal, J. R. Chelikowsky, and L. Kronik, "Size-dependent spintronic properties of dilute magnetic semiconductor nanocrystals," *Physical Review Letters*, vol. 94, no. 23, Article ID 236801, 4 pages, 2005.

## Review Article

# Research Progress of Optical Fabrication and Surface-Microstructure Modification of SiC

**Fang Jiang,<sup>1,2</sup> Yan Liu,<sup>1</sup> Yong Yang,<sup>1</sup> Zheng-Ren Huang,<sup>1</sup>  
Dan Li,<sup>1,2</sup> Gui-ling Liu,<sup>1</sup> and Xue-Jian Liu<sup>1</sup>**

<sup>1</sup> State Key Laboratory of High Performance Ceramics and Superfine Microstructure, Shanghai Institute of Ceramics, Chinese Academy of Sciences, Shanghai 200050, China

<sup>2</sup> Graduate University of the Chinese Academy of Sciences, Beijing 100049, China

Correspondence should be addressed to Yong Yang, yangyong@mail.sic.ac.cn

Received 3 October 2012; Accepted 11 December 2012

Academic Editor: Yongsheng Li

Copyright © 2012 Fang Jiang et al. This is an open access article distributed under the Creative Commons Attribution License, which permits unrestricted use, distribution, and reproduction in any medium, provided the original work is properly cited.

SiC has become the best candidate material for space mirror and optical devices due to a series of favorable physical and chemical properties. Fine surface optical quality with the surface roughness (RMS) less than 1 nm is necessary for fine optical application. However, various defects are present in SiC ceramics, and it is very difficult to polish SiC ceramic matrix with the 1 nm RMS. Surface modification of SiC ceramics must be done on the SiC substrate. Four kinds of surface-modification routes including the hot pressed glass, the C/SiC clapping, SiC clapping, and Si clapping on SiC surface have been reported and reviewed here. The methods of surface modification, the mechanism of preparation, and the disadvantages and advantages are focused on in this paper. In our view, PVD Si is the best choice for surface modification of SiC mirror.

## 1. Introduction

At present, mirror systems as the most important device are applied commonly in the optical system with high precision. Until now, three generations of reflector materials have been developed. The first generation is glass-ceramic; the second one is mainly made of metal, such as Beryllium metal and its alloys; the third generation of the reflector material is based on silicon carbide. SiC may be the best material available for mirror optics because of its outstanding combination of thermal and mechanical properties. It has remarkable dimensional stability even under the disturbances of temperature, humidity, and chemicals. Its specific stiffness and elastic modulus are higher than that of beryllium, which has toxicity. The density of SiC is slightly higher than aluminum and its fracture toughness is higher than glass. The remarkable properties of SiC in terms of hardness, stiffness, and thermal stability combined with a reasonable density are indeed of primary importance for all space applications. This combination of material advantages

makes SiC an excellent material candidate for space optical instruments [1, 2].

Based on microstructure and processing routes, four kinds of SiC ceramics including hot-pressed SiC (HP-SiC), reaction-bonded SiC (RB-SiC), sintered SiC (S-SiC), and chemical vapor deposition SiC (CVD-SiC) were developed. The properties of different SiC materials and the brief description of various SiC component manufacturing techniques are summarized in Table 1 [2, 17]. Whatever the preparation process, it is difficult to obtain high-quality optical surface due to polishing the bare SiC very difficultly. Moreover, microstructure defects, like pores, steps at different phases, and grain boundary damages, are unavoidable under certain surfacing condition and present further difficulty in polishing this material. The AFM topography images of surfaces polished by 1 μm abrasive grains of different SiC ceramics are shown in Figure 1. The steps still exist at the interfaces between two phases both in RB-SiC and S-SiC, and it cannot meet the optical requirements (<1 nm RMS). The rms surface roughness values of SiC ceramics

TABLE 1: Different preparation methods and properties of silicon carbide.

Materials	Density (g/cm <sup>3</sup> )	Free state of Si	Isotropic	Cost	Preparation cycle	Surface modification
HP-SiC	3.20	No	Bad	High	Short term	Requirement
RB-SiC	3.04	Yes	Good	Low	Short term	Requirement
S-SiC	3.10	No	Worse	Lower	Long term	Requirement
CVD-SiC	3.21	No	Best	High	Long term	Nonrequirement

are 6.464 nm and 3.017 nm [18]. The high hardness and complex crystal-phase structure of the SiC material indicate that the fabrication of high precision optical components is costly and slow. The key to solving this problem is to select the appropriate preparation process for surface modification of SiC matrix material, the dense SiC mirror optics plated coating, and the coating polishing. Efficiency of surface finishing for large optical components can be greatly improved as well. Moreover, microstructure defects on polished surface of SiC ceramic mentioned above can be covered up by the coating process. This paper presents the optical surface processes and the recent developments of SiC substrate by hot pressed glass, C/SiC clapping, CVD- and PVD-coated SiC and Si coating method in detail [19–21].

## 2. Optical Fabrication of Silicon Carbide

However, RB-SiC is typically a difficult material to machine. SiC is harder than most other materials except diamond, cubic boron nitride (cBN), and boron carbide (B<sub>4</sub>C), and hence available cutting tool materials for machining RB-SiC are very limited. Recent efforts have focused on the precision machining of RB-SiC by grinding, lapping, polishing, and combinations of these [24, 25]. Main features and classification of optical fabrication methods of SiC are shown in Table 2 [26–28].

## 3. Surface Modification

Surface modification of SiC material is to add a thick film coating to the substrate of SiC for obtaining better surface quality and easier polishing. After fine polishing, the surface shows an extremely smooth surface and it can meet the optical requirement. The earliest study method is hot pressing glass, the recent developments of SiC surface modification is CVD- and PVD-coated SiC and Si, and C/SiC clapping is also applied to space optical devices.

**3.1. Hot Pressed Glass.** The hot pressed glass process was developed by the German IABG Company and the thin reshaped borosilicate glass plate is thoroughly pressed to a preground C/SiC substrate at elevated temperature near the glass softening temperature. After cooling down, the glass plate is bonded to the substrate without the use of any adhesive. The resulted layer of approximate 1 mm thickness is well and economically polishable. But there are some drawbacks for usage of the glass cladding on large surfaces. For example the application of the high pressure led to the

CTE mismatching and residual internal stresses. Now, this process has rarely been used in the size of a large mirror [29].

**3.2. Si/SiC Clapping.** The Si/SiC claddings are processed by an economic deposition of SiC-containing slurry onto the preground surface. Subsequent ceramization of the deposited cladding by thermal treatment leads to the conversion of the slurry cladding into a dense and homogeneous two-phase ceramic surface layer consisting of SiC and silicon. The Si/SiC layer exhibits a strong chemical bonding on the C/SiC base material due to its related chemical nature. By optimizing the ratio of Si to SiC in the layer, its CTE can be tuned to match with that of the C/SiC bulk material over a very broad temperature range. This is important for a thermally stable mirror. Although the described two-phase Si/SiC cladding might not be suitable for superpolished surfaces below 1 nm RMS microroughness, the advantages of the Si/SiC cladding technology for conventional optical components can be summarized as that surface roughness with <2 nm RMS can be obtained with standard optical polishing techniques. A series of studies for this technology [29–31] have been reported by IABG and DSS company.

**3.3. SiC Clapping.** SiC clapping has the same mechanical properties and thermal physical properties as the SiC matrix, so that SiC clapping as a surface modification coating of silicon carbide mirrors attracts extensive attention of researchers. SiC coatings exhibit many outstanding properties, like good isotropic, high hardness, high thermal conductivity, and excellent optical performance characteristics. The amorphous SiC coating prepared by PVD technique with the low temperature and short cycle has also been reported.

**3.3.1. CVD SiC Clapping.** Chemical vapor deposition has been widely applied in thick-film preparation from the 1960s, and its principle is that the reaction materials resulted from the decomposition of Si-containing precursors are deposited on the substrate surface to form a thin film. The film is of good uniformity and repeatability. Such a method is applied to the preparation of SiC coating. Polished CVD-SiC (crystalline cubic  $\alpha$ -SiC) holds also good physical properties for making mirrors such as low density, high melting point, and low expansion coefficient.

The main precursors for CVD SiC is CH<sub>3</sub>SiCl<sub>3</sub>, and the reaction equations are as follows: CH<sub>3</sub>SiCl<sub>3</sub>(g) → SiC(s) + 3HCl(g). The dense SiC coating with excellent optical properties (surface roughness <0.3 nm RMS) can be obtained. It can meet the application requirements of the mirror surface

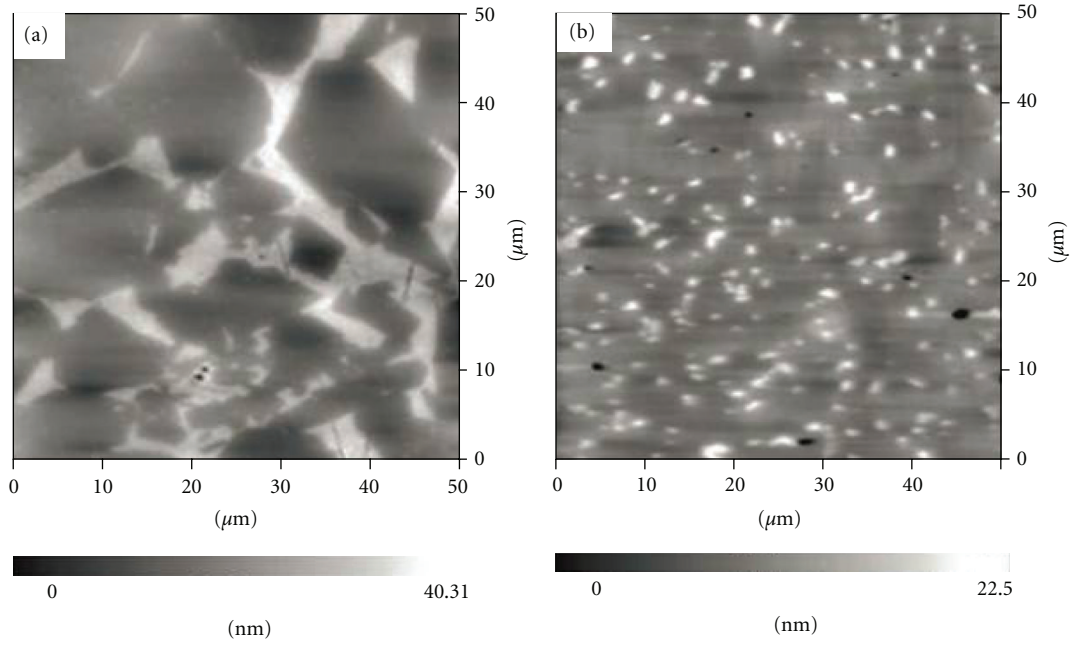


FIGURE 1: AFM images of SiC surfaces polished by 1 μm abrasive grains within 50 μm × 50 μm area: (a) RB-SiC, (b) S-SiC, reprinted with permission from [18].

TABLE 2: Main features of optical fabrication methods of SiC.

Optical fabrication of silicon carbide	Principle	Characteristic	Example
Mechanical polishing	Mechanical friction and material removal	Low efficiency	The final surface accuracy of 1 nm RMS was reported by Paquin et al. [3]
Wet polishing	Polished mold is immersed in the slurry, RMS becomes lower by an abrasive	High surface accuracy	The final surface accuracy of 0.75 nm RMS was reported by Xu et al. [4]
Ultraprecision grinding	Ductility grinding	Equipment require high	Bifano et al. [5] has used CVD SiC to obtain the 5.5 nm RMS
Tribochemical polishing	The tribochemical reaction	Low efficiency	In [6], final surface accuracy of 1 nm RMS
Electrolytic in-process dressing (ELID)	The electrolysis process so that the grinding wheel functions	Good surface quality	In [7], final surface accuracy of 1.4 nm RMS
Chemical mechanical Polishing (CMP)	Combination of mechanical grinding and chemical etching	Good surface quality, but is corrosive	In [8], final surface accuracy of 0.5 nm RMS
Magneto rheological Finishing (MRF)	Magnetorheological polishing fluid viscosity increases the shear force generated for material removal in the magnetic field gradient	Low efficiency	Johnson et al. have used this method to fabricate CVD SiC [9]
Laser-induced photochemical polishing	Laser-induced photochemical reactions	High efficiency, but is corrosive	The final surface accuracy of 80 nm RMS was reported by Murahara [10]
Ion beam milling	High-speed ion beam hits the surface of the sample	Good surface quality, expensive equipment	The final surface accuracy of 1 nm RMS was reported by Johnson et al. [11]
Float polishing	The sample is floating on the polishing plate by the high-speed rotating fluid dynamic pressure	Good surface quality	In [12], final surface accuracy of 3 nm RMS

TABLE 3: Different methods for preparing CVD SiC.

Methods	Advantages and disadvantages	Example
APCVD	The process is simple and has fast response, but with poor uniformity	Chung and Kim [13] use APCVD growth of single-crystalline 3C-SiC (cubic silicon carbide) thin films. The 3C-SiC film had a very good crystal quality without twins, defects, or dislocations, and a very low residual stress
LPCVD	It is possible to grow thin films with uniform and smooth morphology during the 3C-SiC film growth. LPCVD has disadvantages of low growth rate	Clavaguera-Mora et al. [14] have used Si (CH <sub>3</sub> ) <sub>4</sub> as the source materials to deposit SiC film by hot CVD device. Films grown at 900–980°C are amorphous with nanocrystals of mean grain size 10 nm and have smooth surfaces. Surface profilometry measurements give a root mean square roughness (RMS) of 6 nm
PECVD	Substrate temperature is low and deposition rate is fast. SiC films deposited by PECVD appeared to be in an amorphous state	Novi et al. [15] have used PECVD to prepare amorphous SiC, and there has been a lot of cubic structures on the surface, which indicates the existence of polycrystalline structures

and it is one of the most effective methods for surface modification to prepare SiC-based reflection mirror. But the CVD process with high substrate temperature (>1000°C) would lead to the deformation of SiC-matrix. Another disadvantage of the CVD process is time consumption.

There are different treating methods for CVD SiC process, including atmospheric pressure chemical vapor deposition SiC (APCVD SiC), low-pressure chemical vapor deposition SiC (LPCVD SiC), and plasma enhanced chemical vapor deposition SiC (PECVD SiC) [32–34]. Different methods for preparing CVD SiC are shown in Table 3.

CVD SiC coating has been widely applied to surface modification of SiC matrix. For example, CVD SiC with 0.2 nm RMS on the C/SiC substrates had been reported by Trex Advanced Materials [21]. The CVD SiC on S-SiC substrates in the polished roughness of less than 0.1 nm has also been reported by BOOSTEC. In China, Zhang [35] applied this method to obtain CVD-SiC with the surface roughness of 1.478 nm RMS.

**3.3.2. PVD SiC.** High temperature (typically 1300°C) in the preparation process of CVD SiC may result in stronger film stress on the SiC mirror. This is due to the unacceptable high residual stress buildup in heavy cross-sections. The cost of producing CVD SiC as a large self-supporting substrate is very high. However, PVD SiC appears to be very attractive due to its relative simplicity, low substrate temperature, and wide accessibility by industry.

***Ion-Assisted Deposition SiC (IAD SiC).*** The ion implantation of semiconductors rapidly became an accessible technology from the 1970s because of its ability to produce superior electronic devices. Ion beam modification of nonsemiconductor materials for enhancing surface sensitive properties has been actively pursued in the international R&D community. The advantages of this technique include high density, superior adhesion, and the ability to produce arbitrarily thick

coatings. Perhaps the most important feature of the IBAD technology is the frequently demonstrated ability to control many coatings properties such as morphology, adhesion, and stress, as well as stoichiometry. The amorphous SiC coating with large area can be prepared by this method on the SiC substrate. The  $\alpha$ -SiC coating has been prepared on the RB SiC and polished with surface roughness up to 0.2 nm RMS by U.S. HDOS [3, 36] using ion beam deposition method. Hall ion source [37] and high-energy Kaufman ion source [38] can both be used as the ion-beam resources for preparing  $\alpha$ -SiC and its system of SiC-modified membrane and the surface roughness can be down to 0.867 nm RMS and 0.743 nm RMS.

***Magnetron Sputtering SiC Clapping.*** Magnetron sputtering is used widely due to its low cost, high deposition rate, low deposition temperature, and good adhesion of the film feature. The SiC coatings were deposited by RF magnetron sputtering from a sintered SiC target onto commercially monpolished RB SiC substrate kept at low temperature. The deposition rate is fast and the desired temperature is low, but the film stability of its system is not sustainable [39]. Magnetron sputtering SiC clapping was prepared with the roughness down to 1.394 nm RMS [40] and 3.184 nm RMS as shown in Figure 2 by Tang et al. [22] and the surface roughness of 2 angstrom by Kortright and Windt [41].

***Pulsed Laser Deposition SiC (PLD SiC).*** PLD is a relatively new technique and attracting great attention for its simplicity, reduced investment cost, and flexibility. In the PLD process [42], a high flux pulsed laser beam is focused on the target material leading to the formation of a plasma plume. The high heating rate of the target surface ( $\approx 100$  K/s) due to pulsed laser irradiation leads to a congruent evaporation of the target irrespective of the evaporating point of its constituent elements or compounds, so that the target stoichiometry can be retained in the deposited films.

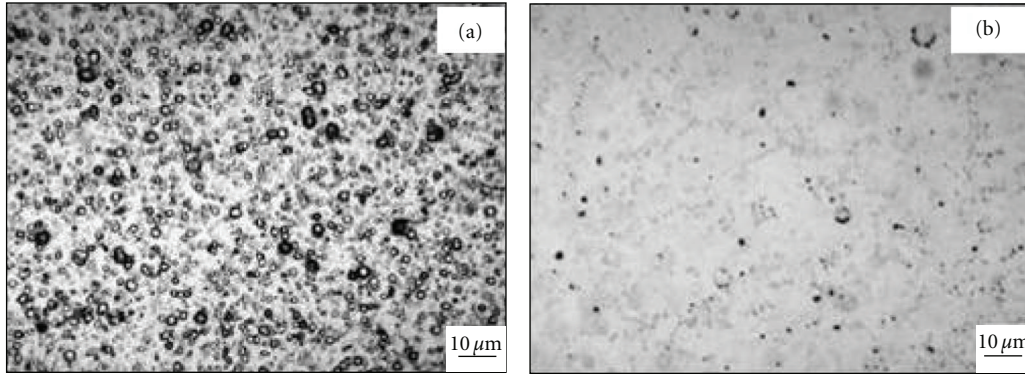


FIGURE 2: Photomicrograph of (a) unpolished, (b) polished PVD SiC coating on RB SiC, reprinted with permission from [22].

TABLE 4: Thermal performance of RB-SiC and Si [16].

Materials	$\alpha$ /(ppm/K)	$K$ /(W/mK)	$D$	$\alpha/K$	$\alpha/D$
RB-SiC	2.4	170	80	0.014	0.03
Si	2.6	156	89	0.017	0.029

Furthermore, because of the high heating rate of the ablated materials, PLD of crystalline films demands a much lower substrate temperature than other film growing techniques. The major drawback of this technique is that the high energy involved in the process also leads to the formation of microparticulate on the thin film surface. Vendan et al. [43] has prepared  $\alpha$ -SiC thin films by fs-PLD and ns-PLD techniques and found that the surface roughness of SiC films by the ns-PLD technique was bigger than that by fs-PLD. Magida et al. [32] has prepared SiC thin films which exhibit high reflectivity in the ultraviolet band (40.7 nm–121.6 nm) and the surface roughness of 1 nm RMS.

*Ion Beam Sputtering SiC (IBS SiC).* The ion beam engine concept was firstly developed in the United States. By the IBS technique, the SiC films being flat and smooth, a large area of dense internal stress and low defect density can be obtained. For example, the IBS SiC coatings have been prepared and polished to be less than 2 Å RMS by Johnson [36] for the optical system requiring ultralow scatter performance.

*3.4. Si Clapping.* The thermal properties of Si coating match well with that of SiC as shown in Table 4, then Si clapping can be used for the surface modification of SiC. It can be seen that their thermal performance is well matched, and Si can be used as a good reflector material. CVD and PVD are the main preparation methods.

*3.4.1. CVD Si Clapping.* The Si clapping is easier to be polished well with better surface quality and low-cost SiC-clapping. Polycrystalline Si produced by a scalable CVD process has exhibited a surface finish of 0.2 nm RMS. Polycrystalline Si was fabricated by reacting trichlorosilane ( $\text{SiHCl}_3$ ) with excess  $\text{H}_2$  in a hot-wall CVD reactor according

to the reaction:  $\text{SiHCl}_3 + 2\text{H}_2 \rightarrow \text{Si(s)} + 4\text{HCl(g)}$ . However, it is not widely applied [14, 44] because columnar structure is often present in CVD Si.

Polycrystalline Si [19] was also used to clad on several advanced ceramic materials such as SiC, sapphire, pyrolytic BN, and Si by a chemical vapor deposition (CVD) process. The thickness of Si cladding ranged from 0.025 to 3.0 mm. CVD Si adhered quite well to all the above materials, where the Si cladding was highly stressed and cracked. The surface roughness can reach 0.2 nm RMS after polishing. Amorphous silicon thin films were formed by chemical vapor deposition by Choi et al. [45]. The amorphous silicon films without reflector bias voltage exhibit 0.119 nm RMS, but down to 0.171 nm RMS with reflector bias voltage of  $-120$  V, respectively.

*3.4.2. PVD Si Clapping.* CVD Si is generally prepared with high temperature ( $>600^\circ\text{C}$ ), and the PVD Si film is widely used. The application of Si coating can reduce surface wearing resistance of SiC ceramic without changing mechanical properties of the bulk materials. The efficiency of surface finishing for large optical components can be greatly improved as well [23]. Therefore, PVD Si appears to be very attractive because of its relative simplicity, low substrate temperature, and wide accessibility by industry. Si clapping is easier to be polished well because it is single-phase material without the different heterogeneous phase in the polishing process. PVD Si coating is now becoming a preferred method of the SiC surface modification.

*Vacuum Evaporation Si Clapping.* Vacuum evaporation deposition of Si film is processed in a high vacuum by heating the Si gasification or sublimation condensing into Si film and thus being deposited on SiC substrate surface. The method is relatively simple and has high deposition rate. But the columnar structure is present in Si film and the physical property of Si film is not stable. Zhao [46] has obtained amorphous Si films by thermal evaporation. In recent years, this method has been improved. Fang et al. [47] deposited Si film on steel and alumina substrates by electron beam evaporation of solid silicon.

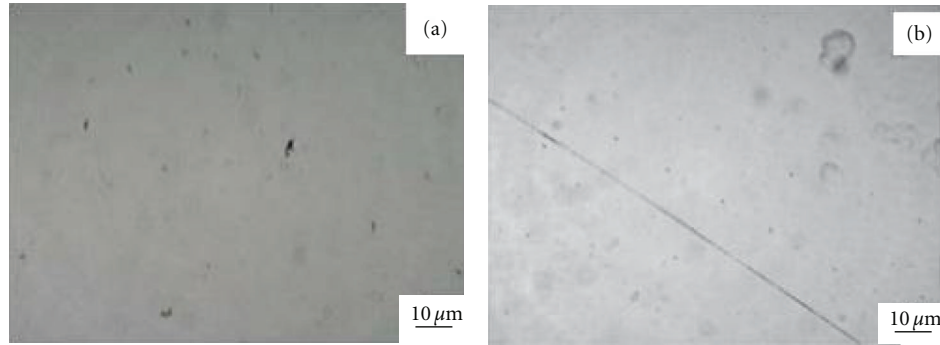


FIGURE 3: Photomicrograph of (a) unpolished, (b) polished PVD Si coating on RB SiC, reprinted with permission from [22].

**Magnetron Sputtering Si Clapping.** Magnetron sputtering (belongs to PVD) appears to be very attractive due to its relative simplicity and low substrate temperature. Many researchers have studied this method, Aoucher et al. [48] deposited amorphous silicon by DC magnetron sputtering on a quartz substrate at a rate around 1.5 nm/s. Tang et al. [22] has used RF magnetron sputtering method to prepare Si film with the surface roughness from 17.992 nm RMS to 1.183 nm RMS as shown in Figure 3.

**Ion-Beam-Assisted Si Clapping.** Hydrogenated amorphous silicon (a-Si:H) films are generally prepared by glow-discharge decomposition of silane or by sputtering of silicon in an argon-hydrogen mixture. The reaction temperature is low (200°C) and the preparation parameters can be controlled. So it was used to prepare amorphous silicon films.

Photoconductive hydrogenated amorphous silicon films were deposited by ion-beam-assisted evaporation using hydrogen-argon plasma. Surface modification for the RB-SiC substrate [49] is carried out using e-beam evaporation with plasma ion assisted. The surface roughness of the RB-SiC substrate is reduced to 0.0632 nm, the scattering coefficient is reduced to 2.81%, and the average reflectance from 500 nm to 1000 nm is raised to 97.05%; these data indicate that good optical quality similar to that of the fine polished glass ceramics can be obtained by the modification process.

**Plasma-Ion-Assisted of Deposition Si Clapping.** For the production of thin films of high quality standard, thermal evaporation techniques are applied with the assistance of ion sources which provide additional energy and momentum to influence the growth process. Larger ion current densities on increased substrate areas can be generated by employing plasma sources, and the process is plasma-ion-assisted deposition (PIAD) [50]. In PIAD, a growing thin film is bombarded by energetic ions from a plasma ion source and the columnar microstructure of the film is disrupted, resulting in the improved optical and mechanical properties of thin films [51]. Liu et al. [23] has prepared Si thin film by this method and obtained continuous, homogenous, well-bonded amorphous Si coatings on SiC ceramics. It means that the SiC substrate can be fully covered up and the effect

of substrate surface defects on the surface morphology of the Si coating can be overlooked as shown in Figure 4.

Recently, the PVD Si coatings on SiC substrates have been investigated. SSG has applied PVD Si in optical systems of the GEO telescope [52], designed and constructed for an SBIR program funded by NASA's Marshall Space Flight Center (MSFC). The SiC telescope and "GOES-like" scan mirror are designed to "generic" GEO specifications, and the surface roughness decreased to 0.4 nm RMS after polishing. In China, the PVD Si coatings deposited on the surface of polished RB-SiC and S-SiC were demonstrated to improve the optical surface quality after being polished by Tang et al. [22]. Both the surfaces of PVD Si coating on RB-SiC and S-SiC are smoother than that of bare SiC. The RMS can reach to the angstrom grade, and the reflectance improves significantly.

#### 4. Conclusion

Silicon carbide as the third generation of space mirror material has attracted more and more attention and is widely applied. Silicon carbides prepared by different preparation methods have their advantages, but still cannot meet the optical requirements (<1 nm RMS) after the current optical processing. The surface roughness and reflection rate of the SiC material can be well improved after surface modification. Especially in the CVD SiC coating and PVD-Si coating on the SiC ceramic, surface roughness of Angstrom level can be reached. All kinds of surface-modification methods have been developed and every method has its disadvantages. The hot press glass has some drawbacks for usage of the glass cladding on large surfaces. The C/SiC coating may not be suitable for low surface roughness (<1 nm RMS). The CVD process with high temperature (>1000°C) would lead to the deformation of SiC matrix. PVD method to prepare SiC-film is slower and the modified film is very difficult to be polished. In our view, PIAD Si has low reaction temperature (<300°C) and is very easy to be polished. The preparation process is relatively simple, and reproducible preparation of silicon-modified layer gives a dense structure, combined with the base firmly. Therefore, PVD Si is the best choice for surface modification of SiC mirror because of its relative simplicity, low substrate temperature, and wide accessibility by industry, especial PIAD Si.

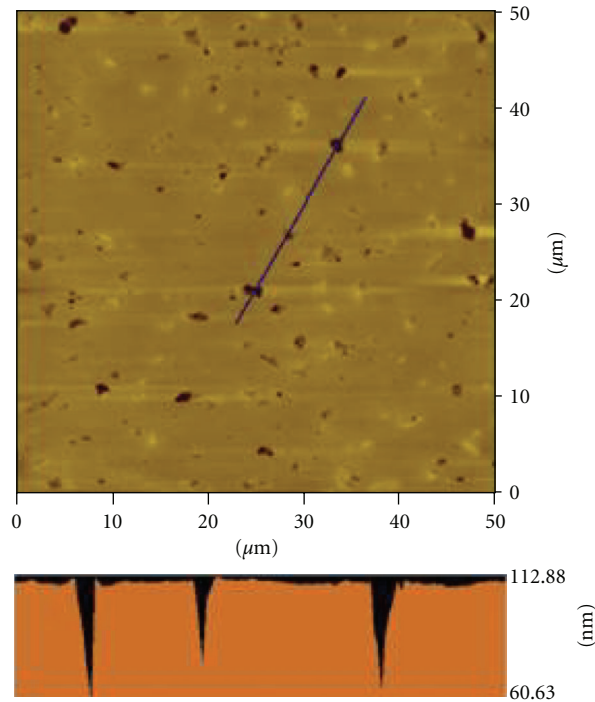


FIGURE 4: Surface topography of Si coating tested by AFM, reprinted with permission from [23].

## Acknowledgments

Y. Yang thanks the Century Program (One-Hundred-Talent Program) of the Chinese Academy of Sciences for special funding support. This study was also supported in part by a fund from the National Natural Science Foundation of China (no. 51071167, 51102266), the Shanghai Yangtze River Delta Science Project (no. 11495810100), and the Shanghai Pujiang Program (10PJ1410700).

## References

- [1] J. Robichaud, J. J. Guregian, and M. Schwalm, "SiC optics for Earth observing applications," in *Earth Observing Systems VIII*, vol. 5151 of *Proceedings of SPIE*, pp. 53–62, August 2003.
- [2] S. G. Johnson, "SiC coatings on RB SiC mirrors for ultra-smooth surfaces," vol. 2018 of *Proceedings of SPIE*, no. 1993, pp. 237–247.
- [3] R. A. Paquin, M. B. Magida, and C. L. Vernold, "Large optics from silicon carbide," in *Large Optics II*, vol. 1618 of *Proceedings of SPIE*, pp. 53–60, October 1991.
- [4] Q. L. Xu, F. Wu, and S. B. Wu, "Super smooth surfacing fabrication for lightweight silicon carbide plan mirror," *Opto-Electronic Engineering*, vol. 31, pp. 22–25, 2004.
- [5] T. Bifano, Y. Yi, and K. Kahl, "Fixed abrasive grinding of CVD SiC mirrors," *Precision Engineering*, vol. 16, no. 2, pp. 109–116, 1994.
- [6] Z. Z. Zhu, V. Muratov, and T. E. Fischer, "Tribochemical polishing of silicon carbide in oxidant solution," in *Proceedings of the 12th International Conference on Wear of Materials*, vol. 225–229, pp. 848–856, Atlanta, Ga, USA, 1999.
- [7] W. Lin, H. Ohmori, T. Suzuki, Y. Uehara, and S. Morita, "Polishing characteristics of ELID-ground surface of nano precision optical elements," *Key Engineering Materials*, vol. 291–292, pp. 365–370, 2005.
- [8] L. Zhou, V. Audurier, P. Pirouz, and J. A. Powell, "Chemomechanical polishing of silicon carbide," *Journal of the Electrochemical Society*, vol. 144, no. 6, pp. L161–L163, 1997.
- [9] J. S. Johnson, K. Grobbsky, and D. J. Bray, "Rapid fabrication of lightweight silicon carbide mirrors," in *Optomechanical Design and Engineering*, vol. 4771 of *Proceedings of SPIE*, pp. 243–253, July 2002.
- [10] M. Murahara, "Excimer laser-induced photochemical polishing of SiC mirror," in *Laser-Induced Damage in Optical Materials*, vol. 4679 of *Proceedings of SPIE*, pp. 69–74, October 2001.
- [11] J. S. Johnson, K. Grobbsky, and D. J. Bray, "Rapid fabrication of lightweight silicon carbide mirrors," in *Optomechanical Design and Engineering*, *Proceedings of SPIE*, pp. 243–253, July 2002.
- [12] D. Fan, Z. Y. Zhang, and H. Y. Niu, "Surfacing fabrication of silicon carbide optical mirror," *Journal of Inorganic Materials*, vol. 31, pp. 1096–1100, 2003.
- [13] G. S. Chung and K. S. Kim, "Heteroepitaxial growth of single 3C-SiC thin films on Si(100) substrates using a single-source precursor of hexamethyldisilane by APCVD," *Bulletin of the Korean Chemical Society*, vol. 28, no. 4, pp. 533–537, 2007.
- [14] M. T. Clavaguera-Mora, J. Rodríguez-Viejo, Z. El Felk et al., "Growth of SiC films obtained by LPCVD," *Diamond and Related Materials*, vol. 6, no. 10, pp. 1306–1310, 1997.
- [15] A. Novi, G. Taglioni, and L. Novella, "Silicon carbide for mirrors by plasma enhanced chemical vapour deposition at low temperature," *European Space Agency ESA SP*, vol. 554, pp. 687–691, 2004.
- [16] L. D. Xu, X. J. Zhang, and X. Wang, "Surface coating technique of reaction bonded sic mirrors," *Opto-Electronic Engineering*, vol. 36, no. 1, pp. 120–124, 2009.

- [17] C. J. Shih and A. Ezis, "Application of hot-pressed silicon carbide to large high-precision optical structures," in *Silicon Carbide Materials for Optics and Precision Structures*, vol. 2543 of *Proceedings of SPIE*, pp. 24–37, July 1995.
- [18] G. Liu, Z. Huang, X. Liu, and D. Jiang, "Removal behaviors of different SiC ceramics during polishing," *Journal of Materials Science and Technology*, vol. 26, no. 2, pp. 125–130, 2010.
- [19] J. S. Goela and R. L. Taylor, "Chemical vapor deposition for silicon cladding on advanced ceramics," *Journal of the American Ceramic Society*, vol. 72, pp. 1747–1750, 1989.
- [20] Y. Y. Han, Y. M. Zhang, and J. C. Han, "Current status of research on silicon carbide mirror technology," *Materials Review*, vol. 19, pp. 5–8, 2005.
- [21] H. Zhou, C. R. Zhang, and Y. B. Cao, "Lightweight C/SiC mirrors for space application," *Large Mirrors and Telescopes*, vol. 6148, pp. L1480–L1486, 2006.
- [22] H. Tang, Z. Huang, and S. Tan, "PVD SiC and PVD Si coatings on RB SiC for surface modification," in *Proceedings of the 2nd International Symposium on Advanced Optical Manufacturing and Testing Technologies—Advanced Optical Manufacturing and Testing Technologies*, pp. 1–6, November 2005.
- [23] G. L. Liu, Z. R. Huang, J. H. Wu, and X. J. Liu, "Surface morphology evolution and properties of silicon coating on silicon carbide ceramics by advanced plasma source ion plating," *Surface and Coatings Technology*, vol. 207, pp. 204–210, 2012.
- [24] J. Yan, Z. Zhang, and T. Kuriyagawa, "Mechanism for material removal in diamond turning of reaction-bonded silicon carbide," *International Journal of Machine Tools and Manufacture*, vol. 49, no. 5, pp. 366–374, 2009.
- [25] H. Y. Tam, H. B. Cheng, and Y. W. Wang, "Removal rate and surface roughness in the lapping and polishing of RB-SiC optical components," *Journal of Materials Processing Technology*, vol. 192–193, pp. 276–280, 2007.
- [26] G. L. Liu, Z. R. Huang, and X. J. Liu, "Recent developments of surface coatings and optical fabrication of silicon carbide," *Journal of Inorganic Materials*, vol. 22, pp. 769–774, 2007.
- [27] A. Venu Gopal and P. V. Rao, "The optimisation of the grinding of silicon carbide with diamond wheels using genetic algorithms," *International Journal of Advanced Manufacturing Technology*, vol. 22, no. 7–8, pp. 475–480, 2003.
- [28] H. B. Cheng, Z. J. Feng, and Y. W. Wang, "Magnetorheological finishing of SiC aspheric mirrors," *Materials and Manufacturing Processes*, vol. 20, pp. 917–931, 2005.
- [29] M. Deyerler, N. Pailer, R. Wagner, and C. Mueller, "Ultra-lightweight mirrors: recent developments of C/SiC," in *Optical Design, Materials, Fabrication, and Maintenance*, vol. 4003 of *Proceedings of SPIE*, pp. 73–79, March 2000.
- [30] A. Novi, G. Mondello, C. Devilliers et al., "Comparison of sintered-SiC and C/SiC mirrors behaviour at cryo-temperatures," in *Optical Materials and Structures Technologies*, vol. 5179 of *Proceedings of SPIE*, pp. 246–253, August 2003.
- [31] B. Harnisch, B. Kunkel, M. Deyerler, and S. Bauereisen, "Ultra-lightweight C/SiC Mirrors and Structures," *ESA Bulletin-European Space Agency*, vol. 95, pp. 108–112, 1998.
- [32] M. B. Magida, R. A. Paquin, and J. J. Richmond, "Dimensional stability of bare and coated reaction bonded silicon carbide," in *Dimensional Stability*, vol. 1335 of *Proceedings of SPIE*, pp. 60–68, July 1990.
- [33] C. Hung Wu, C. A. Zorman, and M. Mehregany, "Growth of polycrystalline SiC films on SiO<sub>2</sub> and Si<sub>3</sub>N<sub>4</sub> by APCVD," *Thin Solid Films*, vol. 355–356, pp. 179–183, 1999.
- [34] R. J. Liu, C. R. Zhang, X. G. Zhou, and Y. B. Cao, "SiC coatings for mirrors prepared by low pressure chemical vapor deposition," *Journal of Materials Science Letters*, vol. 22, no. 11, pp. 841–843, 2003.
- [35] J. H. Zhang, Y. M. Zhang, J. C. Han, X. D. He, and W. Yao, "Design, fabrication and testing of space-borne SiC mirror," *Optics and Precision Engineering*, vol. 14, no. 2, pp. 179–184, 2006.
- [36] S. Johnson, "SiC coating on RB SiC mirror for ultra-smooth surface," vol. 2018 of *Proceedings of SPIE*, pp. 237–247, 1993.
- [37] T. T. Wang, J. S. Gao, X. Y. Wang et al., "Preliminary study of reaction bonded silicon carbide surface modification," *Optics and Precision Engineering*, vol. 16, no. 9, pp. 1603–1607, 2008.
- [38] J. S. Gao, T. T. Wang, Q. Song et al., "Preparation of silicon carbide surface-modified coatings with end hall ion source assisted," *Infrared and Laser Engineering*, vol. 37, no. 4, pp. 710–713, 2008.
- [39] G. Monaco, M. Gastaldi, and P. Nicolosi, "Silicon carbide thin films for EUV and soft X-ray applications," *European Physical Journal*, vol. 169, pp. 159–165, 2009.
- [40] H. Tang, S. Tan, Z. Huang, S. Dong, and D. Jiang, "Surface morphology of  $\alpha$ -SiC coatings deposited by RF magnetron sputtering," *Surface and Coatings Technology*, vol. 197, no. 2–3, pp. 161–167, 2005.
- [41] J. B. Kortright and D. L. Windt, "Amorphous silicon carbide coatings for extreme ultraviolet optics," *Applied Optics*, vol. 27, no. 14, pp. 2841–2846, 1988.
- [42] I. Hanyecz, J. Budai, E. Szilágyi, and Z. Tóth, "Characterization of pulsed laser deposited hydrogenated amorphous silicon films by spectroscopic ellipsometry," *Thin Solid Films*, vol. 519, no. 9, pp. 2855–2858, 2011.
- [43] M. Vendan, P. Molian, A. Bastawros, and J. Anderegg, "Ultra-short pulsed laser deposition and patterning of SiC thin films for MEMS fabrication," *Materials Science in Semiconductor Processing*, vol. 8, no. 6, pp. 630–645, 2005.
- [44] Y. F. Zhou, Y. M. Zhang, and J. C. Han, "Preparation of silicon coating," *Materials Review*, vol. 19, pp. 84–86, 2005.
- [45] S. G. Choi, S. J. Wang, H. H. Park et al., "Properties of amorphous silicon thin films synthesized by reactive particle beam assisted chemical vapor deposition," *Thin Solid Films*, vol. 518, no. 24, pp. 7372–7376, 2010.
- [46] X. J. Zhao, "Investigation of silicon carbide mirror's reflective performance and film design," Harbin Harbin Institute of Technology, 2007.
- [47] P. H. Fang, P. Bai, J. H. Kinnier, Z. Huan, and C. C. Schubert, "Temperature dependent formation of microcrystal and amorphous silicon by vacuum evaporation," *Journal of Non-Crystalline Solids*, vol. 59–60, no. 2, pp. 819–821, 1983.
- [48] M. Aoucher, G. Farhi, and T. Mohammed-Brahim, "Crystallization of hydrogenated amorphous silicon deposited at high rate by dc magnetron sputtering," *Journal of Non-Crystalline Solids*, vol. 227–230, no. 2, pp. 958–961, 1998.
- [49] Z. F. Shen, J. S. Gao, H. Chen, X. Y. Wang, T. T. Wang, and X. M. Zheng, "Performance and reliability evaluation for the surface modification of space used silicon carbide mirror," *Acta Photonica Sinica*, vol. 38, no. 9, pp. 2353–2358, 2009.
- [50] J. Harhausen, I. Meyenburg, A. Ohl, and R. Foest, "Characterization of the plasma plume of a PIAD plasma source by means of optical emission spectroscopy," *Surface and Coatings Technology*, vol. 205, no. 2, pp. S407–S410, 2011.
- [51] S. H. Woo and C. K. Hwangbo, "Influence of plasma ion-beam assistance on TiO<sub>2</sub> and MgF<sub>2</sub> thin films deposited by plasma

ion-assisted deposition,” *Surface and Coatings Technology*, vol. 201, no. 19-20, pp. 8250–8257, 2007.

- [52] M. I. Anapol, L. R. Gardner, T. W. Tucker, and R. J. Koczor, “Lightweight 0.5-m silicon carbide telescope for a geostationary earth observatory mission,” in *Silicon Carbide Materials for Optics and Precision Structures*, Proceedings of SPIE, pp. 164–172, July 1995.

## Research Article

# Microstructure and Glass Phase of Inorganic Binder Coated on Mold for Thin Casting

Eun-Hee Kim,<sup>1</sup> Geun-Ho Cho,<sup>1</sup> Yeon-Gil Jung,<sup>1</sup> Je-Hyun Lee,<sup>1</sup>  
Baig-Gyu Choi,<sup>2</sup> and Chang Young Jo<sup>2</sup>

<sup>1</sup>School of Nano and Advanced Materials Engineering, Changwon National University, No. 9 Sarim-dong, Changwon, Gyeongnam 641-773, Republic of Korea

<sup>2</sup>High Temperature Materials Research Group, Korea Institute of Materials Science, 797 Changwondaero, Changwon, Gyeongnam 641-831, Republic of Korea

Correspondence should be addressed to Eun-Hee Kim, udam99@changwon.ac.kr and Yeon-Gil Jung, jungyg@changwon.ac.kr

Received 11 June 2012; Accepted 4 December 2012

Academic Editor: Zhengren Huang

Copyright © 2012 Eun-Hee Kim et al. This is an open access article distributed under the Creative Commons Attribution License, which permits unrestricted use, distribution, and reproduction in any medium, provided the original work is properly cited.

A new dual dipping process has been introduced for the increase in the fracture strength of casting mold through the effective glassification of inorganic binder precursors. Two different dipping processes have been employed to investigate the reactivity of the precursors. Process I is that the substrate was coated with a sodium oxide ( $\text{Na}_2\text{O}$ ) precursor through dipping in the solution, and then a silicon dioxide ( $\text{SiO}_2$ ) precursor was coated onto the substrate coated with the  $\text{Na}_2\text{O}$  precursor. Process II is the inverse coating sequence for process I. In the case of the mold prepared by process I, the glass phase converted from the precursors is uniformly observed at the surface of the particle and the interface between particles, compared with that by process II, inducing that the fracture strength of the mold prepared by process I is significantly improved. In addition, when the PDMS without a sol-gel reaction was used as the  $\text{SiO}_2$  precursor, especially in process II, the glass phase is not absolutely observed at the surface of the particle owing to the evaporation of PDMS and Na ion during the heat treatment, resulting in the collapse of the mold sample after the heat treatment.

## 1. Introduction

Recently, the convert mold process has been introduced to fabricate molds in a thin casting [1, 2]. The convert mold process has many advantages, such as high strength, excellent collapse, easy processability, and high thermal stability, making it useful in fabricating components of automobile and aircraft. Typically, the convert mold process is divided into five main processes: (1) fabricating the starting mold coated with an organic binder, (2) dipping the coated mold into a slurry containing inorganic binder precursors, (3) 1st drying for 1 h at 80°C, (4) 2nd drying for 1 h at 200°C, and (5) heat treatment for 1 h at 1000°C, resulting in the conversion of the organic binder-coated mold to the inorganic binder-coated mold [3, 4]. The hydrolysis and condensation reactions (generally called a sol-gel reaction) and glassification take place during the above (3 and 4) and (5) processes, respectively [5–7]. The

mechanical and thermal properties of the mold are induced from the glass phase generated during the heat treatment process, even though the organic binder is decomposed after the heat treatment. Therefore, the generated glass phase must be homogeneously formed on the surfaces of starting particles in the mold as well the conversion efficiency of inorganic binder precursors into the glass phase should be increased, which are related to the reactivity between precursors. Our early work has researched about the new inorganic precursors without the sol-gel reaction instead of the inorganic binder used in the conventional convert mold process, showing a higher glassification efficiency of inorganic binder precursors and a better fracture strength. In addition, the morphology and structure of inorganic binder obtained after the dry and heat treatment processes were investigated in detail [8, 9]. However, the previous works were related to the new precursors for the increase in the strength of the mold.

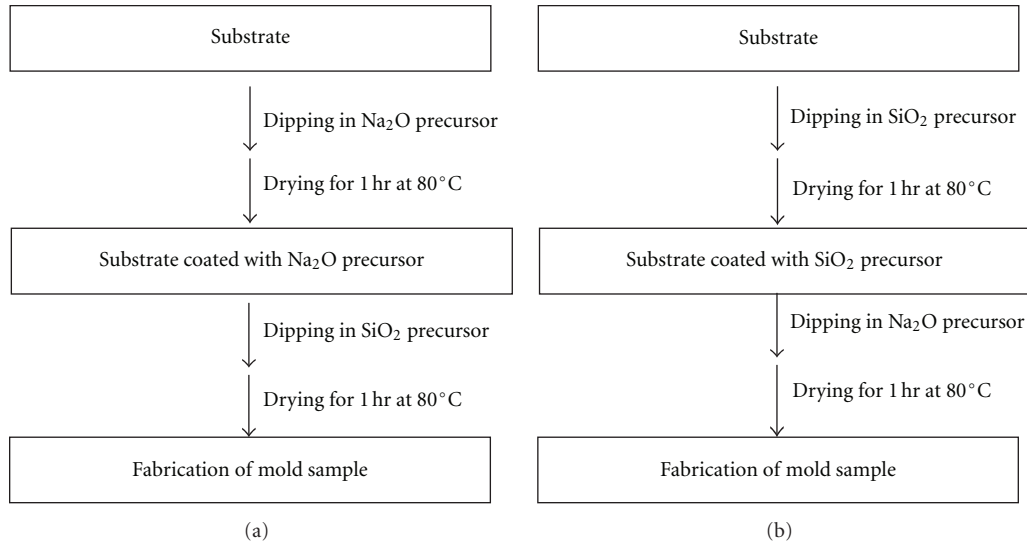


FIGURE 1: Schematic diagram for fabricating mold samples through the new dual dipping process: (a) process I and (b) process II.

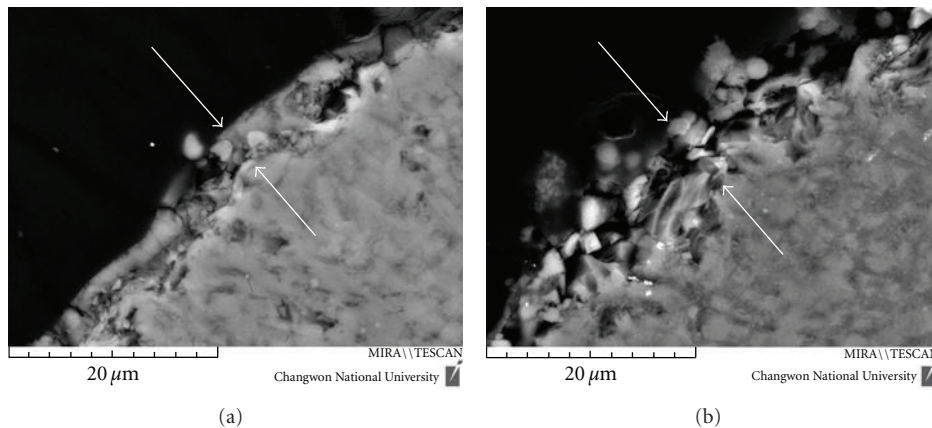


FIGURE 2: SEM morphologies of particle surfaces in mold samples prepared by (a) process I and (b) process II before the heat treatment. TEOS was used as the SiO<sub>2</sub> precursor. Arrows indicate the coated layers in each particle.

For that reason, in this work, a new dipping process has been introduced for inducing the uniform coating of glass phase and improving the conversion efficiency of inorganic binder precursors into the glass phase, leading to the optimum fracture strength of the mold for the thin casting. The inorganic binder system consisted of a mixture of alkyl silicate (or siloxane compound) and sodium alkoxide used as the silicon dioxide (SiO<sub>2</sub>) and sodium oxide (Na<sub>2</sub>O) precursors, respectively. Respective precursors were independently coated on the particles of the mold through the continuous dipping process, called a dual dipping process, compared with the convention process dipped into a mixture with two precursors at a time. The properties of mold samples prepared by the dual dipping process were measured using various analytical techniques. The influences of precursor species and dipping sequence in the dual dipping process on fracture strength have been investigated and discussed based on the microstructures observed before and after the heat treatment.

## 2. Experimental Procedure

Composite binder systems for fabricating mold samples through the dual dipping process were prepared using tetraethyl orthosilicate (TEOS, Sigma-Aldrich Korea, Yongin, Korea) of silicate type or poly(dimethyl siloxane) (PDMS, bp 160°C, Sigma-Aldrich Korea, Yongin, Korea) of siloxane type used as a SiO<sub>2</sub> precursor, and sodium methoxide (NaOMe, Sigma-Aldrich Korea, Yongin, Korea) used as an Na<sub>2</sub>O precursor. The size of a substrate prepared with the bead composed of SiO<sub>2</sub> and Al<sub>2</sub>O<sub>3</sub> was 10 × 10 × 50 mm, which was coated with an organic binder of phenol resin. In this work, two different dual dipping processes were employed for preparing mold samples, as shown in Figure 1. In the first process, the substrate was coated with the Na<sub>2</sub>O precursor, and then the treated substrate was coated with the SiO<sub>2</sub> precursor, which is process I. In the second process, the coating sequence of process I was inverted, which is process II. The mold samples coated with the precursors were dried

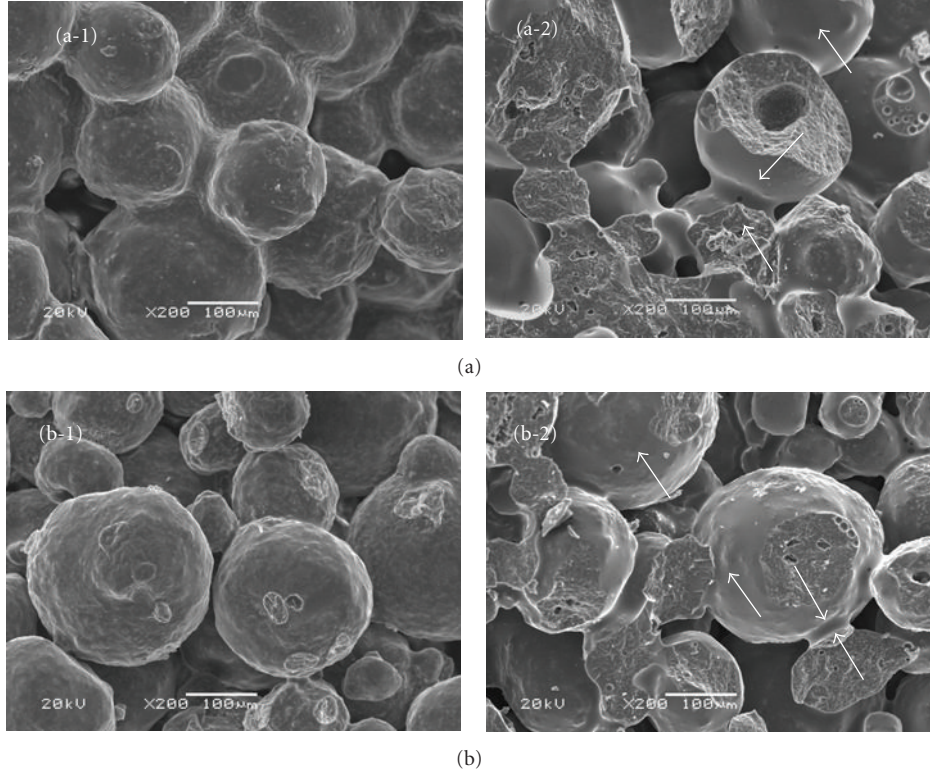


FIGURE 3: SEM morphologies on the fracture surfaces of mold samples through process I as a function of  $\text{SiO}_2$  precursor: (a) TEOS and (b) PDMS. Each number indicates SEM morphologies before and after the heat treatment, respectively. Arrows indicate the glass phase formed in mold samples.

TABLE 1: Basic formulations and experimental ranges to prepare mold samples through the new dual dipping process.

Run number	$\text{SiO}_2$ precursor	$\text{Na}_2\text{O}$ precursor	Process	Condition of heat treatment
Run-1	TEOS		Process I	1000°C for 1 h
Run-2	PDMS	NaOMe		
Run-3	TEOS		Process II	
Run-4	PDMS			

at 80°C for 1 h after each coating or dipping process, and then heat-treated at 1000°C for 1 h. The molten metal based on iron (Fe) was poured into the real mold prepared through process I with TEOS as the  $\text{SiO}_2$  precursor for thin casting. Basic formulations and experimental ranges for preparing the mold through the dual dipping process are shown in Table 1.

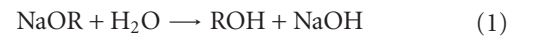
The surface morphology and microstructure before and after the heat treatment were observed using a scanning electron microscope (SEM, JEOL Model JSM-5610, Tokyo, Japan). The fracture strength of mold samples after the heat treatment was measured using a universal testing machine (UTM, Instron 5566, Instron Corp., Norwood, MA, USA) in the bending mode at a rate of 0.5 mm min<sup>-1</sup>. Tests were carried out at room temperature, and five runs were performed to determine the standard deviation of the

strength. The support spans of the low and upper noses were 2.5 cm and 1.0 cm, respectively.

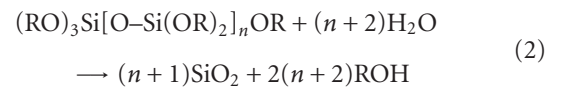
### 3. Results and Discussion

The reaction mechanism of precursor materials is divided into hydrolysis reaction, sol-gel reaction, and heat-treatment stages [3, 4], as shown in the following reactions.

Hydrolysis reaction:



Sol-gel reaction:



where NaOR, ROH, NaOH,  $(\text{RO})_3\text{Si}[\text{O}-\text{Si}(\text{OR})_2]_n\text{OR}$ , and  $\text{SiO}_2$  denote sodium alkoxide, an alcohol, sodium hydroxide, alkyl silicate, and silicon dioxide (silica), respectively [5, 10]. NaOR is hydrolyzed to form NaOH (by (1)), and alkyl silicate is hydrolyzed to form silica and alcohol (by (2)).

Heat-treatment reaction:



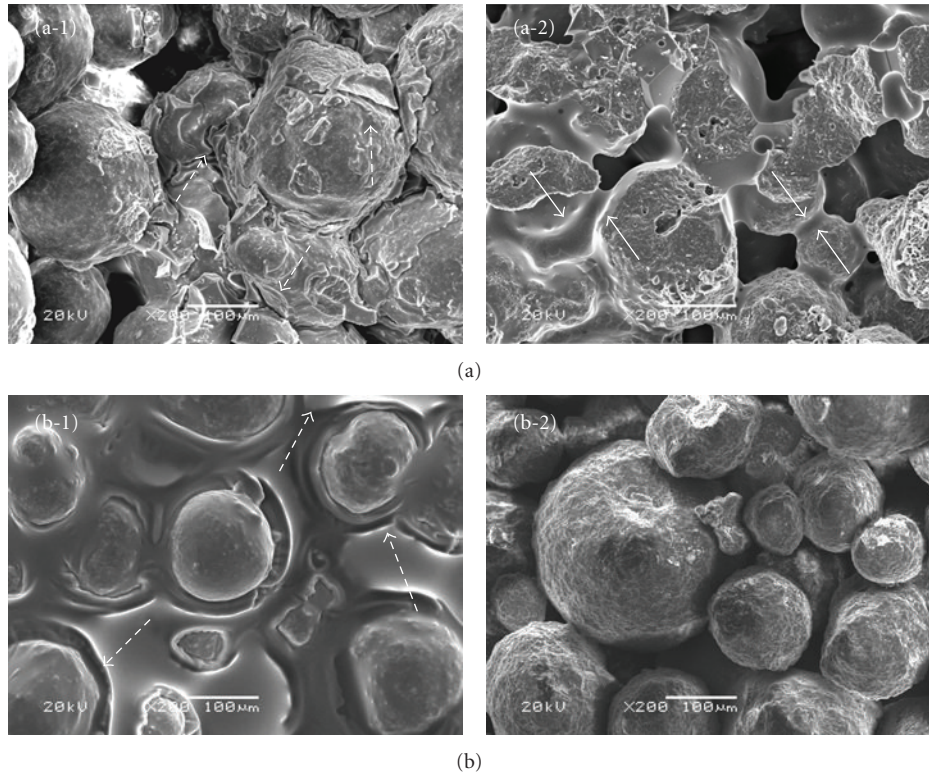


FIGURE 4: SEM morphologies on the fracture surfaces of mold samples through process II as a function of  $\text{SiO}_2$  precursor: (a) TEOS and (b) PDMS. Each number indicates SEM morphologies before and after the heat treatment, respectively. Dotted and solid arrows indicate the crack created (series-1) and glass phase formed (series-2) in mold samples, respectively.

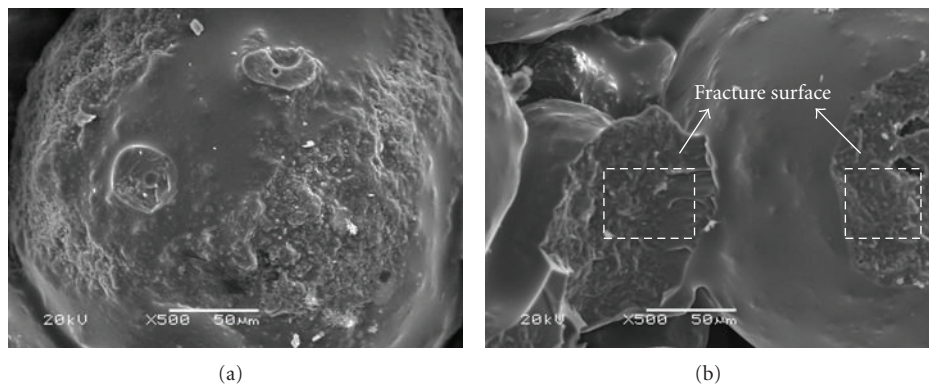


FIGURE 5: SEM morphologies of particle surfaces in mold samples prepared by (a) conventional process and (b) process I with TEOS as the  $\text{SiO}_2$  precursor after the heat treatment.

The glass phase of sodium silicate ( $\text{Na}_2\text{O}\cdot\text{SiO}_2$ ) is produced by the reaction between sodium hydroxide and silica at a temperature of about  $1000^\circ\text{C}$  [11], which can give a certain strength to the mold. Therefore, the inorganic precursors should be homogeneously coated on the surfaces of starting particles and the conversion efficiency of the precursors coated on the substrate (starting particles) should be increased to improve the fracture strength.

Typical cross-sectional morphologies of particles in mold samples prepared by the dual dipping process used TEOS as

the  $\text{SiO}_2$  precursor before the heat treatment are presented in Figure 2. The NaOH generated by the hydrolysis reaction of NaOMe has a particle layer with a polygonal shape, while the  $\text{SiO}_2$  by the sol-gel reaction of TEOS shows a layer with a continuous solid state on the surface of particle. The layer with a mixture of  $\text{SiO}_2$  and NaOH phases observed in the SEM image of the particle surface prepared through process I (Figure 2(a)) is due to the permeation of  $\text{SiO}_2$  precursor between the generated NaOH particles. However, in the case of Figure 2(b), two layers with  $\text{SiO}_2$  and NaOH

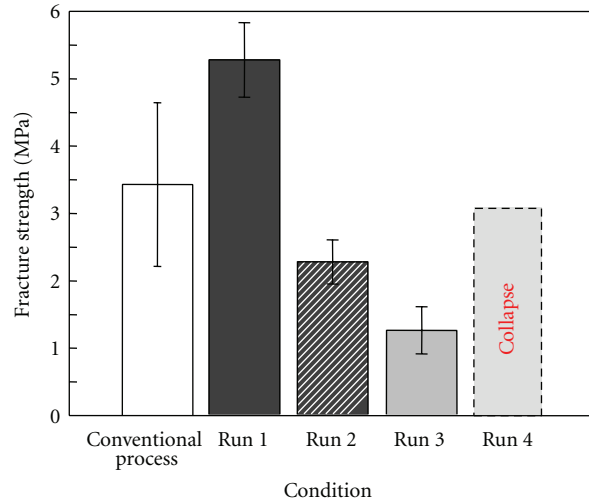


FIGURE 6: Fracture strength of mold samples after the heat treatment as functions of process and SiO<sub>2</sub> precursor.



FIGURE 7: Photographs of real mold through process I with TEOS as the SiO<sub>2</sub> precursor after the heat treatment at 950°C and fabricated product: (a) real mold and (b) casted product.

phases are independently formed on the surface of particle. This is because the continuous glass phase of SiO<sub>2</sub> restricts the infiltration of Na<sub>2</sub>O precursor. Therefore, the layer formed by process I shows thinner thickness than that by process II. In process I, the mixture phases of SiO<sub>2</sub> and NaOH are converted into the glass phase of Na<sub>2</sub>O·SiO<sub>2</sub> prior to the evaporation of Na ion decomposed from NaOH during the heat treatment, whereas in process II, NaOH existed at the outside of the layer is easily degraded and partially evaporated in the heat treatment. Therefore, the layer prepared by process I would be mainly composed of Na<sub>2</sub>O·SiO<sub>2</sub>, while in process II the layer would have the mixture composition of Na<sub>2</sub>O·SiO<sub>2</sub> and SiO<sub>2</sub>. In addition, the inorganic precursors in process II have the lower

conversion efficiency into the glass phase than those in process I owing to the easy evaporation of Na ion used to decrease the formation temperature of glass phase. It could be expected that the mold prepared through process I has a higher fracture strength than that prepared by process II.

The morphologies on the fracture surfaces of mold samples prepared through process I as a function of SiO<sub>2</sub> precursor are shown in Figure 3. The surfaces of particles coated with the precursors are changed from rough to smooth during the heat treatment, caused by the generation of glass phase. In the case of PDMS used as the SiO<sub>2</sub> precursor (Figure 3(b)), the glass phase is not fully developed at the interface and/or on the surface of particles. PDMS without the sol-gel reaction remains as a liquid phase and

is easily evaporated during the heat treatment. However, TEOS is already converted into solid-phase silica before the heat treatment. Therefore, the fracture strength of samples prepared with PDMS could be significantly decreased, compared with that with TEOS. Typical SEM morphologies on the fracture surfaces of mold samples prepared by process II before and after the heat treatment are shown in Figure 4 as a function of SiO<sub>2</sub> precursor. In process II, cracks are formed at the interface between particles and on the surface of particles before the heat treatment, denoted by the dotted arrow, whereas these cracks are not observed in process I (Figure 3). This is because the evaporation of alcohol used as the solvent of NaOMe. In process I, the evaporation of Na ion is disturbed by the layer of SiO<sub>2</sub> precursor, whereas Na ion can be freely evaporated in process II, as pointed out in Figure 2. It is verified that the Na strongly affects the generation of glass phase, causing the higher strength in the mold prepared by process I than process II. In addition, in Figure 4(b-2), the glass phase is not presented at the interface and on the surface after the heat treatment, arising from the nonformation of glass phase owing to the easy evaporation of Na ion and PDMS existed as liquid phase during the heat treatment. Figure 5 is the SEM images of particle surfaces in the mold samples prepared by the conventional process and process I using TEOS as the SiO<sub>2</sub> precursor. In Figure 5(b), the glass phase is homogeneous and uniform formed on the surface of particle. However, in Figure 5(a), the glass phase is locally and partially seen on the surface of particle.

The fracture strength of mold samples with the different processes and SiO<sub>2</sub> precursors was measured at room temperature, and the results are shown in Figure 6. In general, the fracture strengths of mold samples prepared by process I (Runs 1 and 2) represent higher values than that by process II (Runs 3) due to the high reactivity between precursors, already mentioned at the results of SEM morphology. The mold treated by PDMS without the sol-gel reaction, especially in process II, absolutely collapsed owing to the deterioration in the formation of glass phase by the evaporation of Na ion and PDMS. In addition, the fracture strength through Run 1 is significantly enhanced, compared with the conventional binder process, caused by the enhancement of conversion efficiency and by the homogeneous formation of glass phase through the dual dipping process. It indicates that the mold for thin casting with reasonable mechanical properties could be fabricated by the new dual dipping process using inorganic binder precursors, inducing the reduction of product price. In addition, the dipping sequence in the dual dipping process is an essential point for increasing the efficiency and homogeneity of glassification and the fracture strength in the mold. Figure 7 shows a photograph of the real mold prepared through process I with TEOS as the SiO<sub>2</sub> precursor after the heat treatment at 950°C for and the product fabricated by thin casting. The real mold prepared by the dual dipping process is perfectly produced and the casted product shows clean surface without defects such as dross, nonmetallic inclusions, and crack. Consequently, the new dual dipping process can be applied for preparing the mold for thin casting having high thermomechanical properties.

## 4. Conclusions

A new dual dipping process has been developed for the homogeneous formation of the glass phase on the surface of particles and at the interface between particles in the mold and to increase the reactivity between precursors, leading to the enhancement in the fracture strength of the mold. The glass phase is well and uniformly formed both at the interface and on the surface of particles in the mold prepared by process I, compared with that by process II. This is because the evaporation of Na ion generated by decomposition of NaOH is interrupted by the layers of SiO<sub>2</sub> precursor in process I, while Na ion existed at the outside of particle surface is easily and partially evaporated in process II. In addition, when PDMS is used as the SiO<sub>2</sub> precursor, the glass phase is partially or not absolutely formed in the mold, because PDMS existed as liquid phase without the sol-gel reaction after the dry process is deformed before the generation of glass phase during the heat treatment.

## Acknowledgments

This work was supported by the National Research Foundation of Korea (NRF) Grant funded by the Korean government (MEST) (2011-0030797/2012-0009450), by the Korea Institute of Materials Science (KIMS) in 2012, and by the Changwon National University in 2011.

## References

- [1] Y. Meng and B. G. Thomas, "Modeling transient slag-layer phenomena in the shell/mold gap in continuous casting of steel," *Metallurgical and Materials Transactions B*, vol. 34, no. 5, pp. 707–725, 2003.
- [2] M. Şimşir, L. C. Kumruoğlu, and A. Özer, "An investigation into stainless-steel/structural-alloy-steel bimetal produced by shell mould casting," *Materials and Design*, vol. 30, no. 2, pp. 264–270, 2009.
- [3] M. Barsoum, *Fundamentals of Ceramics*, McGraw-Hill, Seoul, Republic of Korea, 1997.
- [4] W. D. Callister, *Materials Science and Engineering: An Introduction*, John Wiley & Sons, New York, NY, USA, 1997.
- [5] S. Ege, *Organic Chemistry*, D. C. Heath and Company, Toronto, Canada, 1994.
- [6] N. Sasaki, *Foundry Management & Technology* February, 2009.
- [7] B. M. Michael, *Organic Chemistry*, McGraw-Hill, New York, NY, USA, 1994.
- [8] E. H. Kim, J. H. Lee, Y. G. Jung, C. S. Lee, and U. Paik, "A new in situ process in precision casting for mold fabrication," *Journal of the European Ceramic Society*, vol. 31, no. 9, pp. 1581–1588, 2011.
- [9] E. H. Kim, W. R. Lee, Y. G. Jung, and C. S. Lee, "A new binder system for preparing high strength inorganic molds in precision casting," *Materials Chemistry and Physics*, vol. 126, no. 1-2, pp. 344–351, 2011.
- [10] F. M. Herman, M. B. Norbert, G. O. Charles, and M. Georg, *Encyclopedia of Polymer Science and Engineering*, John Wiley & Sons, New York, NY, USA, 1989.
- [11] P. G. Shewmon, *Diffusion in Solids*, McGraw-Hill, New York, NY, USA, 1963.

## Research Article

# GaN Schottky Diode with TiW Electrodes on Silicon Substrate Based on AlN/AlGaN Buffer Layer

**Sheng-Po Chang**

*Institute of Microelectronics & Department of Electrical Engineering, Center for Micro/Nano Science and Technology, Advanced Optoelectronic Technology Center, National Cheng Kung University, Tainan 70101, Taiwan*

Correspondence should be addressed to Sheng-Po Chang, changsp@mail.ncku.edu.tw

Received 30 May 2012; Revised 12 November 2012; Accepted 26 November 2012

Academic Editor: Yong Yang

Copyright © 2012 Sheng-Po Chang. This is an open access article distributed under the Creative Commons Attribution License, which permits unrestricted use, distribution, and reproduction in any medium, provided the original work is properly cited.

We report the fabrication of GaN Schottky photodiodes (PDs) on Si(111) substrates coated with an AlN/AlGaN buffer multilayer. It was found that their dark current was much smaller than that of identical devices prepared on sapphire substrates. With an incident wavelength of 359 nm, the maximum responsivity of the  $n^-$ -GaN Schottky photodetectors with TiW contact electrodes was 0.1544 A/W, corresponding to a quantum efficiency of 53.4%. For a given bandwidth of 1 kHz and bias of 5 V, the resultant noise equivalent power (NEP) of  $n^-$ -GaN Schottky photodetectors with TiW electrodes was  $1.033 \times 10^{-12}$  W, corresponding to a detectivity ( $D^*$ ) of  $1.079 \times 10^{12}$  cm-Hz<sup>0.5</sup> W<sup>-1</sup>.

## 1. Introduction

There are numerous applications demanding the usage of ultraviolet (UV) photodetectors (PDs). Both civil and military disciplines require high-performance UV PDs for solar UV monitoring, source calibration, UV astronomy, flame sensors, detection of missile plumes, space-to-space communications, and many other applications. GaN has a wide direct band gap ( $E_g = 3.4$  eV) and a high saturation velocity ( $v_s = 2.7 \times 10^7$  cm/s) and is therefore widely considered to be one of the most promising materials for realizing UV PDs [1–13]. Moreover, this material is also remarkably tolerant of aggressive environments because of its thermal stability and radiation hardness.

Traditionally, GaN-based epitaxial layers are grown on sapphire or SiC substrates. Sapphire substrates are electrically insulating and poor thermal conductors. On the other hand, although SiC substrates are comparably good thermal and electrical conductors, their high cost precludes wide use. Compared with sapphire and SiC substrates, GaN epitaxial layers on Si appear to be a reasonably good substitute, not to mention the fact that the use of Si substrates also has the unique advantage of allowing

monolithic integration of GaN-based devices with Si-based microelectronics.

Even though it is rather difficult to grow high-quality GaN epitaxial layers on Si, GaN-based light-emitting diodes (LEDs) and heterostructure field-effect transistors have nevertheless already been realized on Si substrates [14–19]. Our earlier report successfully documented the growth of high-quality InGaN/GaN LED epilayers on a Si(111) substrate [20]. Growth of high-quality InGaN/GaN films on a silicon substrate was possible owing to prior deposition of an AlGaN buffer and two high-temperature (HT) AlN interlayers before attempting GaN growth. This particular growth scheme effectively confined the threading dislocation to the vicinity of the interfacial layer in the AlGaN/HT-AlN buffer layers. In fact, our transmission electron microscopy (TEM) and scanning electron microscopy (SEM) studies carried out earlier had clearly demonstrated a smooth and crack-free GaN surface with a noticeable reduction in threading dislocation density [20].

In this paper, the deposition of titanium tungsten (TiW) metal contacts on GaN surfaces via RF magnetron sputtering is described. The growth of  $n^-$ -GaN epitaxial layers on Si substrates and the subsequent fabrication of GaN

Schottky photodiodes are discussed thereafter, along with their resultant optical and electrical properties.

## 2. Experimental

Epitaxial samples investigated in our study were all grown on Si(111) substrates using metalorganic chemical vapor deposition (MOCVD) [21–24]. Trimethylgallium (TMGa), trimethylaluminum (TMAI), and ammonia ( $\text{NH}_3$ ) were used as source materials for gallium (Ga), aluminum (Al), and nitrogen (N), respectively. To obtain a lightly Si-doped n-type GaN ( $n^-$ -GaN) structure, a 25-nm-thick AlN buffer layer was deposited on a Si(111) substrate at  $1090^\circ\text{C}$ . Then, two stacks of buffer multilayers were inserted between the 25-nm-thick AlN buffer layer and the topmost 500-nm-thick  $1090^\circ\text{C}$ -grown  $n^-$ -GaN epitaxial layer. Each stack of buffer multilayers consisted of a 30-nm-thick  $540^\circ\text{C}$ -grown AlN layer, a 50-nm-thick  $1090^\circ\text{C}$ -grown AlN layer, a 60-nm-thick  $1090^\circ\text{C}$ -grown  $\text{Al}_{0.3}\text{Ga}_{0.7}\text{N}$  layer, a 40-nm-thick  $1090^\circ\text{C}$ -grown  $\text{Al}_{0.2}\text{Ga}_{0.8}\text{N}$  layer, and a 100-nm-thick  $1090^\circ\text{C}$ -grown undoped-GaN layer.

TiW (100 nm) contact layers were then deposited on the samples using an RF magnetron sputter system. Because the Si(111) substrate was heavily doped, the devices were bonded on TO-Can with Ag rubber for ohmic contact. Then,  $n^-$ -GaN Schottky diodes were fabricated by standard photolithography and a lift-off process. The active area of photodetectors was  $1.26 \times 10^{-3} \text{ cm}^2$ . An HP-4156 semiconductor parameter analyzer was then used to evaluate the dark current-voltage ( $I$ - $V$ ) characteristics. Spectral responsivity measurements were also performed using a JOBIN-YVON SPEX system equipped with a 450-W xenon arc lamp and a standard synchronous detection scheme. Furthermore, the noise characteristics of the GaN Schottky diodes were measured within a frequency range of 1 Hz–1 kHz using a low-noise current preamplifier and a dynamic signal analyzer.

## 3. Results and Discussion

Figure 1 shows the (002) Bragg reflection double-crystal X-ray diffraction (DCXRD) spectra for a 500 nm  $n^-$ -GaN epitaxial layer prepared on a Si substrate. The full width at half maximum (FWHM) of the  $n^-$ -GaN epitaxial layer was measured as  $232.11''$ . Figure 2 shows the  $I$ - $V$  characteristics of a Schottky diode with a TiW contact electrode. Under a 5-V applied bias, the measured dark current of photodetectors with TiW electrodes was  $7.72 \times 10^{-12} \text{ A}$ . It should be noted that a relatively small dark leakage current could still be observed even though these III-nitrides layers were grown on a lattice-mismatched silicon substrate. The small dark current was in fact a clear benefit derived from the insertion of two additional stacks of buffer multilayers into the overall device structure. Evidently, by further improving the crystalline quality of GaN films, this scheme alleviated the impact of GaN-Si lattice mismatch imposed on the epitaxial growth [25]. Furthermore, the much smaller dark current in the vertical PDs was most likely due to the high resistivity

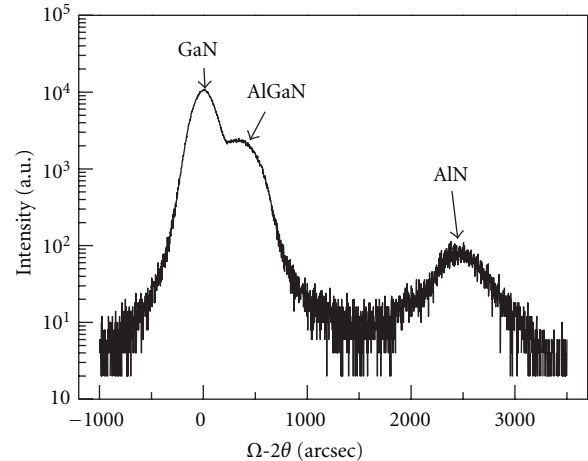


FIGURE 1: The DC-XRD analysis of  $n^-$ -GaN epitaxial structure.

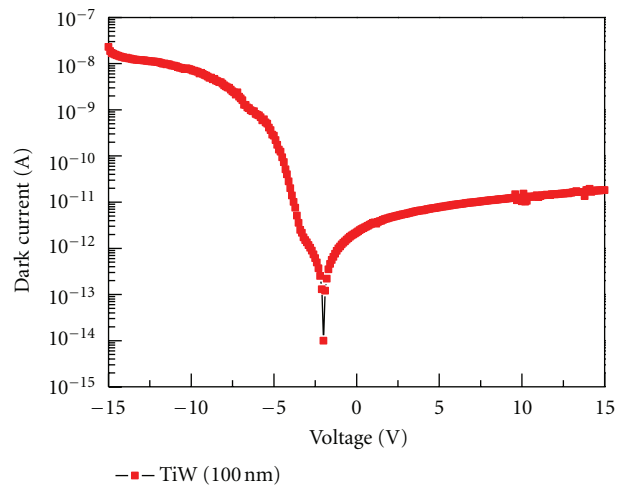


FIGURE 2: Dark  $I$ - $V$  characteristics of the Schottky diode with TiW contact electrodes.

of the HT-AlN layers used. Consequently, a larger Schottky barrier height between the contact electrode and the epitaxial film was realized.

Figure 3 shows the room temperature spectral responses of PDs under various applied bias voltages. In order to quantify the peak responsivity, the xenon lamp intensity was first measured by a calibrated GaP UV detector. The difference in sensor-detecting areas between the GaP UV detector and our PDs was then determined in order to reliably estimate the PD responsivity.

As shown in Figure 4, the peak responsivity occurred at 359 nm. The maximum responsivity of photodetectors with TiW contact electrodes was  $0.1544 \text{ A/W}$ , corresponding to a quantum efficiency of 53.4%. Compared with III-nitride PDs grown on a sapphire substrate [25, 26], the smaller peak responsivity observed from samples grown on Si substrates can be directly attributed to a highly defective epitaxial layer. Similar results were also reported by Osinsky et al. [27]. In our case, the responsivity is highly dependent on

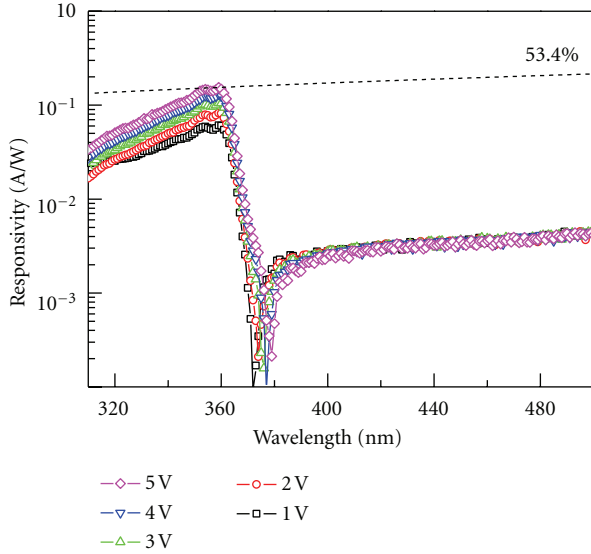


FIGURE 3: Spectral responses of the fabricated detectors with various applied bias.

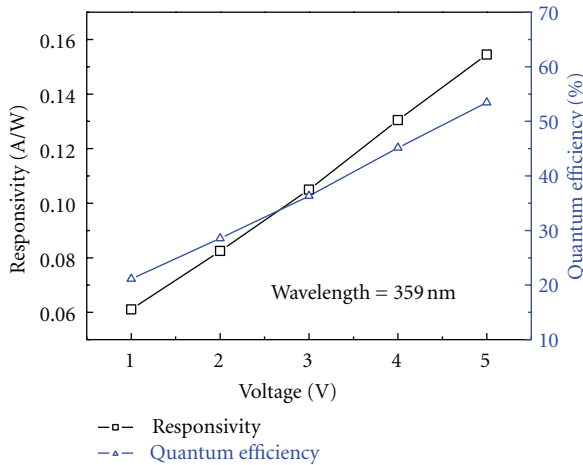


FIGURE 4: Spectral responses and quantum efficiency of photodetectors as functions of applied bias.

the transmittance of the contact electrode, so the higher transmittance of TiW contributes in part to the larger responsivity obtained [25]. In addition, the rejection ratio was determined as the ratio between the spectral responsivity measured at 359 nm and at 385 nm. With an applied voltage of 5 V, the rejection ratio was 114.4 for photodetectors with TiW contact electrodes. The large rejection ratio can be attributed in part to a high light transparency of TiW electrodes. Figure 4 depicts the peak responsivity (359 nm) and quantum efficiency of PDs on Si as a function of bias.

Similar results were also found for AlGaIn metal-semiconductor-metal PDs prepared on an Si substrate [28]. The higher voltage enhances the penetration of electron-hole pairs through the grain boundary so as to effectively facilitate the collection by electrodes of these charge carriers.

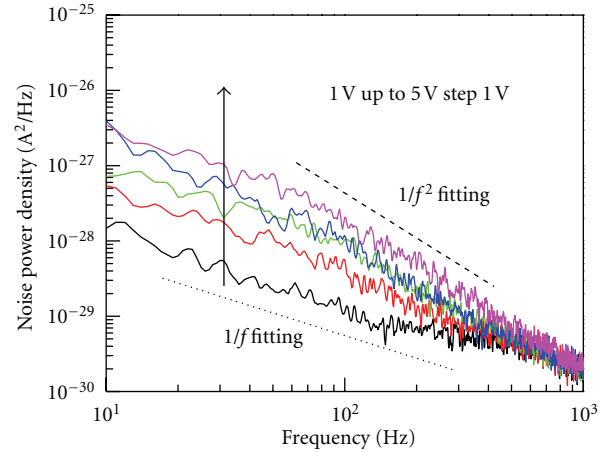


FIGURE 5: Measured noise power densities of the GaN Schottky diode with TiW contact electrodes.

The observation of bias-dependent responsivity of PDs-on-Si was also reported by Osinsky et al. [27].

Figure 5 shows the measured noise power density of the GaN Schottky photodetectors with TiW contact electrodes. Noise curves reveal that  $1/f$  (flicker) is a dominant noise mechanism, which is expected for Schottky photodetectors operating at low frequency. Moreover, the noise curves obey the relation of Hooge-type equation with a fitting parameter  $\alpha$ . It should be noted that the measured low-frequency noise was classified as a  $1/f$ -type ( $\alpha = 1$ ) noise for low bias and a  $1/f^2$ -type ( $\alpha = 2$ ) noise for high bias. For a specified bandwidth ( $B$ ), the total square of noise current,  $\langle i_n \rangle^2$ , can be determined by integrating the noise power density  $S_n(f)$  such that

$$\langle i_n \rangle^2 = \int S_n(f) df. \quad (1)$$

On the other hand, the noise equivalent power (NEP) can be calculated by

$$\text{NEP} = \sqrt{\frac{\langle i_n \rangle^2}{R}}, \quad (2)$$

where  $R$  is the responsivity of the PDs. Furthermore, the normalized detectivity ( $D^*$ ) can be determined by

$$D^* = \frac{\sqrt{A} \sqrt{B}}{\text{NEP}}, \quad (3)$$

where  $A$  is the area of the photodetector and  $B$  is the bandwidth. For a given bandwidth of 1 kHz and a given bias of 5 V, the corresponding noise equivalent power of Schottky photodetectors with TiW electrodes was  $1.033 \times 10^{-12}$  W. These values in turn led to the calculated detectivity ( $D^*$ ) of  $1.079 \times 10^{12}$  cm-Hz<sup>0.5</sup>W<sup>-1</sup>. A smaller current density was responsible for the smaller NEP observed for Schottky photodetectors on Si. It should be noted that on an average, higher  $D^*$  was obtained compared with that of devices with similar interdigitated electrode dimensions fabricated on sapphire substrates [25, 29]. These results were again

attributed to the smaller noise power density of the PDs prepared on Si(111) substrates. The benchmark values realized for the noise and detectivity of our devices fabricated on silicon show that these Schottky photodetectors are well suited for low-noise applications.

#### 4. Summary

In summary, GaN Schottky photodiodes were prepared on Si(111) substrates with an AlN/AlGa<sub>N</sub> buffer multilayer. It was found that the dark current of PDs fabricated on Si substrates was substantially smaller than that of identical devices prepared on sapphire substrates. With an incident wavelength of 359 nm, the maximum responsivity of the n<sup>-</sup>-GaN Schottky photodetectors with TiW contact electrodes was 0.1544 A/W, corresponding to a quantum efficiency of 53.4%. For a given bandwidth of 1 kHz and a given bias of 5 V, the corresponding noise equivalent power (NEP) of n<sup>-</sup>-GaN Schottky photodetectors with TiW electrodes was  $1.033 \times 10^{-12}$  W. Finally, the detectivity ( $D^*$ ) was determined, therefore, to be  $1.079 \times 10^{12}$  cm-Hz<sup>0.5</sup>W<sup>-1</sup>.

#### Acknowledgments

The authors would like to thank the National Science Council and Bureau of Energy, Ministry of Economic Affairs of Taiwan, Taiwan, for the financial support under Contracts no. 100-2221-E-006-18 and 101-D0204-6, and the LED Lighting Research Center of NCKU for the assistance of device characterization. This work was also supported in part by the Center for Frontier Materials and Micro/Nano Science and Technology, the National Cheng Kung University, Taiwan, as well as the Advanced Optoelectronic Technology Center, the National Cheng Kung University, under projects from the Ministry of Education.

#### References

- [1] Y. Z. Chiou, Y. K. Su, S. J. Chang et al., "High detectivity InGa<sub>N</sub>-Ga<sub>N</sub> multi-quantum well p-n junction photodiodes," *IEEE Journal of Quantum Electronics*, vol. 39, no. 5, pp. 681–685, 2003.
- [2] E. Monroy, E. Muñoz, F. J. Sánchez et al., "High-performance GaN p-n junction photodetectors for solar ultraviolet applications," *Semiconductor Science and Technology*, vol. 13, no. 9, p. 1042, 1998.
- [3] G. Y. Xu, A. Salvador, W. Kim et al., "High speed, low noise ultraviolet photodetectors based on GaN p-i-n and AlGa<sub>N</sub>(p)-Ga<sub>N</sub>(i)-Ga<sub>N</sub>(n) structures," *Applied Physics Letters*, vol. 71, no. 15, p. 2154, 1997.
- [4] M. Mosca, J. L. Reverchon, N. Grandjean, and J. Y. Duboz, "Multilayer (Al,Ga)<sub>N</sub> structures for solar-blind detection," *IEEE Journal on Selected Topics in Quantum Electronics*, vol. 10, no. 4, pp. 752–758, 2004.
- [5] N. Biyikli, I. Kimukin, O. Aytur, and E. Ozbay, "Solar-blind AlGa<sub>N</sub>-based p-i-n photodiodes with low dark current and high detectivity," *IEEE Photonics Technology Letters*, vol. 16, no. 7, pp. 1718–1720, 2004.
- [6] N. Biyikli, I. Kimukin, T. Tut, T. Kartaloglu, O. Aytur, and E. Ozbay, "High-speed characterization of solar-blind Al<sub>x</sub>Ga<sub>1-x</sub>N p-i-n photodiodes," *Semiconductor Science and Technology*, vol. 19, no. 11, pp. 1259–1262, 2004.
- [7] G. Parish, S. Keller, P. Kozodoy et al., "High-performance (Al,Ga)<sub>N</sub>-based solar-blind ultraviolet p-i-n detectors on laterally epitaxially overgrown GaN," *Applied Physics Letters*, vol. 75, no. 2, pp. 247–249, 1999.
- [8] A. Osinsky, S. Gangopadhyay, R. Gaska et al., "Low noise p-n GaN ultraviolet photodetectors," *Applied Physics Letters*, vol. 71, no. 16, pp. 2334–2336, 1997.
- [9] V. Adivarahan, G. Simin, J. W. Yang et al., "SiO<sub>2</sub> lateral-geometry GaN transparent Schottky-barrier detectors," *Applied Physics Letters*, vol. 77, no. 6, pp. 863–865, 2000.
- [10] S. J. Chang, M. L. Lee, J. K. Sheu et al., "GaN metal-semiconductor-metal photodetectors with low-temperature-GaN cap layers and ITO metal contacts," *IEEE Electron Device Letters*, vol. 24, no. 4, pp. 212–214, 2003.
- [11] O. Katz, V. Garber, B. Meyler, G. Bahir, and J. Salzman, "Gain mechanism in GaN Schottky ultraviolet detectors," *Applied Physics Letters*, vol. 79, no. 10, pp. 1417–1419, 2001.
- [12] E. Monroy, T. Palacios, O. Hainaut, F. Omnès, F. Calle, and J. F. Hochedez, "Assessment of GaN metal-semiconductor-metal photodiodes for high-energy ultraviolet photodetection," *Applied Physics Letters*, vol. 80, no. 17, p. 3198, 2002.
- [13] J. L. Pau, C. Rivera, E. Muñoz et al., "Response of ultra-low dislocation density GaN photodetectors in the near- and vacuum-ultraviolet," *Journal of Applied Physics*, vol. 95, no. 12, p. 8275, 2004.
- [14] C. F. Shih, N. C. Chen, C. A. Chang, and K. S. Liu, "Blue, Green and White InGa<sub>N</sub> Light-Emitting Diodes Grown on Si," *Japanese Journal of Applied Physics*, vol. 44, pp. L140–L143, 2005.
- [15] H. Ishikawa, K. Asano, B. Zhang, T. Egawa, and T. Jimbo, "Improved characteristics of GaN-based light-emitting diodes by distributed Bragg reflector grown on Si," *Physica Status Solidi*, vol. 201, no. 12, pp. 2653–2657, 2004.
- [16] S. Iwakami, M. Yanagihara, O. Machida et al., "AlGa<sub>N</sub>/Ga<sub>N</sub> heterostructure field-effect transistors (HFETs) on Si substrates for large-current operation," *Japanese Journal of Applied Physics*, vol. 43, pp. L831–L833, 2004.
- [17] A. Curutchet, N. Malbert, N. Labat et al., "Low frequency drain noise comparison of AlGa<sub>N</sub>/Ga<sub>N</sub> HEMT's grown on silicon, SiC and sapphire substrates," *Microelectronics Reliability*, vol. 43, no. 9–11, pp. 1713–1718, 2003.
- [18] P. Javorka, A. Alam, M. Marso et al., "Material and device issues of AlGa<sub>N</sub>/Ga<sub>N</sub> HEMTs on silicon substrates," *Microelectronics Journal*, vol. 34, no. 5–8, pp. 435–437, 2003.
- [19] V. Hoël, Y. Guhel, B. Boudart et al., "Static measurements of GaN MESFETs on (111) Si substrates," *Electronics Letters*, vol. 37, no. 17, pp. 1095–1096, 2001.
- [20] Y. P. Hsu, S. J. Chang, W. S. Chen, J. K. Sheu, J. Y. Chu, and C. T. Kuo, "Crack-free high-brightness InGa<sub>N</sub>/Ga<sub>N</sub> LEDs on Si(111) with initial AlGa<sub>N</sub> buffer and two LT-Al interlayers," *Journal of the Electrochemical Society*, vol. 154, no. 3, pp. H191–H193, 2007.
- [21] S. J. Chang, W. C. Lai, Y. K. Su, J. F. Chen, C. H. Liu, and U. H. Liaw, "InGa<sub>N</sub>-Ga<sub>N</sub> multi-quantum-well blue and green light-emitting diodes," *IEEE Journal of Selected Topics in Quantum Electronics*, vol. 8, no. 2, pp. 278–283, 2002.
- [22] S. J. Chang, C. S. Chang, Y. K. Su et al., "Highly reliable nitride-based LEDs with SPS+ITO upper contacts," *IEEE Journal of Quantum Electronics*, vol. 39, no. 11, pp. 1439–1443, 2003.
- [23] S. J. Chang, C. H. Kuo, Y. K. Su et al., "400-nm InGa<sub>N</sub>-Ga<sub>N</sub> and InGa<sub>N</sub>-AlGa<sub>N</sub> multi-quantum well light-emitting diodes,"

- IEEE Journal on Selected Topics in Quantum Electronics*, vol. 8, no. 4, pp. 744–748, 2002.
- [24] S. J. Chang, C. S. Chang, Y. K. Su et al., “Nitride-based flip-chip ITO LEDs,” *IEEE Transactions on Advanced Packaging*, vol. 28, no. 2, pp. 273–277, 2005.
- [25] C. K. Wang, S. J. Chang, Y. K. Su et al., “GaN MSM UV photodetectors with titanium tungsten transparent electrodes,” *IEEE Trans. Electron Dev*, vol. 53, no. 1, pp. 38–42, 2006.
- [26] Y. Z. Chiou, “Nitride-based p-i-n bandpass photodetectors,” *IEEE Electron Device Letters*, vol. 26, no. 3, pp. 172–174, 2005.
- [27] A. Osinsky, S. Gangopadhyay, J. W. Yang, and R. Gaska, “Visible-blind GaN Schottky barrier detectors grown on Si(111),” *Applied Physics Letters*, vol. 72, no. 5, p. 551, 1998.
- [28] Y. Z. Chiou, Y. C. Lin, and C. K. Wang, “AlGaIn photodetectors prepared on Si substrates,” *IEEE Electron Device Letters*, vol. 28, no. 4, pp. 264–266, 2007.
- [29] Y. K. Su, P. C. Chang, C. H. Chen et al., “Nitride-based MSM UV photodetectors with photo-chemical annealing Schottky contacts,” *Solid-State Electron*, vol. 49, no. 3, pp. 459–463, 2005.

## Research Article

# Polyol-Free Synthesis of Uniformly Dispersed Pt/Graphene Oxide Electrocatalyst by Sulfuric Acid Treatment

Tae Kyu Lee, Hyang Jin Park, Min Ki Kwon, Ju Hae Jung, Junbom Kim, and Seung Hyun Hur

School of Chemical Engineering, University of Ulsan, Daehak-ro 102, Nam-gu, Ulsan 680-749, Republic of Korea

Correspondence should be addressed to Seung Hyun Hur, shhur@ulsan.ac.kr

Received 25 September 2012; Revised 26 November 2012; Accepted 10 December 2012

Academic Editor: Yongsheng Li

Copyright © 2012 Tae Kyu Lee et al. This is an open access article distributed under the Creative Commons Attribution License, which permits unrestricted use, distribution, and reproduction in any medium, provided the original work is properly cited.

Polyol-free synthesis of highly loaded Pt catalysts on sulfuric-acid-treated graphene oxide (SGO) was reported. Sulfuric acid treatment increased the surface hydroxyl groups on graphene oxide (GO), which contributed to the reduction of Pt precursors in the absence of external reducing agent. By adjusting pH during the Pt reduction, we can get uniformly dispersed 2.5 nm size Pt nanoparticles on GO surface even at 50 wt% Pt loading amount. Cyclic voltammetry showed that increased pH resulted in increased electrochemical surface area.

## 1. Introduction

Polymer electrolyte membrane fuel cell (PEMFC) is regarded as one of the best candidates for the future energy sources as it can generate the electricity in a carbon-free way through the carbon dioxide free electrochemical reaction. Generally, only hydrogen and oxygen (or air) are used as the fuel gas and the oxidant gas, respectively. Moreover, the product generated during this reaction is only pure water, which will not cause any harms to the environment and also can be used as the essential ingredient for human and nature [1]. Nevertheless, its high cost impedes the commercialization. To reduce materials cost by improving the catalyst performance, robust catalytic supporting materials must be developed to achieve high dispersion, utilization, activity, and stability [2]. Recently, the majority of the catalyst support research has focused on the use of graphitic materials such as carbon nanotube and graphene [3–5].

Graphene is extensively studied due to its excellent properties such as a large theoretical specific surface area, high intrinsic mobility, high Young's modulus and thermal conductivity, and its optical transmittance and good electrical conductivity [6–9]. There are several pathways to fabricate graphene nanosheets including chemical vapor deposition, mechanical exfoliation, and chemical exfoliation; among them chemical exfoliation is regarded as the most suitable one for fuel cell application due to its versatility

of their surface modifications, unique defect behaviors, functional groups, and advantages associated with low cost and easy scale up [10].

The Pt catalyst for PEMFC can be prepared by impregnation, polyol, and colloidal method [11, 12]. Generally, wet impregnation followed by reduction by gaseous hydrogen atmosphere at high temperatures or the chemical reduction of the metal precursors using reducing agents can be used but achieving small particle size and uniform size distribution of Pt in this ways is very difficult especially at high Pt loading amount. Instead, the colloidal method using diverse stabilizing agents that prevent the Pt agglomeration can be used alternatively but the residual organic materials can deteriorate the fuel cell properties. Recently, polyol process is preferred due to its several advantages but it still needs chemicals such as ethylene glycol as reducing agent [13]. In this paper, we report a facile polyol-free synthesis of graphene oxide (GO) supported Pt catalyst at high loading condition. By modifying GO surface with sulfuric acid and controlling pH of catalyst loading process, we can successfully get as small as 2.5 nm Pt size even at very high Pt loading amount (45 wt%). We also used X-ray photoelectron spectroscopy (XPS, Thermo Fisher), X-ray diffraction (XRD, Rigaku) and Transmission electron microscope (TEM, JEOL) to verify the chemical and physical structures of fabricated catalysts and cyclic voltammetry (CV) to see the Pt size effect on the electrochemical activity.

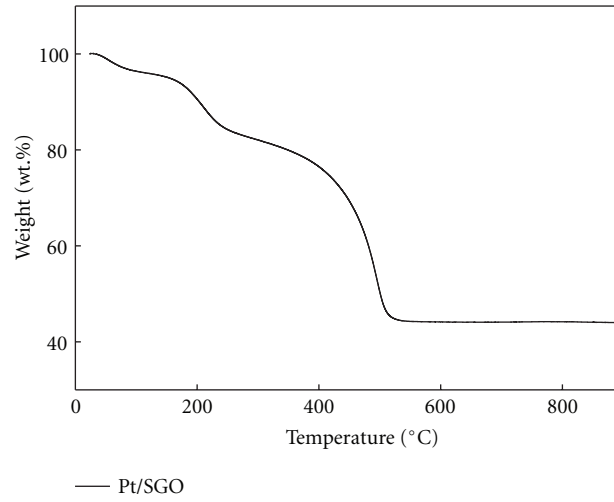


FIGURE 1: TGA curves of Pt/SGO catalyst.

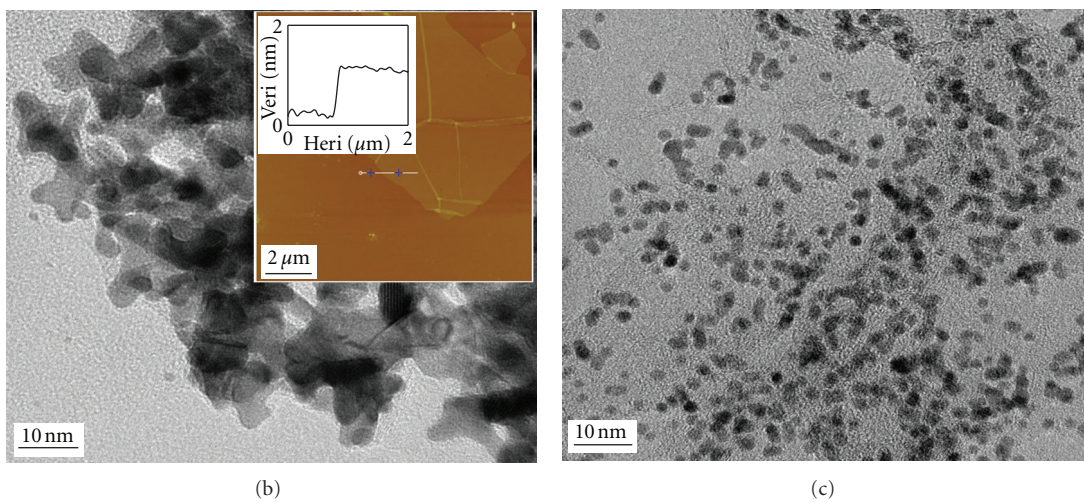
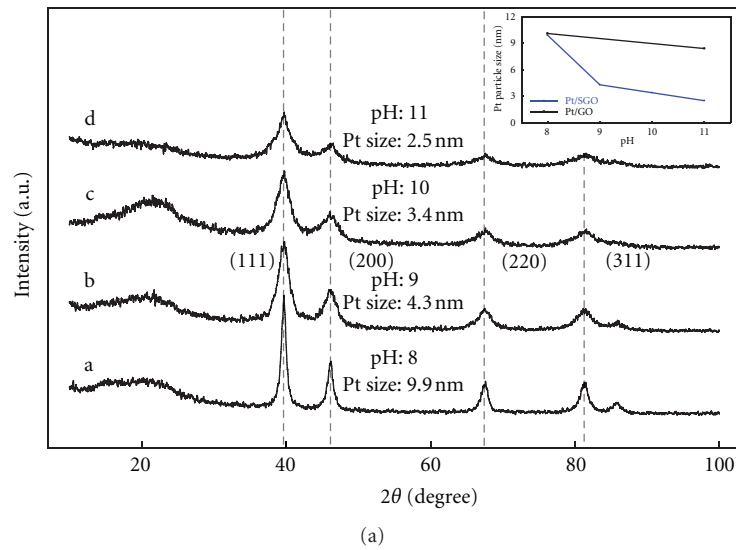


FIGURE 2: (a) XRD patterns of Pt/SGOs fabricated at different pH. TEM images of Pt/SGOs fabricated (b) at pH 8 and (c) at pH 11, respectively. The inset of (b) is AFM image of GO.

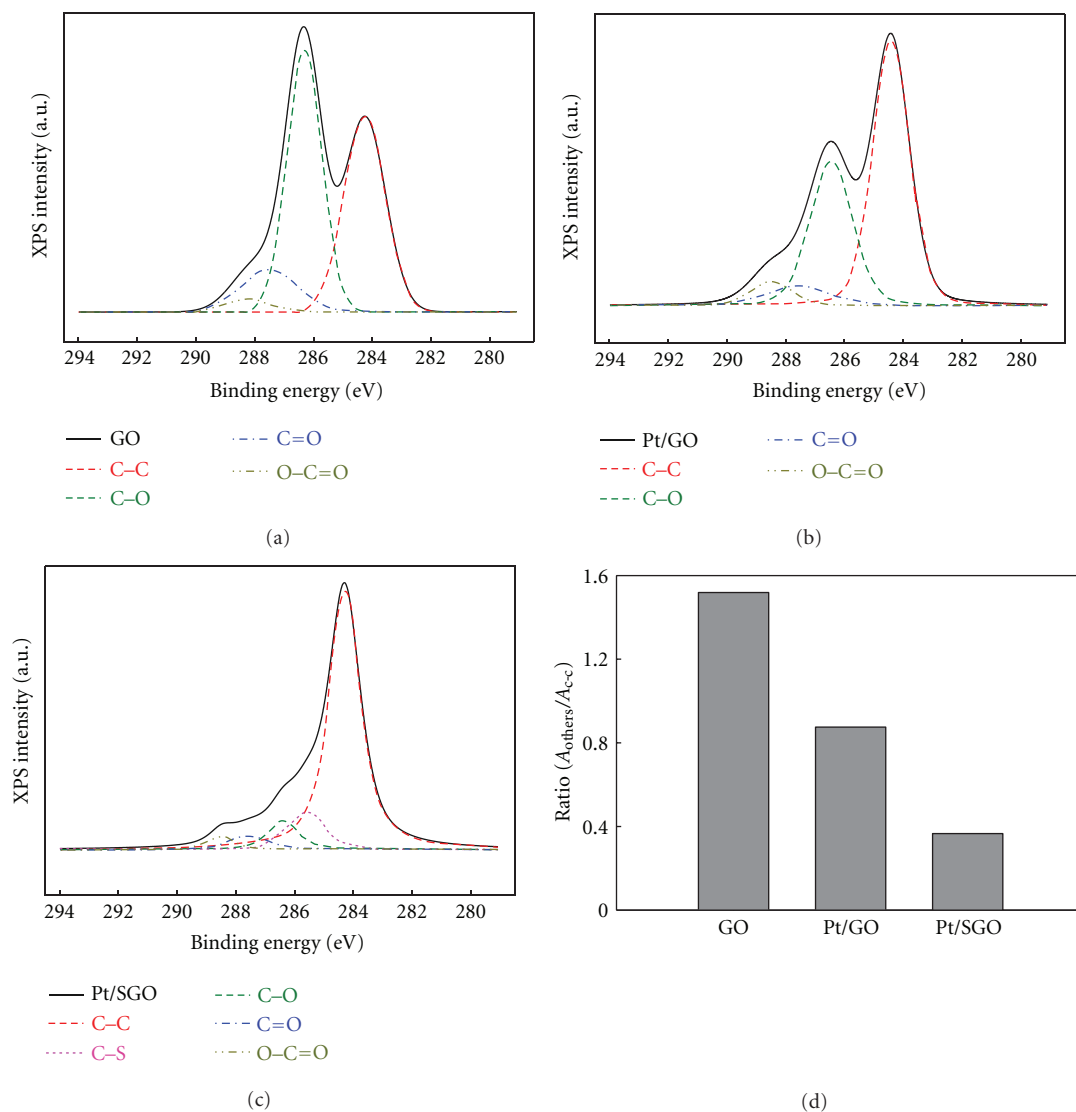


FIGURE 3: X-ray photoelectron C1s spectra of (a) GO, (b) Pt/GO, and (c) Pt/SGO. (d) Area ratio between C–C bond and sum of others including C–O and C=O related bonds.

## 2. Experimental Details

GO was prepared according to the modified Hummer's method from expandable graphite (Grade 1721, Ashbury Carbon) described in previous works [14, 15]. The sulfuric acid treated GO (SGO) was prepared by immersing GO to 4 M  $\text{H}_2\text{SO}_4$  (aq.) solution for 24 h at 60°C. During that process, carbonyl and epoxy functional groups can be converted to hydroxyl group by the keto-enol tautomerism and acid catalyzed ring opening reactions [16]. The Pt/GO and Pt/SGO catalysts were synthesized by reacting Pt salt precursor,  $\text{H}_2\text{PtCl}_6 \cdot 6\text{H}_2\text{O}$  (Sigma-Aldrich Corporation) and GO or SGO in the water at 90°C for 2 h. Different amounts of NaOH were added to adjust the pH of the solution. The product was collected by filtering and washing with ethanol and deionized water followed by vacuum drying for 2 h at 60°C. The final loading amount of Pt was 45 wt% when

measured with thermogravimetry analysis (TGA) as shown in Figure 1.

The cyclic voltammetry (CV) analysis was performed at 25°C with a three-electrode system using 0.5 M  $\text{H}_2\text{SO}_4$  (aq.) as the electrolyte, Ag/AgCl reference electrode, and Pt counter electrode. The scan range was  $-0.2 \sim 1.0$  V and scan rate was  $50 \text{ mV s}^{-1}$ , respectively. To prepare catalyst ink, each catalyst was mixed with 5 wt% Nafion ionomer dissolved in isopropanol (IPA) solvent. Polarization curves of a unit cell with  $5 \text{ cm}^2$  MEA were measured at a cell temperature of 70°C under ambient pressure, using  $\text{H}_2$  and air to the anode and cathode, respectively.

## 3. Results and Discussion

The thickness of GO used in this study was around 1 nm when measured with Atomic force microscope (AFM) as

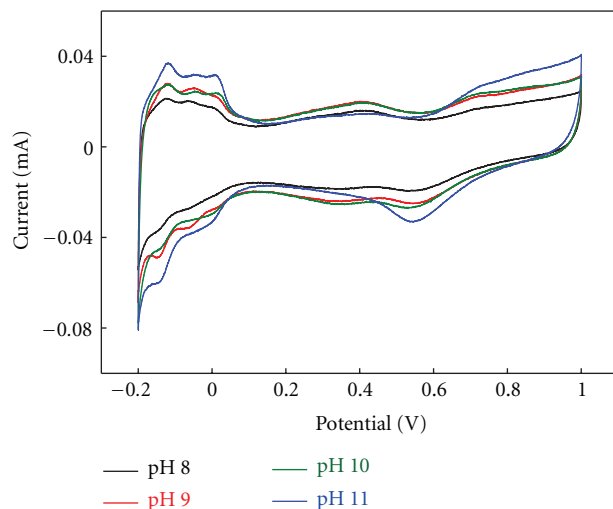


FIGURE 4: Cyclic voltammograms of Pt/SGOs fabricated at different pH. The scan rate was  $50 \text{ mV s}^{-1}$  in  $0.5 \text{ M H}_2\text{SO}_4$  electrolyte.

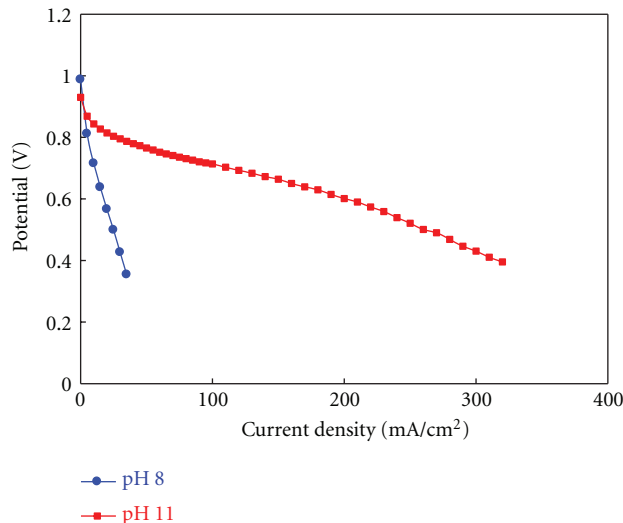
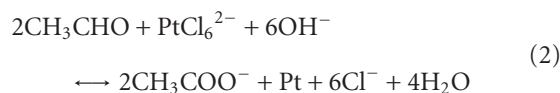


FIGURE 5: Polarization curves of Pt/SGO fabricated at different pH.

shown in inset of Figure 2(b). The mean particle size of Pt was calculated from XRD patterns by Scheerer's formula based on the Pt (111), (200), (220) and (311) peaks [17]. As shown in Figure 2, when SGO used as catalyst support the Pt size decreased to as low as 2.5 nm as the pH of the solution increased to 11 in the absence of any external reducing reagents such as ethylene glycol. On the other hand, when unmodified GO was used, the Pt size remained around 9 nm even at high pH condition (inset of Figure 2(a)). TEM image shown in Figure 2(c) clearly demonstrates the uniform distribution of small Pt particles on SGO surface fabricated at pH 11. This result indicates that sulfuric acid treatment enhanced the reaction between GO and Pt precursor by the effect of formation of large amount of hydroxyl group. The relation between pH and particle size is known due to the glycolates, the reaction intermediates produced during reaction between ethylene glycol [18, 19] and similar relation in this study exhibits similar reaction path as conventional

polyol synthesis. The reaction mechanism between ethylene glycol and Pt precursor involves the following reactions:



At first reaction, the interaction of  $-\text{OH}$  groups of ethylene glycol with Pt-ion sites results in the oxidation of the alcohol groups to aldehydes. These aldehydes are not very stable and undergo further oxidation to carboxylic acid at second step, which may again be oxidized to  $\text{CO}_2$  or carbonate in alkaline media, finally. The electrons donated by oxidation reactions result in the reduction of the Pt metal ions. The large amount of surface hydroxyl group of SGO after sulfuric acid treatment is believed to act like ethylene glycol and might undergo above reactions with Pt precursors.

This can be confirmed by the XPS data after Pt loading on GO or SGO surface as shown in Figure 3. The XPS C1s peak of GO at 284.3 eV corresponds to the C–C bonds of the graphite carbon, and the peaks at 285.5, 286.5, 287.5, and 288.6 eV can be attributed to C–S, C–O, C=O, and O–C=O bonding, respectively. Initially, GO contained large amount of surface functional groups, but after reaction with Pt precursor without external polyol, loss of functional groups was observed both GO and SGO. As shown in Figure 3(d), more loss of functional group in SGO over unmodified GO was seen and especially C–O bond which includes hydroxyl (–OH) and epoxy (C–O–C) decreased a lot. As the large amount of epoxy group exists in unmodified GO instead of hydroxyl group, there is limited loss in C–O related functional groups during the first reaction. We think that larger amount of hydroxyl groups in SGO generated by sulfuric acid treatment contributed better reaction with Pt precursor, which resulted in the smaller Pt size on SGO surface and more loss of oxygen related functional groups.

To see the electrocatalytic activity of Pt/SGO catalysts at different pH, the CV was performed and the results were shown at Figure 4. The Pt/SGO catalyst prepared at higher pH showed larger electrochemical surface area ( $13.4 \text{ m}^2 \text{ g}^{-1}_{\text{Pt}}$  at pH = 11 and  $5.2 \text{ m}^2 \text{ g}^{-1}_{\text{Pt}}$  at pH = 8), which might be due to the smaller Pt size of catalyst fabricated at higher pH. As shown in Figure 5, Pt/SGO fabricated at higher pH showed better fuel cell performance than that prepared at lower pH. This is presumably due to the smaller Pt particle size and larger Pt active area of Pt/SGO prepared at higher pH.

#### 4. Conclusion

In this study, we successfully fabricated uniformly distributed 2.5 nm size Pt catalysts supported on graphene oxide (GO) without any external reducing agent such as ethylene glycol. By treating GO with sulfuric acid, we can increase the population of surface hydroxyl groups on GO surface which can act as polyol and reduce Pt precursor to metallic Pt nanoparticles. XRD and TEM data showed that Pt supported on sulfuric acid treated GO exhibited smaller Pt size than that fabricated unmodified GO. XPS data showed that large amount of hydroxyl groups generated by sulfuric acid enhanced the Pt reduction. Cyclic voltammetry showed that as the pH increased the electrochemical surface area increased. We believe that this facile and environmentally friendly approach can provide new way to commercialize the grapheme-based PEMFC devices in near future.

#### Acknowledgment

This research was supported by the Basic Science Research Program through the National Research Foundation of Korea (NRF) funded by the Ministry of Education, Science, and Technology (2012-0002567).

#### References

- [1] S. Gottesfeld and T. Zawodzinski, "Polymer electrolyte fuel cells," *Advances in Electrochemical Science and Engineering*, vol. 5, chapter 4, pp. 195–301, 1997.
- [2] J. Zhang, Z. Xie, J. Zhang et al., "High temperature PEM fuel cells," *Journal of Power Sources*, vol. 160, no. 2, pp. 872–891, 2006.
- [3] S. Kim, T. Lee, J. Jung et al., "Catalytic performance of acid-treated multi-walled carbon nanotube-supported platinum catalyst for PEM fuel cells," *Materials Research Bulletin*, vol. 47, no. 10, pp. 2760–2764, 2012.
- [4] R. Kou, Y. Shao, D. Wang et al., "Enhanced activity and stability of Pt catalysts on functionalized graphene sheets for electrocatalytic oxygen reduction," *Electrochemistry Communications*, vol. 11, no. 5, pp. 954–957, 2009.
- [5] Y. Si and E. T. Samulski, "Exfoliated graphene separated by platinum nanoparticles," *Chemistry of Materials*, vol. 20, no. 21, pp. 6792–6797, 2008.
- [6] A. K. Geim and K. S. Novoselov, "The rise of graphene," *Nature Materials*, vol. 6, no. 3, pp. 183–191, 2007.
- [7] B. Kim, M. Kang, V. Pham et al., "Low-voltage solution-processed graphene transistors based on chemically and solvothermally reduced graphene oxide," *Journal of Materials Chemistry*, vol. 21, no. 34, pp. 13068–13073, 2011.
- [8] T. V. Cuong, H. N. Tien, V. H. Luan et al., "Solution-processed semitransparent p-n graphene oxide: CNT/ZnO heterojunction diodes for visible-blind UV sensors," *Physica Status Solidi A*, vol. 208, no. 4, pp. 943–946, 2011.
- [9] V. Luan, H. Tien, T. Cuong et al., "Novel conductive epoxy composites composed of 2-D chemically reduced graphene and 1-D silver nanowire hybrid fillers," *Journal of Materials Chemistry*, vol. 22, no. 17, pp. 8649–8653, 2012.
- [10] S. Hur and J. Park, "Graphene and its application in fuel cell catalysis: a review," *Asia-Pacific Journal of Chemical Engineering*. In press.
- [11] T. Herricks, J. Chen, and Y. Xia, "Polyol synthesis of platinum nanoparticles: control of morphology with sodium nitrate," *Nano Letters*, vol. 4, no. 12, pp. 2367–2371, 2004.
- [12] H. S. Oh, J. G. Oh, Y. G. Hong, and H. Kim, "Investigation of carbon-supported Pt nanocatalyst preparation by the polyol process for fuel cell applications," *Electrochimica Acta*, vol. 52, no. 25, pp. 7278–7285, 2007.
- [13] C. Bock, C. Paquet, M. Couillard, G. A. Botton, and B. R. MacDougall, "Size-selected synthesis of PtRu nano-catalysts: reaction and size control mechanism," *Journal of the American Chemical Society*, vol. 126, no. 25, pp. 8028–8037, 2004.
- [14] W. S. Hummers and R. E. Offeman, "Preparation of graphitic oxide," *Journal of the American Chemical Society*, vol. 80, no. 6, p. 1339, 1958.
- [15] V. Pham, T. Dang, T. Cuong et al., "Synthesis of highly concentrated suspension of chemically converted graphene in organic solvents: effect of temperature on the extent of reduction and dispersibility," *Korean Journal of Chemical Engineering*, vol. 29, no. 5, pp. 680–685, 2012.
- [16] D. Kim, S. J. Yang, Y. S. Kim, H. Jung, and C. R. Park, "Simple and cost-effective reduction of graphite oxide by sulfuric acid," *Carbon*, vol. 50, no. 9, pp. 3229–3232, 2012.
- [17] B. E. Warren, *X-Ray Diffraction*, Dover, New York, NY, USA, 1990.
- [18] C. Bock, C. Paquet, M. Couillard, G. A. Botton, and B. R. MacDougall, "Size-selected synthesis of PtRu nano-catalysts:

reaction and size control mechanism,” *Journal of the American Chemical Society*, vol. 126, no. 25, pp. 8028–8037, 2004.

- [19] C. K. Rhee, B. J. Kim, C. Ham, Y. J. Kim, K. Song, and K. Kwon, “Size effect of Pt nanoparticle on catalytic activity in oxidation of methanol and formic acid: comparison to Pt(111), Pt(100), and polycrystalline pt electrodes,” *Langmuir*, vol. 25, no. 12, pp. 7140–7147, 2009.

## Research Article

# Aluminum Silicate Nanotube Coating of Siloxane-Poly(lactic acid)-Vaterite Composite Fibermats for Bone Regeneration

Shuji Yamazaki,<sup>1</sup> Hirotaka Maeda,<sup>2</sup> Akiko Obata,<sup>1</sup> Keiichi Inukai,<sup>3</sup>  
Katsuya Kato,<sup>4</sup> and Toshihiro Kasuga<sup>1</sup>

<sup>1</sup> Department of Frontier Materials, Nagoya Institute of Technology, Gokiso-cho, Showa-ku, Nagoya 466-8555, Japan

<sup>2</sup> Center for Fostering Young and Innovative Researchers, Nagoya Institute of Technology, Gokiso-cho, Showa-ku, Nagoya 466-8555, Japan

<sup>3</sup> Ecological Ceramics Group, Materials Research Institute for Sustainable Development, National Institute of Advanced Industrial Science and Technology, Anagahora Shimo-shidami, Moriyama-ku, Nagoya 463-8560, Japan

<sup>4</sup> Bio-integration Processing Research Group, Advanced Manufacturing Research Institute, National Institute of Advanced Industrial Science and Technology, Anagahora Shimo-shidami, Moriyama-ku, Nagoya 463-8560, Japan

Correspondence should be addressed to Toshihiro Kasuga, kasuga.toshihiro@nitech.ac.jp

Received 20 July 2012; Revised 16 November 2012; Accepted 26 November 2012

Academic Editor: Yong Yang

Copyright © 2012 Shuji Yamazaki et al. This is an open access article distributed under the Creative Commons Attribution License, which permits unrestricted use, distribution, and reproduction in any medium, provided the original work is properly cited.

In our earlier work, a flexible fibermat consisting of a biodegradable composite with soluble silicate species, which has been reported to enhance bone formation, was prepared successfully using poly(L-lactic acid) and siloxane-containing calcium carbonate particles by electrospinning. The fibermat showed enhanced bone formation in an *in vivo* test. In the present work, to improve the hydrophilicity of skeletal fibers in a fibermat, they were coated with nanotubular aluminum silicate crystals, which have a hydrophilic surface that has excellent affinity to body fluids and a high surface area advantageous for pronounced protein adsorption. The nanotubes were coated easily on the fiber surface using an electrophoretic method. In a conventional contact angle test, a drop of water rapidly penetrated into the nanotube-coated fibermat. The culture test using murine osteoblast-like cells (MC3T3-E1) showed that the cell attachment to the nanotube-coated fibermat at an early stage after seeding was enhanced in comparison with that to the noncoated one. This approach may provide a new method of improving the surface of polymer-based biomaterials.

## 1. Introduction

Many types of scaffolds have been investigated for use in bone regeneration [1, 2], which serve as templates for cell interaction and the formation of a bone extracellular matrix (ECM) to provide structural support to newly formed tissues. Ceramics, such as hydroxyapatite (HA) and  $\beta$ -tricalcium phosphate ( $\beta$ -TCP), show good biocompatibility, but they are brittle and thus are difficult to form into various shapes. In contrast, synthetic biodegradable polymers are more easily shaped and show flexibility. However, they may elicit an inflammatory response in the host tissue because of the release of acidic degradation products [3]. Considering these problems, composites have been fabricated using

biodegradable polymers coupled with calcium phosphate ceramics, whose excellent biocompatibility is established [4, 5].

The present authors have developed a novel composite consisting of poly(L-lactic acid) (PLLA), which is a biodegradable polymer that has already been applied clinically, and siloxane-containing vaterite (SiV); the siloxane-PLLA-vaterite hybrid-composite is denoted as SiPVH, hereafter. It can release calcium and silicate ions, which have been reported to enhance the proliferation, differentiation, and mineralization of osteoblasts [6–8]. The cellular compatibility of SiPVH was tested using mouse osteoblast-like cells [9]. A film of SiPVH was prepared by dip-coating a coverglass with the composite solution. The film showed the release

of calcium and silicate ions into the culture medium. Cell proliferation and mineralization on the composite film were enhanced in comparison with those on an undoped vaterite-PLA composite film, which showed no silicon release.

Three-dimensional scaffolds are common in biomaterials. Electrospinning is a process for forming fiber mats with a high porosity and a high flexibility [10–12]. These fiber mats are very promising for the regeneration of tissues and organs [11, 13] owing to the possibility of mimicking some structural features of natural ECM [14]. Numerous studies have shown the enhanced cellular attachment and proliferation on fibrous materials [15–17]. The present authors have successfully prepared a SiPVH fiber mat by an electrospinning method and then performed *in vivo* experiments by placing the fiber mat with 8 mm defects in the front midline of the calvaria of New Zealand rabbits [18, 19]. They found enhanced bone formation on SiPVH fiber mats. PLLA as a matrix phase in SiPVH is relatively hydrophobic. This is a property to be improved for the adhesion of bone-forming cells at the initial stage after implantation in the body.

A naturally occurring hydrated aluminum silicate,  $(\text{HO})_3\text{Al}_2\text{O}_3\text{Si}(\text{OH})$ , which is called imogolite, has a nanotubular structure of  $\sim 2.2$  nm external and  $\sim 1.0$  nm internal diameters [20], with a length of up to several hundreds of micrometers. The imogolite nanotube (INT) is a hydrophilic material owing to numerous hydroxyl groups on its surface and has a high surface area, resulting in a high protein adsorption activity [21–23]. Ishikawa and coworkers reported that the amount of normalized protein per osteoblast-like cell (SaOS-2) cultured on INTs is two times larger than that cultured on a culture dish, and that the cells bond more strongly to INTs than to a culture dish [24, 25]. These results demonstrate the good biocompatibility between cells and INTs; thus, INTs may be useful for various biomedical applications.

In the present work, SiPVH fiber mats were coated with INTs to improve their hydrophilicity to enhance cellular compatibility at the early stage after implantation.

## 2. Materials and Methods

**2.1. Preparation of SiPVH Fiber Mats.** SiV particles of  $1\ \mu\text{m}$  diameter, containing 2.6 wt% silicon, were prepared by a carbonation method using methanol and  $\gamma$ -aminopropyltriethoxysilane (APTES; Momentive Performance Materials, Japan) as the silica precursor, as described in our previous works [9, 18, 19]. One hundred and fifty grams of  $\text{Ca}(\text{OH})_2$ , 60 mL of APTES and 2 L of methanol were mixed by bubbling a  $\text{CO}_2$  gas in the resulting mixture for 75 min at a rate of  $2\ \text{L}\cdot\text{min}^{-1}$ . The resulting slurry was dried at  $110^\circ\text{C}$ , resulting in the formation of spherical SiV particles.

SiPVH was prepared by kneading PLLA (Mitsui Chemicals, LACIA; molecular weight:  $M_w = \sim 140$  kDa) with SiV particles at  $200^\circ\text{C}$  for 10 min in a weight ratio of PLLA/SiV = 7/3.

SiPVH was dissolved in chloroform for electrospinning to prepare 10 wt% PLLA solution. The fiber mats were prepared by electrospinning at a voltage of 20 kV using the conditions and compositions previously found to be optimal

for preparing microfibers of  $\sim 10\ \mu\text{m}$  diameter [18, 19]. The flow rate of the chloroform solution was  $50\ \mu\text{L}\cdot\text{min}^{-1}$ , and the distance between the nozzle and the collector was 150 mm. The drum-shaped collector was rotated at  $2\ \text{m}\cdot\text{min}^{-1}$ , and the syringe filled with the SiPVH solution was traversed at  $70\text{--}100\ \text{mm}\cdot\text{min}^{-1}$  from side to side.

**2.2. Preparation of INT-Dispersed Aqueous Solution.** INTs were synthesized, essentially following a method described by Suzuki et al. [26]. In 500 mL of distilled water (DW), 18.47 g of aluminum chloride ( $\text{AlCl}_3\cdot 6\text{H}_2\text{O}$ ; Wako Pure Chemicals) and 9.2 g of sodium silicate ( $\text{Na}_4\text{SiO}_4\cdot n\text{H}_2\text{O}$ ; Wako Pure Chemicals) were dissolved to yield a Si/Al molar ratio of 0.41.

Sodium hydroxide (NaOH; Wako Pure Chemicals) aqueous solution of 1 M was slowly added to the above-described sodium silicate/aluminum chloride solution at a rate of  $2\ \text{mL}\cdot\text{min}^{-1}$  until the pH of the solution reached 6.8. The sample was separated by centrifugation and the obtained precipitates were rinsed in DW with stirring. After the centrifugation-rinsing process was repeated three times, the resulting aluminum silicate precursors were dispersed again in 12 L of DW. Subsequently, the solution was acidified again by the addition of 12 mL of hydrochloric acid (HCl; Wako Pure Chemicals) with a concentration of 5 M and then heated at  $95^\circ\text{C}$  for 1 or 4 d for INT formation. Consequently, the resulting INTs were dispersed in an aqueous solution with a concentration of 0.087 wt%. The INTs were observed by atomic force microscopy (AFM) in the tapping mode. Figure 1 shows AFM images of the products after heating at  $95^\circ\text{C}$ . The average lengths of the INTs obtained after the heating for 1 and 4 d were 220 and 570 nm, respectively. They are denoted as INT<sub>220</sub> and INT<sub>570</sub>, respectively, hereafter.

**2.3. INT Coating of SiPVH Fiber Mats.** The INT coating of SiPVH fiber mats was achieved using an electrophoretic deposition (EPD) method.

Each fiber mat was cut into  $15\ \text{mm} \times 15\ \text{mm} \times 0.2\ \text{mm}$  dimensions with scissors and then placed on  $15\ \text{mm} \times 60\ \text{mm} \times 0.25\ \text{mm}$  aluminum foil. One hundred microliters of ethanol were dropped on the foil to fix each fiber mat on the cathode electrode.

The objective of the present work is to prepare a hydrophilic coating with an extremely thin layer of INTs on skeletal fibers. Our preliminary work showed the EPD conditions for the preparation. The point of zero charge (PZC) in an INT-containing solution has been reported to be pH 6.0 [27]. The INT-dispersed aqueous solution described in Section 2.2 was adjusted to pH 5.5 with dilute NaOH solution of 0.1 M. The resulting solution was considered to be slightly charged positively. The cathode and anode made of aluminum of  $15\ \text{mm} \times 60\ \text{mm} \times 0.25\ \text{mm}$  dimensions were dipped in 30 mL of the solution, and EPD was carried out for 1 min at 0.1 V of applied voltage. The separation distance between the electrodes was 10 mm. After EPD, the sample was dried at  $50^\circ\text{C}$  for 3 h in air.

**2.4. Scanning Electron Microscopy.** The samples were coated with amorphous osmium using plasma chemical vapor

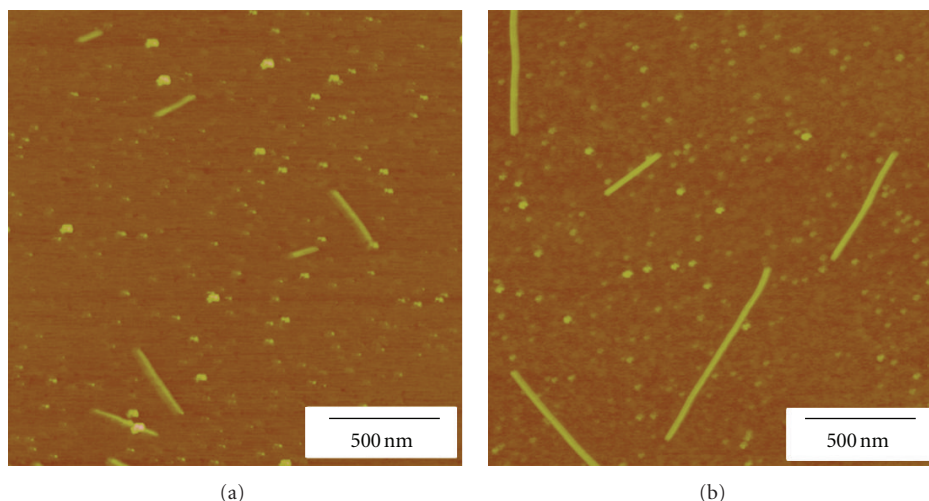


FIGURE 1: AFM images of products after heating at 95°C for (a) 1 d and (b) 4 d.

deposition (CVD) and then observed morphologically using a field emission scanning electron microscopy (SEM) system (JSM-6301F, JEOL, Japan), with an energy-dispersive spectrometer (EDS).

**2.5. Contact Angle Measurement.** The static contact angle of water on the fibermats was measured using a CCD camera and SImage mini ver. 5.01 software. The average contact angle was determined from the measurements at ten random points per sample.

**2.6. Cell Culture Tests.** The fibermats were cut into disk-shaped pieces of 15 mm in diameter with scissors for cell culture tests, and the resulting samples were sterilized using ethylene oxide gas. Murine osteoblast-like cells (MC3T3-E1 cells) were seeded onto the samples in 24-well plates at a density of 50,000 or 80,000 cells·well<sup>-1</sup> to evaluate their proliferation or initial adhesion, respectively, and cultured in alpha minimum essential medium ( $\alpha$ -MEM) containing 10% fetal bovine serum (FBS) at 37°C in 5% CO<sub>2</sub>.

The number of murine osteoblast-like cells (MC3T3-E1 cells) was evaluated using Cell Counting Kit-8 (Dojindo, Japan). The cells were rinsed with  $\alpha$ -MEM and then incubated in the culture medium containing the reagent of the kit at 37°C for 2 h. Cell number was evaluated after measuring the absorbance of the resulting medium at 450 nm. The differences between the samples were determined by Student's *t*-test, with  $P < 0.05$ , which is considered to be statistically significant.

The cells cultured on the samples for 3 h were fixed in 2.5% glutaraldehyde for 40 min at 4°C, dehydrated through a series of increasing concentrations of ethanol, and finally dried with hexamethyldisilazane. The dried samples were observed by SEM after they were coated with amorphous osmium.

To evaluate the initial adhesion of the cells on the fibers, they were cultured on the samples for 3 h and then fixed in phosphate buffer solution (PBS) containing 4% paraformaldehyde for 30 min at 4°C. The cells were then

treated with PBS containing 1% bovine serum albumin (BSA) and 0.1% Triton X for 25 min at 4°C. Finally, they were fluorescence-stained with 50  $\mu$ L of Alexa Fluor 488 Phalloidin (Molecular Probe), which was diluted to a concentration of 2.5% with PBS, for 30 min at 37°C. The samples were observed with a fluorescence microscope (Keyence, BZ-9000).

### 3. Results and Discussion

**3.1. Preparation of INT-Coated Fibermats.** In our earlier work, PLLA fibermats consisting of skeletal fibers of  $\sim 10 \mu$ m diameter and  $\sim 40 \mu$ m spaces between them, on average, were reported to be suitable for cellular in-growth [28]. Figure 2 shows SEM images of the surface morphologies of the noncoated and INT-coated SiPVH fibermats. Microfibers of  $\sim 10 \mu$ m diameter were observed on the surface and found to be intertwined. The sizes of the spaces between the microfibers varied between 10  $\mu$ m and several hundred micrometers, as shown in Figure 2(a). Numerous pores of submicrometer diameter were found on the surfaces of the fibers, which were due to the volatilization of the solvent of the polymer solution during electrospinning [29, 30].

There are almost no significant differences in the appearance between the SiPVH fibermat coated with INT<sub>220</sub> and the noncoated one, as shown in Figures 2(a) and 2(b), respectively. On the other hand, in the fibermat coated with INT<sub>570</sub> shown in Figure 2(c), weblike plates around cross-linked points of the fibers can be observed.

The EDS spectrum in Figure 2(a) shows the peaks of Ca and Si due to SiV. The Si peak is small, since the silicon content of SiV is very small (2.6 wt%). In the spectra of the INT-coated SiPVH fibermats (Figures 2(b) and 2(c)), Al peaks are seen in addition to the peaks of Ca and Si due to SiV. The Si peak intensities are higher than that in Figure 2(a). The Al contents of the fibermats coated with INT<sub>220</sub> and INT<sub>570</sub> were estimated to be  $\sim 2$  and  $\sim 7$  %, respectively. The element originates from INTs on the surface, since no Al is included in SiPVH. This indicates

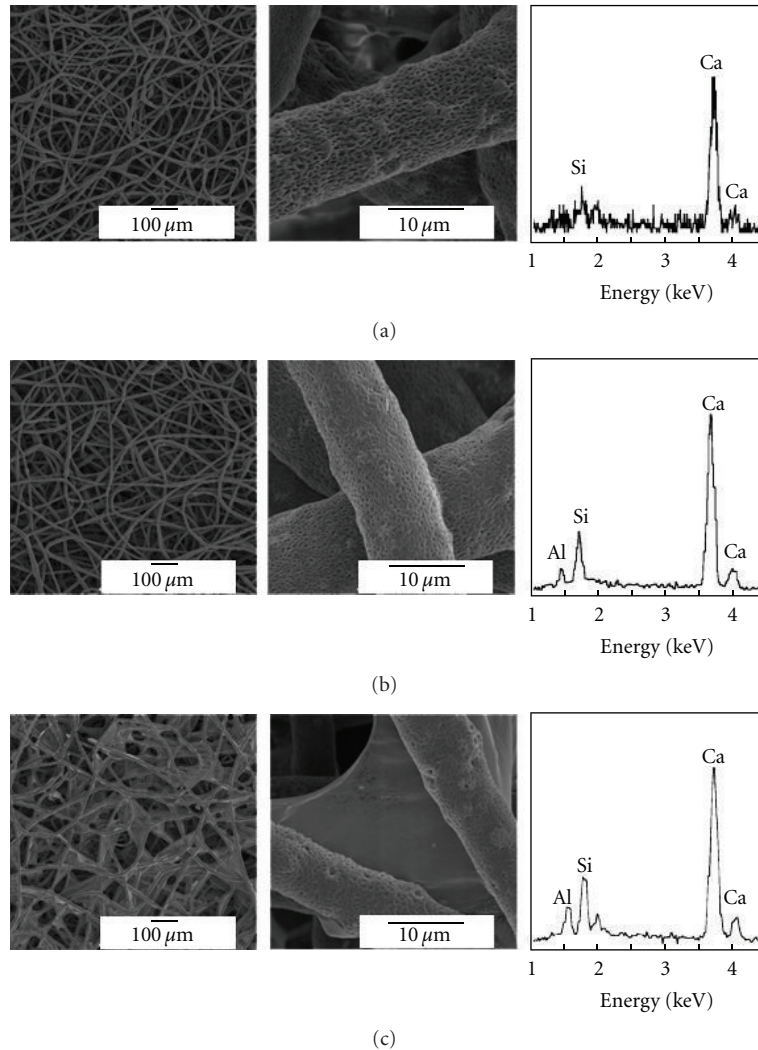


FIGURE 2: SEM images and EDS spectra of (a) noncoated and (b, c) INT-coated SiPVH fiber mats. (b) INT<sub>220</sub>-coated and (c) INT<sub>570</sub>-coated SiPVH fiber mats. Center: magnified views; right: EDS spectra.

that INTs were coated on the fiber mats by EPD. The weblike plates around cross-linked points, as shown in Figure 2(c), were found to consist of aluminum silicates with a Si/Al ratio of  $\sim 0.5$ , which corresponds to the INT composition. That is, the plates were concluded to be an aggregation of INTs. It has been reported that the viscosity of the INT-dispersed aqueous solution increases with increasing INT length and the number or forming net texture of INTs [24]. INTs attracted to an electrode in an electric field would easily aggregate around the surface of the fibers, since the number of INTs in a dispersed aqueous solution increases. Then, the attracted INTs would likely form bridges around cross-linked points. Since INT<sub>220</sub> was shorter than INT<sub>570</sub>, the incidence possibility of aggregation would be lower.

To discuss the EPD effect, a dip-coating method was used: after the SiPVH fiber mat was dipped in the INT-dispersed aqueous solution (0.087%), it was drawn up at a speed of  $\sim 1 \text{ mm} \cdot \text{s}^{-1}$  and then dried. The EDS analysis of the resulting fiber mat showed no Al peak (under the analytical limit). That is, it is difficult to coat the fiber mats with INTs

by dip coating, and thus EPD is concluded to be a powerful method for such coating. Since the INT concentration in the solution is considerably small, almost no INTs would adhere to the skeletal fibers after the dip coating. It is not easy to prepare the dispersed solution containing a large number of INTs owing to some technical problems, such as impurity formation in the solution, and gelation owing to its concentration. The hydrophobic surface of SiPVH fibers may also be one of the causes of the difficulty in dip coating. In the case of EPD, INTs would pass through the porous structure of fiber mats in an electric field and concentrate around the surfaces of skeletal fibers, and then accumulate on them.

The noncoated fiber mat exhibited hydrophobicity of a contact angle of  $121^\circ$ . In contrast, a drop of water immediately penetrated the fiber mats coated with INTs, which indicated that the hydrophilicity of these fiber mats was improved markedly after INT coating. This is because INTs are hydrophilic owing to the hydroxyl groups on their surfaces and have a high water absorbency, attributed to their nanotubular structure. In particular, the fiber mat coated

with INT<sub>220</sub> showed excellent hydrophilicity as well as that coated with INT<sub>570</sub>, although it is difficult to morphologically distinguish them from the noncoated one. A very small number of INTs seem to be sufficient for improving the hydrophilicity of fibermats.

**3.2. Cellular Compatibility.** The cellular proliferation behavior of the INT-coated fibermats in comparison with that of the noncoated one was evaluated using MC3T3-E1 cells. Figure 3 shows the numbers of cells after culturing on them for 3 days. The numbers of cells after culture on INT<sub>220</sub>- and INT<sub>570</sub>-coated fibermats were significantly higher ( $P < 0.05$ ) than those on the noncoated one on both day 1 and day 3. There were no significant differences in the number between the two types of INT-coated fibermat. This might have been due to the effects of the INT coating, which shows high cellular compatibility [24, 25]. Even with coating with a trace amount of INT<sub>220</sub>, excellent improvement in the compatibility on the fibermat was achieved.

The doubling time (DT) of the number of cells for discussing proliferation behavior is determined by

$$DT = \frac{(t_2 - t_1) \log 2}{\log N_2 - \log N_1}, \quad (1)$$

where  $N_1$  and  $N_2$  are the numbers of cells at the culture time points  $t_1$  and  $t_2$  (h), respectively. The DTs of the noncoated, INT<sub>220</sub>-coated, and INT<sub>570</sub>-coated fibermats were estimated to be 33.0 h, 33.7 h, and 33.7 h, respectively, which are not significantly different. The difference in the numbers of cells after culture between the noncoated and INT-coated fibermats might have originated from the adhesion behavior of the cells at an early stage after seeding.

Figure 4 shows the numbers of cells attached to the noncoated and INT-coated fibermats at 3 h after seeding. The numbers of cells cultured on the INT-coated fibermats were significantly higher than that on the noncoated one. INTs were suggested to enhance the initial cell attachment to the fibermats. However, there was no significant difference in the number of cells cultured between INT<sub>220</sub> and INT<sub>570</sub>.

Figures 5 and 6 show the morphologies of the cells attached to the fibermats at 3 h after seeding. The cells adhering to the noncoated fibermat were still spherical and were preferentially attached to the surface around cross-linked points between skeletal fibers, as shown in Figure 5(a). On the other hand, as shown in Figures 5(b) and 5(c), the cells on the INT-coated fibermats were elongated not only on the surface around the cross-linked points but also on individual fibers and actin filaments were aligned to the fibers. The cells were attached over the entire surface of the INT-coated fibermats, as shown in Figures 6(b) and 6(c). These cell culture tests suggested that INTs enhanced cell adhesion and growth.

Watari and coworkers reported that protein adsorption on nanofibrous scaffolds contributes to excellent cell adhesion and growth [21–23]. In our preliminary work, INTs showed a high adsorbability to various types of protein including acidic, neutral, and basic ones, owing to the large specific surface area of the nanotubular structure. Thus, it is proposed that cell-adhesive proteins, such as fibronectin

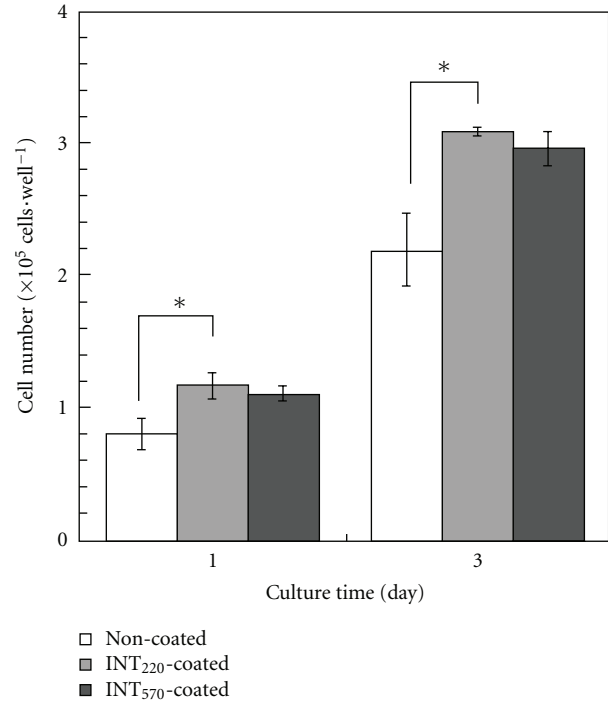


FIGURE 3: Numbers of cells attached to noncoated and INT-coated fibermats after 3 days of culture.

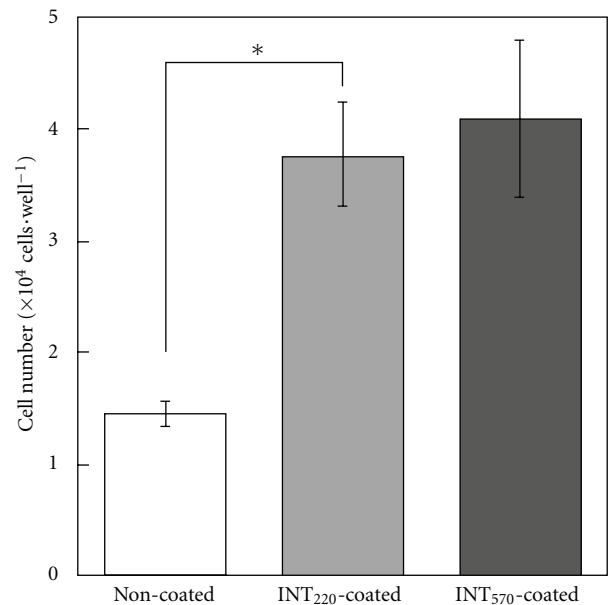


FIGURE 4: Numbers of cells attached to noncoated and INT-coated fibermats at 3 h after seeding.

and vitronectin, could be easily adsorbed on the INT surface [31, 32].

Furthermore, the INT nanostructure may also be related to cell adhesion. Hirata et al. reported that the nanostructure of multiwalled carbon nanotubes might be effective in cell entrapment [33]. The geometrical factor in the INT nanostructure may be beneficial for cell attachment to surfaces.

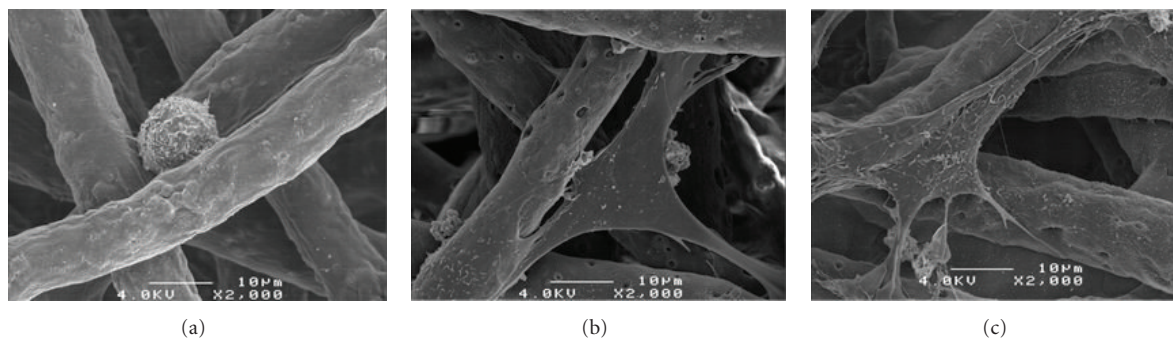


FIGURE 5: SEM images of cells on (a) noncoated and (b, c) INT-coated SiPVH fiber mats at 3 h after seeding. (b) INT<sub>220</sub>-coated and (c) INT<sub>570</sub>-coated SiPVH fiber mats.

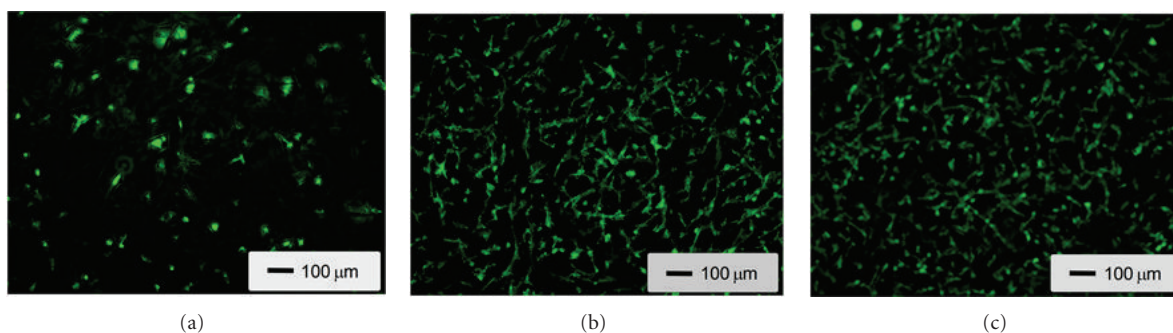


FIGURE 6: Fluorescence micrographs of cells on (a) noncoated and (b, c) INT-coated SiPVH fiber mats at 3 h after seeding. (b) INT<sub>220</sub>-coated and (c) INT<sub>570</sub>-coated SiPVH fiber mats.

In the present work, a trace amount of INT was coated on SiPVH fibers: no existence could be observed by SEM. The measurement of the INT amount on the fibers is not easy and the investigation is in progress. Although there might be almost no need to consider the influence of the Al<sup>3+</sup> ion dissolved from the trace amount of INT on living body, we would have to discuss its behavior in future.

There are almost no reports on the solubility of aluminum silicates in living body or under its simulated environment, to the best of our knowledge. Although imogolite has been reported to dissolve slightly in alkaline solutions of pH > 10 [34] and in acid solutions of pH < 3 [35], almost no information around the neutrality is seen. It would be important to examine the solubility of INTs in detail.

#### 4. Conclusion

Aluminum silicate INTs were coated successfully on an electrospun fiber mat, consisting of poly(L-lactic acid)-based composite microfibers containing siloxane-doped calcium carbonate particles by electrophoretic deposition using an applied voltage of 0.1 V for 1 min. INTs of 220 and 570 nm lengths on average were coated very thinly such that their presence could not be observed by SEM. In the case of coating with INTs of 570 nm length, weblike plates formed around cross-linked points of skeletal fibers owing to their aggregation. Shorter INTs were better for preparing a homogeneous coating on a fiber mat. The hydrophilicity of the fiber mat was improved markedly after INT coating. Cell

culture tests indicated that INT enhanced the attachment and extension of MC3T3-E1 cells. The excellent compatibility might have originated from the protein adsorbability and geometrical factor of the nanostructure. Thus INT coating may be one of the best approaches to improving the hydrophilicity and cellular compatibility of biomaterials for bone regeneration.

#### Acknowledgments

The authors are indebted to Dr. Yoshio Ota, Dr. Xianfeng Yao, and Dr. Kazuya Oribe of Orthorebirth Co., Ltd., for their helpful discussions. This work was supported in part by Adaptable and Seamless Technology Transfer Program through Target-driven R&D (A-STEP; Seeds actualization type: AS2311416F) from Japan Science and Technology Agency.

#### References

- [1] S.-S. Kim, M. S. Park, O. Jeon, C.-Y. Choi, and B. S. Kim, "Poly(lactide-coglycolide)/hydroxyl-apatite composite scaffolds for bone tissue engineering," *Biomaterials*, vol. 27, no. 8, pp. 1399–1409, 2006.
- [2] K. Zhang, Y. Wang, M. A. Hillmyer, and L. F. Francis, "Processing and properties of porous poly(L-lactic)/bioactive glass composites," *Biomaterials*, vol. 25, no. 13, pp. 2489–2500, 2004.
- [3] L. G. Griffith, "Polymeric biomaterials," *Acta Materialia*, vol. 48, no. 1, pp. 263–277, 2000.

- [4] R. Zhang and P. X. Ma, "Porous poly(L-lactic acid)/apatite composites created by biomimetic process," *Journal of Biomedical Materials Research*, vol. 45, no. 4, pp. 285–293, 1999.
- [5] J. A. Roether, A. R. Boccaccini, L. L. Hench, V. Maquet, S. Gautier, and R. Jérôme, "Development and in vitro characterisation of novel bioresorbable and bioactive composite materials based on polylactide foams and Bioglass for tissue engineering applications," *Biomaterials*, vol. 23, no. 18, pp. 3871–3878, 2002.
- [6] I. D. Xynos, A. J. Edgar, L. D. K. Buttery, L. L. Hench, and J. M. Polak, "Ionic products of bioactive glass dissolution increase proliferation of human osteoblasts and induce insulin-like growth factor II mRNA expression and protein synthesis," *Biochemical and Biophysical Research Communications*, vol. 276, no. 2, pp. 461–465, 2000.
- [7] D. M. Reffitt, N. Ogston, R. Jugdaohsingh et al., "Orthosilicic acid stimulates collagen type 1 synthesis and osteoblastic differentiation in human osteoblast-like cells in vitro," *Bone*, vol. 32, no. 2, pp. 127–135, 2003.
- [8] N. Patel, S. M. Best, W. Bonfield et al., "A comparative study on the in vivo behavior of hydroxyapatite and silicon substituted hydroxyapatite granules," *Journal of Materials Science*, vol. 13, no. 12, pp. 1199–1206, 2002.
- [9] A. Obata, S. Tokuda, and T. Kasuga, "Enhanced in vitro cell activity on silicon-doped vaterite/poly(lactic acid) composites," *Acta Biomaterialia*, vol. 5, no. 1, pp. 57–62, 2009.
- [10] T. J. Still and H. A. von Recum, "Electrospinning: applications in drug delivery and tissue engineering," *Biomaterials*, vol. 29, no. 13, pp. 1989–2006, 2008.
- [11] W. J. Li, C. T. Laurencin, E. J. Caterson, R. S. Tuan, and F. K. Ko, "Electrospun nanofibrous structure: a novel scaffold for tissue engineering," *Journal of Biomedical Materials Research*, vol. 60, no. 4, pp. 613–621, 2002.
- [12] X. Xin, M. Hussain, and J. J. Mao, "Continuing differentiation of human mesenchymal stem cells and induced chondrogenic and osteogenic lineages in electrospun PLGA nanofiber scaffold," *Biomaterials*, vol. 28, no. 2, pp. 316–325, 2007.
- [13] Y. Z. Zhang, B. Su, J. Venugopal, S. Ramakrishna, and C. T. Lim, "Biomimetic and bioactive nanofibrous scaffolds from electrospun composite nanofibers," *International Journal of Nanomedicine*, vol. 2, no. 4, pp. 623–638, 2007.
- [14] A. O. Brightman, B. P. Rajwa, J. E. Sturgis, M. E. McCallister, J. P. Robinson, and S. L. Voytk-Harbin, "Timelapse confocal reflection microscopy of collagen fibrillogenesis and extracellular matrix assembly in vitro," *Biopolymers*, vol. 54, no. 3, pp. 222–234, 2000.
- [15] A. S. Badami, M. R. Kreke, M. S. Thompson, J. S. Riffle, and A. S. Goldstein, "Effect of fiber diameter on spreading, proliferation, and differentiation of osteoblastic cells on electrospun poly(lactic acid) substrates," *Biomaterials*, vol. 27, no. 4, pp. 596–606, 2006.
- [16] M. M. Stevens and J. H. George, "Exploring and engineering the cell surface interface," *Science*, vol. 310, no. 18, pp. 1135–1138, 2005.
- [17] J.-H. Jang, O. Castano, and H. W. Kim, "Electrospun materials as potential platforms for bone tissue engineering," *Advanced Drug Delivery Reviews*, vol. 61, no. 12, pp. 1065–1083, 2009.
- [18] A. Obata, T. Hotta, T. Wakita, Y. Ota, and T. Kasuga, "Electrospun microfiber meshes of silicon-doped vaterite/poly(lactic acid) hybrid for guided bone regeneration," *Acta Biomaterialia*, vol. 6, no. 4, pp. 1248–1257, 2010.
- [19] T. Wakita, A. Obata, G. Poologasundarampillai, J. R. Jones, and T. Kasuga, "Preparation of electrospun siloxane-poly(lactic acid)-vaterite hybrid fibrous membranes for guided bone regeneration," *Composites Science and Technology*, vol. 70, no. 13, pp. 1889–1893, 2010.
- [20] P. D. G. Cradwick, V. C. Farmer, J. D. Russell, C. R. Masson, K. Wada, and N. Yoshinaga, "Imogolite, a hydrated aluminum silicate of tubular structure," *Nature Physical Science*, vol. 240, no. 104, pp. 187–189, 1972.
- [21] F. Watari, S. Abe, C. Koyama et al., "Behavior of in vitro, in vivo and internal motion of micro/nano particles of titanium, titanium oxides and others," *Journal of the Ceramic Society of Japan*, vol. 116, no. 1349, pp. 1–5, 2008.
- [22] F. Watari, N. Takashi, A. Yokoyama et al., "Material nanosizing effect on living organisms: non-specific, biointeractive, physical size effects," *Journal of the Royal Society Interface*, vol. 6, no. 3, pp. S371–S388, 2009.
- [23] F. Watari, "Biointeractive and bioactive nature of nanomaterials," *Nano Biomedicine*, vol. 1, no. 1, pp. 2–8, 2009.
- [24] K. Ishikawa, T. Akasaka, Y. Nodasaka et al., "Physical properties of aluminosilicate nanotubes, imogolite, as scaffold and effect on osteoblastic mineralization," *Nano Biomedicine*, vol. 1, no. 2, pp. 109–120, 2009.
- [25] K. Ishikawa, S. Abe, Y. Yawaka, M. Suzuki, and F. Watari, "Osteoblastic cellular responses to aluminosilicate nanotubes, imogolite using Saos-2 and MC3T3-E1 cells," *Journal of the Ceramic Society of Japan*, vol. 118, no. 1378, pp. 516–520, 2010.
- [26] M. Suzuki, H. Sato, C. Ikeda, R. Nakanishi, K. Inukai, and M. Maeda, "State change of imogolite according to heating duration on synthesizing," *Journal of Clay Science Society of Japan*, vol. 46, no. 4, pp. 194–199, 2007 (Japanese).
- [27] H. Tsuchida, S. Ooi, K. Nakaishi, and Y. Adachi, "Effects of pH and ionic strength on electrokinetic properties of imogolite," *Colloids and Surfaces A*, vol. 265, no. 1–3, pp. 131–134, 2005.
- [28] K. Fujikura, A. Obata, and T. Kasuga, "Cellular migration to electrospun poly(lactic acid) fiber mats," *Journal of Biomaterials Science*, vol. 23, pp. 1939–1950, 2012.
- [29] Z. M. Huang, Y. Z. Zhang, M. Kotaki, and S. Ramakrishna, "A review on polymer nanofibers by electrospinning and their applications in nanocomposites," *Composites Science and Technology*, vol. 63, no. 15, pp. 2223–2253, 2003.
- [30] G.-T. Kim, J.-S. Lee, J.-H. Shin et al., "Investigation of pore formation for polystyrene electrospun fiber: effect of relative humidity," *Korean Journal of Chemical Engineering*, vol. 22, no. 5, pp. 783–788, 2005.
- [31] J. G. Steele, G. Johnson, and P. A. Underwood, "Role of serum vitronectin and fibronectin in adhesion of fibroblasts following seeding onto tissue culture polystyrene," *Journal of Biomedical Materials Research*, vol. 26, no. 7, pp. 861–884, 1992.
- [32] T. A. Horbett and M. B. Schway, "Correlations between mouse 3T3 cell spreading and serum fibronectin adsorption on glass and hydroxyethylmethacrylate-ethylmethacrylate copolymers," *Journal of Biomedical Materials Research*, vol. 22, no. 9, pp. 763–793, 1988.
- [33] E. Hirata, M. Uo, Y. Nodasaka et al., "3D collagen scaffolds coated with multiwalled carbon nanotubes: initial cell attachment to internal surface," *Journal of Biomedical Materials Research B*, vol. 93, no. 2, pp. 544–550, 2010.
- [34] Z. Abidin, N. Matsue, and T. Henmi, "Dissolution mechanism of nano-ball allophone with dilute alkali solution," *Clay Science*, vol. 12, no. 4, pp. 213–222, 2004.
- [35] C. Su, J. B. Harsh, and J. S. Boyle, "Solubility of hydroxy-aluminum interlayers and imogolite in a Spodosol," *Soil Science Society of America Journal*, vol. 59, no. 2, pp. 373–379, 1995.

## Research Article

# Effect Factors of Benzene Adsorption and Degradation by Nano-TiO<sub>2</sub> Immobilized on Diatomite

Lijun Cheng,<sup>1</sup> Yong Kang,<sup>1</sup> and Guishui Li<sup>2</sup>

<sup>1</sup> School of Chemical Engineering and Technology, Tianjin University, Tianjin 300072, China

<sup>2</sup> College of Mechanical Engineering, Tianjin University of Science and Technology, Tianjin 300222, China

Correspondence should be addressed to Yong Kang, ykang@eyou.com

Received 25 October 2012; Revised 11 November 2012; Accepted 26 November 2012

Academic Editor: Yong Yang

Copyright © 2012 Lijun Cheng et al. This is an open access article distributed under the Creative Commons Attribution License, which permits unrestricted use, distribution, and reproduction in any medium, provided the original work is properly cited.

Difference between adsorption of benzene by diatomite and nano-TiO<sub>2</sub> immobilized on diatomite was investigated. And effects of temperature, light intensity, relative humidity, and initial benzene concentration on adsorption and degradation of benzene by nano-TiO<sub>2</sub> immobilized on diatomite were also studied. The experimental results showed that when initial benzene concentration was  $2.2 \times 10^{-3} \text{ mg L}^{-1}$ , it could be degraded to below safe concentration ( $1.1 \times 10^{-4} \text{ mg L}^{-1}$ ) after 50 h when temperature was 20°C, but it just needed 30 h at 35°C. When light intensity was 6750 Lx, it needed 30 h for benzene to be degraded to below safe concentration, but benzene could barely be degraded without light. When relative humidity was 50%, benzene could be degraded to  $1.0 \times 10^{-4} \text{ mg L}^{-1}$  after 30 h, while its concentration could be reduced to  $7.0 \times 10^{-5} \text{ mg L}^{-1}$  at the relative humidity of 80%.

## 1. Introduction

Benzene, which primarily comes from coating, painting, adhesives, and other organic solvents inside buildings, has become one of the most toxic substances and has been identified as a kind of strong carcinogenic substance by World Health Organization. So it is very important and meaningful to remove benzene in houses and workplaces considering human health.

At present, there are some methods employed to remove benzene such as microbial degradation [1, 2], adsorption [3–7], catalytic oxidation [8–14], and so forth, among which photocatalytic degradation of benzene by TiO<sub>2</sub> has attracted wide attention [11–14]. This is because TiO<sub>2</sub> can degrade many toxic substances under mild conditions and cannot cause secondary pollution [15–18], besides being quite easy to operate, making it become a simple way to remove poisonous gases indoors. But as nano-size TiO<sub>2</sub> powder is inclined to aggregate to clusters and hard to be fixed, if being directly doped into coatings to paint walls or furnitures, it is very easy to fall off. So researchers have investigated many methods to fix TiO<sub>2</sub> on certain supports, among which diatomite is just a good carrier. As there exists a lot of silicon hydroxyls and hydrogen bonds on the surface

of diatomite, it can form strong force with TiO<sub>2</sub>, thus overcoming the difficulty of TiO<sub>2</sub> fixing. In addition, nano-TiO<sub>2</sub> immobilized on diatomite combines both large specific area of diatomite and strong oxidation ability of TiO<sub>2</sub>, which shows broad prospect in green adornments.

Based on our previous work [19–21], nano-TiO<sub>2</sub> immobilized on diatomite prepared by using TiOSO<sub>4</sub> as raw material, urea as precipitator and diatomite as support was employed to degrade benzene in this work. To verify advantage of nano-TiO<sub>2</sub> immobilized on diatomite, difference between adsorption of benzene by diatomite and nano-TiO<sub>2</sub> immobilized on diatomite was compared and effects of temperature, light intensity, relative humidity, and initial concentration of benzene on adsorption and degradation of benzene by nano-TiO<sub>2</sub> immobilized on diatomite were also discussed.

## 2. Experimental

Diatomite and nano-TiO<sub>2</sub> immobilized on diatomite were used as the adsorption and degradation materials, as discussed elsewhere [20]. Their morphology is shown in

TABLE 1: Chemical compositions and characteristics of diatomite and nano-TiO<sub>2</sub> immobilized on diatomite.

	Diatomite	Nano-TiO <sub>2</sub> immobilized on diatomite
Chemical compositions	Main: SiO <sub>2</sub> Other: Al <sub>2</sub> O <sub>3</sub> Fe <sub>2</sub> O <sub>3</sub> CaO MgO K <sub>2</sub> O Na <sub>2</sub> O and other organic substances	Main: SiO <sub>2</sub> TiO <sub>2</sub> Other: Al <sub>2</sub> O <sub>3</sub> Fe <sub>2</sub> O <sub>3</sub> CaO MgO K <sub>2</sub> O Na <sub>2</sub> O and other organic substances
Characteristics	Grain size and specific area were 10~100 μm and 1.2995 m <sup>2</sup> /g, respectively	Crystalline phase of TiO <sub>2</sub> was anatase, grain size was 150 nm and cover percent was 75%

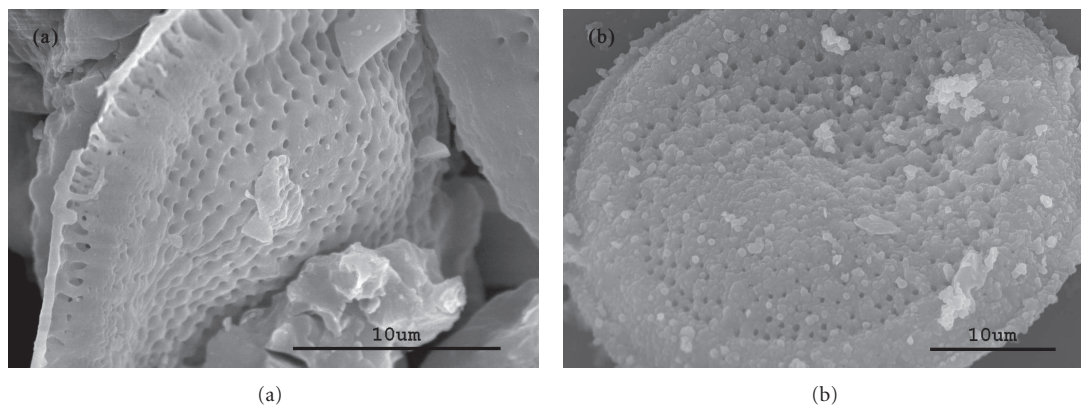
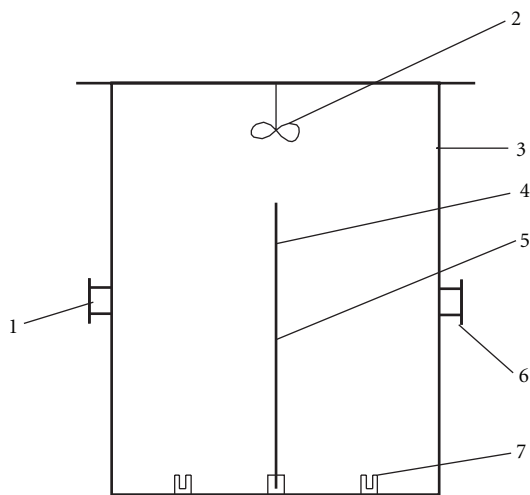
FIGURE 1: (a) The morphology of diatomite. (b) The morphology of nano-TiO<sub>2</sub> immobilized on diatomite.FIGURE 2: The innercircle reactor for degrading benzene (1-sample connection, 2-fan, 3-shell, 4-glass plate, 5-nano-TiO<sub>2</sub>, 6-injection port, 7-slot).

Figure 1. And their chemical compositions and characteristics are shown in Table 1. Benzene obtained by evaporating its standard solution (the concentration was 100 mg L<sup>-1</sup>) was used as the target degraded gas, initial concentration of which was 0.0022 mg L<sup>-1</sup>. Ground glass, the effective area of which was 0.08 m<sup>2</sup>, was used as the support of photocatalysts. The structure of the photocatalytic reactor (the volume was 5 L) is shown in Figure 2.

Adsorption by reactor: before experiment, the reactor was cleaned, dried, and sealed. Then the standard solution of benzene was injected into it. When the solvent evaporated thoroughly, it was put into illumination incubator with temperature of 35°C. During adsorption process, 1 mL gas was taken out from the reactor at regular intervals and analyzed by Gas Chromatography to determine the concentration of benzene.

Comparison of adsorption by diatomite and nano-TiO<sub>2</sub> immobilized on diatomite: nano-TiO<sub>2</sub> immobilized on diatomite of 2 g was put into the reactor and benzene's standard solution of 0.29 mL was also injected into it. Then the reactor was put into illumination incubator with temperature of 35°C and 5 fluorescent lamps opened. Like the above experiment, 1 mL gas was taken out from the reactor at regular intervals and analyzed by gas chromatography to determine the concentration of benzene. When finished, the reactor was cleaned and dried, and experiment was repeated with diatomite of 2 g under the same conditions to compare the difference of these two materials.

Effect of reaction conditions on degradation of benzene by nano-TiO<sub>2</sub> immobilized on diatomite: take the experiment about effect of temperature as example, nano-TiO<sub>2</sub> immobilized on diatomite of 2 g was put into the reactor and benzene's standard solution of 0.11 mL was also injected into it. Then the reactor was put into illumination incubator with temperature of 35°C and 5 fluorescent lamps opened. Similarly, 1 mL gas was taken out from the reactor at regular intervals and analyzed by gas chromatography to determine the concentration of benzene. The process ended when the concentration of benzene decreased to below its safe

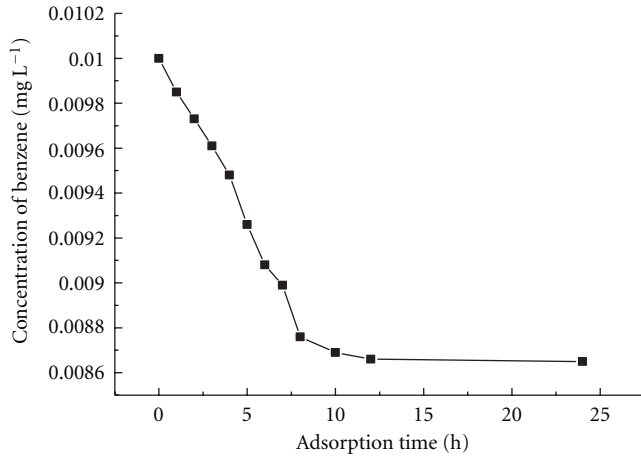


FIGURE 3: Curve of adsorption equilibrium by reactor.

concentration. Experiment was repeated at 20°C to study the effect of temperature on degradation of benzene.

### 3. Results and Discussion

**3.1. Adsorption by Reactor.** When benzene is injected into a closed reactor, some gas will be adsorbed to the wall of the reactor. Accordingly, the degradation ability of nano-TiO<sub>2</sub> immobilized on diatomite will be artificially increased if this part of adsorption capacity does not be excluded. In order to reduce this kind of error, the experiment about the adsorption of benzene by the reactor was conducted and the curve of adsorption equilibrium was obtained, as seen in Figure 3.

From Figure 3, it can be seen that the adsorption at the first 8 h was almost linear. The concentration of benzene reduced from 0.01 mg L<sup>-1</sup> to 0.00866 mg L<sup>-1</sup> after adsorption for 12 h and almost maintained unchanged until 24 h, implying the saturated concentration of benzene for the reactor was 0.00134 mg L<sup>-1</sup>. To avoid relative error, in the following experiments, the real adsorbed concentration of benzene by nano-TiO<sub>2</sub> was the concentration obtained by experiment minus 0.00134 mg L<sup>-1</sup>.

**3.2. Comparison of Adsorption by Diatomite and Nano-TiO<sub>2</sub> Immobilized on Diatomite.** The concentration changes of benzene adsorbed by diatomite and nano-TiO<sub>2</sub> immobilized on diatomite under the same mass are shown in Figure 4.

It can be seen from Figure 4 that adsorption and degradation of benzene by different materials were quite different. Diatomite has strong adsorption capacity owing to its many holes, as seen in Figure 1(a). At the first 12 h, the concentration of benzene decreased sharply. At this period, the adsorption rate of benzene on diatomite was much larger than the desorption rate. While at the later 12 h, the slope of the curve greatly decreased and tended to become unchanged, which demonstrated that the adsorption rate of benzene on diatomite was almost equal to the desorption rate and the concentration of benzene kept

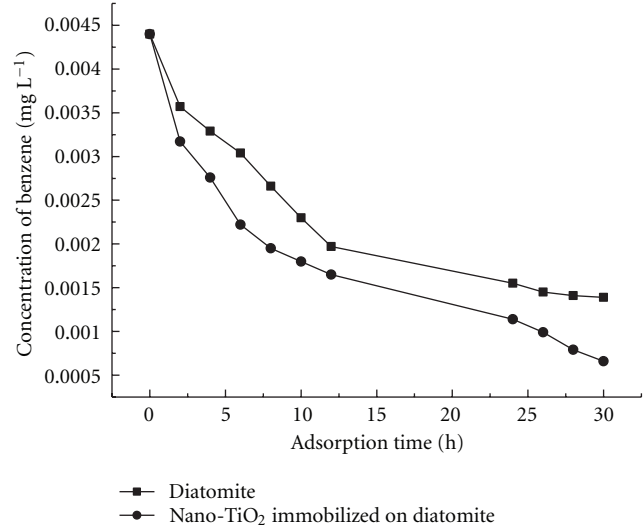


FIGURE 4: Comparison of adsorption between diatomite and nano-TiO<sub>2</sub> immobilized on diatomite.

steady. From the figure, it can be found that after adsorption by diatomite of 2 g, the concentration of benzene reduced from 0.0044 mg L<sup>-1</sup> to 0.00139 mg L<sup>-1</sup>.

While for the nano-TiO<sub>2</sub> immobilized on diatomite, the adsorption rate at the first 12 h was greater than that of diatomite. This was because benzene was not only adsorbed to the diatomite through physical effect but also oxidized to CO<sub>2</sub> and H<sub>2</sub>O by light-generated holes on the surface of the nano-TiO<sub>2</sub>, which led to more adsorption of benzene on nano-TiO<sub>2</sub> immobilized on diatomite than on diatomite alone. Moreover, the concentration of benzene still kept decreasing until 30 h, although the degradation rate was smaller than that of the first 12 h. At this stage, desorption of benzene from the nano-TiO<sub>2</sub> immobilized on diatomite gradually appeared, but the desorption rate was still smaller than the adsorption rate, so the concentration of benzene still kept reducing, indicating that the nano-TiO<sub>2</sub> had lasting degradation effect on benzene.

**3.3. Effect of Temperature on Adsorption and Degradation of Benzene by Nano-TiO<sub>2</sub> Immobilized on Diatomite.** The change tendencies of benzene's concentration under different temperature are shown in Figure 5.

It demonstrated that the degradation rate of benzene increased with the rise of reaction temperature. From the figure, it can be seen that when the temperature was 20°C, it needed 50 h for benzene of 0.0022 mg L<sup>-1</sup> to be degraded to below the safe concentration, while it just needed 32 h when the reaction temperature was 35°C. This may be explained as follows. First, the internal energy of benzene molecules increased with the rise of temperature and their irregular movement became fiercer, which made the cyclic process of benzene's adsorption and desorption on the surface of nano-TiO<sub>2</sub> much faster, but the adsorption rate and degradation rate were larger than that of desorption, so the concentration of benzene kept decreasing. Second, when the temperature

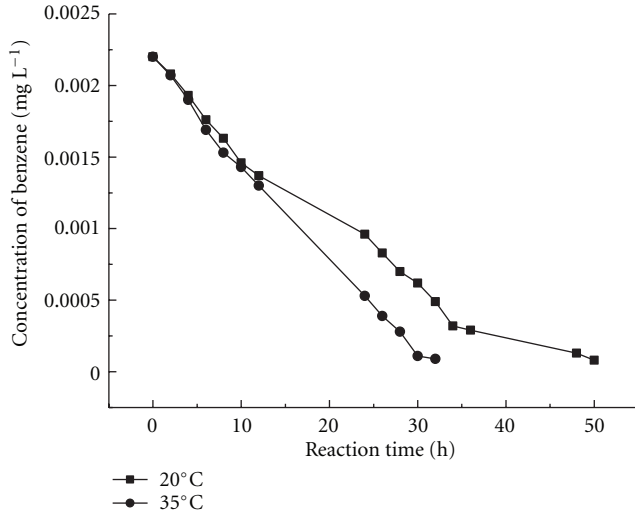


FIGURE 5: Effect of temperature on degradation of benzene by nano-TiO<sub>2</sub> immobilized on diatomite.

was high, the saturation vapor pressure of steam increased, which led to decrease of relative humidity in the reactor. In this case, the nano-TiO<sub>2</sub> would release the steam and other dissolved gases adsorbed before to relieve the decrease of humidity. So the diatomite would adsorb more benzene and more benzene could be oxidized to nontoxic gases by nano-TiO<sub>2</sub>. While at low temperature, the benzene molecules were relatively steady and the rates of adsorption, degradation, and desorption were much slower, so the decrease rate of benzene's concentration at high temperature was relatively larger.

**3.4. Effect of Light Intensity on Adsorption and Degradation of Benzene by Nano-TiO<sub>2</sub> Immobilized on Diatomite.** Light intensity is another factor which has important effect on degradation of benzene by nano-TiO<sub>2</sub> immobilized on diatomite. As known, TiO<sub>2</sub> can be activated by ultraviolet light. After being activated, the photogenerated electrons and holes will reduce or oxidize the organics and inorganics adsorbed to the surface of the nano-TiO<sub>2</sub>. When the wavelength is definite, the intensity of the light will determine the number of electrons and holes generated by illumination, thus determining the concentration of benzene degraded by TiO<sub>2</sub>. It is the same for ultraviolet in visible light. Besides, as the light intensity at every point in the light range is different for different light source and different light space, so average light intensity is used as the intensity in certain space. According to the following formula [22]:

$$E_{av} = \frac{N \times \Phi_s \times U \times K}{A}, \quad (1)$$

$E_{av}$ —average light intensity, Lx;  $N$ —number of fluorescent lamp;  $\Phi_s$ —light flux of a fluorescent lamp, Lm;  $U$ —use coefficient, generally 0.4;  $K$ —maintenance coefficient, 0.8;  $A$ —Incubator's bottom surface area, 0.2 m<sup>2</sup> the average light intensity with different number of fluorescent lamp is listed in Table 2.

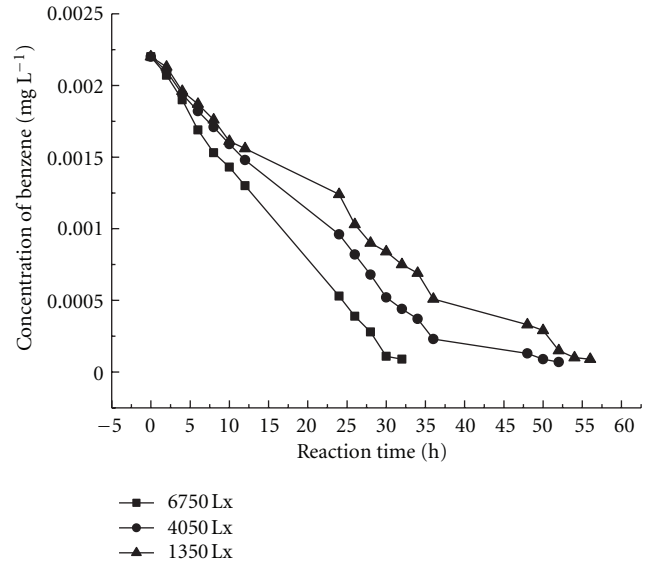


FIGURE 6: Effect of light intensity on degradation of benzene by nano-TiO<sub>2</sub> immobilized on diatomite.

TABLE 2: The average light intensity for different number of lamp.

$N$ (number of lamps)	$E_{av}$ (Lx)
1	1350
3	4050
5	6750

The changes of benzene's concentration at different light intensity are shown in Figure 6.

It can be found that when the light intensity was definite, the concentration of benzene decreased with time going on. For example, when the light intensity was 4050 Lx, the concentration of benzene reduced sharply at the first 35 h, while the rate became much smaller after that; this was also because at the first 35 h, the adsorption rate and the degradation rate were much greater than the desorption rate, so decrease of benzene's concentration was significant, with time increasing, the desorption of benzene from the surface of photocatalyst gradually became apparent, causing the decrease rate of benzene's concentration become small. Besides, it can be seen that the stronger the light intensity was, the larger the decrease rate of benzene was. When the light intensity was 6750 Lx it just needed 30 h for benzene to be degraded to below the safe concentration, while it cost more than 30 h when the light intensity was 1350 Lx and 4050 Lx. This was because more holes were generated at large light intensity than at small light intensity, leading to faster degradation of benzene.

**3.5. Effect of Relative Humidity on Adsorption and Degradation of Benzene by Nano-TiO<sub>2</sub> Immobilized on Diatomite.** Relative humidity is also an effect which has important impact on degradation of benzene. In this section, the standard solution of 0.27 mL was first injected into the reactor, implying the water's volume was 0.27 mL. To realize

TABLE 3: Volume of deionized water needed to be added at different relative humidity.

Relative humidity (%)	Volume of deionized water (mL)
50	0.110
60	0.132
70	0.154
80	0.176

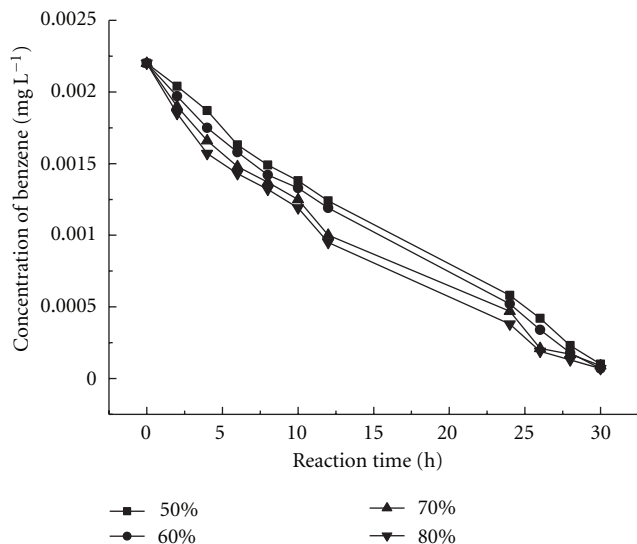


FIGURE 7: Effect of relative humidity on degradation of benzene by nano-TiO<sub>2</sub> immobilized on diatomite.

relative humidity of 50%, 60%, 70%, and 80%, the volumes of deionized water needed to be added into the reactor were calculated according to gas state equation when the temperature was 35°C. The results are listed in Table 3.

Figure 7 shows the changes of benzene's concentration with reaction time under different relative humidity.

As is known, when the photogenerated holes transfer to the surface of TiO<sub>2</sub>, they can accept electrons from O<sub>2</sub> and H<sub>2</sub>O to generate •O<sup>2-</sup> and •OH, which have strong oxidation ability. Undoubtedly, the more H<sub>2</sub>O there is, the more free radical there can produce. So it is beneficial for degradation of benzene when the relative humidity increases. It can also be found from Figure 7 that the degradation rate of benzene increased with the relative humidity ranging from 50% to 80%. But it is not to say the relative humidity can be infinite. In practice, there is certain range of humidity for people to endure, about 40% to 70%. So for degradation of benzene, the principle is the bigger the relative humidity is, the better the effect is, but people's comfort is the first to be considered.

**3.6. Effect of Benzene's Initial Concentration on Adsorption and Degradation of Benzene by Nano-TiO<sub>2</sub> Immobilized on Diatomite.** When benzene's initial concentration is different, the degradation situation will be quite different. To verify effect of initial concentration on the degradation of benzene by nano-TiO<sub>2</sub> immobilized on diatomite, two groups of

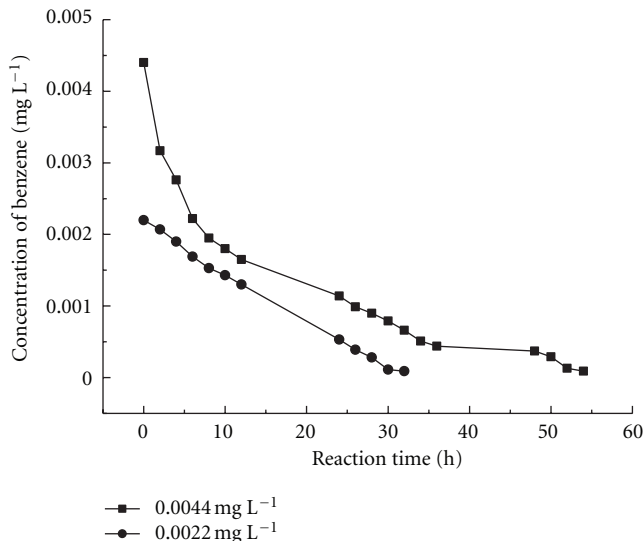


FIGURE 8: Effect of initial concentration on degradation of benzene by nano-TiO<sub>2</sub> immobilized on diatomite.

experiments were carried out and the results are shown in Figure 8.

As Figure 8 shown, at first hours, the higher the initial concentration was, the larger the degradation rate was. This could be explained by degradation process of benzene by TiO<sub>2</sub>. First, benzene was adsorbed to the surface of TiO<sub>2</sub>. Second, it was oxidized to nontoxic organics or even CO<sub>2</sub> and H<sub>2</sub>O. Third, the products were desorbed from the surface of TiO<sub>2</sub>. When the initial concentration of benzene was higher, there was more benzene adsorbed to the surface of TiO<sub>2</sub>, so the decrease rate of benzene was larger at first hours. But with time going on, the desorption of benzene from the surface of catalyst gradually appeared, which hampered the further adsorption and degradation of benzene, so the decrease rate of benzene's concentration became smaller. When initial concentration was 0.0022 mg L<sup>-1</sup>, it could decrease about 95% after 30 h, which was higher than that of Pd/TiO<sub>2</sub> [11] in efficiency.

## 4. Conclusions

Diatomite can only adsorb benzene, while nano-TiO<sub>2</sub> immobilized on diatomite not only can adsorb benzene but also can degrade benzene to nontoxic organics. Experiments about effect of reaction conditions on adsorption and degradation of benzene by nano-TiO<sub>2</sub> immobilized on diatomite showed that temperature had great effect on the adsorption and degradation process, when the initial concentration of benzene was 0.0022 mg L<sup>-1</sup>, it could be degraded to below the safe concentration by nano-TiO<sub>2</sub> immobilized on diatomite after 30 h when temperature was 35°C, while 50 h was needed when temperature was 20°C. Light intensity was direct driving of the degradation process. TiO<sub>2</sub> could not play role of degradation when there was no light, while it just needed 32 h to degrade benzene to below the safe concentration when light intensity was 6750 Lx. Relative

humidity also impacted the degradation process. When relative humidity was 50%, the concentration of benzene could reduce from  $0.0022 \text{ mg L}^{-1}$  to  $0.0001 \text{ mg L}^{-1}$  after 30 h, but it could reduce to  $0.00007 \text{ mg L}^{-1}$  at humidity of 80%. Besides, when initial concentration was  $0.0022 \text{ mg L}^{-1}$ , it could decrease to below safe concentration after 30 h, while the time was 54 h when initial concentration was  $0.0044 \text{ mg L}^{-1}$ . In short, the nano-TiO<sub>2</sub> immobilized on diatomite not only showed high adsorption and degradation capacity for benzene, but also could be used in decorative materials to remove benzene indoors conveniently.

## References

- [1] H. Masumoto, F. Kurisu, I. Kasuga et al., "Complete mineralization of benzene by a methanogenic enrichment culture and effect of putative metabolites on the degradation," *Chemosphere*, vol. 86, no. 8, pp. 822–828, 2012.
- [2] J. Rakoczy, K. M. Schleinitz, N. Müller, H. H. Richnow, and C. Vogt, "Effects of hydrogen and acetate on benzene mineralisation under sulphate-reducing conditions," *FEMS Microbiology Ecology*, vol. 77, no. 2, pp. 238–247, 2011.
- [3] C. Long, Y. Li, W. Yu et al., "Removal of benzene and methyl ethyl ketone vapor: comparison of hypercrosslinked polymeric adsorbent with activated carbon," *Journal of Hazardous Materials*, vol. 203–204, pp. 251–256, 2012.
- [4] A. B. Ene, T. Archipov, and E. Roduner, "Competitive adsorption and interaction of benzene and oxygen on Cu/HZSM5 zeolites," *Journal of Physical Chemistry C*, vol. 115, no. 9, pp. 3688–3694, 2011.
- [5] M. A. Lillo-Ródenas, D. Cazorla-Amorós, and A. Linares-Solano, "Benzene and toluene adsorption at low concentration on activated carbon fibres," *Adsorption*, vol. 17, no. 3, pp. 473–481, 2011.
- [6] L. Serrano, I. Urruzola, D. Nemeth, K. Belafi-Bako, and J. Labidi, "Modified cellulose microfibrils as benzene adsorbent," *Desalination*, vol. 270, no. 1–3, pp. 143–150, 2011.
- [7] M. Aivalioti, I. Vamvasakis, and E. Gidarakos, "BTEX and MTBE adsorption onto raw and thermally modified diatomite," *Journal of Hazardous Materials*, vol. 178, no. 1–3, pp. 136–143, 2010.
- [8] S. Zuo and C. Qi, "Modification of Co/Al<sub>2</sub>O<sub>3</sub> with Pd and Ce and their effects on benzene oxidation," *Catalysis Communications*, vol. 15, no. 1, pp. 74–77, 2011.
- [9] Q. Ye, J. Zhao, F. Huo et al., "Nanosized Ag/α-MnO<sub>2</sub> catalysts highly active for the low-temperature oxidation of carbon monoxide and benzene," *Catalysis Today*, vol. 175, no. 1, pp. 603–609, 2011.
- [10] W. Zhao, Y. Liu, L. Wang et al., "Catalytic combustion of benzene on the Pd/nanosize Al-HMS," *Microporous and Mesoporous Materials*, vol. 138, no. 1–3, pp. 215–220, 2011.
- [11] J. B. Zhong, Y. Lu, W. D. Jiang et al., "Characterization and photocatalytic property of Pd/TiO<sub>2</sub> with the oxidation of gaseous benzene," *Journal of Hazardous Materials*, vol. 168, no. 2–3, pp. 1632–1635, 2009.
- [12] T. D. Bui, A. Kimura, S. Higashida, S. Ikeda, and M. Matsumura, "Two routes for mineralizing benzene by TiO<sub>2</sub>-photocatalyzed reaction," *Applied Catalysis B*, vol. 107, no. 1–2, pp. 119–127, 2011.
- [13] Y. Hu, D. Li, Y. Zheng et al., "BiVO<sub>4</sub>/TiO<sub>2</sub> nanocrystalline heterostructure: a wide spectrum responsive photocatalyst towards the highly efficient decomposition of gaseous benzene," *Applied Catalysis B*, vol. 104, no. 1–2, pp. 30–36, 2011.
- [14] Y. J. Xu, Y. Zhuang, and X. Fu, "New insight for enhanced photocatalytic activity of TiO<sub>2</sub> by doping carbon nanotubes: a case study on degradation of benzene and methyl orange," *Journal of Physical Chemistry C*, vol. 114, no. 6, pp. 2669–2676, 2010.
- [15] S. Liu, B. Liu, K. Nakata et al., "Electrospinning preparation and photocatalytic activity of porous TiO<sub>2</sub> nanofibers," *Journal of Nanomaterials*, vol. 2012, Article ID 491927, 5 pages, 2012.
- [16] Y. Dong, J. Chao, Z. Xie et al., "Highly ordered TiO<sub>2</sub> macropore arrays as transparent photocatalysts," *Journal of Nanomaterials*, vol. 2012, Article ID 762510, 6 pages, 2012.
- [17] G. Hong and C. Ma, "Photocatalytic degradation of indoor air pollutants by Pt–TiO<sub>2</sub>," *Journal of Nanomaterials*, vol. 2012, Article ID 405361, 5 pages, 2012.
- [18] Y. Han, H. S. Kim, and H. Kim, "Relationship between synthesis conditions and photocatalytic activity of nanocrystalline TiO<sub>2</sub>," *Journal of Nanomaterials*, vol. 2012, Article ID 427453, 10 pages, 2012.
- [19] C. Yu, *The Study on Preparation of Nanosized TiO<sub>2</sub> Immobilized to Diatomite Particles and Degradation Process of Formaldehyde*, Tianjin University, Tianjin, China, 2007.
- [20] C. L. Yu, Y. Kang, and W. Zhao, "Preparation of nano-TiO<sub>2</sub> immobilized onto diatomite micro-particles," *Nanotechnology and Precision Engineering*, vol. 6, no. 4, pp. 254–260, 2008.
- [21] C. Yu, H. Quan, and Y. Kang, "Experimental study on the formaldehyde degradation by nano-TiO<sub>2</sub> immobilized on diatomite," *Acta Scientiae Circumstantiae*, vol. 32, no. 1, pp. 1–6, 2012.
- [22] H. Xiao, *Electric Lighting Technology*, chapter 5, China Machine Press, 2009.

## Research Article

# Participation of the Third Order Optical Nonlinearities in Nanostructured Silver Doped Zinc Oxide Thin Solid Films

C. Torres-Torres,<sup>1</sup> L. Castañeda,<sup>2</sup> M. Trejo-Valdez,<sup>3</sup> A. Maldonado,<sup>4</sup> and R. Torres-Martínez<sup>5</sup>

<sup>1</sup> *Sección de Estudios de Posgrado e Investigación, ESIME-Z, Instituto Politécnico Nacional, 07738 México, DF, Mexico*

<sup>2</sup> *Escuela Superior de Ingeniería Mecánica y Eléctrica Unidad Ticomán, Instituto Politécnico Nacional, 07340 México, DF, Mexico*

<sup>3</sup> *ESIQIE, Instituto Politécnico Nacional, 07738 México, DF, Mexico*

<sup>4</sup> *Departamento de Ingeniería Eléctrica, CINVESTAV IPN-SEES, A. P. 14740, 07000 México, DF, Mexico*

<sup>5</sup> *Centro de Investigación en Ciencia Aplicada y Tecnología Avanzada Unidad Querétaro, Instituto Politécnico Nacional, 76090 Santiago de Querétaro, QRO, Mexico*

Correspondence should be addressed to L. Castañeda, [luisca@cablevision.net.mx](mailto:luisca@cablevision.net.mx)

Received 9 October 2012; Accepted 19 November 2012

Academic Editor: Masayuki Nogami

Copyright © 2012 C. Torres-Torres et al. This is an open access article distributed under the Creative Commons Attribution License, which permits unrestricted use, distribution, and reproduction in any medium, provided the original work is properly cited.

We report the transmittance modulation of optical signals in a nanocomposite integrated by two different silver doped zinc oxide thin solid films. An ultrasonic spray pyrolysis approach was employed for the preparation of the samples. Measurements of the third-order nonlinear optical response at a nonresonant 532 nm wavelength of excitation were performed using a vectorial two-wave mixing. It seems that the separated contribution of the optical nonlinearity associated with each film noticeable differs in the resulting nonlinear effects with respect to the additive response exhibited by the bilayer system. An enhancement of the optical Kerr nonlinearity is predicted for prime number arrays of the studied nanoclusters in a two-wave interaction. We consider that the nanostructured morphology of the thin solid films originates a strong modification of the third-order optical phenomena exhibited by multilayer films based on zinc oxide.

## 1. Introduction

The attractive features related to nonlinear optical media are mainly given by the potential applications in diverse areas for optical communications, instrumentation techniques, sensors, actuators, and processing of signals, among other purposes [1]. Certainly, all materials can exhibit a third order optical nonlinearity; but those that are functionally considered third-order optical materials, in a higher level, are capable to present noteworthy changes in absorptive and refractive effects with dependence on irradiance excitations. Several scientific researches about distinct processing routes for preparing advanced optical materials have been carried out [2]; however, the powerful and ultrafast optical response of nanostructures has given rise to their relevance in the development of low-dimensional nonlinear optical devices for photonic effects or electrical phenomena [3]. In this respect, one of the most important physical behaviors

responsible of the modification of the optical features of nanoparticles is given by the quantum confinement, which originates a discrete and sharp selective participation of the electronic nature in a sample with physical properties strongly dependent on size and shape [4]. Besides, it also has been demonstrated that a reinforcement of particular optical processes can be engineered by quantum conditions [5]. Apparently, the influence of the environment on the nanoparticles also should be taken into account in order to better describe their optical and electrical characteristics [6, 7]. Therefore, with the inclusion of dopants to produce changes in the morphology of a nanostructured material, it is expected to accomplish the possibility to tailor the optical nonlinearities [8]. Zinc oxide (ZnO) is a promising transparent material with fascinating optical and photoconductive properties [9, 10]. An outstanding participation of silver (Ag) ions in the improved optical response of ZnO thin films has been pointed out [11]. Thus, in this work, we

analyze a nonlinear optical experiment with a nonresonant excitation in Ag doped ZnO samples. We study the nonlinear optical response of two different thin solid films in order to make notice of the resulting nonlinearity dependent on the duplication of the thickness of the film. Finally, we find that a prime number array of the studied nanoclusters in a two-wave interaction can generate an important enhancement of the optical Kerr effect.

## 2. Experimental Details

**2.1. Processing Route of the Samples.** ZnO:Ag thin solid films were deposited from a 0.4 M solution of zinc (II) acetate  $[\text{Zn}(\text{O}_2\text{CCH}_3)_2]$  (from Alfa, 98%), dissolved in a mix of deionized water, acetic acid  $[\text{CH}_3\text{CO}_2\text{H}]$  (from Baker, 98%), and methanol  $[\text{CH}_3\text{OH}]$  (from Baker, 98%) (100:100:800 volume proportion). Separately, a 0.2 M solution of silver nitrate  $[\text{Ag}(\text{NO}_3)]$  (from Baker, 98%) dissolved in a mix of deionized water and acetic acid  $[\text{CH}_3\text{CO}_2\text{H}]$  (from Baker, 98%) (1:1 vol. proportion) was prepared, in order to be used as doping source. A constant  $[\text{Ag}]/[\text{Zn}]$  ratio of 2 at. % was used. The deposition system used in this work includes a piezoelectric transducer operating at variable frequency, which was set to 1.2 MHz and the ultrasonic power at 120 W. ZnO:Ag films were deposited onto soda-lime glass substrates with an area of  $2.0 \times 1.0 \text{ cm}^2$ . The details of the deposition system have been previously described [12]. The cleaning process of the substrates is as follows: (i) sonication for 5 minutes in trichloroethylene ( $(\text{C}_2\text{HCl}_3)$  from Baker, 98%) for degreasing the substrates, followed by (ii) sonication in methyl alcohol ( $(\text{CH}_3\text{OH})$  from Aldrich, 98%), (iii) sonication in acetone ( $(\text{CH}_3\text{COCH}_3)$  from Baker, 98%), and finally, (iv) the substrates are dried by a jet of pure and dry nitrogen ( $(\text{N}_2)$  from PRAXAIR, 99.997%). Then the substrates were placed on a fused tin bath, whose temperature was measured just below the substrate using a chromel-alumel thermocouple, which is contained in a stainless steel metal jacket. The substrate temperature ( $T_s$ ) was  $400^\circ\text{C}$ , within an accuracy of  $\pm 0.5^\circ\text{C}$ . Pure  $\text{N}_2$  (from PRAXAIR, 99.997%) was used as the solution carrier and director gas, with flow rates of 3.5 and 0.5 L/min, respectively. In order to promote the crystallization, the samples were annealed at  $400^\circ\text{C}$  in a  $\text{N}_2$  atmosphere showing a better densification traduced as a reduction of particle size when the annealing lasts 4 hrs. The thickness of the deposited films onto soda-lime glass was manipulated by controlling the time of deposition. The film thickness obtained after 10 and 5 minutes of deposition was measured with a KLA Tencor P15 profilometer, resulting in approximately 500 nm and 250 nm, respectively. The morphology of the thin films was analyzed using Scanning Electronic Microscopy (SEM) performed with a FEI Quanta 3D FEG Microscope system in STEM mode (Scanning Transmission Electronic Microscopy). The elemental composition of the samples was obtained by Auger Electron Spectroscopy (AES) using a JAMP-7800 (JEOL) equipment, with a base pressure of  $8.6 \times 10^{-8} \text{ Pa}$  ( $6.15 \times 10^{-10} \text{ torr}$ ). The parameters of the primary electron beam were 10 keV of energy and  $0.34 \mu\text{A}$  of current. The samples were inclined at  $55^\circ$  with respect to the normal

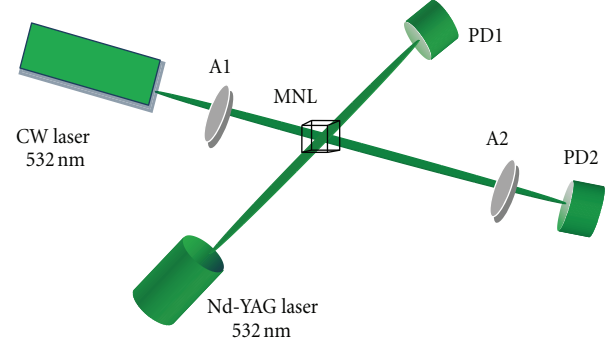


FIGURE 1: Schematic illustration of the experimental setup for the vectorial two-wave interaction.

of the surface. The linear transmittance spectra of the thin films were acquired with a Perkin Elmer XLS UV-visible spectrophotometer.

**2.2. Third Order Nonlinear Optical Response.** The annealed thin solid film samples were investigated measuring the optical transmittance in a vectorial two-wave mixing experiment. Separated measurements on different thin solid films with thickness of 500 nm and 250 nm were performed. Then, we measured a tandem configuration integrated initially by two films with 250 nm thickness put together to obtain a 500 nm sample width; finally another tandem configuration was measured in the same fashion with the two films of 500 nm thickness giving a 1000 nm thickness of total sample width. Figure 1 illustrates the experimental setup. MNL represents the sample, A1-2 are polarizers, and PD1-2 are photodetectors with integrated filters. Pump and probe beams, with linear polarizations making an angle of  $45^\circ$ , are in simultaneous propagation in the same region of interaction of the studied sample. A solid state laser with 1.5 W of average power and 532 nm wavelength was employed as a probe beam; whereas a nanosecond Nd:YAG laser with 532 nm wavelength and maximum energy of 375 mJ per pulse at 1 Hz was employed as a pump. The diameter of the beam waist for the probe beam in the sample was measured to be 1 mm and for the pump beam was 6 mm.

In order to describe the propagation of the electric fields in the two-wave interaction taking into account a null self-diffraction phenomenon, we follow the procedure to obtain the expressions for the amplitudes of the transmitted fields derived elsewhere [13]

$$E_{1\pm}(z) = \left[ E_{1\pm}^0 J_0(\Psi_{\pm}^{(1)}) + iE_{2\pm}^0 J_1(\Psi_{\pm}^{(1)}) \right] \exp\left(-i\Psi_{\pm}^{(0)} - \frac{\alpha z}{2}\right), \quad (1)$$

$$E_{2\pm}(z) = \left[ E_{2\pm}^0 J_0(\Psi_{\pm}^{(1)}) - iE_{1\pm}^0 J_1(\Psi_{\pm}^{(1)}) \right] \exp\left(-i\Psi_{\pm}^{(0)} - \frac{\alpha z}{2}\right), \quad (2)$$

where  $E_{1\pm}(z)$  and  $E_{2\pm}(z)$  are the complex amplitudes of the circular components of the transmitted waves beams; while  $E_{1\pm}^0$  and  $E_{2\pm}^0$  are the amplitudes of the incident waves at the surface of the sample;  $\alpha$  is the optical absorption coefficient;

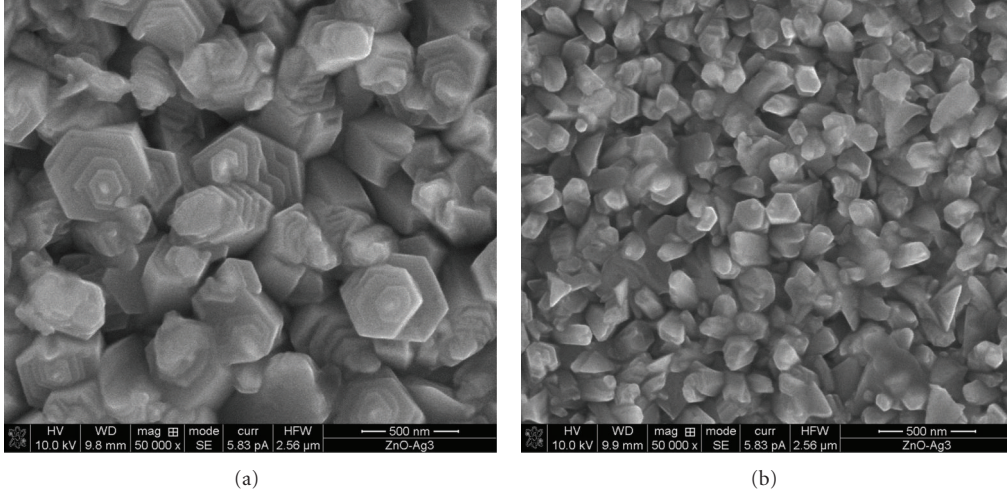


FIGURE 2: Typical SEM micrograph of the ZnO:Ag films (a) as-deposited (b) after annealing at 400°C in nitrogen.

$J_m(\Psi_{\pm}^{(1)})$  stands for the Bessel function of order  $m$ ,  $z$  is the thickness of the nonlinear media, and

$$\Psi_{\pm}^{(0)} = \frac{4\pi^2 z}{n_0 \lambda} \left[ A \sum_{j=1}^2 |E_{j\pm}|^2 + (A+B) \sum_{j=1}^2 |E_{j\mp}|^2 \right], \quad (3)$$

$$\Psi_{\pm}^{(1)} = \frac{4\pi^2 z}{n_0 \lambda} [A E_{1\pm} E_{2\pm}^* + (A+B) E_{1\mp} E_{2\mp}^*], \quad (4)$$

are the nonlinear phase changes. Here  $A = 6\chi_{1122}^{(3)}$  and  $B = 6\chi_{1221}^{(3)}$ , which are the independent components of the third-order susceptibility tensor  $\chi^{(3)}$  for an isotropic material. The optical wavelength is represented by  $\lambda$  and the refractive index is  $n_o$ .

### 3. Results and Discussion

From Figure 2, it can be observed a representative panoramic view of one region of the samples obtained by Scanning Electronic Microscopy (SEM). Both images show evidence of the nanostructured morphology that can be obtained with the ultrasonic spray pyrolysis deposition technique. The grain size distribution range results in grains with 400 nm to 500 nm for the as-deposited sample, while these grain size distributions are reduced by the annealing process as it has been previously indicated [12] resulting in values from 100 nm to 200 nm. The surface morphology of ZnO:Ag thin films is composed of individual grains resembling slices with hexagonal shape; it can also be noted that secondary grains are formed by stacks of slices, on top of which there is a kind of spiral. This type of defects can be identified as screw dislocations. It is usual to find out similar characteristics in ZnO thin films deposited by ultrasonic spray pyrolysis [14]. Columnar grains with a hexagonal shaped form were observed in both cases.

The doping concentration through the films was determined by AES. A uniform distribution of the Ag and an absence of segregation were observed. The Ag content within

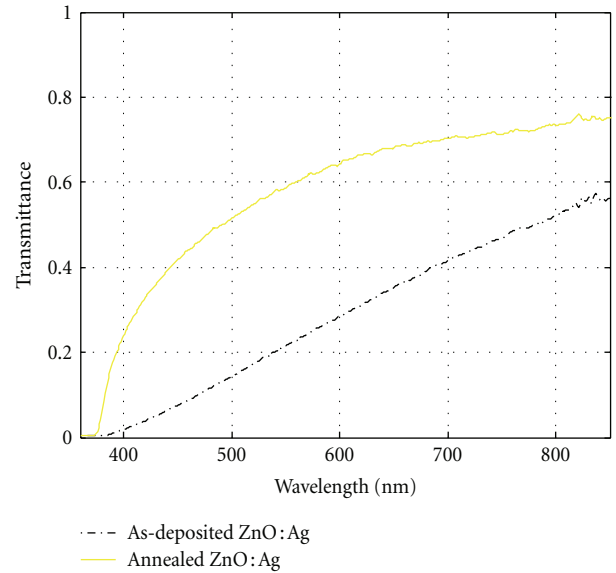


FIGURE 3: Transmittance spectra of the samples.

the films was always below the values corresponding to the starting solution, possibly due to the evaporation of an Ag fraction during the film growth. However, it was confirmed that the annealing process does not participate in the evaporation of Ag after the deposition process. The resulting distribution of Ag in the ZnO:Ag samples were found to be close 1.0 at.%. Finally a stoichiometric relationship between Zn and O, corresponding to ZnO was observed throughout the whole films.

The corresponding linear transmittance spectra obtained for the studied ZnO:Ag thin solid films are shown in Figure 3. One can clearly notice a significant effect of transparency resulting from the annealing process in the film for wavelengths above about 400 nm in the plot.

The polarized irradiances of the transmitted beams in the two-wave interaction were measured in different cases

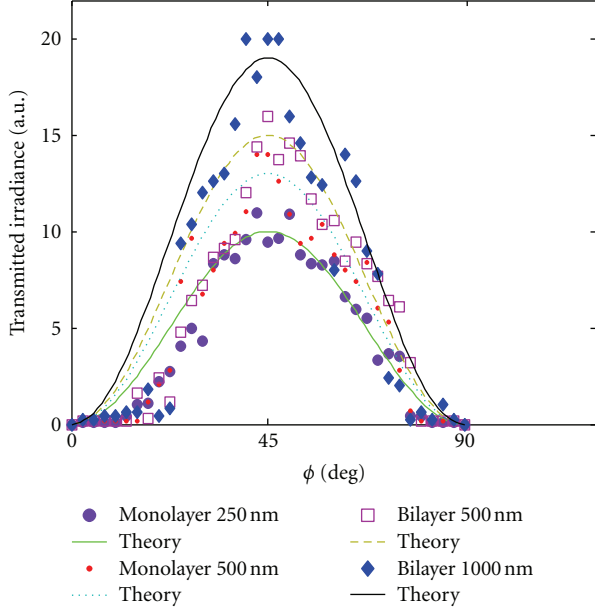


FIGURE 4: Nonlinear optical results.

TABLE 1: Magnitude of the third-order optical susceptibility in the studied samples.

		$ \chi^{(3)} $ [esu]	
Monolayer 250 nm	Monolayer 500 nm	Bilayer 500 nm	Bilayer 1000 nm
$4.4 \times 10^{-9}$	$1.9 \times 10^{-9}$	$3.7 \times 10^{-9}$	$1.8 \times 10^{-9}$

of polarization of the incident beams making an angle  $\varphi$  between their planes of polarization. The axes of transmission of the analyzers A1-2 were aligned in order to detect the orthogonal components of the polarization of the probe waves. An error bar of  $\pm 10\%$  was estimated for the experimental irradiance data. By comparing numerical simulations of (1)–(4) with the data obtained from the transmitted irradiances in the thin film samples, we obtained the nonlinear optical parameters. Figure 4 shows the experimental transmittance of the probe beam with the best fitting of the numerical simulations.

The estimated  $|\chi^{(3)}|$  parameters are presented in Table 1.

As a comparative result, we measured the nonlinear optical response for a pure ZnO thin solid film sample and then we find that  $|\chi^{(3)}| = 6.2 \times 10^{-11}$  esu. These last results are comparable with the nanosecond nonlinear optical response previously reported for ZnO and ZnO:Ag samples were prepared with different processing techniques [15].

Numerical simulations made by (1)–(4) allow us to compare the nonlinear optical enhancement related to the spatial period of the distributions of the nanoclusters in a bilayer ZnO thin solid film. We consider that the first and the second layer display periodic periods,  $T_A$  and  $T_B$ , respectively. Figure 5 illustrates the variation in the predicted nonlinear optical response for the studied samples when we consider that a periodic distribution of nanoclusters can be founded

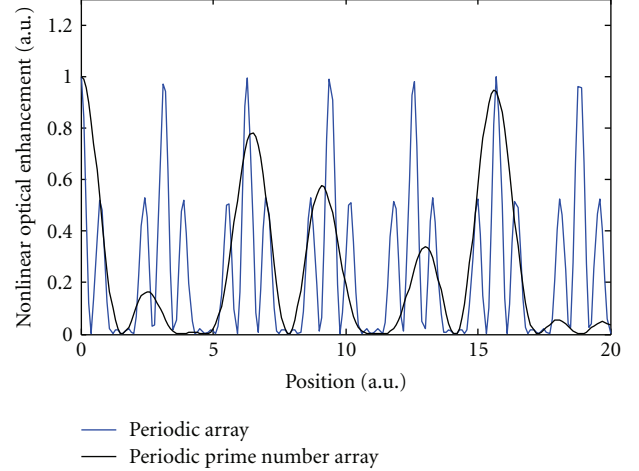


FIGURE 5: Third-order nonlinear optical response as a function of the distribution of the nanoclusters in a bilayer film.

in each film and the resulting rate relation between these two periodicities,  $T_A/T_B$ , is a pair number or a prime number.

Remarkable differences in the nonlinear optical response of aligned periodic arrays are shown in Figure 5. It is worth noting to mention that this contrast is absent when the comparison concerns to arrays with pairs or odds  $T_A/T_B$  numbers. Nevertheless, pertaining to the studied prime number case, the distinctiveness is consequence from the irregular contributions from each particular region provided by the first nanocluster-containing film to the second one in a bilayer system of samples. Similar deductions have been achieved for plasmonic arrays of nanoparticles [16, 17]. Regarding the expanded distribution of interacting nanoclusters in multilayer arrays of thin films, it could be derived an increase in the participation of the nanoclusters by the modification of the volume fraction with respect to the area of the total interacting sample. Therefore, the opportunity to give rise to an enhancement of multiphotonic interactions seems to be possible. We consider that the major role about the involvement of the nanoclusters in a cascade nonlinear optical effect is to promote radiative recombination and excitations concerning to quantum confinement, with the benefits on the optical Kerr response by stronger accumulations of irradiance in the whole sample.

#### 4. Conclusion

Within this work, we identified important differences in the nonlinear optical properties exhibited by monolayer and bilayer silver doped zinc oxide thin solid films prepared by an ultrasonic spray pyrolysis technique. A vectorial two-wave mixing experiment allows us to modulate the optical transmittance of a nonresonant 532 nm wavelength of excitation in the samples for evaluating the magnitude of the third order nonlinearities. We observed that a strong enhancement in the nonlinear optical response of zinc oxide can be obtained by silver doping and by prime number arrays in multiwave mixing interactions. Apparently, the thickness and the nanostructured morphology of the thin solid films

originate a strong modification of the third order optical phenomena exhibited by zinc oxide thin films. Potential applications for developing all-optical devices can be contemplated.

## Acknowledgments

The authors kindly acknowledge the financial support from Instituto Politécnico Nacional, COFAA-IPN, Centro de Investigación y de Estudios Avanzados del Instituto Politécnico Nacional, Instituto de Ciencia y Tecnología del DF through grants PIUTE10-129 and PIUTE-082, and Consejo Nacional de Ciencia y Tecnología. The authors are also thankful to the Central Microscopy facilities of the Centro de Nanociencias y MicroNanotecnologías del IPN.

## References

- [1] R. W. Boyd, *Nonlinear Optics*, Academic Press, San Diego, Calif, USA, 1992.
- [2] M. B. de La Mora, J. A. del Río, R. Nava et al., “Anomalous patterned scattering spectra of one-dimensional porous silicon photonic crystals,” *Optics Express*, vol. 18, no. 22, pp. 22808–22816, 2010.
- [3] H. Rigneault, J.-M. Lourtioz, C. Delalande, and A. Leven, *Nanophotonics*, ISTE Ltd, Newport Beach, Calif, USA, 2006.
- [4] M. A. Reed, J. N. Randall, R. J. Aggarwal, R. J. Matyi, T. M. Moore, and A. E. Wetsel, “Observation of discrete electronic states in a zero-dimensional semiconductor nanostructure,” *Physical Review Letters*, vol. 60, no. 6, pp. 535–537, 1988.
- [5] H. C. Ramirez, R. Ramirez-Alarcon, M. Corona, K. Garay-Palmett, and A. B. U’Ren, “Spontaneous parametric processes in modern optics,” *Optics & Photonics News*, vol. 22, pp. 36–41, 2011.
- [6] B. Clafin, D. C. Look, and D. R. Norton, “Changes in electrical characteristics of ZnO thin films due to environmental factors,” *Journal of Electronic Materials*, vol. 36, no. 4, pp. 442–445, 2007.
- [7] B. M. Monroy, G. Santana, A. Benami et al., “Photoluminescence of as-grown silicon nanocrystals embedded in silicon nitride: influence of atomic hydrogen abundance,” *Journal of Nanoscience and Nanotechnology*, vol. 9, no. 5, pp. 2902–2909, 2009.
- [8] C. Torres-Torres, L. Castañeda, and R. Torres-Martínez, “Evolution of the optical response in a nanostructured fluorine doped zinc oxide thin film,” *Semiconductor Science and Technology*, vol. 27, no. 11, p. 115016, 2012.
- [9] E. Fortunato, A. Gonçalves, A. Pimentel et al., “Zinc oxide, a multifunctional material: from material to device applications,” *Applied Physics A*, vol. 96, no. 1, pp. 197–205, 2009.
- [10] Ü. Özü, Y. I. Alivov, C. Liu et al., “A comprehensive review of ZnO materials and devices,” *Journal of Applied Physics*, vol. 98, no. 4, Article ID 041301, pp. 1–103, 2005.
- [11] K. Kyoungwon, C. D. Pulak, L. Deuk-Hee, K. Sangsig, and Y. L. Sang, “Effects of silver impurity on the structural, electrical and optical properties of ZnO nanowires,” *Nanoscale Research Letters*, vol. 6, p. 552, 2011.
- [12] L. Castañeda, M. Trejo-Valdez, and C. Torres-Torres, “Optical and photoconductive properties exhibited by silver doped zinc oxide thin films,” *Journal of Optics*. In press.
- [13] C. Torres-Torres, M. Trejo-Valdez, H. Sobral, P. Santiago-Jacinto, and J. A. Reyes-Esqueda, “Stimulated emission and optical third-order nonlinearity in Li-doped ZnO nanorods,” *Journal of Physical Chemistry C*, vol. 113, no. 31, pp. 13515–13521, 2009.
- [14] A. Smith and R. Rodríguez-Clemente, “Morphological differences in ZnO films deposited by the pyrosol technique: effect of HCl,” *Thin Solid Films*, vol. 345, no. 2, pp. 192–196, 1999.
- [15] L. Irimpan, V. P. N. Nampoore, and P. Radhakrishnan, “Spectral and nonlinear optical characteristics of ZnO nanocomposites,” *Science of Advanced Materials*, vol. 2, no. 2, pp. 117–137, 2010.
- [16] C. Torres-Torres, L. Tamayo-Rivera, R. Rangel-Rojo et al., “Ultrafast optical phase modulation with metallic nanoparticles in ion-implanted bilayer silica,” *Nanotechnol*, vol. 22, no. 35, Article ID 355710, 2011.
- [17] C. Forestiere, G. F. Walsh, G. Miano, and L. Dal Negro, “Nanoplasmonics of prime number arrays,” *Optics Express*, vol. 17, no. 26, pp. 24288–24303, 2009.